Controlled variation of intermolecular coupling in polycrystalline thin films of singlet fission chromophores

Dissertation
der Mathematisch-Naturwissenschaftlichen Fakultät
der Eberhard Karls Universität Tübingen
zur Erlangung des Grades eines
Doktors der Naturwissenschaften
(Dr. rer. nat.)

vorgelegt von
Clemens Frederik Zeiser
aus Berlin

Tübingen
2021

Gedruckt mit Genehmigung der Mathematisch-Naturwissenschaftlichen Fakultät der Eberhard Karls Universität Tübingen.

Tag der mündlichen Qualifikation:	29.09.2021
Dekan:	Prof. Dr. Thilo Stehle
1. Berichterstatterin:	JProf. Dr. Katharina Broch
2. Berichterstatterin:	Prof. Dr. Monika Fleischer
3. Berichterstatter:	Prof. Dr. Wolfgang Brütting

Deutsche Zusammenfassung

Organische Halbleiter sind kohlenstoffbasierte Verbindungen und vielversprechende Materialien für Anwendungen in optoelektronischen Bauteilen. Sie werden bereits vielfach in OLED-Displays eingesetzt, doch auch an einem Einsatz in der organischen Elektronik und organischen Photovoltaik wird intensiv geforscht. Unter anderem ist die Singulett-Spaltung (SF, von engl. singlet fission) im Bereich Photovoltaik aufgrund der verlustlosen Exzitonen-Vervielfältigung ein interessanter photophysikalischer Prozess. SF ist der spontane, Spin-erlaubte Übergang eines Singulett-Exzitons in zwei Triplett Exzitonen niedrigerer Energie, welcher die dissipationsfreie Konversion von hochenergetischen Photonen in zwei niederenergetischere Ladungsträgerpaare ermöglicht. Dieser Übergang resultiert aus dem Transfer von Elektronen zwischen benachbarten Molekülen, sodass ein gekoppelter Triplett-Paar-Zustand mit einem Gesamtspin von null ensteht, der anschließend in zwei unabhängige Triplett Exzitonen dissoziiert. Trotz intensiver Forschung ist SF nicht vollständig verstanden, was vor allem am komplexen Wechselspiel von intermolekularen Wechselwirkungen, Orbitalüberlapp, Molekülanordnung und der facettenreichen Anatomie des Triplett-Paar Zustands in verschiedenen Materialien liegt.

Eine der häufigsten Ansätze zur Untersuchung des SF Prozesses ist die künstliche Änderung der intermolekularen Wechselwirkung durch chemische Modifikationen und Messung derer Auswirkungen auf die SF. Beispielsweise kann durch Synthese von Dimeren die relative Anordnung von Chromophoren variiert, und der Einfluss des Orbitalüberlapps auf die SF Rate untersucht werden. In dieser Arbeit wird von drei verschiedenen Ansätzen zur Änderung von intermolekularen Wechselwirkungen berichtet, deren Auswirkungen auf die SF mit Hilfe von zeitaufgelösten Spektroskopiemessungen bestimmt wurden.

Im ersten Fall wird mit Hilfe von Fluorierung eines prototypischen SF Materials der Einfluss verschiedener Molekülorientierungen sowie der Änderung der Partialladungsverteilung auf SF untersucht. Es wird gezeigt, dass beide Parameter großen Einfluss auf den SF Prozess haben können. Insbesondere wird ein stark beschleunigter SF Prozess beobachtet, wenn Wechselwirkungen zwischen Partialladungen benachbarter Moleküle den intermolekularen Transfer von Elektronen begünstigen.

Im zweiten Fall werden SF Materialien mit schwach wechselwirkenden Materialien gemischt, um zu prüfen, ob eine veränderte Anzahl der benachbarten SF Moleküle eines angeregten Moleküls den SF Prozess beeinflusst. Es wird belegt, dass für bestimmte SF

Materialien ein linearer Zusammenhang zwischen der Anzahl der Nachbarn und der SF Rate besteht. Dies steht in starkem Kontrast zu früheren Berichten einer anderen Kategorie von SF Materialien, für welche eine reduzierte Anzahl an Nachbarn keinen Einfluss auf die SF hat. Durch Vergleich mit Berechnungen anderer Arbeitsgruppen, die die experimentellen Daten dieser Arbeit stützen, wird aufgezeigt, dass der Unterschied aus unterschiedlichen mikroskopischen Mechanismen der SF Prozesse resultiert und sich deshalb zur deren Identifikation eignet.

Schlussendlich werden zwei verschiedene SF Materialien gemischt, um zu erforschen inwieweit SF zu zwei Triplett Exzitonen auf chemisch unterschiedlichen Molekülen auftreten kann. Die zeitaufgelöste Beobachtung eines solchen Prozesses wird erstmals berichtet und dessen Zeitkonstante diskutiert. Des Weiteren wird untersucht, unter welchen Umständen er auftritt oder von konkurrierenden Prozessen unterdrückt wird. Die Ergebnisse dieses dritten Teils zeigen damit die Existenz eines weiteren Zerfallskanals für Singulett Exzitonen in Mischungen zweier SF Materialien auf.

Insbesondere durch das Mischen von SF Materialien werden in dieser Arbeit neue Ansätze zur Modifikation bisher kaum beachteter Parameter zur Untersuchung von SF Prozessen aufgezeigt. Die Untersuchungen dienen dem besseren Verständnis der Photophysik organischer Halbleiter und begünstigen eine gezieltere Entwicklung neuer Materialien.

Contents

1 Introduction **9**

2 Fundamentals **13**

2.1 Small-molecule organic semiconductors 13

2.2 Thin films of organic semiconductors 15

2.2.1 Molecular structure of neat thin films 16

2.2.2 Blends 18

2.3 Excited states and photophysical processes 21

2.3.1 Excited states of conjugated molecules 21

2.3.2 Excitons in aggregates 28

2.3.3 Exciton migration 35

2.4 Singlet exciton fission 37

2.4.1 Energetic requirements for the singlet fission process 38

2.4.2 The wavefunction of the triplet-pair state 38

2.4.3 History and techniques for experimental observation 39

2.4.4 Singlet fission mechanisms 40

2.4.5 Singlet fission in blends 43

2.4.6 Current research on singlet fission 46

3 Experimental techniques **49**

3.1 Organic molecular beam deposition 49

3.2 Structural and optical characterization 51

3.2.1 X-ray diffraction 51

3.2.2 Absorbance spectroscopy 54

3.3 Time-resolved techniques 56

3.3.1 Transient absorption (TA) spectroscopy 56

3.3.2 Time-resolved photoluminescence (TRPL) 60

4 Materials **65**

4.1 Acenes: tetracene and pentacene 65

4.2 Fluorinated pentacenes 70

4.3 Acene derivatives: anthradithiophene and rubrene 72

4.4 Phenacenes: picene and [6]-phenacene . . . 75

5 Results I: Singlet fission in fluorinated pentacenes 79
5.1 Structural characterization . . . 80
5.2 Optical characterization . . . 86
5.3 TA spectroscopy . . . 88
5.3.1 Feature assignment . . . 88
5.3.2 Global analysis . . . 91
5.4 Discussion . . . 96
5.4.1 Impact of face-to-face arrangement of molecules . . . 97
5.4.2 Altered coupling of electronic states . . . 99
5.5 Conclusion . . . 102

6 Results II: Singlet fission in blends with spacer molecules 105
6.1 Structural characterization . . . 106
6.2 Optical characterization . . . 110
6.3 TRPL spectroscopy . . . 113
6.3.1 Simulation of the fluorescence decays . . . 113
6.3.2 Experimental fluorescence decays . . . 115
6.3.3 Analysis of the initial decay rate . . . 116
6.3.4 Effects in addition to the replacement effect . . . 118
6.4 Comparison to previously reported spacer blend systems . . . 119
6.5 Calculations on the impact of vacancies on singlet fission in acenes . . . 121
6.6 Discussion . . . 123
6.7 Comparison with anthradithiophene blends . . . 124

7 Results III: Singlet heterofission 129
7.1 Structural characterization . . . 130
7.2 Optical characterization . . . 132
7.3 TA spectroscopy of the neat compounds . . . 133
7.4 TA spectroscopy without excitation of tetracene . . . 134
7.4.1 Feature assignment and global analysis . . . 134
7.4.2 Thermal artifacts . . . 136
7.4.3 5% pentacene blend . . . 138
7.5 TA spectroscopy with excitation of tetracene . . . 142
7.5.1 Feature assignment and global analysis . . . 142
7.5.2 Calculation of the Förster resonance energy transfer rate . . . 146
7.5.3 5% pentacene blend . . . 148
7.6 Conclusion . . . 150
7.7 Comparison with rubrene blends . . . 152
7.7.1 Optical microscopy . . . 152

7.7.2 Structural and optical characterization . . . 153
7.7.3 Fluorescence decays . . . 155

8 Conclusion and Outlook **161**
8.1 Conclusion . . . 161
8.2 Outlook . . . 163

A Appendix: Techniques and materials **165**
A.1 Description of molecular orientations in the unit cell . . . 165
A.2 Calculation of growth rates from the molar mixing ratio . . . 168

B Appendix: Fluorinated pentacenes **171**
B.1 Orientation of crystallites in reciprocal space maps . . . 171
B.2 Relation between molecular length and lattice spacing . . . 173
B.3 Davydov-splitting fits and photoluminescence spectra . . . 174
B.4 Fluence-dependent TA spectroscopy . . . 175
B.5 Degradation of samples during TA measurements . . . 182
B.6 Quantum chemistry calculations of molecular orbitals . . . 183

C Appendix: Spacer blends **185**
C.1 Magnetic field dependence of fluorescence decays . . . 185
C.2 Davydov splitting . . . 186
C.3 Details on TRPL measurements . . . 187

D Appendix: Blends of pentacene and tetracene **189**
D.1 Fluence-dependence of TA measurements on tetracene . . . 189
D.2 Global analysis results . . . 190
D.3 Förster resonance energy transfer rate . . . 192
D.4 Diffusion-limited energy transfer rate . . . 193

E Sample lists **195**

F List of contributions **201**

List of abbreviations **203**

Bibliography **205**

1. Introduction

Semiconducting materials are substantial for today's technological world, especially due to their use in integrated circuits [1, 2] and optoelectronic devices [3–5], including computers, displays, charge-coupled devices (CCDs), solar cells and many more. In the first decades after the invention of the field-effect-transistor, all these technologies were based on inorganic semiconductors such as silicon [6, 7]. In the past decades, however, carbon-based organic semiconductors (OSCs) emerged as alternative materials [8, 9], which can reach similar electron mobilities as amorphous silicon due to efficient migration of charge carriers between van der Waals bound molecules [10, 11]. OSCs feature a variety of advantages, such as strong absorption and emission of visible light [12, 13], tuning of the absorption and emission spectra through chemical modification [14, 15] as well as thin film production at low temperature from solution even on flexible substrates [16–18]. With these advantages, OSCs are already widely implemented in many displays as organic light emitting diodes (OLEDs) [19, 20] and current research also focuses on the improvement of organic photovoltaics (OPV) [21, 22], which is a promising cost-efficient alternative to silicon solar cells.

In particular the photophysical properties of OSCs render them interesting for OLEDs and OPV. In this work, a photophysical process in various OSCs named singlet fission (SF) is examined. SF is the spontaneous, spin-allowed conversion of a singlet exciton into two triplet excitons, mediated by the transfer of electrons between neighboring chromophores [23–26]. Several interests motivate the research on SF. First, SF is an interesting process from the viewpoint of fundamental research, since it is the dominating decay channel of singlet excitons in many OSCs [23, 27–29] and it involves a doubly excited state [23, 30–32]. Second, in devices, advantage can be taken of the non-dissipative downconversion from high-energy into low-energy excitons [33]. For instance, SF can help to overcome the Shockley-Queisser limit (34 % power efficiency for silicon [34–36]) of single-junction solar cells that arises from the dissipative relaxation of charge-carrier pairs to the band gap. With a sensitizing layer in which SF occurs, high-energy photons are converted into two low-energy excitons, which are subsequently transferred to the solar cell [37–43]. Using this downconversion, the power efficiency in OPV can be enhanced without the requirement of matching current outputs in tandem cells [34]. Finally, also in nature downconversion by SF can be found, for example in photosynthetic bacteria,

in which SF plays an important role as a photoprotection mechanism against harmful singlet oxygen production by chlorophyll [44–46].

For an efficient SF process, first, the energy of the triplet state in SF compounds has to be approximately half the energy of singlet states, a condition that is fulfilled for a large number of compounds [47, 48]. Second, strong interaction between the chromophores is required to facilitate the transfer of electrons to create a pair of neighboring triplet excitons [23, 26]. Third, a weak coupling between the created triplet excitons is needed to allow for their spatial separation [23, 26, 49]. Therefore, the rate and efficiency of the SF process can be very sensitive to the details of the intermolecular coupling, which has been found in recent years to be influenced by several system-dependent parameters. The most prominent of these parameters are the energy of charge-transfer states [50–52], the orbital overlap of the participating chromophores [53–55], the overall exothermicity [56–59], the electronic configuration of the excited state [60–63], the intermolecular potential energy surface [64–67] and the strength of electron-phonon coupling [68–73]. Despite progress in the understanding of SF in many systems, a complete picture of the microscopic mechanisms and key parameters of SF is still sought-after. In particular the various microscopic mechanisms for the conversion from the photoexcited singlet to an electronically coupled triplet-pair state complicate the development of such a unified picture. These mechanisms include the direct photoexcitation of triplet-pair contributions [50, 74], the mediation by intra- and intermolecular vibrations [61, 69–71, 75], the population of intermediate charge-transfer states [76–79] and nuclear reorganization [64–66, 80]. The conditions for the occurrence of one of these types are yet largely unclear and require further research [26].

There are several conceptually different, experimental approaches for studying the impact of the above mentioned parameters on the SF process [30, 67, 81–83]. Besides sophisticated spectroscopic techniques [81] for obtaining signatures of the SF mechanism, a very prominent approach is the variation of the coupling between chromophores and measurement of the impact on the SF process [49, 84–87]. This variation can for instance be achieved by altering the relative orientation of chromophores in dimers [76, 86–90]. However, studying SF with dissolved dimers has some disadvantages such as potential excimer formation [91–93], a relatively localized singlet exciton

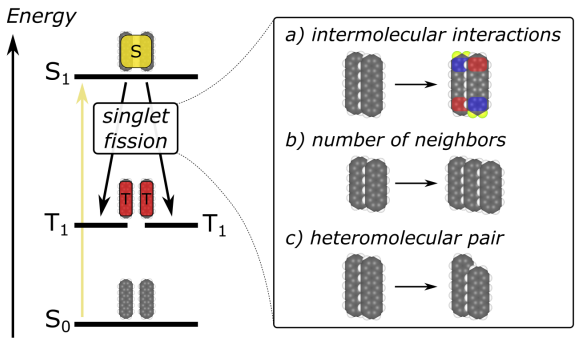


Figure 1.1: Scheme representing the investigations in this work.

compared to aggregates [59, 94, 95] and a restriction of triplets to neighboring chromophores [89, 96].

In this work, again the impact of varied intermolecular interactions and molecular environments on the SF process is investigated, see Fig. 1.1. In contrast to the above mentioned dimers, the investigated systems in this work are polycrystalline thin films [97, 98], in which the molecules are in a more rigid environment [72], singlet excitons can be delocalized [59, 94, 95] and created triplets can freely diffuse [49, 89, 96]. The variation is here achieved by partial fluorination of a known SF compound leading to altered molecular arrangements and couplings between electronic states (Ch. 5, see Fig. 1.1a) [84, 99, 100], or by mixing SF compounds with other OSCs (Ch. 6 and Ch. 7). Mixed thin films (blends) of OSCs prepared by vacuum co-deposition have been widely used as active layers in devices [101–103], as well as a tool for studying fundamental properties of OSCs by dilution of molecular aggregates [52, 104]. In blends of SF materials with high band gap spacer materials, as examined in Ch. 6, the impact of a reduced number of neighbors of an excited SF molecule on the SF rate can be investigated, see Fig. 1.1b [52, 105]. In Ch. 7, two different SF materials are mixed with each other, which opens up the possibility for heterofission of a singlet exciton into two triplet excitons located on different types of molecules (Fig. 1.1c) [78, 106–108].

The aim of this work is to gain a better understanding of the role of intermolecular interactions and molecular environments in the SF process by investigating how the partial charge distribution, the replacement of SF molecules or the possibility of heterofission impact the SF process in polycrystalline thin films.

The dissertation is organized as follows. In Ch. 2, the fundamentals for this work are briefly summarized. Details on the experimental techniques used in this work are provided in Ch. 3, including sample preparation, their basic characterization and the time-resolved techniques with which the SF process is probed. In Ch. 4 the materials employed in this work are listed and basic properties and observations previously reported are summarized.

In Chs. 5– 7, the results of this work are presented. Each of these chapters starts with a structural and steady-state optical characterization of the prepared samples, followed by the description and analysis of time-resolved measurements and a discussion with respect to literature. The subject of Ch. 5 is the investigation of the SF process in fluorinated compounds, which exhibit different molecular arrangements and couplings between electronic states compared to the parent SF material. In Ch. 6, the effect of a reduced number of neighbors of a SF molecule is investigated using blends of SF materials with high band gap spacer materials. The subject of Ch. 7 is heterofission in blends of two prototypical SF materials. In the final chapter of this work (Ch. 8), the results are summarized and an outlook on possible future work is given.

2. Fundamentals

This chapter gives a brief overview of the theoretical background relevant for this work. It starts with a brief introduction to OSCs, before thin films and blends of OSCs are discussed. The chapter continues with the description of excited states of conjugated molecules and excitons in aggregates. Finally, different SF mechanisms are discussed and a literature overview of SF is given.

2.1 Small-molecule organic semiconductors

In this section OSCs are briefly introduced. For further information on OSCs, the reader is referred to Refs. 8, 9, 109, 110. OSCs are carbon-based, molecular materials with semiconducting properties in the solid state [8, 9, 111]. The compounds studied in this work belong to the class of small-molecule OSCs [11, 112]. Prototypical small-molecule OSCs are polycyclic aromatic hydrocarbons (PAHs) [113], aromatic molecules that consist of carbon and hydrogen atoms. In PAHs, the tetravalent carbon atoms build a polycyclic backbone, while the monovalent hydrogen atoms simply terminate the remaining bonding sites. However, small-molecule OSCs are neither limited to polycyclic molecules [114, 115], nor to hydrocarbons [116], since also multivalent heteroatoms such as nitrogen, oxygen or sulfur can be incorporated into the backbone [117–120] and monovalent heteroatoms such as fluorine or chloride atoms can terminate the molecule [121–123]. Furthermore,

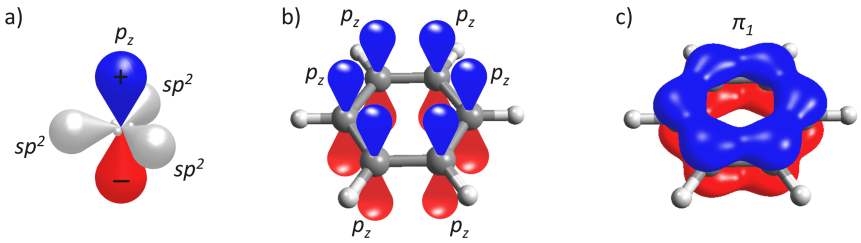


Figure 2.1: a) sp^2-hybridization of atomic orbitals [109]. Blue (+) and red (−) indicate the relative phase within one p_z-orbital. b) Relative orientation of p_z-orbitals of different carbon atoms before hybridization to the energetically lowest π-orbital of benzene. c) Energetically lowest π-orbital of benzene after hybridization of the p_z-orbitals. Calculated with the ArgusLab software using the ZINDO method.

side chains [49, 54, 85] or coordination centers with heavy atoms [124] can be connected to the polycyclic backbone of small-molecule OSCs.

Delocalized molecular orbitals, formed by $2p_z$-orbitals of the atoms in the backbone of OSCs, are fundamental for the electronic and photophysical properties of OSCs. The origin and properties of these molecular orbitals are briefly described in the following, focusing only on the electronic part of the wavefunction, while assuming the nuclei to be fixed at arbitrary coordinates. Additional contributions by vibrations will be discussed in Sec. 2.3.

In molecules, different atomic orbitals $\chi_i(r)$ hybridize to molecular orbitals $\varphi_m(r)$ with the position r of the electron. This hybridization can be described by a linear combination of atomic orbitals (LCAO)

$$\varphi_m(r) = \sum_i c_{mi}\, \chi_i(r) \tag{2.1}$$

with complex coefficients c_{mi} [125]. For bonds to other atoms, carbon atoms typically undergo a hybridization of the atomic orbitals of the second shell. Atoms in the polycyclic backbone of OSCs are typically sp^2-hybridized. Here, the 2s-, $2p_x$- and $2p_y$-orbitals hybridize to three sp^2-orbitals and the $2p_z$-orbital is unaltered, see Fig. 2.1a. The sp^2-hybridization therefore leads to three planar σ-bonds of the carbon atom to neighboring atoms [109].

In many cases it is a good approximation [109, 125] that the remaining p_z-orbitals after σ-bond formation are independent and hybridize to so-called π-orbitals. A hybridization of *two* p_z-orbitals such as in ethene (C_2H_4) leads to a bonding π-orbital and an antibonding $\pi^\star$-orbital, and occupation of the π-orbital with electrons yields a double-bond (a σ- and a π-bond) between the two carbon atoms [109]. For many molecules, such as butadiene (C_4H_6) and benzene (C_6H_6, Fig. 2.1b), the hybridization of p_z-orbitals to π-orbitals involves several atoms. The coupling of all p_z-orbitals and the delocalization of the π-electrons over all contributing atoms, as shown in Fig. 2.1c for benzene, is significantly more stable than the formation of alternating single- and double-bonds with localized electrons between two atoms [109, 125]. Such a coupling of more than two p_z-orbitals to delocalized, molecular π-orbitals is called conjugation and the molecule is called a conjugated molecule [109].

With the LCAO-approximation (Eq. 2.1), the p_z-orbitals of atoms in conjugated molecules can be combined with different complex coefficients to the same number of π-orbitals [125]. These different π-orbitals have different energies in analogy to the π- and the $\pi^\star$-orbital of ethene, and filling of the low-energy π-orbitals with electrons leads to a highest occupied molecular orbital (HOMO) and a lowest unoccupied molecular orbital (LUMO) [126] as shown for pentacene (PEN) in Fig. 2.2.

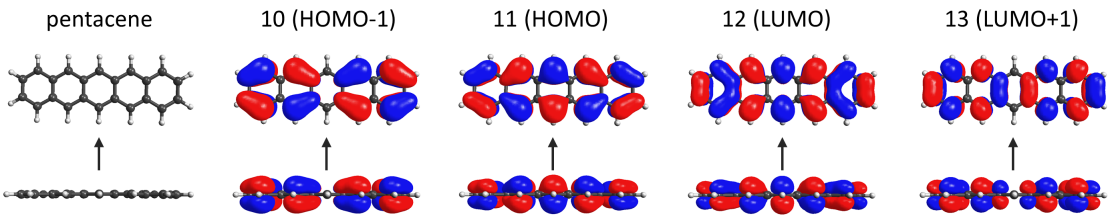


Figure 2.2: Chemical structure and four of the 22 molecular π-orbitals of PEN ($C_{22}H_{14}$). The orbitals are ordered by energy and labeled accordingly. Since low-energy orbitals are occupied with each two electrons, all orbitals until orbital number 11 (HOMO and below) are occupied, and all orbitals above (LUMO and above) are empty. The bottom row shows the side views on the structure and the molecular orbitals. Calculated with the ArgusLab software using the ZINDO method and consistent with Ref. 127.

While in butadiene, despite the conjugation, the bond lengths between the carbon atoms are not the same [128], the benzene molecule is strictly symmetric [129]. According to Hückel theory [125, 130], annulenes with $4n+2$ delocalized π-electrons are particularly stabilized by the symmetric, cyclic conjugation and are called aromatic compounds [109, 125]. For polycyclic molecules the definition of aromaticity is not as straightforward as for annulenes [131]. Prototypical examples are pyrene ($C_{16}H_{10}$) and coronene ($C_{24}H_{12}$), which are aromatic compounds with $4n$ π-electrons [132]. There has been an extensive discussion about the definition of aromaticity in polycyclic compounds [133, 134] and several qualitative rules for the determination of their resonance stability have been established [131].

By providing two important aspects, the presence of molecular π-orbitals with delocalized electrons is a crucial condition for both aromatic and non-aromatic OSCs [128, 131]. First, π-electrons are weakly bound, and the energies of π–$\pi^\star$ transitions are therefore on the order of $1-4\,\mathrm{eV}$, which is in the optical range in contrast to the much higher energies of σ–$\sigma^\star$ transitions of non-conjugated molecules [135]. Furthermore, the energy of π–$\pi^\star$ transitions can be tuned by the size of the conjugated system [127], leading to characteristic colors of conjugated compounds [12]. The conjugated backbones of molecules are therefore also called chromophores [136].

Second, π-orbitals have a high position probability above and below the molecular plane (see bottom row in Fig. 2.2), which facilitates orbital overlap between molecular orbitals of neighboring molecules. Therefore, many conjugated compounds are able to transfer electrons between neighboring molecules and consequently are OSCs [11]. These two properties, absorption of optical photons and intermolecular transfer of electrons, render conjugated molecules the ideal candidates for OPV [102].

2.2 Thin films of organic semiconductors

The investigations in this work are performed on thin films of OSCs, in which the molecules are physically bound to each other by van der Waals forces [8, 137]. The thin films

were prepared by vacuum deposition (see Sec. 3.1), in which evaporated molecules hit a substrate, diffuse, nucleate and form islands on a micrometer-scale [138–140]. As a non-equilibrium process, the description of deposition and island formation is complex, and since the morphology of the thin films is not in the scope of this work, the reader is referred to Refs. 138, 139 and 140 for details. The molecular structure of the thin films, however, can have a large impact on the photophysics of the sample, since it includes the relative orientation and thus the interaction of neighboring molecules. Therefore, the molecular structure of neat thin films and blends is briefly described in this section.

2.2.1 Molecular structure of neat thin films

Depending on their structural order, thin films can be categorized into

- uniaxially anisotropic polycrystalline films
- isotropic polycrystalline films ("powder-like")
- amorphous films

as well as further, special types [141–143]. In contrast to single crystals (one, macroscopically large molecular crystal), polycrystalline films consist of many, microscopically small, coalesced crystallites. In thin films, these crystallites can all have the same orientation with respect to the substrate normal, but a random orientation regarding the rotation around this axis. In this case, the film is uniaxially anisotropic with differing properties in the in-plane and out-of-plane direction. In contrast, also isotropic polycrystalline films exist, for which the crystallites do not exhibit a fixed orientation with respect to the substrate. In amorphous films, no long-range order is present.

The description of the structure [144, 145] of microscopic crystallites is analogous to that of macroscopic molecular or atomic crystals and can be found in Refs 146–148. In brief, a crystal lattice can be described by three linearly independent, primitive lattice vectors $\mathbf{a}_1$, $\mathbf{a}_2$ and $\mathbf{a}_3$, for which a lattice point is reached by a linear combination with integer coefficients. The unit cell, defined by the primitive lattice vectors, is usually described by six parameters: the lengths of the three vectors, called a, b and c, as well as the three angles α, β and γ between the vectors corresponding to b and c, a and c, as well as a and b, respectively, see Fig. 2.3a and 2.3b.

For each lattice point, a repeating unit exists, which consists of one or several molecules with a certain orientation with respect to the crystal lattice and which is called the basis of the crystal. An important type of aggregate for this work is the so-called herringbone (HB) aggregate. The basis of a HB aggregate consists of two molecules and the crystal lattice can be of almost any symmetry [149]. However, the two molecules constituting the basis have a very characteristic orientation [150]. The centers of mass of molecules in a HB aggregate form distinct planes, which are called molecular planes in the following and are typically parallel to the substrate plane for crystallites in uniaxially anisotropic films.

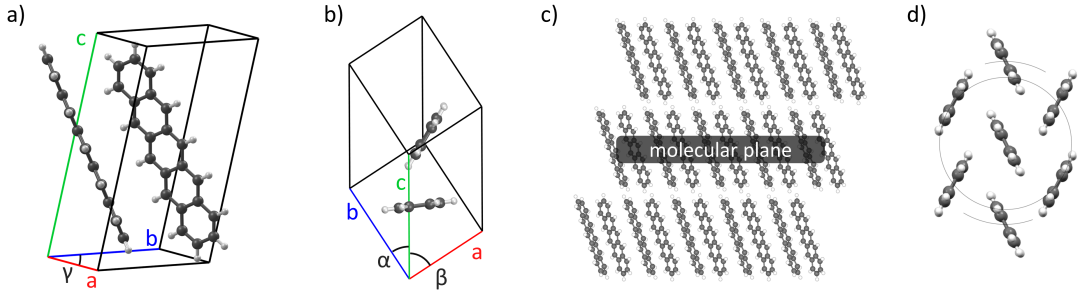


Figure 2.3: Crystal structure of PEN [152]. a) Side view of the unit cell, parallel to the short axis of a molecule. b) Top view of the unit cell, parallel to the long axis of a molecule. c) Side view of molecular planes. d) Top view of a molecular plane, with the four nearest neighbors and the two second-nearest neighbors. The circle and the arcs show the larger difference of the center of mass of the second-nearest neighbor to that of the central molecule compared to the nearest neighbors. Note that the top views are not perpendicular on the molecular planes.

For the description of the HB aggregates, a primitive unit cell is usually chosen, for which the ab-plane is parallel to the molecular planes [151] (see Fig. 2.3a and 2.3b). The molecular long axes of the two basis molecules are oriented parallel to each other and with a large angle to the molecular planes (Fig. 2.3c). Furthermore, the short axes of the two molecules have a nonzero angle, see Fig. 2.3b, which is called the HB angle [150].

Since within each molecular plane the intermolecular distances are much smaller and thus the electronic interactions are much larger than between molecular planes, the relative orientation of molecules in one molecular plane has a much larger impact on electronic and optical properties than that of molecules in different molecular planes [153]. Within a molecular plane, a molecule has four nearest neighbors [52], which are translationally inequivalent, and two second-nearest neighbors, which are translationally equivalent molecules along the shorter in-plane axis of the unit cell, see Fig. 2.3d.

The orientation of molecules with respect to the molecular plane can be described with three Euler angles [154], which are the direction of the long axis within the molecular plane Θ, the inclination angle χ of the long axis to the substrate normal as well as the tilt angle φ around the long axis (see Apx. A.1) [154]. With parallel long axes of molecules in a HB aggregate, the difference between φ of the two molecules is the HB angle, which is typically between 50° and 60° [150, 154].

Besides the HB angle also the values of φ of the two basis-molecules can be used for comparison of different HB aggregates and further (sub-) categorization. While some HB aggregates like crystalline phenacenes exhibit the same absolute value of φ for the two basis molecules [155, 156], acenes exhibit HB aggregates with very different absolute values of φ for the two basis-molecules (see Apx. A.1) [149, 152]. The two basis-molecules in HB aggregates of the latter category can therefore be distinguished by one rather facing the substrate with its molecular plane, and one rather being oriented with the edge pointing to the substrate. For further details the reader is referred to Apx. A.1 [149, 152].

2.2.2 Blends

In this work, mixed thin films were prepared by co-deposition of OSCs (see Sec. 3.1) in order to study the differences of their photophysical properties compared to those of neat compounds [157, 158]. In the following, different scenarios of mixing are briefly described. For further details on the formation of mixed crystals, see Refs. 157 and 159.

Free energy of a mixed crystal

A simple model for the mixing behavior of two compounds A and B with relative concentrations x_A and x_B is obtained by regarding the molecules as spheres with only nearest-neighbor interaction (see Fig. 2.4) and minimizing the free energy

$$\Delta F_{\text{mix}} = k_{\text{B}}T\left[(x_A \ln x_A + x_B \ln x_B) + \chi x_A x_B\right] \ , \tag{2.2}$$

where χ is the interaction parameter [157, 159]. The first term in Eq. 2.2 is the entropic contribution to the free energy, which always favors intermixing [157], while the latter term is the energy gain. The interaction parameter χ is determined by the interaction energy between same (W_{AA} and W_{BB}) and different (W_{AB}) neighboring spheres in the lattice, and is

$$\chi = \frac{Z}{k_{\text{B}}T}\left(W_{\text{AA}} + W_{\text{BB}} - 2W_{\text{AB}}\right) \tag{2.3}$$

with the coordination number Z. Different values of χ can lead to three mixing scenarios at low temperature and close to equilibrium [157], which are sketched in Fig. 2.4. If $2W_{\text{AB}}$ is much larger than the sum of W_{AA} and W_{BB} ($\chi < 0$), the free energy is minimized by neighboring molecules of different kinds and an ordered complex forms (Fig. 2.4a). With an excess of molecules of either compound, the system phase separates in a neat phase and a phase of equimolar mixture [104]. If the sum of W_{AA} and W_{BB} is much larger than $2W_{\text{AB}}$ ($\chi > 2$), neighboring molecules of the same kind reduce the energy and the system phase separates into neat phases (Fig. 2.4c).

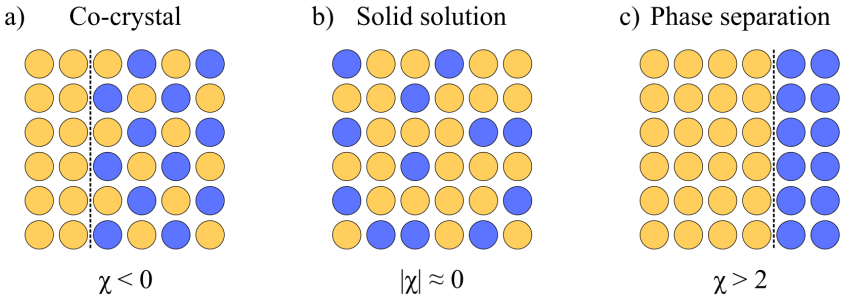


Figure 2.4: Mixing scenarios of spheres at low temperature and in equilibrium [157]. Blue ($x_A = 33\,\%$) and yellow ($x_B = 67\,\%$) spheres show different compounds [159]. Inspired by Ref. 157.



Figure 2.5: Simulation of binary solid solutions in a 30x30 grid. Blue and yellow colored pixels represent molecules of the different compounds. The concentration of yellow pixels is given in the respective panel.

Finally, if the entropic contribution is much larger than the energy gain ($\chi \approx 0$), the state with the largest entropy minimizes the free energy, i.e. the random occupation of all lattice sites by either molecule (Fig. 2.4b and Fig. 2.5). This type of intermixing is called a solid solution [157, 160].

Coefficient of geometrical similarity

The above model for intermixing is valid for spheres, whose interaction can be described with the three system-specific parameters W_{AA}, W_{BB} and W_{AB}. This model is well suited for the description of atomic crystals and already captures the mixing behavior of molecules with similar shapes [157]. Nevertheless, for mixed molecular crystals, not only the interaction between two neighboring molecules is of importance, but also their ability to arrange in a common crystal lattice without steric hindrance [145, 159].

Therefore, another important criterion for molecular intermixing is a large coefficient of geometrical similarity ε [145, 159]. This coefficient describes the maximum overlap of two different, superimposed molecules and thus their similarity in shape and size. Geometrically similar molecules (i.e. a large ε) are more likely to arrange in a common crystal lattice than geometrically rather different molecules (i.e. a small ε) and are therefore more likely to intermix [145, 159]. Connected to this criterion is the long known tendency of molecular crystals to maximize the density [145, 159], hence closely packed structures are favored.

Local environment configurations of solid solutions

In this work, solid solutions are employed for the investigation of the impact of different molecular environments on the photophysics of an excited molecule. Solid solutions allow for a replacement of the nearest neighbors (see Fig. 2.3d) of a molecule of interest (MOI). However, since the occupation of lattice sites in a solid solution is random (see Fig. 2.5), different MOIs within a blend have different local environment configurations (LECs), see Fig. 2.6a. Regarding the photophysics, this distribution of LECs can lead to the observation of a superposition of different behaviors and is therefore important to include in the discussion.

For the description of the photophysics of a solid solution that is a HB aggregate, in a first approximation, one can consider the interaction of the four nearest neighbors

of a MOI (Fig. 2.3d), although coupling to non-nearest neighbors can also impact the photophysics [153]. With four nearest neighbors of a MOI, there are five different LECs, as shown in Fig. 2.6a. With the LEC_n, the MOI has n molecules of the same kind as nearest neighbors, and $4-n$ molecules of the respective other kind. The number of nearest neighbors of the same kind of a MOI is for simplicity only called the number of nearest neighbors in this work. The probability $B_n(c)$ of a MOI for a LEC_n in a blend with molar mixing ratio c is described by a binomial distribution,

$$B_n(c) = \binom{4}{n} \cdot c^n \cdot (1-c)^{4-n} \,, \tag{2.4}$$

which is shown for all five LECs in Fig. 2.6b. As a result, most MOIs are surrounded by none, one, two, three or four molecules of the same kind for concentrations between $0-20\,\%$, $20-40\,\%$, $40-60\,\%$, $60-80\,\%$ and $80-100\,\%$, respectively. The average number of nearest neighbors n_{AvNN} of MOIs in a solid solution is calculated by

$$n_{\mathrm{AvNN}} = \sum_{n=1}^{4} n\, B_n(c) = \sum_{n=1}^{4} n \binom{4}{n} \cdot c^n \cdot (1-c)^{4-n} = 4\,c \,, \tag{2.5}$$

and hence is four times the concentration c due to the linear expectation value of a binomial distribution.

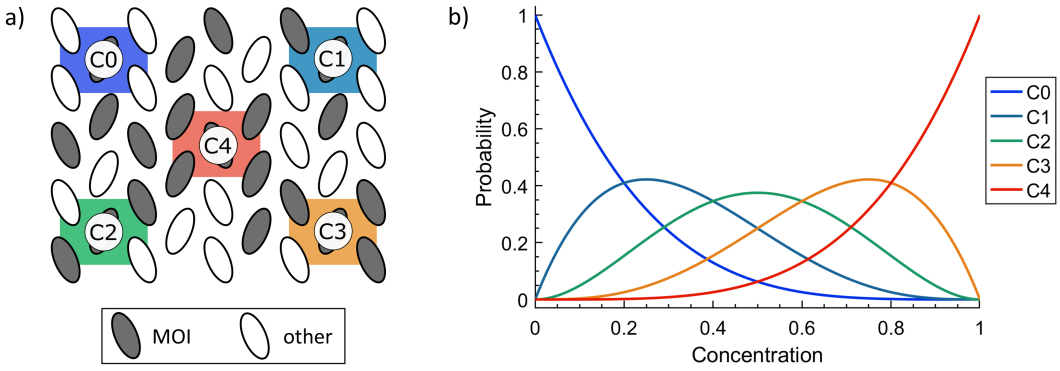


Figure 2.6: a) Sketch of a molecular plane of a mixed HB aggregate in top view (compare Fig. 2.3d) as well as the five configurations (LECs, see text) that occur therein. b) Probability of LEC_n in a solid solution with four nearest neighbors of a molecule of interest (MOI), described by a binomial distribution. The LEC_n are named Cn in this figure.

2.3 Excited states and photophysical processes

Absorption of optical photons by molecules brings the latter into electronically excited states, in which electrons are transferred to orbitals of higher energy and leave a hole in their initial orbital. Bound electron-hole pairs in aggregates are called excitons in both organic and inorganic materials. In this section, excited states of isolated molecules, excitons and some of their relevant properties for this work are discussed. Comprehensive overviews and further details on excitons and molecular photophysics can be found in the literature, e.g. in Refs. 8, 110 and 161.

2.3.1 Excited states of conjugated molecules

A basis for the description of excitons in molecular aggregates are excited states of single molecules, which are therefore briefly described in the following.

Born-Oppenheimer-approximation

The description of excited states of conjugated molecules relies on the molecular orbitals $\varphi_m(r)$ described in Sec. 2.1. There, the nuclei have been assumed to be fixed at arbitrary coordinates. However, since vibrations of molecules can strongly impact their photophysics, the impact of nuclear degrees of freedom is briefly discussed before the description of electronically excited states. For details on this description, see Refs. 162 and 163.

The hamiltonian of a molecule can be written as [162],

$$H = T_{\mathrm{el}}(r) + T_{\mathrm{nuc}}(Q) + U(r,Q) \tag{2.6}$$

with the electronic coordinates r, the nuclear coordinates Q, the kinetic energy of the electrons $T_{\mathrm{el}}(r)$ and the nuclei $T_{\mathrm{nuc}}(Q)$, as well as the Coulomb interaction of all electrons and nuclei $U(r,Q)$. Within the Born-Oppenheimer-approximation (BOA), the electrons react much faster to external disturbances due to their lower mass, and hence their wavefunction solves a Schrödinger equation without the nuclear kinetic energy term,

$$[T_{\mathrm{el}}(r) + U(r,Q)]\ \psi^n_{\mathrm{el}}(r,Q) = E_n(Q)\ \psi^n_{\mathrm{el}}(r,Q) \tag{2.7}$$

with the electronic wavefunctions $\psi^n_{\mathrm{el}}(r,Q)$ that parametrically depend on the quasi-static nuclear configuration Q. With varying Q, the electronic energy $E_n(Q)$ also changes along with this wavefunction. Therefore, a potential energy surface (PES) is determined by the above Schrödinger equation in the multi-dimensional space of the nuclear coordinates Q with a minimum at some configuration Q_0. The wavefunctions of the nuclei $\psi^{n\nu}_{\mathrm{nuc}}(Q)$ within this potential $E_n(Q)$ solve the equation

$$[T_{\mathrm{nuc}}(Q) + E_n(Q)]\ \psi^{n\nu}_{\mathrm{nuc}}(Q) = E^{n\nu}_{\mathrm{mol}}\ \psi^{n\nu}_{\mathrm{nuc}}(Q) \tag{2.8}$$

with the total molecular energy $E^{n\nu}_{\mathrm{mol}} = E_n(Q_0) + E_\nu$ of electrons and nuclei. The different solutions of this equation describe the vibration of the nuclei with quantum number ν in the PES given by the electronic state with quantum number n. The states, in which the molecule is neither in the electronic ($n > 1$), nor in the vibrational ($\nu > 1$) ground state, are called vibronic (vibrational + electronic) states. Finally, within the BOA, the total wavefunction of the molecule is the product

$$\Psi^{n\nu}_{\mathrm{mol}}(r, Q) = \psi^{n}_{\mathrm{el}}(r, Q) \cdot \psi^{n\nu}_{\mathrm{nuc}}(Q) \tag{2.9}$$

of the electronic and the nuclear wavefunction. Notice that the BOA is only valid if energy levels of the same spin multiplicity are well separated. If the energy levels are close and if the electronic and the nuclear wavefunction cannot be separated, the BOA breaks down and avoided crossings and conical intersections are formed [164, 165]. If translations and rotations of the whole molecule play a minor role, the nuclear wavefunction can further be restricted to only describe vibrations [163]. Nuclear wavefunctions in molecules typically have a spatial extent of a few picometers to a few tens of picometers [163, 166].

In the following, the electronic wavefunction $\psi^{n}_{\mathrm{el}}(r, Q)$ is discussed in more detail. Since this wavefunction only parametrically depends on Q within the BOA, the dependence is not always explicitly mentioned in this description.

Electron configurations

The molecular orbitals $\varphi_m(r)$ in Eq. 2.1 are spatial wavefunctions of a single electron with the orbital index m and the position r of the electron. Under the assumption that N electrons indexed by i independently occupy these one-electron orbitals, product wavefunctions

$$\psi^{n}_{\mathrm{el}}(r_1, r_2, ..., r_N) = \prod_i \varphi_m(r_i) \tag{2.10}$$

with different combinations of m are the spatial many-electron wavefunctions [110]. With these product wavefunctions, electrons are assumed to behave independently from each other, i.e. electron correlation is neglected. Electron correlation due to Coulomb repulsion between the electrons, however, can strongly impact the excited states of molecules [110], and for their description a basis of different many-electron wavefunctions is required.

Such a basis for the description of many-electron wavefunctions are Slater determinants [167] (or configurations) of one-electron spin orbitals. Most configurations correspond to very high energies (those with many electrons occupying the high-energy orbitals) and only those configurations with most electrons in low-energy molecular orbitals are significant for the description of the energetically lowest excited states.

The configuration of lowest energy is for most molecules the one in which all electrons pairwise occupy the spin orbitals with the lowest energies. Other configurations with overall spin zero (singlets) but next higher energy typically correspond to a promotion of

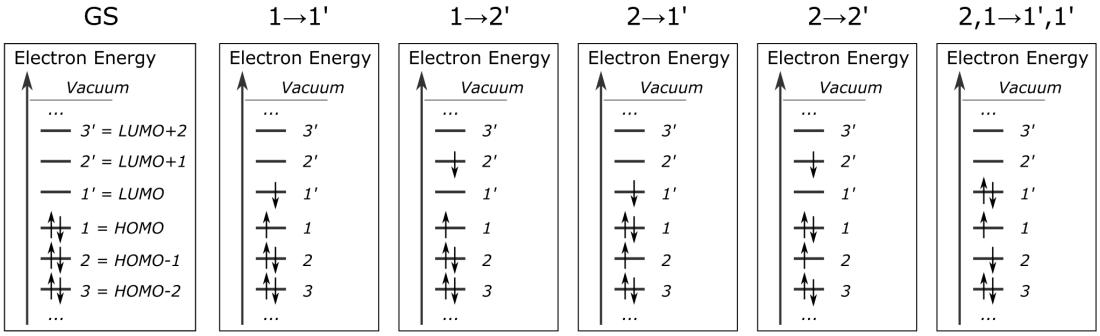


Figure 2.7: Selected configurations of electrons in a molecule [110, 127]. A configuration $n_1, n_2, ... \rightarrow m_1', m_2', ...$ is reached from the ground state (GS) upon transferring electrons from molecular orbital n_i to m_i' as labeled in the figure. Inspired by Ref. 110.

one electron to a spin orbital of higher energy, as shown for four representatives in Fig. 2.7. However, also configurations with two electrons being transferred (last configuration in Fig. 2.7) can play a role for the description of excited states. In addition to the spin-singlet configurations as defined in Fig. 2.7, there are also configurations of higher spin-multiplicity (triplet, quintet,...) reached by spin-flips of one or some of the electrons.

Electronic eigenstates of a molecule

The configurations of one-electron orbitals are not eigenstates of the electronic hamiltonian at fixed Q due to the repulsive Coulomb interaction between electrons. This interaction can be seen as a perturbation of the configurations and mixes those of same spin-multiplicity into true electronic eigenstates, which is called configuration interaction (CI) [110]. After determination of the electronic eigenstates and their energies, the singlet states are labeled S_n ($n \geq 0$) and the triplet states T_n ($n \geq 1$), with n being an integer number describing the energetic ordering as shown in Fig. 2.8. Due to the Coulomb attraction between electrons and holes, the energy difference between S_0 and S_1 is generally smaller than that between HOMO and LUMO (see Fig. 2.8).

The CI depends on the nuclear configuration Q, which leads to changing superpositions of electron configurations (called character of the state) with varying Q [168]. The eigenstates of the electronic hamiltonian at fixed Q are called adiabatic states. In contrast, so-called diabatic states can be defined, whose characters do not depend on Q [75, 168].

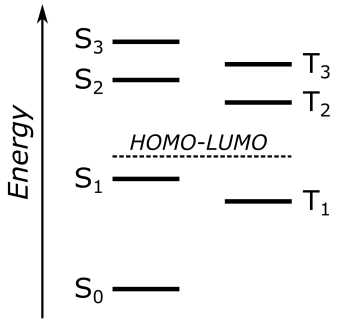


Figure 2.8: Qualitative singlet (S_n) and triplet (T_n) state energies of a typical conjugated molecule [110]. The dotted line labeled by HOMO-LUMO shows the energetic difference between the two one-electron orbitals.

For example, the different states $n \to m'$ are diabatic states, even though the molecular orbitals are altered with varying Q. Diabatic states have a clear physical interpretation but are in general no eigenstates of the electronic hamiltonian.

Since $1 \to 2'$ and $2 \to 1'$ are typically very close in energy, these states are mixed by CI with almost equal coefficients. Therefore, the first excited states of many PAHs can be classified into four states based on HOMO-1, HOMO, LUMO and LUMO+1, as proposed and named by J. R. Platt in 1949 [169–171]. In this classification the state ^1L_a has a dominant $1 \to 1'$ configuration, ^1L_b and ^1B_b are dominantly a superposition of $1 \to 2'$ and $2 \to 1'$ and ^1B_a has a dominant $2 \to 2'$ configuration [171], also see Tab. 2.1 later on.

Singlet-triplet splitting

Additional to CI, another effect of the Coulomb repulsion between electrons is the exchange energy, which leads to an energy difference between the S_n and the T_n states [110], see Fig. 2.8 mentioned before. Exchange energy results from the indistinguishability of the interacting electrons and is obtained from off-diagonal matrix elements of the electron interaction operator. Each of these matrix elements are calculated from two configurations with exchanged electrons. In an $n \to m'$ state, reached by the promotion of a single electron, there are several electrons in closed shells as well as two unpaired electrons, one in the HOMO$-n+1$ and one in the LUMO$+m-1$. These unpaired electrons lead to a different exchange energy depending on their total spin. A total spin of zero (one) denotes an antisymmetric (symmetric) spin function upon exchange of the two electrons. Since the total wavefunction of the two fermions must be antisymmetric, the spin impacts the symmetry of the spatial wavefunction and thus the sign of the exchange energy. Due to the positive sign of the contribution of the Coulomb repulsion, the energy of the triplet state (antisymmetric spatial wavefunction) is lowered by the exchange interaction relative to the energy of the singlet state (symmetric spatial wavefunction).

This energy difference between singlet and triplet states can be seen to originate from a larger average distance of the two unpaired electrons in the triplet state relative to that in the singlet state, which minimizes Coulomb repulsion. The exchange energy depends on the product of different spatial orbitals and therefore strongly varies with their overlap. If the orbitals of two unpaired electrons are localized at different sites of a molecule, singlet-triplet splitting does not occur [23].

Electronic transitions by electromagnetic radiation

Conjugated molecules can be excited by electromagnetic waves with a typical photon energy of $1-4\,\mathrm{eV}$. The influence of the electromagnetic wave on the molecule can be approximated as a perturbation to the eigenstates of the molecular hamiltonian, and is proportional to $\boldsymbol{E}(t) \cdot \boldsymbol{d}$ assuming the photon wavelength is much larger than the molecule (dipole-approximation) [172]. Here, $\boldsymbol{E}(t)$ is the electromagnetic field with amplitude $\boldsymbol{E}_0$ and $\boldsymbol{d} = e\boldsymbol{r}$ is the dipole of the molecule with the position vector $\boldsymbol{r}$ and the elementary

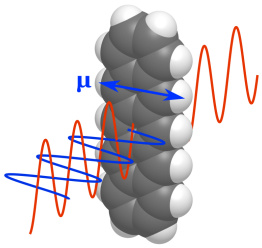


Figure 2.9: Transition dipole moment $\boldsymbol{\mu}$ along the short axis of a molecule and an electromagnetic wave with parallel (blue) and perpendicular (red) polarization relative to $\boldsymbol{\mu}$. While the photons with the parallel polarization can be absorbed, photons with perpendicular polarization are transmitted.

charge e. Using Fermi's golden rule for this perturbation, the transition rate between the molecular states $|S_0, \nu\rangle$ and $|S_n, \tilde{\nu}\rangle$ with the electronic wavefunctions $|S_n\rangle$ and $|S_0\rangle$ and the vibrational wavefunctions $|\tilde{\nu}\rangle$ and $|\nu\rangle$ in the respective PES (see Eq. 2.9) can be calculated. Note that the description of absorption or emission from or to other electronic states is analogous. For simplicity, the spin part of the electronic wavefunction is here omitted and only the spatial part is considered. Without spin-orbit coupling, the spin part prevents transitions between different spin states. One obtains

$$\begin{aligned} \Gamma^{\nu-\tilde{\nu}}_{S_0 \to S_n} &\propto |\langle S_n, \tilde{\nu}| \, \boldsymbol{E}_0 \cdot \boldsymbol{d} \, |S_0, \nu\rangle|^2 = |\boldsymbol{E}_0 \cdot \langle S_n| \, \boldsymbol{d} \, |S_0\rangle|^2 \cdot |\langle \tilde{\nu} \,|\, \nu\rangle|^2 \\ &= |\boldsymbol{E}_0 \cdot \boldsymbol{\mu}_n|^2 \cdot |\langle \tilde{\nu} \,|\, \nu\rangle|^2 \end{aligned} \tag{2.11}$$

with the transition dipole moment (TDM) $\boldsymbol{\mu}$ of the $S_0 \to S_n$ transition [110], which is an off-diagonal matrix element of the dipole operator,

$$\boldsymbol{\mu}_n = \langle S_n| \, \boldsymbol{d} \, |S_0\rangle \ . \tag{2.12}$$

The first factor in Eq. 2.11 is a scalar product between the electric field and the TDM. The absolute value of the TDM is related to the oscillator strength, which describes the ability to absorb photons [110]. Furthermore, the TDM is a vector that points in a certain direction relative to the molecule. An electromagnetic wave can only excite the molecule, if (part of) its polarization points along the TDM, while an electromagnetic wave perpendicular to the TDM cannot excite the molecule, as sketched in Fig. 2.9. Transitions from S_0 to electronically higher lying singlet states (see Sec. 2.3.1) typically have characteris-

Table 2.1: Typical first excited states of PAHs and absorption band names from S_0 after J. R. Platt [169–171]. The last four columns qualitatively give oscillator strengths with respect to the p-band and polarizations with respect to the molecular axes of the absorption bands for anthracene and phenanthrene [170, 173, 174].

			anthracene		*phenanthrene*	
state	dom. config.	band	rel. $\lvert\mu\rvert$	axis	rel. $\lvert\mu\rvert$	axis
^1L_a	$1 \to 1'$	p	medium (ref.)	short	medium (ref.)	long
^1L_b	$1 \to 2' - 2 \to 1'$	α	very small	long	very small	short
^1B_b	$1 \to 2' + 2 \to 1'$	β	high	long	medium	short
^1B_a	$2 \to 2'$	β'	medium	short	high	long

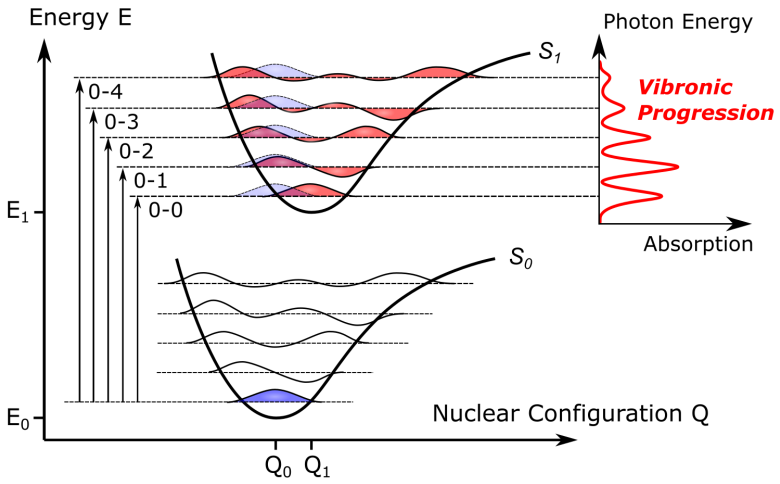


Figure 2.10: PESs of the singlet ground and excited state with wavefunctions of the nuclei [110]. The overlap of the blue initial nuclear wavefunction and the red final nuclear wavefunctions is the probability for a transition into this new state of the nuclei upon electronic excitation from S_0 to S_1. The inset shows a typical vibronic progression due to absorption into the vibronic sublevels. Inspired by Ref. 110.

tic oscillator strengths and polarizations depending on the electron configurations of the states, see Tab. 2.1.

The second factor $|\langle\tilde{\nu}\,|\,\nu\rangle|^2$ in Eq. 2.11 is called Franck-Condon factor and describes the spatial overlap of initial and final nuclear wavefunction. Upon photoexcitation, the electronic state of the whole molecule changes without movement of the nuclei (Franck-Condon-principle [175]), and therefore the transition rate decreases with a decreasing Franck-Condon factor.

In the proximity of a minimum of a PES (Eq. 2.7), it can be approximated as a multi-dimensional harmonic oscillator, giving rise to equidistant energy levels of the nuclei in each electronic state (Eq. 2.8), as sketched for S_0 and S_1 states in Fig. 2.10. Vibronic transitions into these different states lead to a so-called vibronic progression of optical spectra, as it is shown schematically in the inset of Fig. 2.10. Generally, a transition from a vibrational state ν in any PES to a vibrational state $\tilde{\nu}$ in another PES is called a ν-$\tilde{\nu}$ transition, e.g. the 0-0, 0-1, ... 0-4 transitions between the PESs of S_0 and S_1 as shown in Fig. 2.10. The Franck-Condon factors related to these transitions can be observed as their relative absorption strengths in the vibronic progression.

If the PES of the initial and the final state would have the same Q_0 and shape, all Franck-Condon factors except the one corresponding to the 0-0 transition would be zero. However, different electronic states generally create PESs with a slightly different Q_0 and different shapes, leading to nonzero Franck-Condon factors also of the other transitions. It can be shown that for shifted harmonic potentials, the intensities of a vibronic progression follow a Poisson distribution [153]. Due to the multi-dimensional PES with non-degenerate vibrational states, the actual experimental vibronic progression is a superposition of many energetically different absorption peaks [162].

Photophysical processes of single molecules

Photophysical processes are processes that occur after photoexcitation of a material and include transitions between electronic and vibronic states of single molecules. These transitions are shown in the so-called Jablonski diagram in Fig. 2.11. For a comprehensive overview and details on photophysical processes, see Refs. 161 and 176.

Transitions between electronic and vibronic states can occur spontaneous or externally stimulated and can include the absorption or emission of a photon. They can further be divided in three categories, namely

1) transitions between vibrational states of the same electronic state

2) transitions between electronic and vibronic states of same spin-multiplicity

3) transitions between electronic and vibronic states of different spin-multiplicity.

One important transition of the first category is the radiationless vibrational relaxation of a vibrationally excited state to the vibrational ground state, which is typically very fast [177]. Therefore, the latter two types of photophysical processes commonly start in the vibrational ground state of the initial electronic state and may end in vibrationally excited states of the final electronic state, which is determined by the energy conservation (see Fig. 2.11).

Spontaneous transitions of the second category are internal conversion (IC) [178], which is the radiationless transition to another electronic state, and fluorescence, which involves

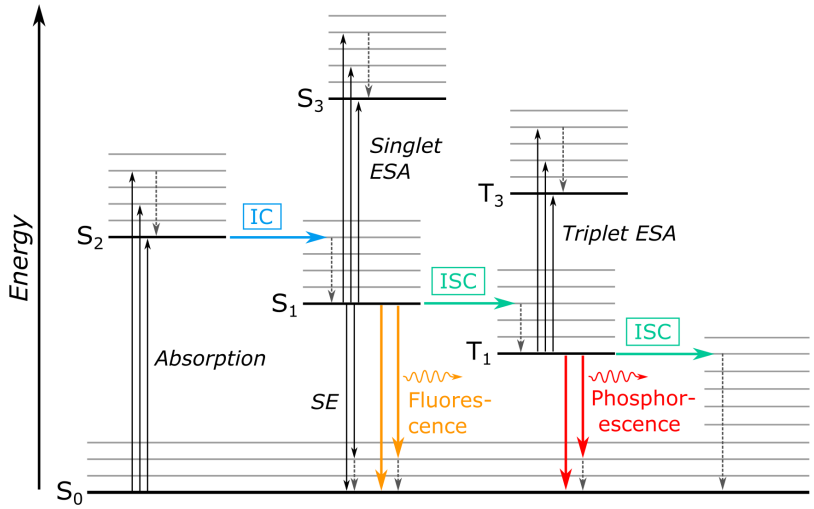


Figure 2.11: Jablonski diagram with photophysical processes that can occur after excitation of S_2 [110]. The thick lines are the vibrational ground states of the respective electronic state, the grey lines are higher lying vibrational states. Dotted arrows represent vibrational relaxation processes. Solid, black arrows indicate transitions that require external stimulation, colored arrows indicate spontaneous transitions. The horizontal axis has no deeper meaning than a typical temporal ordering of the processes that are shown. Inspired by Ref. 110.

the emission of a photon. Externally stimulated processes of the second category are the absorption of a photon starting from S_0 (ground state absorption), S_1 and T_1 (excited state absorption, ESA), as well as stimulated emission (SE) from S_1 to S_0. The third category includes the radiationless intersystem crossing (ISC) from a singlet to a triplet state or vice versa [177, 178], as well as phosphorescence from T_1 to S_0 upon emission of a photon.

After photoexcitation and subsequent vibrational relaxation, electronic relaxation within the singlet manifold can occur via IC and fluorescence. Although it is noteworthy that also fluorescence from S_2 to S_1 and from S_2 to S_0 can be observed in rare cases [179, 180], for most compounds, IC dominates for the relaxation from $S_{n\geq 2}$ stepwise down to S_1, while fluorescence dominates over IC for the transition from S_1 to S_0 due to a larger energy gap [178, 181]. Therefore, even excitation of $S_{n\geq 2}$ leads to fluorescence only from the S_1 state, which is called Kasha's rule [182].

While IC from $S_{n\geq 2}$ is typically too fast for ISC to occur, ISC can be very efficient from S_1 for molecules with strong spin-orbit coupling [183]. Therefore, in particular molecules including heavy atoms or non-planar molecules like C_{60} tend to quench fluorescence by ISC [183]. After ISC to T_1 has occurred, the molecule can finally relax back to S_0 either by ISC or by phosphorescence.

2.3.2 Excitons in aggregates

Molecules in a molecular crystal interact via van der Waals forces [9, 137], which can be divided into

- electrostatic interactions of permanent dipoles (or other multipoles) (*orientation effect, Keesom interaction*)
- interactions of permanent dipoles with induced dipoles in a polarizable environment (*induction effect, Debye interaction*)
- interactions of fluctuating dipoles with induced dipoles in a polarizable environment (*dispersion effect, London interaction*)

These interactions are also present for excited molecules and can lead to collectively excited states of multiple molecules.

Dimer excitons

As a first demonstration of the impact of intermolecular interactions on the excited states of molecular aggregates, the impact of van der Waals interactions on the excited states of a pair of equal molecules (dimer) is briefly discussed in the following.

The description of a dimer system with arbitrary orientation, but with only two electronic states per molecule, has its origin in M. Kasha's work in 1965 [110, 184]. Here, the basis set of states are the product-functions of the ground state (S_0) and the first excited

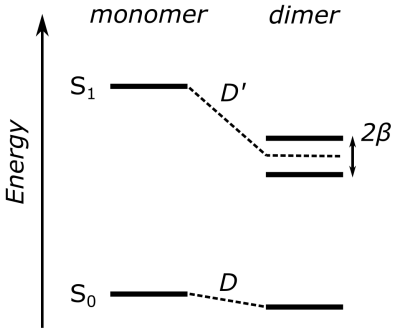


Figure 2.12: Schematic ordering of the excited states of a pair of molecules with same ground states S_0 and excited states S_1 [110]. The interaction energies D, D' and β are described in the main text. Inspired by Ref. 110.

singlet state (S_1) of each molecule, thus, $|S_0, S_0\rangle$, $|S_0, S_1\rangle$, $|S_1, S_0\rangle$ and $|S_1, S_1\rangle$, where the first entry is the state of molecule 1 and the second entry that of molecule 2. These basis states are eigenstates of the sum of the single-molecule (monomer) hamiltonians $\hat{H}_i$, but generally not for the hamiltonian that includes coupling between the two molecules,

$$\hat{H}^{(2)} = \hat{H}_1 + \hat{H}_2 + \hat{U}_{12}^{(2)} \tag{2.13}$$

with the van der Waals interaction $\hat{U}_{12}^{(2)}$ between the two molecules. The interaction can be treated with perturbation theory, in which only states close to each other in energy couple. In the four-state-basis, $|S_0, S_0\rangle$ is much lower and $|S_1, S_1\rangle$ much higher in energy than the other two states. Therefore, the ground state $|S_0, S_0\rangle$ of the dimer does not mix with the other basis states, and its energy is

$$E_0^{(2)} = 2\,E_0^{(1)} + D, \qquad D = \left\langle S_0, S_0 \,|\, \hat{U}_{12}^{(2)} \,|\, S_0, S_0 \right\rangle \tag{2.14}$$

with the ground state energies of the monomers $E_0^{(1)}$ as well as the ground state interaction energy D. The two degenerate basis states $|S_0, S_1\rangle$ and $|S_1, S_0\rangle$ can be mixed into superposition states

$$\Psi_{\pm}^{(2)} = \frac{1}{\sqrt{2}}\left(|S_0, S_1\rangle \pm |S_1, S_0\rangle \right) \tag{2.15}$$

with same coefficients, since the molecules are the same. The energy of these two states obtained by the dimer-hamiltonian in Eq. 2.13 are

$$E_{\pm}^{(2)} = E_0^{(1)} + E_1^{(1)} + D' \pm \beta \tag{2.16}$$

with the excited state energies of the monomers $E_1^{(1)}$, the sign of the contribution of β depending on the respective state in Eq. 2.15, and the interaction matrix elements D' and β defined by

$$D' = \left\langle S_0, S_1 \,|\, \hat{U}_{12}^{(2)} \,|\, S_0, S_1 \right\rangle \tag{2.17}$$

$$\beta = \left\langle S_0, S_1 \,|\, \hat{U}_{12}^{(2)} \,|\, S_1, S_0 \right\rangle \quad . \tag{2.18}$$

The last basis state $|S_1, S_1\rangle$ is disregarded here, since this state is too high in energy to mix. In the following, the interaction energies of the ground state (D) and the excited states (D' and β) will be discussed.

The ground-state interaction energy D results from van der Waals forces between two molecules in the ground state. D', however, results from van der Waals forces between one molecule in the excited state and the other molecule in the ground state. The magnitudes of D and D' depend on the electrostatic multipoles of the molecule, the strength of dipole fluctuation as well as the polarizability of the respective other molecule. Since the formation of the electron-hole pair increases the fluctuating dipole in the excited state compared to the ground state, the London-type contribution to D' is generally larger than D [110]. The London-type contributions to D and D' are always negative and reduce the energy of the ground state and the excited states of the dimer, as shown in Fig. 2.12.

Furthermore, D and D' are functions of the intermolecular coordinates $\tilde{Q}$ [110]. Thus, $D'(\tilde{Q})$ can have an energetic minimum $\tilde{Q}_1$ that is different from the ground state geometry $\tilde{Q}_0$ of the dimer. In this case the system relaxes after photoexcitation along an intermolecular coordinate from the ground state geometry $\tilde{Q}_0$ to the excited state geometry $\tilde{Q}_1$. Such a process can efficiently outcompete other decay channels, and the dimer in the excited state geometry $\tilde{Q}_1$ is called an excimer [92, 110, 185, 186].

The off-diagonal matrix element β of the interaction operator leads to different energies of the symmetric and the antisymmetric dimer states defined in Eq. 2.15 and thus lifts the degeneracy between $\Psi_+^{(2)}$ and $\Psi_-^{(2)}$. Since it is an off-diagonal matrix element, the interpretation of the so-called resonance interaction β is not as straightforward as for D and D'. As obvious from Eq. 2.18, β contains integrals over products of the $|S_0\rangle$ and $|S_1\rangle$ wavefunctions of each molecule. Since such an integral is also contained in the definition of the TDM (Eq. 2.12), the resonance interaction can be seen as an interaction of TDMs. It

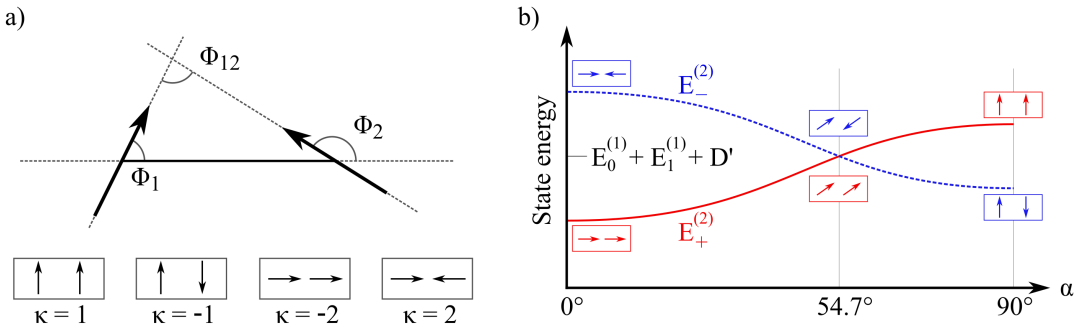


Figure 2.13: a) Angle definitions for description of the interaction between point dipoles [153], κ for special orientations are shown below [110]. b) Dependence of the excited state energy splitting in dimers on the angle α of their TDMs (see arrows and text) [153, 184]. The transition from the ground state to the state corresponding to the blue, dotted energy curve ($\Psi_-^{(2)}$) has zero oscillator strength, the transition to the state corresponding to the red, solid energy curve ($\Psi_+^{(2)}$) has nonzero oscillator strength. Inspired by Refs. 153 and 184.

is, however, noteworthy that absorption of photons is not necessary for this coupling and these states can also be reached by relaxation from higher electronic states of the dimer.

Using the point-dipole approximation [110] for the coupling of the TDMs, thus assuming a point-TDM on each molecule, one can approximate the absolute value of β by the absolute value of interaction energy between the TDMs

$$V_{\mathrm{PDA}} = \frac{\boldsymbol{\mu}_1 \cdot \boldsymbol{\mu}_2 - 3\,(\hat{\boldsymbol{r}} \cdot \boldsymbol{\mu}_1)(\hat{\boldsymbol{r}} \cdot \boldsymbol{\mu}_2)}{4\pi\varepsilon_0 r^3} \tag{2.19}$$

with the two TDMs $\boldsymbol{\mu}_1$ and $\boldsymbol{\mu}_2$ of the monomers, the unit vector $\hat{\boldsymbol{r}}$ connecting the two TDMs and the distance between the TDMs r (Fig. 2.13a) [153]. If the TDMs are coplanar and have the same absolute value ($|\boldsymbol{\mu}_1| = |\boldsymbol{\mu}_2| = |\boldsymbol{\mu}|$), Eq. 2.19 simplifies to

$$V_{\mathrm{PDA}} = \frac{\kappa \cdot |\boldsymbol{\mu}|^2}{4\pi\varepsilon_0 r^3}\,, \quad \kappa = \cos(\phi_{12}) - 3\,\cos(\phi_1)\,\cos(\phi_2)\,, \tag{2.20}$$

with the orientation factor κ, the angle ϕ_{12} between the two TDMs, and the angles ϕ_1 and ϕ_2 between the molecular stacking direction and the respective TDM [187] as depicted in Fig. 2.13a. More generally, κ can be defined also for non-coplanar TDMs as

$$\kappa = 4\pi\varepsilon_0\,\frac{V_{\mathrm{PDA}}\,r^3}{|\boldsymbol{\mu}|^2}\,, \tag{2.21}$$

and is a real number between -2 and 2, see Fig. 2.13a for the extreme cases. If the TDMs are parallel ($\phi_{12} = 0$) with $\phi_1 = \phi_2 = \alpha$, the orientation factor is

$$\kappa_p = 1 - 3\,\cos^2\alpha\,. \tag{2.22}$$

Due to the restriction in Eq. 2.22 that the TDMs are parallel, the antiparallel orientations (see Fig. 2.13a) are not captured, and κ_p is only a number between -2 (for $\alpha = 0$) and 1 (for $\alpha = \frac{\pi}{2}$).

From Eq. 2.22 one can qualitatively derive the splitting energy from the orientation of the TDMs at a fixed distance, as illustrated in Fig. 2.13b. β changes its sign due to κ_p from negative to positive upon rotating the TDMs from $\alpha = 0°$ to $\alpha = 90°$. With Eq. 2.16 it results that at $\alpha = 0°$, the higher-energy state is $\Psi_-^{(2)}$ and the lower-energy state is $\Psi_+^{(2)}$, while at $\alpha = 90°$ the state ordering is opposite (Fig. 2.13b). The change occurs at an angle of [184]

$$\alpha_{\kappa_p=0} = \arccos\left(\frac{1}{\sqrt{3}}\right) = 54.7°\,. \tag{2.23}$$

The overall oscillator strength of the transition from the ground state to the two energetically different superposition states $\Psi_\pm^{(2)}$ is proportional to the vectorial addition of the two monomer TDMs. With parallel TDMs, this sum is always zero for $\Psi_-^{(2)}$ and only the

transition to $\Psi_+^{(2)}$ has a nonzero oscillator strength, as indicated with dotted and solid lines in Fig. 2.13b [184].

Exciton bands

The case of parallel TDMs of Kasha's dimer model can be generalized to molecular crystals, leading to multiple collectively excited states of the crystal with state energies forming a quasi-continuous energy band (exciton band). The following description of collectively excited states in linear stacks of molecules is based on Refs. 110 and 153. The eigenfunctions of the electronic hamiltonian for the nearest-neighbor coupling of N linearly arranged molecules with parallel TDMs and periodic boundary conditions are

$$\Psi_k^{(\mathrm{N})} = \frac{1}{\sqrt{N}} \sum_n e^{ikn} \, |n\rangle \ , \quad |n\rangle = |S_0, \, S_0, \, ... \, S_1 \, ... \, S_0\rangle \ , \tag{2.24}$$

with S_1 in $|n\rangle$ at the n-th position. These N different states are superpositions of states with only one molecule being excited with wave vectors

$$k = 0, \, \pm\frac{2\pi}{N}, \, \pm\frac{4\pi}{N}, \, ..., \, \pi \tag{2.25}$$

and are called Frenkel states, named after J. Frenkel [188], who first described such states in 1931. The dimer case as described in Sec. 2.3.2 is obtained in this solution with $N = 2$ and two states with $k = 0$ and $k = \pi$. For $N > 2$, these two states are special cases, for which in the $k = 0$ state all monomers are coupled with the same phase (corresponding to $\Psi_+^{(2)}$ in the dimer case), and in the $k = \pi$ state neighboring monomers all have a phase differing by π (corresponding to $\Psi_-^{(2)}$ in the dimer case). Depending on the wave vector of the Frenkel state between these two extreme cases, its energy lies in a range around a central energy $E_0 + D'$, which corresponds to $E_0^{(1)} + E_1^{(1)} + D'$ in the dimer case and now includes the interaction of a molecule in the excited state with all neighboring molecules in their ground state. The total energy of a Frenkel exciton with wave vector k is

$$E(k) = E_0 + D' + W(k), \qquad W(k) = -2\beta \cos(k) \, , \tag{2.26}$$

where β is the resonance integral for coupling of each two molecules of the linear stack (Eq. 2.18) and the energy range of $-2\beta \leq W(k) \leq 2\beta$ is called the exciton bandwidth, which is now 4β, whereas in the dimer case the splitting was only 2β. This larger energy range is due to the fact that each monomer now has two nearest neighbors instead of only one as in the case of the dimer. Analogously to the dimer case, in which the resonant interaction of excited states of two monomers created two new states with different energies, the resonant interaction of excited states of N monomers (in reality limited by crystal defects) creates N new Frenkel states with quantum number k and energies distributed within the exciton bandwidth, see Fig. 2.14. The number N relates to the exciton coherence length defined by $l_{\mathrm{coh}} = N \cdot a$ with the distance a between molecules [189].

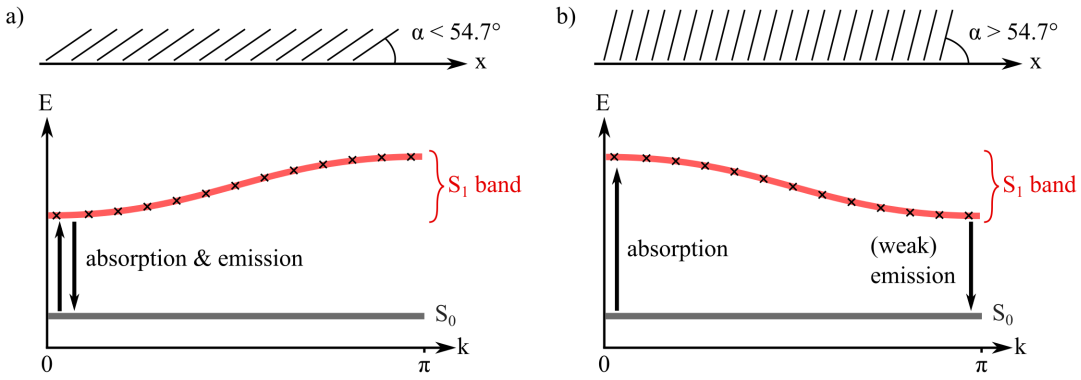


Figure 2.14: Frenkel states of a) J-aggregates and b) H-aggregates [153]. The critical angle α is calculated in Eq. 2.23. Inspired by Ref. 153.

The oscillator strength of the transition from the ground state to a Frenkel state of a linear stack of molecules depends strongly on the wave vector of the Frenkel state. For the $k=0$ exciton and parallel TDMs of the molecules, all TDMs are in-phase and sum up to a large oscillator strength. For the $k=\pi$ exciton, the TDMs have opposite phase for neighboring molecules, leading to a vanishing oscillator strength of the corresponding transition from the ground state. This phenomenon has already been mentioned for the $\Psi_{-}^{(2)}$ state of a dimer in Sec. 2.3.2. Analogously, also the oscillator strengths of all transitions from the ground state to states except $k=0$ are zero [153]. Based on the oscillator strength, the $k=0$ Frenkel exciton is frequently called the bright Frenkel exciton or bright edge of the exciton band, while the other side ($k=\pi$) is called the dark Frenkel exciton, or dark edge. The energetic ordering of bright and dark Frenkel exciton, which depends on the sign of β and therefore the angle α (see Eq. 2.22 and Fig. 2.13b) leads to very different photophysical behaviors of the molecular stack (Fig. 2.14):

- **J-aggregate**: If the bright state ($k=0$) is at the bottom edge of the exciton band, the system is called a J-aggregate [190], named after E. Jelley, who experimentally first observed this effect in 1936 [191]. Photons are absorbed at this bottom edge and due to the large oscillator strength of the transition also fast and efficiently emitted from this state (see Fig. 2.14a), which is referred to as superradiance [153, 190]. J-aggregates result from stacked molecules with an angle between the stacking direction and the TDMs of less than 54.7°, see Eq. 2.23 [184].

- **H-aggregate**: If the bright state ($k=0$) is at the top edge of the exciton band, the system is called an H-aggregate (from *hypsochromic* shift, greek for blue-shift) [190]. Only the transition to the top edge of the band corresponds to a large oscillator strength, and created Frenkel excitons relax fast to the dark bottom edge (see Fig. 2.14b). From there, emission is very inefficient and other relaxation pathways such as intersystem crossing to T_1 or internal conversion to S_0 compete with the radiative relaxation. Therefore, H-aggregates are very weak emitters [153, 190].

H-aggregates result from stacked molecules with an angle between the stacking direction and the TDMs of more than 54.7°, see Eq. 2.23 [184].

Davydov splitting

For non-parallel TDMs in Kasha's dimer model, transitions from the ground state to both $\Psi_{-}^{(2)}$ and $\Psi_{+}^{(2)}$ have nonzero oscillator strengths and even different polarizations of the overall TDMs. Therefore, in this case the dimer exhibits a splitting of the respective absorption peaks, which is referred to as Davydov splitting (DS) named after A. S. Davydov [192].

A DS can be observed for covalently coupled dimers [193, 194], but more prominently also for molecular crystals with two (or more) molecules per unit cell, such as the HB aggregate. In this case, the two basis molecules can be seen as a dimer with two energetically different states. The TDMs of the transitions from the ground state to these two states have different polarizations (Fig. 2.15). Combining these dimers to a crystal, the two dimer levels lead to exciton bands, and transitions from the ground state to the two bands are differently polarized [153].

While Kasha's simple dimer model can capture the origin of photophysical properties of molecular crystals such as H- or J-aggregation and Davydov-splitting, it is important to note that regarding the generalization to molecular crystals, the two cases of parallel and non-parallel TDMs lead to two different effects. The dimer case with parallel TDMs can be considered as the first step of band formation, while non-parallel TDMs in molecular crystals is a necessary requirement for band splitting, see Fig. 2.16.

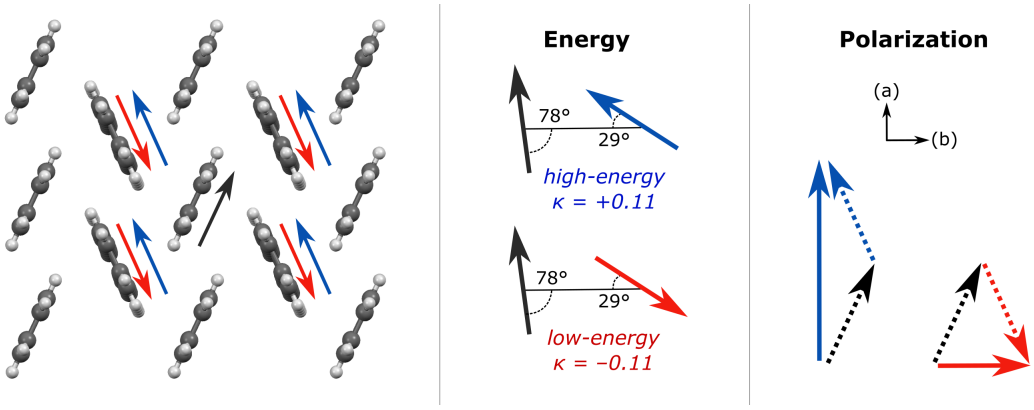


Figure 2.15: Dimer coupling with non-parallel TDMs between the two translationally inequivalent molecules in a HB aggregate [153]. Due to the symmetry of the crystal, the coupling to all four nearest neighbors is the same. The orientation factors κ are those defined in Eq. 2.21 and demonstrate the energetic ordering. Vectorial addition of the TDMs demonstrates the nonzero oscillator strength and different polarization of transitions from the ground state to the two states.

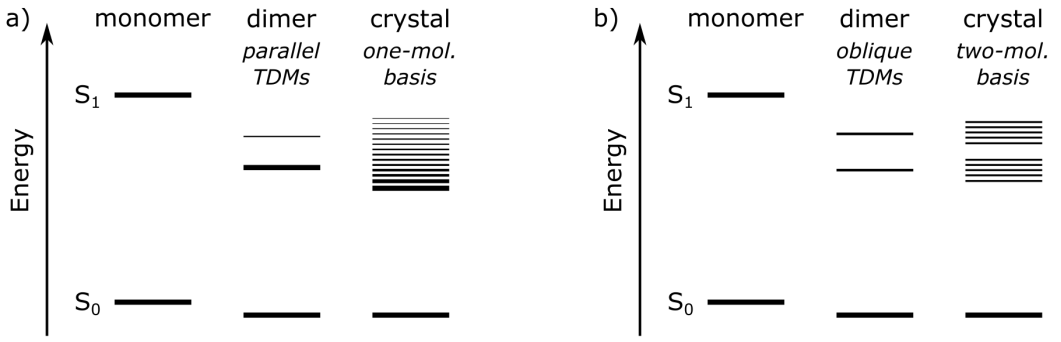


Figure 2.16: Dimer approach for the coupling between molecules in a crystal with a) one basis molecule (for a J-aggregate), b) two basis molecules [110]. The thickness of the lines representing state energies are meant to demonstrate the oscillator strength of the transition from the ground state to the corresponding state. Inspired by Ref. 110.

Charge-transfer states

Even though the excitation energy of Frenkel excitons is delocalized over the exciton coherence length, electron and hole are restricted in this description to reside on the same molecule (small exciton radius). Besides Frenkel exciton (FE) states there are also states in molecular crystals, for which the restriction of electron and hole on the same molecule is repealed. If electron and hole reside on neighboring molecules this state is called a charge-transfer (CT) state [153], since it can be reached from $|S_0, S_0\rangle$ via a transfer of an electron from a HOMO of one molecule to a LUMO of a neighboring molecule. Like diabatic FE states, also different diabatic CT states can resonantly couple to form delocalized superposition states [195].

The oscillator strength for photon absorption depends on the orbital overlap of initial and final state (see Eq. 2.12) and this overlap is strictly zero for diabatic CT states. Therefore, the transitions from the ground state to CT states have no oscillator strength. However, diabatic FE and CT states can also couple to each other, leading to adiabatic states of mixed FE/CT character [26]. With small contributions of FE states, transitions from the ground state to adiabatic states with dominant CT character can therefore gain oscillator strength, while contributions of diabatic CT states in adiabatic states with dominant FE character can have a significant impact on their energy and thus also affect the DS [52, 153, 195, 196].

In theoretical calculations of excited states of molecular aggregates, the admixture of CT states to bright states (CT character) can be observed from the electron-hole radial distribution function that describes the spatial separation of electrons and holes [197]. This spatial separation should, however, not be confused with the exciton coherence length that can be large even without admixtures of CT states.

2.3.3 Exciton migration

After the creation of an exciton in a molecular crystal, it can generally migrate through the aggregate before it decays [198, 199]. Two mechanisms exist for the migration of excitons,

Dexter energy transfer [200, 201] and Förster resonance energy transfer (FRET) [187, 202–204]. In both mechanisms an exciton is transferred from an excited donor molecule $D^\star$ to an acceptor molecule A, resulting in a ground state donor molecule D and an excited acceptor molecule $A^\star$,

$$D^\star + A \xrightarrow{\text{energy transfer}} D + A^\star \,, \tag{2.27}$$

independent of whether D and A are molecules of different type or the same. FRET describes the transfer of an exciton through resonant coupling of molecular dipoles. A detailed description based on quantum electrodynamics can be quite complicated [205], but simplified theories are well established [187, 204]. The FRET rate of exciton transfer depends to the sixth power on the distance R between the two molecules [187, 204],

$$k_{\mathrm{FRET}}(R) = k_{\mathrm{rad}} \left(\frac{R_{\mathrm{F}}}{R}\right)^6 \,, \tag{2.28}$$

where k_{rad} is the radiative rate of the donor molecule and R_F is the so-called Förster radius that is the distance between donor and acceptor for which the probability of FRET and a radiative decay of the donor are equal. Since the FRET mechanism includes the emission and absorption of a virtual photon, its rate is calculated not only from the radiative rate of the donor, but also from the spectral overlap of the emission spectrum of the donor and the absorption spectrum of the acceptor. The Förster radius is therefore calculated via [187, 204]

$$R_{\mathrm{F}}^6 = \frac{9\log(10)\kappa^2}{2^7\pi^5 n^4 N_{\mathrm{A}}} \cdot \underbrace{\int_{-\infty}^{\infty} I_{\mathrm{D}}(\lambda)\,\varepsilon_{\mathrm{A}}(\lambda)\lambda^4 \mathrm{d}\lambda}_{J} \tag{2.29}$$

with the orientation factor κ of donor and acceptor TDM as defined in Eq. 2.21, the refractive index of the medium n, Avogadro's constant N_{A}, the normalized donor emission spectrum $I_{\mathrm{D}}(\lambda)$, the molar extinction coefficient $\varepsilon_{\mathrm{A}}(\lambda)$ of the acceptor and the photon wavelength λ.

Dexter energy transfer proceeds via an exchange of a HOMO and a LUMO electron of neighboring molecules. This electron exchange requires orbital overlap and is therefore short-ranged. For singlet excitons FRET is generally faster and Dexter energy transfer plays a minor role. For triplet excitons, however, FRET is spin-forbidden and Dexter energy transfer is the only possible migration mechanism.

There are two categories of exciton migration between molecules that are of the same type, which differ in the excited state energy of the acceptor molecule relative to that of the donor molecule, e.g. due to disorder in the aggregate. If the excited state energy of the acceptor and the donor is the same, energy back-transfer is equally probable, which leads to a non-directional diffusion of the exciton through the aggregate [187, 201, 204].

If, in contrast, the excited state energy of some molecules in the aggregate is lower, back- and forth energy transfer are not equally probable, which leads to directional exciton migration. This directional migration of excitons between molecules of the same type is called hopping to low-energy sites in the aggregate [52]. The energy transfer between molecules of different types is obviously always directional [203].

Finally, for high excitation densities, excitons might encounter each other due to their migration. This encounter might lead to processes, in which two excitons of lower energy (S_1 or T_1 state) form one exciton in a higher electronic state (e.g. S_2 and T_2, respectively), which subsequently relaxes via IC. Thus, after the relaxation, one exciton has been effectively annihilated. Depending on the spin multiplicity, these processes are therefore known as singlet-singlet annihilation (SSA) [64, 206] or triplet-triplet annihilation (TTA) [206]. The decay of exciton population due to SSA or TTA is described by a rate equation of second order and is therefore a non-exponential function [64]. The impact of SSA and TTA on time-resolved measurements can be minimized by low excitation densities [206].

2.4 Singlet exciton fission

Singlet fission (SF) is a spontaneous, dipole-allowed, bimolecular process that converts a singlet exciton (simply named singlet in the following) into two triplet excitons (triplets) via a spin-entangled triplet-pair state [23–25]. The whole process can generally be described by three steps [26],

$$S_1 \rightleftharpoons {}^1(TT) \rightleftharpoons {}^1(T...T) \rightleftharpoons T_1 + T_1 \,. \tag{2.30}$$

The process starts from the adiabatic S_1 state of an aggregate. The first SF step converts this S_1 state into $^1(TT)$, which is a triplet-pair state consisting of two triplets on neighboring molecules (Fig. 2.17). This first step is achieved by the transfer of electrons,

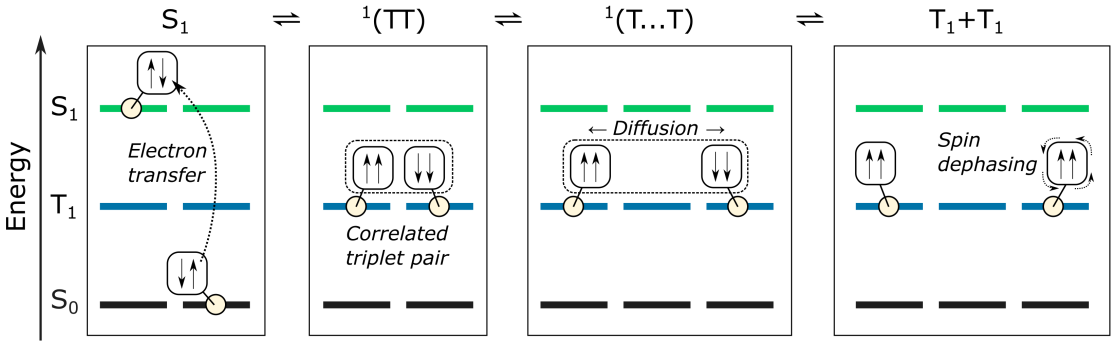


Figure 2.17: Simplified scheme of the singlet fission process. The horizontally neighboring energy levels represent those of different molecules. Note that the initial excitation energy is symmetrically shared between both molecules and might include CT states, the $^1(T...T)$ can also be accessed without diffusion [26, 67], and the dephasing of spins requires interaction with the environment. Inspired by Refs. 49 and 26.

as shown in Fig. 2.17. Since the transfer of electrons requires electronic coupling between the two molecules, the two triplets in ^{1}(TT) are also electronically coupled. The next step breaks up this electronic coupling, e.g. by separating the triplets through incoherent energy transfer [207]. In the resulting ^{1}(T...T) state the triplets do not reside on neighboring molecules anymore, are electronically identical to T_1, but still spin-entangled. Finally, the spin-entanglement is broken by mixing with states of higher spin multiplicity [30, 208–210].

Since the spin-entanglement in ^{1}(T...T) does not impact the subsequent behavior of the triplets, SF has been suggested to be defined as the conversion from S_1 to ^{1}(T...T) [26]. With this definition, SF as a whole is a spin-allowed process, since its final state is still an overall singlet. The reverse process from ^{1}(T...T) to S_1 is called triplet fusion [82].

2.4.1 Energetic requirements for the singlet fission process

For a fast SF process that outcompetes other decay channels of the S_1 exciton, it needs to be an energetically favorable process. Since the ^{1}(T...T) state has an energy of twice that of T_1, this translates into the criterion that the SF energy balance

$$\Delta E_{\mathrm{SF}} = 2E(T_1) - E(S_1) \tag{2.31}$$

with $E(X)$ denoting the energy of state X, is negative or only slightly positive (maximum few hundred meV, as discussed in Sec. 4.1) [23, 29, 211]. For a system with $\Delta E_{\mathrm{SF}} < 0$ (exothermic SF), SF is generally faster than with $\Delta E_{\mathrm{SF}} > 0$ (endothermic SF). Furthermore, since exothermic SF implies endothermic triplet fusion, SF is also highly efficient in this case, meaning it ultimately results in a large number of free triplets. Therefore, the above mentioned criterion is not only a criterion for fast SF, but also facilitates the efficient generation of free triplets. A second energetic requirement for an efficient triplet generation is, that

$$\Delta E_{\mathrm{TTA}} = E(T_2) - 2E(T_1) \tag{2.32}$$

is positive [23, 29, 211], since a negative value would imply an exothermic annihilation process of two triplets with overall spin one to a T_2 and an S_0 state on the two molecules, respectively, followed by an IC from T_2 to T_1, thus only yielding a single triplet instead of two. There are plenty of molecules that fulfill the two requirements for ΔE_{SF} and ΔE_{TTA} [23, 29, 211], rendering the SF process highly efficient in the respective material.

2.4.2 The wavefunction of the triplet-pair state

Since at least four electrons (doublets) are involved in SF, the description of spin states in the SF process requires a minimal spin basis of sixteen states. Diagonalization of the overall spin operator for four electrons yields two overall singlet states, nine triplet states as well as five quintet states [82]. Nine of these sixteen four-electron spin states

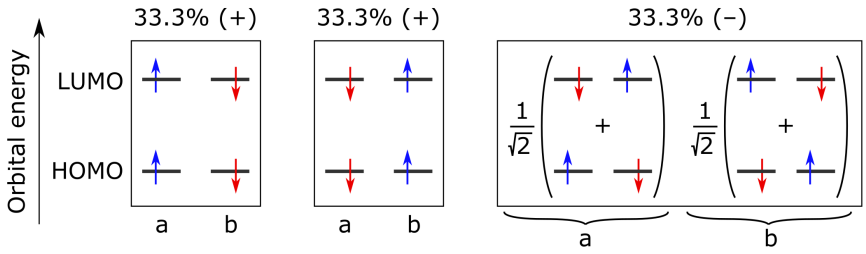


Figure 2.18: Wavefunction of the ^{1}(TT) state in a four-electron picture [26]. The letters a and b indicate two different molecules. For each configuration the sub-configuration at each molecule is a triplet state (spin function $|\uparrow\uparrow\rangle$, $|\downarrow\downarrow\rangle$ or $\frac{1}{\sqrt{2}}(|\uparrow\downarrow\rangle + |\downarrow\uparrow\rangle)$), rendering all three configurations pairs of triplet states. The relative contribution and phase (+/−) to ^{1}(TT) are indicated above each configuration. Note that the percentages are squared amplitudes.

are products of two-electron triplet states, called triplet-pair states [26, 212]. The nine triplet-pair states are one overall singlet state (^{1}(TT)), five triplet states (^{3}(TT)) as well as three quintet states (^{5}(TT)). The second four-electron singlet spin state besides ^{1}(TT) is a product of two-electron singlet states and is the initial spin state of the system (spin state of S_1). During SF, this initial spin state transitions to ^{1}(TT).

The ^{1}(TT) wavefunction is a superposition of different configurations [26, 212], see Fig. 2.18. For a four-electron system, only the superposition of the three triplet-pair configurations shown in Fig. 2.18 is the eigenstate of the total spin operator $\hat{S}^2$ with zero eigenvalue, while any pure triplet-pair configuration or a superposition with other phases is not such an eigenstate.

With intra- and intertriplet electron-electron interactions such as the zero-field splitting interaction [212], ^{1}(TT) is no eigenstate of the electronic hamiltonian and therefore periodically evolves in time by changing the phase differences between the three states shown in Fig. 2.18. During this evolution, contributions of ^{5}(TT) and secondarily also ^{3}(TT) are mixed into the spin state of the system, before it decays to independent triplets [30, 208–210]. The periodical evolution can lead to the observation of quantum beats due to an oscillating rate of triplet fusion [82, 83].

2.4.3 History and techniques for experimental observation

There are various ways how SF can be observed experimentally. Historically, first the existence of an annihilation process of two triplets in anthracene was proposed by R. G. Kepler in 1963 based on time-delayed singlet emission after the generation of triplets [213]. One year later, S. Singh mentioned the possibility also for the reverse SF process, i.e. triplet-pair generation from singlets, in anthracene [214] and C. Swenberg proposed in 1968 that SF could explain the long known, but misinterpreted, exceptionally low fluorescence quantum yields of anthracene, tetracene (TET) and pentacene (PEN) in the solid state [215].

The first observation of SF has been made by R. E. Merrifield in 1969 using photoluminescence (PL) spectroscopy on single crystals of TET in the presence of an external

magnetic field [27]. The magnetic field impacted the rate of triplet fusion, which is exothermic in TET, and led to a change in the PL intensity with different magnetic field strengths and orientations with respect to the crystal axes. Merrifield was further able to present a model based on the impact of the magnetic field on the nine triplet-pair spin states that described his observations [27].

The comparison of the Merrifield model to PL measurements remained the main technique for detecting SF in the following years [216]. However, this technique was limited to endothermic SF materials, since only in this case triplet fusion is exothermic and thus efficient. Also in early time-resolved PL (TRPL) measurements, the lifetime of the singlet emission was tracked and hence the technique was not applicable to non-emissive, exothermic systems [217, 218]. This explains, why todays most prototypical example of a SF material, PEN, gained less attention compared to anthracene and TET in these early years. Today, time-resolved techniques are available for detecting SF that do not rely on the emission of photons, see Sec. 3.3.1.

2.4.4 Singlet fission mechanisms

The SF scheme shown in Fig. 2.17 is strongly simplified especially due to the first step of electron transfer, to which a variety of different mechanisms can contribute in different compounds that have been extensively discussed in the last decade [50, 57, 60, 61, 69, 71, 74, 75, 77, 80]. A brief overview of these mechanisms is given in the following, but it should be noted that several mechanisms can contribute simultaneously. For simplicity, the FE, CT and ^{1}(TT) states mentioned in the following are meant to be diabatic states. The energetically lowest adiabatic state with dominant contributions of FE states is called S_1, the adiabatic states with dominant ^{1}(TT) or CT character are explicitly called adiabatic states. The adiabatic ^{1}(TT) and adiabatic CT states can contain contributions from the respective other diabatic states.

Charge-transfer state mediated singlet fission

CT states are intermediate states for the two-step conversion of FE states into ^{1}(TT), see Fig. 2.19. In a diabatic picture, there are two trivial mechanisms for this conversion [23, 75]. Either, both electrons are transferred in one step, which is referred to as *direct* SF, or single electrons are sequentially transferred in two steps. The latter mechanism includes a significant transient population of adiabatic CT states and is called *sequential CT-mediated* SF process [23, 75]. The Coulomb coupling integral for the direct SF process has early been recognized to be orders of magnitude too weak to explain ultrafast SF events [75]. The sequential process was seen to be more likely, but the energies of CT states in typical OSCs were too high for an actual transient population of CT states [75].

Therefore, several mechanisms were proposed, how the system might evolve from a photoexcited S_1 state into a final, adiabatic ^{1}(TT) state. A *superexchange CT-mediated* mechanism [23, 75] has been proposed, in which the system uses CT states as virtual

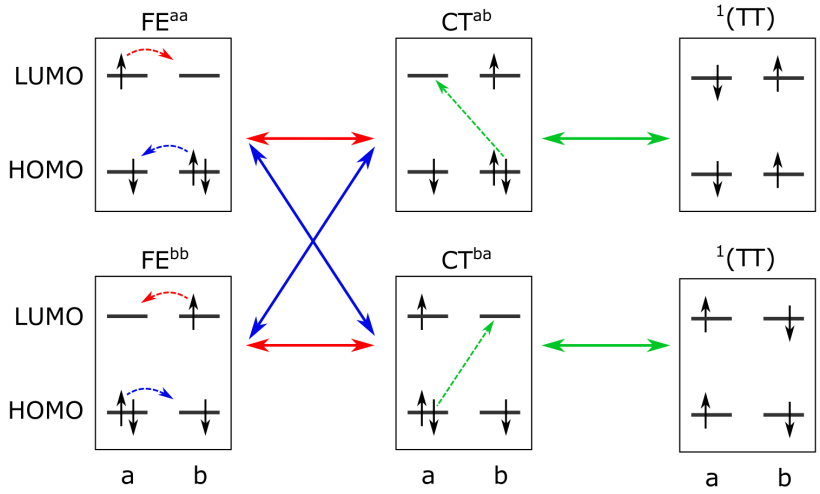


Figure 2.19: CT-mediated electronic coupling between FE and ^{1}(TT) states. Each box shows HOMO and LUMO energy levels of two molecules labeled a and b. Colored solid arrows represent electronic coupling, dotted arrows the respective electron transfers. ^{1}(TT), FE and CT states are actually superpositions of different configurations [26]. Only each one configuration of the FE and CT states is shown for simplicity, although two configurations of ^{1}(TT) are still involved. Inspired by Refs. 26 and 196.

transition states, thus without significant population of adiabatic CT states during the process. The term superexchange is chosen in analogy to superexchange-coupling in antiferromagnetic systems, in which the next-to-nearest neighbor exchange-coupling of electron spins is mediated by paired spins of a non-magnetic atom [219]. Superexchange can be accounted for in theoretical calculations by adding second-order terms to the coupling integrals between FE and ^{1}(TT) states [23, 75, 85].

For compounds in which the adiabatic S_1 and ^{1}(TT) states already contain contributions from CT states due to electronic coupling between diabatic states (solid colored arrows in Fig. 2.19), the superexchange-coupling is already included in the coupling matrix element between the adiabatic S_1 and ^{1}(TT) [57, 220]. Therefore, the superexchange mechanism can be considered as a result of using a diabatic state basis, and the SF process in such a system neither results from direct coupling, nor from a two-step coupling between diabatic states [220]. Another explanation for ultrafast SF events is a coherent mechanism [50, 74], which will be discussed in more detail below.

Impact of nuclear degrees of freedom

In recent years also the impact of intra- and intermolecular nuclear degrees of freedom on the SF process of various compounds has been emphasized [58, 60–62, 69–71, 221–223]. Different mechanisms have been proposed. As long as SF is not isoergic, coupling to a phonon bath is required for the draw or release of energy [58]. In this case, the SF rate critically depends on the availability of phonons corresponding to the SF energy balance ΔE_{SF}. Due to the phonon bottleneck at larger energies and the lower efficiencies of multi-phonon processes, a strongly negative ΔE_{SF} is even expected to be detrimental for SF [58, 118].

Apart from the draw or release of energy, vibrations can further enable vibronic coupling between FE states and ^{1}(TT) [61, 69–71, 221]. In particular those vibrations that are energetically resonant with ΔE_{SF} have been found to promote vibronic coupling between the FE, CT and ^{1}(TT) states [61, 70, 71]. The vibronically mixed states can enhance the coupling for SF or lead to more favorable energetics. Finally, certain vibrations can also lead to a stronger coupling of the states due to the access of distinct nuclear coordinates, at which the SF process in faster [60, 62]. In this case, the main effect of the vibrations is not the vibronic coupling due to energetic resonance, but rather their symmetry-breaking nature [60, 62, 222, 223].

Coherent singlet fission

Independent of the discussion about the role of CT states and vibrational degrees of freedom, two distinct SF mechanisms have been proposed. Based on the observation of ^{1}(TT) states directly upon photoexcitation for several compounds [56, 69, 74], a *coherent SF mechanism* has been proposed to be responsible for the conversion of excited states to separated triplets in these cases [50, 61, 69, 71, 74].

Here, a strong coupling between FE, CT and ^{1}(TT) states (solid colored arrows in Fig. 2.19) leads to eigenstates of the system that are superpositions of the three diabatic states [74]. The photoexcitation creates a quantum superposition of the eigenstates, which evolves in time [50]. Without coupling to an environment, the contributions of FE, CT and ^{1}(TT) states to the quantum state of the system coherently oscillate according to the coupling strength between these three diabatic states [50]. The system therefore remains in a pure state, the oscillation amplitudes do not change and the coherence is conserved.

An environment (a phonon bath), to which the system is coupled, however, leads to population transfer and dephasing of the superposition. Therefore, while the coherence of the system decays, population is rapidly distributed and approaches a Boltzmann distribution among the eigenstates [74], which strongly favors the eigenstate with a dominant ^{1}(TT) contribution (thus, the adiabatic ^{1}(TT) state) for exothermic SF. Subsequently, the coupled triplets in the adiabatic ^{1}(TT) state can then separate.

This mechanism only works, if the electronic coupling between FE, CT and ^{1}(TT) states (Fig. 2.19) is stronger than the coupling to the phonon bath and thus allows for coherent population transfer. The dephasing rate, however, also needs to be sufficiently large to enable energy exchange between the system and the environment [50]. In this case, the population transfer to the adiabatic ^{1}(TT) state is solely determined by the (CT-mediated) coupling strength between the FE and ^{1}(TT) states [50].

Incoherent singlet fission

An electronic coupling between FE and ^{1}(TT) states weaker than the coupling to a phonon bath leads to an *incoherent SF mechanism* [26]. In the weak electronic coupling limit the

transition is non-adiabatic and can be described by Fermi's golden rule formalism [26]. For high temperatures, the formalism for the SF rate k_{SF} reduces to the Arrhenius-type Marcus equation for electron transfer

$$k_{\mathrm{SF}} = \frac{2\pi}{\hbar}\hat{V}^2 \frac{1}{\sqrt{4\pi\lambda k_{\mathrm{B}}T}} \exp\left[-\frac{(\Delta G + \lambda)^2}{4\pi\lambda k_{\mathrm{B}}T}\right] \tag{2.33}$$

where $\hat{V}$ is the (effective CT-mediated) electronic coupling between S_1 and ^{1}(TT), λ the reorganization energy, k_{B} the Boltzmann constant and ΔG the free energy difference between the two states [26, 57]. In this regime, the system undergoes thermally activated, vibrational motion along the S_1 PES and only rare, sudden transitions to the ^{1}(TT) PES at a crossing point drive the SF process. Microscopically, the stochastic transitions occur after several passes of this crossing point, and different singlets cross over to the ^{1}(TT) PES at different times after excitation.

Notably, ΔG in Eq. 2.33 also includes the increase of entropy due to the multiple ^{1}(TT) and ^{1}(T...T) microstates accessible within the coherence length of the S_1 state [56, 59, 224]. The entropic gain has been proposed to be a dominant driving force for SF especially in endothermic systems [56] and to explain slower SF rates in dimers [224, 225]. A strong increase of the entropic contribution during SF might lead to exergonic SF ($\Delta G < 0$ [226]) even if the energy balance ΔE_{SF} is positive. It is, however, an ongoing debate in literature, how large the contribution of entropy to the free energy is [59, 67, 89, 224].

In a regime of stronger electronic coupling, but yet weaker than the coupling to the phonon bath, the above equation does not hold due to PESs of mixed electronic character [57]. After excitation, the system then evolves along a path on a PES for which the character of the adiabatic states continuously changes at an avoided crossing from FE-dominant to ^{1}(TT)-dominant and the SF process is an adiabatic transition [26, 57]. In this case, the SF rate is limited by the velocity of nuclear movement (vibration frequency) and is independent of the strength of electronic coupling [57]. With the same difference in free energy, adiabatic SF is generally faster than non-adiabatic SF [57], since a single vibrational attempt is sufficient for the adiabatic transition. Furthermore, since all created singlets synchronously cross over to the ^{1}(TT) PES, vibrational coherence can be found for vibrations in this new PES in contrast to the non-adiabatic stochastic transitions [65]. A similar scenario has been reported with the non-adiabatic transition from the S_1 to the adiabatic ^{1}(TT) PES through a conical intersection, which also creates vibrational coherence [80].

2.4.5 Singlet fission in blends

In two results chapters of this work (Ch. 6 and 7), investigations on SF in polycrystalline blends of SF compounds and other materials are presented. In the following, some effects are therefore discussed that can lead to differences in the SF rate between blends and the respective neat compounds. These effects include

- the replacement of SF molecules

- a change in the electronic state energies
- a change of the crystal lattice or molecular orientation
- occupational disorder and exciton migration
- a reduction of the entropic driving force
- additional decay channels of singlets, i.e. FRET, charge transfer and heterofission.

Effects in blends that are important for the discussion of the results of this work are briefly described in the following.

The rate of any incoherent process depends on the number of target states (density of states in Fermi's golden rule) [167]. For a chromophore undergoing incoherent SF the number of available states (pairs of triplets) equals the number of nearest neighbors. Therefore, the SF rate decreases upon replacing neighboring SF molecules by spacer molecules (Fig. 2.20a and 2.20b). This replacement effect has been proposed in Ref. 105 as a contribution to a decreased fluorescence rate in a solid solution of TET and spacer materials. To account for this impact, the authors defined a concentration-dependent replacement effect factor as the ratio between the SF rate in a neat film and the SF rate in a blend. For determination of this replacement effect factor, a singlet hopping simulation has been performed and the number of steps to fission were counted, which are inversely proportional to the SF rate [105]. Microscopically, the replacement effect decreases the SF rate of LECs (Sec. 2.2.2) depending on the number of neighboring SF molecules, see Fig. 2.20b. For a HB aggregate, in which each molecule has four nearest neighbors, the LEC_n therefore exhibits a SF rate $k_n = \frac{n}{4} k_4$ with the SF rate of the neat compound k_4.

A further important effect for SF in spacer blends is a variation in the crystal lattice. The crystal lattice of a solid solution generally differs from those of the neat compounds and is continuously varied with the mixing ratio [52]. If the unit cells of the two compounds are orthorhombic, this variation can be a simple expansion (if the unit cell of the spacer compound is larger) and thus leads to larger intermolecular distances as sketched in Fig. 2.20c [52]. These larger distances generally reduce the coupling between electronic states with subsequent impact on SF [227, 228]. For unit cells with non-orthogonal angles also the intermolecular orientation can change [52]. In this case, the orbital overlap between SF molecules is altered, which is known to strongly impact the SF rate [55, 229, 230].

Next, also the migration of singlets after photoexcitation might impact the overall SF rate of the blend. Solid solutions do not consist of a single LEC but are always an ensemble of all five possible LECs (Sec. 2.2.2), which is referred to as occupational disorder [52]. Upon excitation of a spacer blend with a photon energy below the band gap of the spacer compound, singlets are created statistically at various LECs, for which the SF rate might differ. Without singlet migration, the SF processes occur at these statistically distributed LECs with different SF rates, which leads to overall multi-exponential population dynamics of the blend [231]. In general, however, the singlets can migrate via FRET (see Sec. 2.3.3) before undergoing SF and will tend to hop to low-energy LECs in

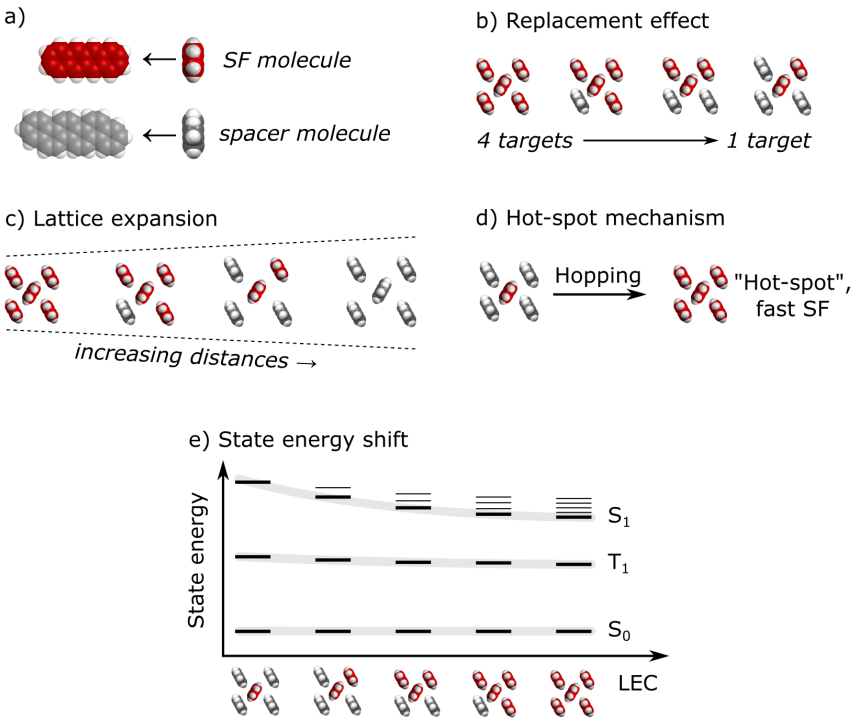


Figure 2.20: Impacts on the SF rate in spacer blends. a) Symbols for SF and spacer molecules used in this work originating from the top view (arrows) on the respective molecule (here TET and [6]-phenacene) drawn in spacefill style. The carbon atoms of SF and spacer molecules are colored red and gray, respectively, hydrogen atoms in both cases white. b) LECs with different numbers of nearest target neighbors for SF leading to the replacement effect. c) Increasing unit cell with increasing spacer concentration. d) Hot-spot mechanism via hopping of singlets from LECs with slow or absent SF to LECs with fast SF. e) Different S_1 and T_1 state energies of different LECs of an arbitrary SF material. The multiple energy levels of S_1 are split state energies due to resonant interaction.

the blend (see Fig. 2.20e) [52, 231]. If these low-energy LECs exhibit faster SF they are called hot-spots [52, 231] and can dominate the overall SF rate of the blend (Fig. 2.20d). This effect is called hot-spot mechanism and has been suggested to explain the observation of a robust SF rate of PEN spacer blends [52].

Another effect that can impact the SF rate in blends is a change in the energy levels of electronic states of the SF materials [52, 104]. Such changes can have different origins like a different polarizability of the environment of SF molecules [52, 95, 104] or a reduced coherence length of singlets and therefore narrower exciton bands [153]. The stabilization of electronic states by a polarizable environment is related to the fluctuating dipole in the excited state (see Sec. 2.3.2 [110]). Thus, especially CT states [62, 95], but also singlet FE states are stabilized by a polarizable environment [52, 104, 232], while there is less stabilization for triplet states [233–235]. Since the polarizability of a molecule is connected to its band gap [236], the energies of electronic states increase with increasing spacer concentration, as sketched in Fig. 2.20e. This effect due to the change in the polarizability of the molecular environment has been observed by a blueshift of the $S_0 \rightarrow S_1$ absorption in

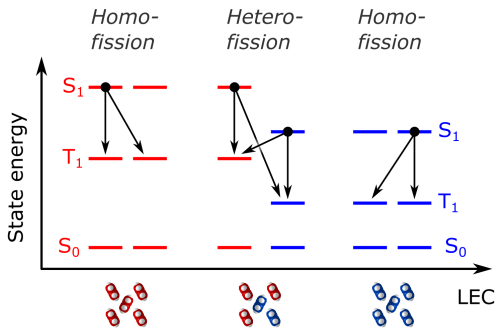


Figure 2.21: Heterofission between two SF compounds. Singlets in neat SF compounds undergo homofission (left, right). In blends of two SF compounds, an additional decay pathway for singlets of either compound is heterofission to two different types of triplets.

several spacer blends [52, 104]. The shifting state energies alter the SF energy balance and might also impact the coupling between electronic states. Notably, a reduced coherence length of photoexcited singlets not only impacts the SF energetics in blends but also the entropic driving force (see Sec. 2.4.4).

Upon mixing two SF compounds, *heterofission* [106, 107] might become an additional decay channel for singlets. In contrast to *homofission*, heterofission creates two triplets located on different types of molecules, see Fig. 2.21. This process has been proposed to explain the magnetic-field dependent PL of PEN-doped TET single crystals in the 1970s [106, 107]. Heterofission can occur from the singlet states of both compounds, as shown in Fig. 2.21. The heterofission process of the energetically higher singlet has always a lower ΔE_{SF} but has to compete with FRET to the compound of lower band gap. This energy transfer has been assumed to be faster in Ref. 106 and heterofission has been proposed to occur starting from the lower-lying singlet state. Recently, heterofission was also found in covalently bound dimers of PEN and TET [90, 108].

2.4.6 Current research on singlet fission

Different aspects of the SF process are investigated in the literature, aiming at a better understanding and development of promising compounds for application. A brief overview of the most prominent approaches used in literature in the last years for this purpose is given in the following.

A large field in the research on SF is the development of design strategies for new SF compounds by substitution with heteroatoms [47, 48, 117–120] or combining electron-donating and -accepting units in polymers [237–239].

Besides the study of new conjugated chromophores, several reports focus on the optimal relative arrangement of prototypical chromophores for SF, either by the design of various covalently linked dimers for investigation of through-space and through-bond interaction in intramolecular SF [76, 86–90] or by altered chromophore arrangement in thin films induced by functional groups [49, 54, 85] or natural polymorphism of pristine compounds [230, 240] in intermolecular SF. The effect of altered electronic coupling between chromophores on SF can be studied for intramolecular SF by using the different polarities of different solvents that vary the CT state energy [62, 76, 77, 241] and for intermolecular SF by (partial) halogenation [84, 85, 94, 99, 242].

Prominent approaches for studying the microscopic pathway of SF in prototypical SF materials, especially regarding the role of vibrations, are the examination of vibrational oscillations in transient absorption signals [60, 65, 72, 80] or the employment of two-dimensional electronic spectroscopy (2DES) [69, 81, 96]. Several studies further report sophisticated theoretical calculations of the electronic and vibronic coupling between states of crystalline clusters [70, 71, 95, 243].

Measurement of the temperature-dependence and determination of triplet-fusion kinetics can help to understand the mechanisms of SF in iso- or endothermic systems [67, 241, 244]. Another tool for the investigation of the electronic coupling between triplets is the detection of subsequent spin states of the triplet-pair state [30, 208–210].

3. Experimental techniques

In this work, several experimental techniques have been used for the sample preparation, the structural and optical characterization of samples, as well as for the examination of their photophysics. This chapter gives a brief overview of these techniques and contains references for further details.

3.1 Organic molecular beam deposition

All thin film samples in this work have been prepared by organic molecular beam deposition (OMBD) [140, 245, 246]. In OMBD, a molecular beam with a well-defined angular distribution is created by a Knudsen cell [247] in an ultra-high vacuum (UHV) chamber, and is used to deposit material onto a substrate (see Fig. 3.1). The Knudsen cell contains the material as a powder in a ceramic crucible surrounded by a tantalum shielding. The crucible can be heated resistively to the evaporation temperature of the material and has a tantalum aperture with a small hole. The temperature of the crucible can be measured by a thermocouple. Furthermore, a rotatable shutter is attached in front of the aperture for a controlled beginning and ending of the deposition process.

Obverse to the Knudsen cell, the substrates as well as a quartz crystal microbalance (QCM) are placed [247, 248]. The QCM enables to measure the molecular flux using the change in oscillation frequency of a crystal due to the mass of deposited material. By taking into account the density of the material, the growth rate, which is defined in the following by film thickness per time interval, can be calculated [247]. The molecular flux at the sample and the QCM can be different due to different distances to the Knudsen cell as well as different positions within the angular distribution of the molecular beam. The ratio between the growth rate at the QCM and at the substrates is called scaling factor and can be obtained by the growth of calibration samples, measurement of their final thickness and a comparison of this measured thickness to the thickness measured by the QCM. The growth rate can be adjusted by varying the temperature of the Knudsen cell [247].

For co-deposition of compounds to obtain thin film blends [157, 158], two Knudsen cells are attached to the chamber and separated by a screen to prevent cross-talk (see Fig. 3.1). The growth rates from both Knudsen cells are measured separately with two QCMs.

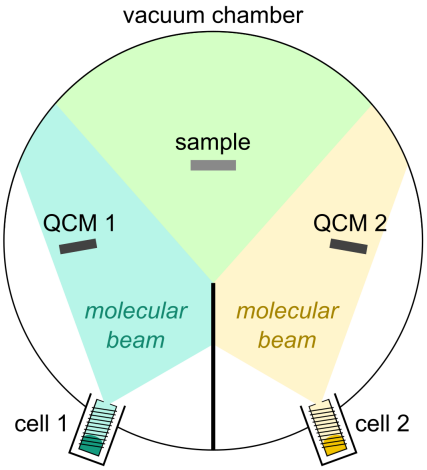


Figure 3.1: OMBD geometry with two Knudsen cells and two QCMs.

The concentration $c \in [0, 100]\%$ of a compound indexed by $i \in \{1, 2\}$ in the blends reported in this work corresponds to molar fractions $p_i \in [0, 1]$. For the calculation of growth rates for a defined concentration, the molecular densities of the two compounds have to be taken into account. The growth rate r_i is given by

$$r_i = \frac{V_i \, \Delta N_i}{A \, \Delta t} \tag{3.1}$$

with the volume V_i of one single molecule of compound i, calculated from a reported crystal structure, and the flux of molecules ΔN_i through an area A within time interval Δt. The molar ratio $x \in [0, \infty)$ of a binary mixture can be defined by

$$x = \frac{\Delta N_1}{\Delta N_2} = \frac{1}{v} \frac{r_1}{r_2} , \qquad v = \frac{V_1}{V_2} . \tag{3.2}$$

and is related to p_1 by $x = p_1/(1 - p_1)$. With given molar fractions p_i and total growth rate $R = r_1 + r_2$ (see Apx. E for R of each film), the growth rates r_i of each compound can therefore be calculated by

$$r_1 = \frac{xv}{1 + xv} R , \qquad r_2 = \frac{1}{1 + xv} R . \tag{3.3}$$

For the uncertainty propagation from the measured QCM rate into the molar fraction, see Apx. A.2. The uncertainty of the growth rate measured by the QCM is estimated to be 10 % for this work. With this uncertainty, the absolute uncertainty of a molar fraction of 0.5 is 0.05 and decreases for molar fractions with excess of either compound (uncertainty of 0.018 for molar fractions of 0.1 and 0.9, see Apx. A.2). These uncertainties in the molar fractions are not shown in figures of this work for better visibility.

As substrates, silicon with a silicon oxide layer of approximately 2 nm thickness as well as different borosilicate glasses (Pyrex, Menzel, MicroChemicals) have been used. The

substrates have been cleaned in acetone and isopropanol in an ultrasonic bath for five minutes each, fixed by silver paste at the sample holder and heated in vacuum to 600 K for at least 12 hours before the deposition process. For some films the substrate was cooled with liquid nitrogen during the deposition process. For the substrate temperature during growth of each film, see Apx. E.

3.2 Structural and optical characterization

For the interpretation of time-resolved measurements on thin films of OSCs, knowledge about the molecular structure and steady-state optical properties is crucial. Therefore, a structural and optical characterization has been performed for all films using X-ray diffraction (XRD) and UV-Vis-NIR absorbance spectroscopy, respectively.

3.2.1 X-ray diffraction

The structural order and unit cell parameters of thin films prepared for this work has been investigated by XRD. For details on XRD the reader is referred to textbooks [147, 249].

X-rays that hit a sample are scattered by electrons, leading to constructive interference in certain directions if the sample has crystalline domains. Molecular crystals have already been discussed in Sec. 2.2. For derivation of the direction of constructive interference by a crystallite it is useful to define a reciprocal lattice via

$$\mathbf{b}_1 = 2\pi \frac{\mathbf{a}_2 \times \mathbf{a}_3}{\mathbf{a}_1 \cdot \mathbf{a}_2 \times \mathbf{a}_3}, \qquad \mathbf{b}_2 = 2\pi \frac{\mathbf{a}_3 \times \mathbf{a}_1}{\mathbf{a}_1 \cdot \mathbf{a}_2 \times \mathbf{a}_3}, \qquad \mathbf{b}_3 = 2\pi \frac{\mathbf{a}_1 \times \mathbf{a}_2}{\mathbf{a}_1 \cdot \mathbf{a}_2 \times \mathbf{a}_3}. \tag{3.4}$$

with the primitive real-space lattice vectors $\mathbf{a}_1$, $\mathbf{a}_2$ and $\mathbf{a}_3$ [147]. A point in the reciprocal lattice can be described by a superposition of the primitive reciprocal lattice vectors (Eq. 3.4) with integer numbers h, k and l,

$$\mathbf{b}_{\mathrm{hkl}} = h \cdot \mathbf{b}_1 + k \cdot \mathbf{b}_2 + l \cdot \mathbf{b}_3. \tag{3.5}$$

By definition (Eq. 3.4), each reciprocal lattice vector $\mathbf{b}_{\mathrm{hkl}}$ is orthogonal to a set of lattice planes in real-space and thus describes their orientation. Furthermore, the length of those $\mathbf{b}_{\mathrm{hkl}}$ corresponding to coprime (hkl) tuples is related to the distance d between the respective crystal lattice planes in real-space by

$$|\mathbf{b}_{\mathrm{hkl}}| = \frac{2\pi}{d}\,. \tag{3.6}$$

The primitive lattice vectors in real-space $\mathbf{a}_1$, $\mathbf{a}_2$ and $\mathbf{a}_3$ define a primitive unit cell, and the lengths of these vectors can be defined as a, b and c (see Sec. 2.2). With this definition, the reciprocal lattice vectors (100), (010) and (001) are orthogonal to the bc-, ac- and ab-plane and are therefore also called $a^\star$, $b^\star$ and $c^\star$, respectively [146].

The constructive interference of X-rays scattered at lattice planes are the origin of Bragg reflections [147, 249], which occur at an angle θ described by

$$2d \sin\theta = n \cdot \lambda \tag{3.7}$$

with the distance between the lattice planes d, an integer number n as well as the X-ray wavelength λ. Since lattice planes can be described by reciprocal lattice vectors (Eq. 3.6), the Bragg equation (Eq. 3.7) is equivalent to the so-called Laue condition, which states that for constructive interference the scattering vector $\mathbf{q}$ of the X-ray beam must coincide with one of the reciprocal lattice vectors,

$$\mathbf{q} = \mathbf{k}_{\text{out}} - \mathbf{k}_{\text{in}} = \mathbf{b}_{\text{hkl}} \ , \tag{3.8}$$

with the incoming and outgoing wave vectors $\mathbf{k}$ that have an absolute value of $2\pi/\lambda$.

For isotropic polycrystalline samples with unoriented crystallites, for all directions of $\mathbf{q}$ with a given absolute value $|\mathbf{q}| = |\mathbf{b}_{\text{hkl}}|$, a crystallite can be found, for which the Laue condition (Eq. 3.8) is fulfilled. This makes the diffraction pattern independent of the direction of $\mathbf{q}$ and only dependent on the absolute value $|\mathbf{q}| = \sqrt{q_x^2 + q_y^2 + q_z^2}$. For uniaxially anisotropic polycrystalline samples, crystallites have a fixed orientation with respect to a preferential axis (say, the z-axis) but are randomly rotated around this axis. Analogous to the case of isotropic polycrystalline samples, the diffraction pattern is now independent of the direction of the component of $\mathbf{q}$ perpendicular to the z-axis, and only depends on the two components q_z and $q_{xy} = \sqrt{q_x^2 + q_y^2}$ of the scattering vector $\mathbf{q}$. In order to access all combinations of q_z and q_{xy}, two different XRD geometries have been applied in this work and are described in the following.

X-ray reflectivity

Using X-ray reflectivity (XRR), the distance between lattice planes oriented parallel to the surface can be probed. In this technique, an X-ray beam hits the sample under an angle of incidence, which is continuously varied. An X-ray detector measures the reflected intensity under specular condition, i.e. at an angle that is the same as the incidence angle. Upon equivalently varying both the incidence angle and the angle of the detector an intensity curve as a function of q_z is obtained. The scattering vector is the difference between wave vectors of the reflected and the incident beam and points along the surface normal (see Fig. 3.2a).

Several features can be observed in XRR curves of organic thin films, and are briefly mentioned in the following. For a more detailed description the reader is referred to Ref. 250. For the beam energies used in this work (either 805 eV or 1300 eV, see X-ray wavelengths later on), silicon exhibits total reflectivity at low q_z until a total reflectivity edge [250]. Above the total reflectivity edge, Kiessig fringes can be observed for smooth films, whose periodicity and damping are associated with the film thickness and roughness,

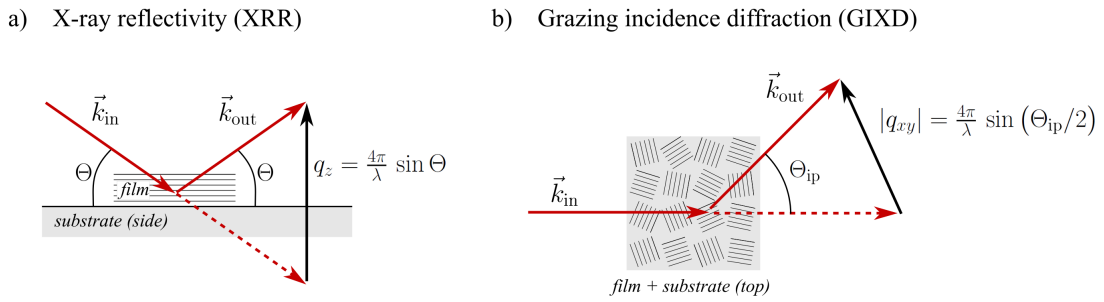


Figure 3.2: Measurement geometry of a) XRR and b) GIWAXS. Inspired by Ref. 140.

respectively. The Kiessig fringes of calibration samples have been used to obtain the scaling factors for the QCM calibration in this work. At larger q_z, Bragg peaks (BPs) originating from diffraction at crystal planes oriented parallel to the surface can be observed. From the position of the BPs in the XRR curve, the out-of-plane lattice spacing can be calculated with Eqs. 3.7 and 3.8 and is of particular interest in this work to examine the mixing behavior of compounds. Relative uncertainties in the lattice spacing are set to 1 % in this work based on typical widths of fitted Gaussian functions to BPs. Finally, Laue oscillations can be observed around BPs, whose periodicity is related to the number of coherently scattering lattice planes [250].

All XRR curves in this work were measured at a diffractometer (3303TT, GE) using Cu K_α-radiation ($\lambda = 1.5406\,\text{Å}$) and a 1D detector (Meteor 1D, XRD Eigenmann).

Grazing incidence X-ray diffraction

By grazing incidence wide-angle X-ray scattering (GIWAXS), the distance between lattice planes with normal vectors oriented parallel or oblique to the surface can be probed. For GIWAXS, an X-ray beam hits the sample under a small, fixed incidence angle Θ_{inc}, chosen in this work close to the total reflectivity edge of silicon to ensure penetration through the entire film. The scattered intensity in different directions behind the sample is measured, yielding a 2D diffraction intensity map.

The intensity map is a function of two angles, the in-plane scattering angle Θ_{ip} and the out-of-plane scattering angle Θ_{op}. From these angles, the scattering vector $\mathbf{q}$ can be calculated with the X-ray wavelength λ by the following equalities [251],

$$q_x = \frac{2\pi}{\lambda}\Big[\cos(\Theta_{op}) \cdot \cos(\Theta_{ip}) - \cos(\Theta_{inc})\Big] \tag{3.9}$$

$$q_y = \frac{2\pi}{\lambda}\Big[\cos(\Theta_{op}) \cdot \sin(\Theta_{ip})\Big] \tag{3.10}$$

$$q_z = \frac{2\pi}{\lambda}\Big[\sin(\Theta_{op}) + \sin(\Theta_{inc})\Big]\,. \tag{3.11}$$

As described before, the dependence of scattered intensity on q_x and q_y is the same if the sample is uniaxially anisotropic with a preferential axis pointing along the substrate normal, and the data can be converted into a reciprocal space map as a function of $|q_{xy}|$

and q_z. As can be seen from Eq. 3.9, it is $q_x = 0$ only for $\Theta_{op} = \Theta_{inc}$ and $\Theta_{ip} = 0$. For all other scattering angles the scattering vector has an in-plane component (from $q_x \neq 0$ it follows $|q_{xy}| \neq 0$), which means that the $|q_{xy}| = 0$ line in the reciprocal space map cannot be measured by GIWAXS but exclusively by XRR.

Reflections with $q_z \approx 0$ originate from diffraction at lattice planes with normal vectors parallel to the substrate (see Fig. 3.2b), while those with $q_z > 0$ originate from diffraction at oblique lattice planes. Reflections in the reciprocal space map can be compared and assigned to calculated reciprocal lattice vectors of know crystal structures. After assignment of reflections, unit cell parameters of the crystal structure can be calculated from their positions with Eqs. 3.5–3.8. Relative uncertainties in the unit cell parameters are set to 3 % in this work, again based on typical widths of fitted Gaussian functions to in-plane BPs.

GIWAXS measurements were performed

- using a Xeuss 2.0 system (Xenocs) with a Dectris Pilatus3 R 300K detector using $\lambda = 1.5406$ Å, a sample-detector distance (SDD) of 170 mm and $\Theta_{inc} = 0.2°$,
- at beamline SixS at the Soleil synchrotron at Gif-sur-Yvette, France with an X-PAD hybrid pixel array detector using $\lambda = 0.9537$ Å, a SDD of 892 mm and $\Theta_{inc} = 0.2°$
- at beamline I07 at the Diamond Light Source at Oxfordshire, United Kingdom with a Dectris Pilatus3 R 100K detector using $\lambda = 0.9537$ Å, a SDD of 1117 mm and $\Theta_{inc} = 0.11°$.

The three systems are referred to in this thesis by *Xeuss system*, *Soleil* and *Diamond*, respectively. For all measurements the sample was either kept in vacuum or in nitrogen atmosphere to reduce air scattering and to avoid beam damage of the sample.

3.2.2 Absorbance spectroscopy

For the steady-state optical characterization of thin films on transparent substrates, absorbance spectroscopy in the ultraviolet (UV), visible (VIS) and near infrared (NIR) spectral range (UV-Vis-NIR absorbance spectroscopy) has been performed [252]. Absorbance spectra of mixed thin films not only contain information about the amount of deposited material on the substrate (thus connecting to the film thickness and for blends to the mixing ratio), but also the energies and oscillator strength of transitions to electronically excited states can be derived [153]. This information can then be correlated to molecular environments and intermolecular interactions.

In UV-Vis-NIR absorbance spectroscopy, a light source creates a white light beam of a broad spectrum (Vis-NIR or UV range depending on its type). This white light beam is spectrally split and all wavelengths except a narrow range of 2 nm (see later on) are blocked. The resulting narrow-band beam is guided through the sample, and the transmitted light

intensity $I_{\mathrm{trans}}(\lambda)$ is measured. Using a reference spectrum $I_0(\lambda)$ measured without the sample, a transmittance spectrum $T(\lambda)$ is calculated via

$$T(\lambda) = \frac{I_{\mathrm{trans}}(\lambda)}{I_0(\lambda)}\,. \tag{3.12}$$

The absorbance $A(\lambda)$ is defined as

$$A(\lambda) = -\log_{10}(T(\lambda)) \tag{3.13}$$

and correlates to the number of photons that do not reach the photodetector due to the sample [253]. Three effects can occur at the sample, leading to a reduction of light intensity at the photodetector, which are absorption, reflection and scattering, for which physical quantities are indexed by *abs*, *ref* and *scat*, respectively, in the following. The transmitted intensity is reduced by these effects each with an own transmission factor

$$I_{\mathrm{trans}}(\lambda) = I_0(\lambda) \cdot T_{\mathrm{abs}}(\lambda) \cdot T_{\mathrm{ref}}(\lambda) \cdot T_{\mathrm{scat}}(\lambda) \tag{3.14}$$

between 0 and 1. Due to the logarithm in the definition of the absorbance (Eq. 3.13) the total absorbance is the sum of the absorbances of the single contributions

$$A_{\mathrm{tot}}(\lambda) = A_{\mathrm{abs}}(\lambda) + A_{\mathrm{ref}}(\lambda) + A_{\mathrm{scat}}(\lambda) \tag{3.15}$$

each defined analogously to Eq. 3.13. The contribution of interest for this work is $A_{\mathrm{abs}}(\lambda)$, which is obtained from the transmittance of a sample with thickness d given by the Beer-Lambert law [254],

$$T_{\mathrm{abs}}(\lambda) = e^{-\alpha(\lambda)\cdot d}\,, \quad \alpha(\lambda) = \frac{4\pi k(\lambda)}{\lambda} \quad \Rightarrow\ A_{\mathrm{abs}}(\lambda) = \log_{10}(\mathrm{e})\,\alpha(\lambda)\,d \tag{3.16}$$

with the attenuation coefficient $\alpha(\lambda)$, and the imaginary part $k(\lambda)$ of the refractive index. For scattering at rough surfaces, the contribution $A_{\mathrm{scat}}(\lambda)$ in Eq. 3.15 is proportional to $1/\lambda^2$ [255]. The contribution A_{ref} is for glass only weakly depending on the wavelength and subtracted together with the absorption of glass by measurement of a reference sample. This subtraction is only possible, since the reflection of thin film samples is not different from that of the substrate due to the small thickness compared to the wavelength [253].

All absorbance spectra in this work were measured with a Lambda 950 spectrometer (Perkin Elmer) equipped with a light source combination of a halogen lamp (Vis-NIR) and a deuterium lamp (UV) (change at 319.2 nm), a double-monochromator optical system with a resolution of 2 nm and a photomultiplier tube (PMT) detector for the spectral range between $200 - 820$ nm. The system further has a lead sulfide (PbS) detector for the IR range between $820 - 2000$ nm, which, however, was not used in this work.

3.3 Time-resolved techniques

After structural and optical characterization of the samples, their photophysics have been studied by time-resolved techniques, with which the temporal evolution of state populations after photoexcitation can be followed. Different time-resolved techniques have been applied due to different requirements such as the time-resolution of the setup.

3.3.1 Transient absorption (TA) spectroscopy

Transient absorption (TA) spectroscopy is a time-resolved pump-probe technique for measuring ultrafast electronic processes based on changes in transmitted light through the sample as a function of time after excitation (Fig. 3.3). TA spectroscopy has the advantage not to rely on the emission of photons in contrast to several other time-resolved techniques [206], as well as its capability to directly measure signatures of triplet excitons and other dark states [97, 256]. Furthermore, TA spectroscopy enables a femtosecond time resolution close to the limit given by time-energy uncertainty (e.g. 10 fs with 600 ± 10 nm excitation wavelength).

In the following, the principle of TA spectroscopy and the data analysis are briefly described. For details the reader is referred to Refs. 256–259.

Principle and setup

For TA spectroscopy a pump and a probe laser pulse are required, which are typically created from a split beam of a single, pulsed laser source. One of these pulses is converted into a narrow-band pump pulse for excitation of the sample. The intensity of the pump pulse is varied for fluence-dependent TA measurements to determine the influence of fluence-dependent processes like SSA and TTA. The other pulse serves as the probe pulse and is converted by a crystal with a nonlinear susceptibility into a white light pulse. The two pulses are focused on the sample and first adjusted to arrive at the same time using a delay stage that extends the path length of the pump pulse. During the measurement, the delay stage is then used to vary the time difference (delay time) between the arrival of pump and probe pulses at the sample. Behind the sample, the pump pulse is blocked and the probe pulse is guided into a spectrophotometer. For calculation of the TA signal, some

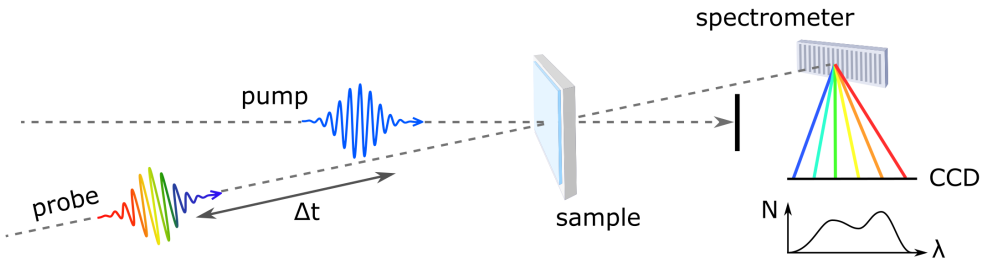


Figure 3.3: Principle of TA spectroscopy.

of the pump pulses are blocked by a chopper before arrival at the sample. The number of photons of the probe pulse arriving at the detector is recorded as an intensity spectrum $I_{\text{pump state}}(\lambda, t)$ by the spectrophotometer for different delay times t between pump and probe pulses, with ($I_{\text{on}}(\lambda, t)$) and without ($I_{\text{off}}(\lambda, t)$) prior excitation by the pump pulse. The whole range of delay times is scanned multiple times, and the intensity spectra at each delay time are averaged. Also some intensity spectra at negative delay times are recorded, corresponding to an arrival of the probe pulse before the pump pulse.

The measured signals are further processed by calculation of the normalized difference between the intensity spectrum with and without excitation by the pump pulse,

$$\frac{\Delta T}{T}(\lambda, t) = \frac{T_{\text{on}}(\lambda, t) - T_{\text{off}}(\lambda, t)}{T_{\text{off}}(\lambda, t)} = \frac{I_{\text{on}}(\lambda, t) - I_{\text{off}}(\lambda, t)}{I_{\text{off}}(\lambda, t)} \,, \tag{3.17}$$

with the definition of transmittance $T(\lambda, t) = I(\lambda, t)/I_0(\lambda, t)$ and the probe pulse intensity spectrum $I_0(\lambda, t)$ before the sample. The $\Delta T/T$ signal is then further converted into a TA signal $\Delta A(\lambda, t)$, which is the difference in absorbance with and without excitation by the pump pulse [256],

$$\begin{aligned} \Delta A(\lambda, t) &= A_{\text{on}}(\lambda, t) - A_{\text{off}}(\lambda, t) = -\log\left(T_{\text{on}}(\lambda, t)\right) + \log\left(T_{\text{off}}(\lambda, t)\right) \\ &= -\log\left(\frac{T_{\text{on}}(\lambda, t)}{T_{\text{off}}(\lambda, t)}\right) \end{aligned} \tag{3.18}$$

with the definition of absorbance $A = -\log(T)$ and further for small signals ($T_{\text{on}}/T_{\text{off}} \approx 1$)

$$\Delta A(\lambda, t) \approx -\left(\frac{T_{\text{on}}(\lambda, t)}{T_{\text{off}}(\lambda, t)} - 1\right) = -\frac{\Delta T}{T}(\lambda, t) \tag{3.19}$$

with Eq. 3.17. Since at negative delay times the TA signal should be zero ($\Delta A(\lambda, t < 0) = 0$), these TA spectra are subtracted as a background, which might originate from scattering of the pump pulse into the spectrophotometer.

Signatures in TA spectra

Different effects can produce sample-related features of different signs in the TA signal, as shown in Fig. 3.4 [256]. After excitation of the sample, a small fraction of molecules is in an excited state. These molecules cannot absorb photons from the probe pulse anymore and lead to a higher transmission (negative ΔA) in the spectral region where the sample absorbs without previous excitation. This higher transmission is called ground state bleach (GSB) and is independent of the nature or evolution of the excited state. The GSB only disappears upon decay of the molecules back to the ground state. If the molecules are in the S_1 state, the probe pulse can be amplified by stimulated emission (SE) of photons by the probe pulse itself. SE leads to a negative ΔA signal in the spectral region of the emission of the sample and disappears upon decay of the molecules to non-emissive states, such as the ground state or triplet states.

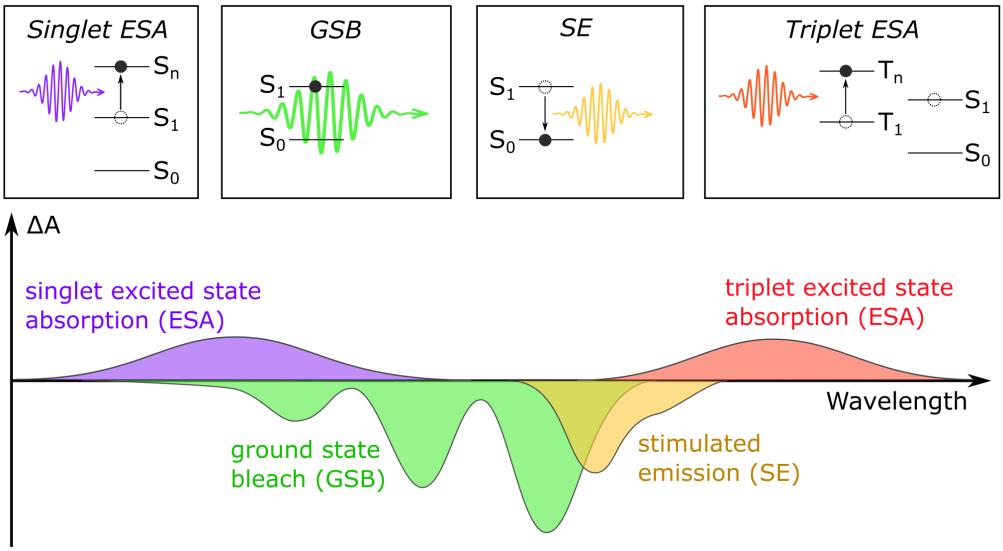


Figure 3.4: Origins of possible contributions to the TA signal and typical spectral shapes and ordering.

In both singlet and triplet excited states there is the possibility for the probe pulse to excite these states by excited state absorption (ESA) into higher electronic states ($S_1 \rightarrow S_n$, $T_1 \rightarrow T_n$) as already discussed in Sec. 2.3.1 and shown in Fig. 2.11. Since the triplet states T_n are ordered more closely in energy than singlet states S_n, triplet ESA typically occurs at longer wavelengths than singlet ESA, as sketched in Fig. 3.4. In particular this low-energy triplet ESA allows for an unambiguous identification of triplets created in the sample.

A fifth contribution to the TA signal shall be briefly mentioned here due to the impact for samples studied in this thesis. Upon interaction with the sample, the pump pulse not only excites molecules electronically within the sample but also creates heat, which rapidly distributes across the sample [260, 261]. This increase in temperature on the order of 1 K can change the absorption of all molecules that are still in the electronic ground state, thus contributing a so-called thermal artifact to the TA signal. The exact spectral shape of the thermal artifact can be determined by measuring the temperature-dependence of the absorption of the sample [260] and typically involves a shift of the absorption spectrum to higher energies for increasing temperature. The amplitude of the thermal artifact depends on the magnitude of the spectral shift, which further depends on the exact increase in temperature and is therefore almost impossible to calculate. Similar shifts of the absorption leading to derivative-like features in TA spectra are in particular known for quantum dots, and originate in this case from the Stark effect due to charges or the interaction with another exciton [262].

Data analysis

A TA measurement yields an experimental TA dataset $\Delta A_{\mathrm{exp}}(\lambda, t)$ as a function of different wavelengths and delay times, and therefore a two-dimensional TA map. From the TA map, TA spectra at different delay times or the temporal evolution of the signal at different

wavelengths (called time trace) can be extracted. The main interest after obtaining a TA map is the determination of spectral signatures of different species and time constants of processes between them. Here, species describes molecules in a specific state. TA spectra at different delay times can give a first indication on the presence of such species according to the spectral signatures discussed above. Furthermore, fits to time traces yield the dynamics between these species.

For strictly parallel or sequential processes, a determination of TA spectra of species and their respective decay time constants can be obtained by global analysis (GA), which is a fit of a modeled TA map $\Delta A_{\mathrm{model}}(\lambda, t)$ to the experimental one [258]. Such a fit is more robust against spectral shifts and intermediate species than time trace fits with independent parameters, since an assumption of too few species becomes evident from fit residuals of the GA. The model TA map is a superposition of TA spectra of N different species

$$\Delta A_{\mathrm{model}}(\lambda, t) = \sum_{i=1}^{N} c_i(t) \Delta A_i(\lambda) \tag{3.20}$$

where $\Delta A_i(\lambda)$ is the TA spectrum of the evolution associated species (EAS) i and c_i is its time-dependent coefficient. There are two common ways of a GA, first, using independent, parallel decays of a variety of excited species to the ground state,

$$c_i(t) = e^{-k_i t} \tag{3.21}$$

with decay rates k_i, or second, using a sequential evolution of the different EAS into each other, starting from only one of them

$$c_1(t) = e^{-k_1 t}, \quad \frac{d}{dt} c_{i>1}(t) = k_{i-1}\, c_{i-1}(t) - k_i c_i(t)\,, \tag{3.22}$$

where k_i is the decay rate from EAS i to EAS i+1, except for k_N, which is the decay rate of species N to the ground state. For both the parallel and the sequential model, the sum of the coefficients is normalized to 1. $\Delta A_{\mathrm{model}}(\lambda, t)$ is fitted by a least-squares routine to $\Delta A_{\mathrm{exp}}(\lambda, t)$ using the free parameters k_i and $\Delta A_i(\lambda)$. The TA map with the dimension $\dim(\lambda) \times \dim(t)$ is thus fitted with $\dim(\lambda) \times N$ free parameters. Starting values for $\Delta A_i(\lambda)$ are usually obtained by a singular value decomposition of $\Delta A_{\mathrm{exp}}(\lambda, t)$, which can also indicate the number of species required to fit the TA map. Typically, however, GA is performed with different numbers of species, and the GA with the lowest number of species that yields a reasonable fit result is chosen as the result of the GA.

Besides the sample-related features in $\Delta A_{\mathrm{exp}}(\lambda, t)$ that are the features of interest, there are also some setup-related features that have to be taken into account in $\Delta A_{\mathrm{model}}(\lambda, t)$ (Eq. 3.20) for a precise fitting. First, the excitation of the sample by the pump pulse does not take place immediately but has a certain temporal evolution, called instrument response function (IRF), which impacts the early times of the measurement and limits the time-resolution. The IRF can be approximated to be a gaussian function and is accounted

for in $\Delta A_{\mathrm{model}}(\lambda, t)$ by convolving each modeled time trace with the IRF. Second, the probe pulse is generally chirped upon arrival at the sample, which means photons of different wavelengths arrive at different times at the sample and the spectrophotometer (see Fig. 3.3), and which distorts the TA map. In this case, the temporal origin of modeled time traces needs to be different for different wavelengths in $\Delta A_{\mathrm{model}}(\lambda, t)$. This effect can easily be taken into account by adding a third-order polynomial description of the wavelength-dependent temporal origin.

Finally, so-called coherent artifacts can have a large impact on the TA signal, which arise from interaction between pump and probe pulse in dielectric media such as the sample and its substrate [263–265]. This interaction takes place around time zero, where pump and probe pulse arrive at the sample at the same time, and varies as the pump pulse is shifted by the delay stage with respect to the probe pulse, thus varying the degree of constructive interference. Therefore, the interaction creates oscillations in the time traces of a TA measurement around time zero. The coherent artifact is usually accounted for by adding to $\Delta A_{\mathrm{model}}(\lambda, t)$ a superposition of TA spectra with a gaussian time evolution around zero delay time, which are not connected to the EAS. For the global analysis of the obtained TA data the open source software Glotaran was used in this work [266].

Setup specifications

The TA measurements shown in this work were performed with Dr. L. Moretti and Dr. M. Maiuri in the research group of Prof. G. Cerullo (Politecnico di Milano, Italy). In this setup, pump and probe pulses had their common origin in a Ti:Sapphire chirped pulse amplified source (Coherent Libra), with 4 mJ output energy, 1 kHz repetition rate, 800 nm central wavelength and 100 fs pulse duration. Excitation pulses of different wavelengths with a sub-40 fs duration were generated by an optical parametric amplifier (OPA) pumped by the second harmonic of the 800 nm pulses using a β-barium borate crystal [267]. Broadband probe pulses are a white-light continuum (WLC) generated in two different ways. A WLC spanning $430 - 780$ nm was obtained by focusing the 800 nm pulses into a 2 mm-thick sapphire plate. A WLC spanning $540 - 1000$ nm was obtained by focusing the 1200 nm output of a second OPA into a 3 mm-thick yttrium aluminum garnet (YAG) plate [267]. The pump pulses were focused to a 350 µm diameter spot, while the probe pulses were focused to a smaller 175 µm diameter spot to ensure an approximately constant lateral exciton density in the probed area. Transient absorption spectra were collected by using a fast optical multichannel analyzer working at the full 1 kHz laser repetition rate. Measurements were performed at room temperature and either with nitrogen-atmosphere encapsulated samples or under vacuum to avoid sample degradation.

3.3.2 Time-resolved photoluminescence (TRPL)

By time-resolved photoluminescence (TRPL) spectroscopy, the temporal evolution of the number and spectral distribution of emitted photons after excitation of a sample is measured [268]. TRPL spectroscopy is a powerful tool to probe the lifetime selectively only

of molecules in emissive states, which prevents the necessity to distinguish between spectral features of singlets, triplets or other dark states and thus strongly simplifies the data interpretation. Furthermore, TRPL spectroscopy has a very high signal-to-noise ratio, so that the population dynamics of emissive states can be followed over up to six orders of magnitude [269]. This is in contrast to TA spectroscopy, where typical signals allow to follow dynamics over maximum two orders of magnitude [97]. Therefore, subtle differences in the population dynamics upon application of a magnetic field can be detected with TRPL spectroscopy [82]. A disadvantage of TRPL spectroscopy is the poorer time resolution of few picoseconds compared to the time resolution of tens of femtoseconds of TA spectroscopy.

For TRPL spectroscopy, the sample is excited by a short laser pulse with an IRF of typically few tens of picoseconds width. The number of photons emitted by the sample is recorded as a function of wavelength and time after excitation by a streak camera, see Ref. 268 for details. A 2D-dataset of the fluorescence intensity at different wavelengths and times after excitation is obtained, which thus contains the temporal evolution the PL spectrum as well as the temporal evolution of the overall number of emitted photons (fluorescence decay). The temporal evolution of the fluorescence decay $f(t)$ can generally be fitted using a superposition of n_{me} exponential functions (indexed by i) with amplitudes A_i and time constants k_i,

$$f(t) = \sum_{i=1}^{n_{\mathrm{me}}} A_i \cdot \exp(-k_i\, t)\,. \tag{3.23}$$

convoluted with the IRF, which might be approximated to be a gaussian function.

If emission only occurs from one state in a homogeneous system, i.e. every photoexcited molecule has the same decay channels, the fluorescence decay describes the temporal evolution of the population of this state. The state can be depopulated by different decay channels with different rates, such as radiative decay (k_{rad}), ISC (k_{ISC}), IC (k_{IC}) or SF (k_{SF}), as discussed in Sec. 2.3.1 and 2.4. The overall depopulation rate of the emissive state equals the sum of all decay rates [270],

$$k_{\mathrm{fl}} = k_{\mathrm{rad}} + k_{\mathrm{ISC}} + k_{\mathrm{IC}} + k_{\mathrm{SF}}\,, \tag{3.24}$$

and is called fluorescence rate k_{fl}. In a homogeneous system without state repopulation, the decay of PL intensity is monoexponential ($n_{\mathrm{me}} = 1$) [270]. The fluorescence rate k_{fl} that describes this monoexponential fluorescence decay (see Fig. 3.5) should be distinguished from the radiative rate k_{rad}, which is the rate with which molecules radiatively relax to the ground state by emitting photons. It is important to note that although the emission of photons is measured, the lifetime of the corresponding excited state is affected by non-radiative decay channels (see Eq. 3.24), and thus, the measured decay reflects both radiative and non-radiative processes.

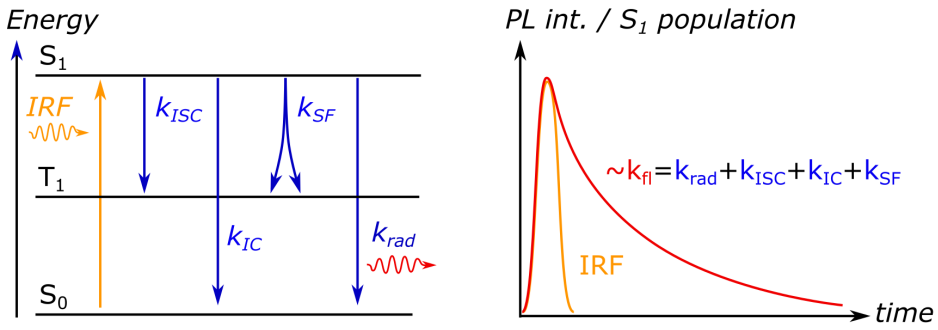


Figure 3.5: Contributions to the fluorescence rate, which is proportional to the population of the S_1 state. The initial population of S_1 takes place with a temporal evolution described by the IRF. Different decay channels then depopulate S_1, and the sum of their rates can be observed with TRPL spectroscopy.

The fluorescence decay can be multi-exponential ($n_{\mathrm{me}} > 1$) either due to a heterogeneous system with several emitting species, or due to back-and-forth population transfer between emissive and non-emissive (dark) states. In the first case, i.e. in a heterogeneous system with several emitting species, the fluorescence decay can be multi-exponential due to different k_{fl} of the species. Since different species generally exhibit different PL spectra, the measured PL spectra at different times after excitation differ in this case. In the second case of a back-and-forth population transfer between an emissive and a dark state, biexponential ($n_{\mathrm{me}} = 2$) population dynamics are observed, of which the decay with the faster time constant is called prompt fluorescence and that with the slower time constant is called delayed fluorescence [269]. The prompt fluorescence originates from the emission of photons by molecules before conversion to the dark state. The delayed fluorescence originates from molecules in emissive states that first evolved to dark states before evolving back to their initial state. Therefore, even long after the first process should have completely depopulated the initial state, PL can still be observed, and since those photons are emitted upon radiative decay from the initial state, the normalized PL spectrum does not change for different times after excitation [269]. A prominent example for prompt and delayed fluorescence is TET, in which SF depopulates the emissive singlet state but triplet fusion brings back some of the population [82, 269].

A similar technique to TRPL spectroscopy is time-correlated single photon counting (TCSPC), since again the time-dependent emission of photons of a sample after excitation is measured [176, 268]. In contrast to TRPL spectroscopy, however, no information about the spectral distribution of the emitted photons is obtained, and only the temporal evolution of the PL intensity can be accessed. In this technique, the emitted radiation is attenuated such that only a single emitted photon is detected after each excitation event. After repeating this measurement many times, a histogram of counted photons over time after excitation can be drawn, which resembles the sum of all time traces of a TRPL spectroscopy measurement using a streak camera.

The TRPL spectroscopy measurements shown in this work were performed by C. Cruz in the research group of Prof. C. J. Bardeen (UC Riverside, USA). The measurements were carried out with a Hamamatsu C4334 Streakscope [67, 271] with a time resolution of 20 ps and a spectral resolution of 2.5 nm. The 800 nm output of an 80 MHz Coherent Vitesse Ti:Sapphire oscillator was frequency doubled to generate the 400 nm excitation pulse. A Pockels cell controlled by a ConOptics pulse picking system was used to adjust the repetition rate of the oscillator to 100 kHz. A 450 nm long wave pass filter was placed before the streak camera to minimize the contribution of laser scatter to the signal. All measurements were performed in a vacuum cryostat (10-5 torr) fitted with optical windows, and pulse fluences remained below 1.2 µJ/cm^2.

The TCSPC measurements shown in this work were conducted with T. Rammler in the research group of Prof. F. Meixner at the Institute of Physical and Theoretical Chemistry at the University of Tübingen (Germany) with a pulsed laser diode LDH-P-C-470 (PicoQuant, Germany). The pulses had a wavelength of 470 nm, a time-averaged power of 0.05 µW and a repetition rate of 40 MHz. Using a Plan-NEOFLUAR 65x/NA 0.75 air-objective (Carl Zeiss AG, Germany), the laser pulses were focused on a spot with 30 µm diameter on the sample, yielding a fluence of 1.77×10^{-4} µJ/cm^2. For TCSPC, emitted photons were detected with an electron multiplying iXon Ultra 888 EMCCD camera (Andor Technology, UK). The Andor Solis software was used for controlling the camera and further data analysis including fits with a convolved IRF. For steady-state PL spectroscopy at the same setup, an Acton SP300 spectrometer with a PIXIS 100 camera (both Princeton Instruments, USA) was used. TCSPC and steady-state PL measurements were always performed at the same spot of the sample.

4. Materials

The properties of materials used in this work are briefly discussed in this chapter. All these materials consist of aromatic molecules, are powdery at room temperature and sublime at elevated temperatures in vacuum. Most of them are prototypical OSCs, have been shown to exhibit high electron mobilities [272, 273] and have therefore been used as active layers in proof-of-principle thin film devices [37–43, 272–274].

The different material classes can be categorized according to their role in the projects of this work. The classes of acenes (Fig. 4.1) and acene derivatives serve to investigate SF processes and are therefore called SF materials/compounds. Phenacenes have high optical band-gaps, weakly interact with the SF compounds and cannot actively contribute to the SF processes in mixtures [52, 210, 275, 276]. Such weakly interacting compounds with high optical band gaps are called spacer compounds and allow to investigate the impact of replacement of SF molecules on the SF rate.

4.1 Acenes: tetracene and pentacene

Acenes are $n \geq 3$ linearly fused benzene rings and consist of $4n+2$ carbon atoms and $2n+4$ hydrogen atoms [127]. As prototypical SF materials, the two acenes TET ($C_{18}H_{12}$) and PEN ($C_{22}H_{14}$) have been employed in this work (Fig. 4.1).

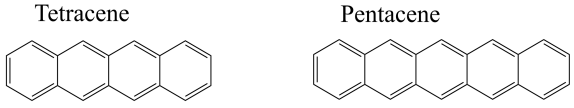


Figure 4.1: Chemical structures of TET and PEN.

Acenes generally form a HB aggregate (see Fig. 4.2a and 4.2b) and at least for TET and PEN, several different polymorphs have been reported [150, 281, 282]. In films grown by OMBD, TET has been found to form either a bulk or a thin film (TF) polymorph depending on growth rate [281, 283], substrate temperature [230] and film thickness [281]. The bulk polymorph seems to be thermodynamically more stable [230], is also found in single crystals (SC) [152] and has a smaller lattice spacing between different molecular planes due to a larger inclination angle of the molecular long axes from the plane normal compared to the thin film polymorph [230]. For PEN, more than two polymorphs have

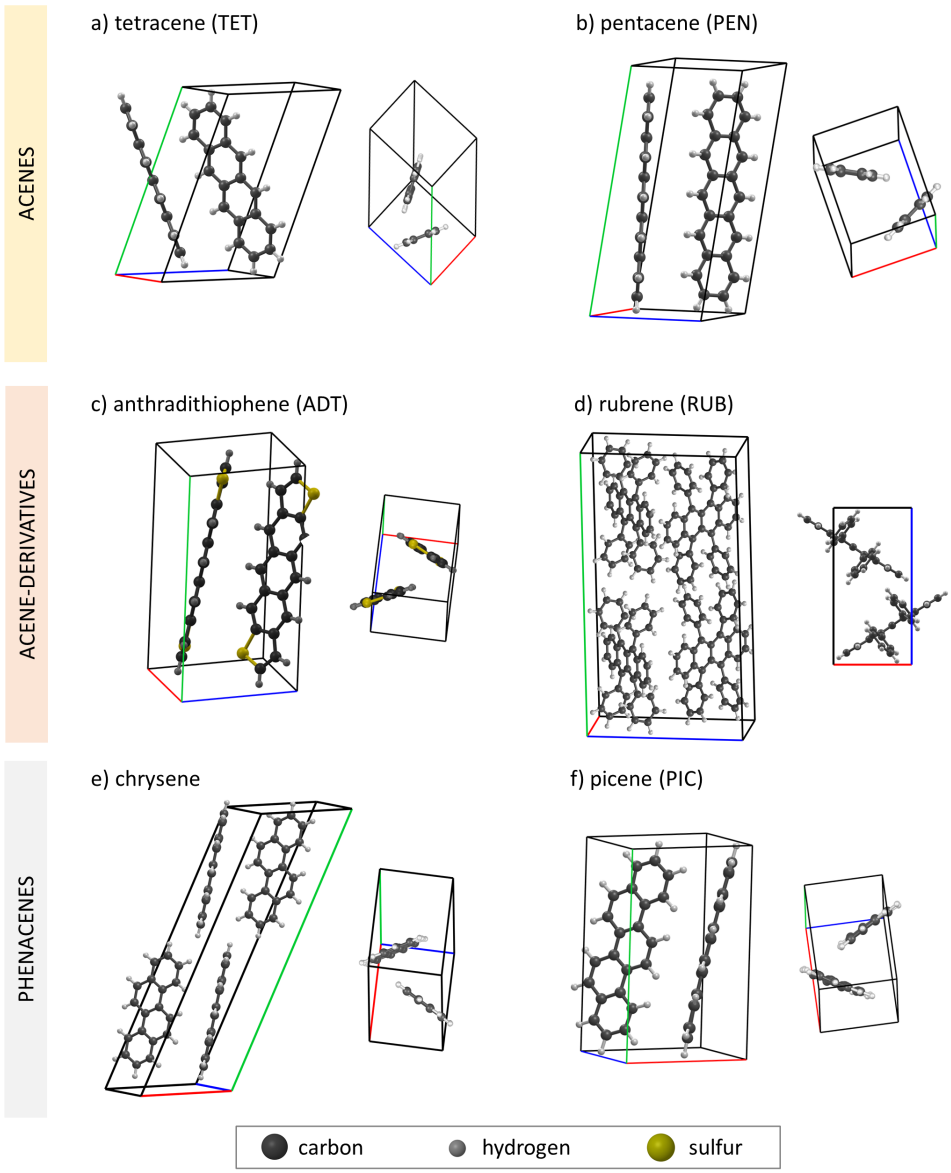


Figure 4.2: Reported unit cells of compounds studied in this work, with two different views. a) TET (TETCEN01 [152]) b) PEN (PENCEN10 [277]) c) anthradithiophene (ADT, AQAXOH [278]) d) rubrene (RUB, QQQCIG11 [279]) e) chrysene (CRY, CRYSEN [156]) f) picene (PIC, ZZZOYC01 [155]), with the structure identifier in the CCDC in parenthesis [280]. Note that for unit cells containing four molecules only two molecules are shown in the top view for clarity.

been reported [149, 150, 277, 282], even though they can still be categorized into bulk and thin film polymorphs, as demonstrated by the inclination angles of the molecular long axes and the lattice spacings [150] (see Apx. A.1). Since the two (types of) polymorphs can be distinguished from their lattice spacing, the presence of either type can be confirmed from the existence of the corresponding BPs using XRD. Selected reported unit cell parameters of TET and PEN are summarized in Tab. 4.1.

The optical band-gap (energy of S_1) of acenes decreases with increasing length [127]. It is defined by short-axis polarized p-bands (see Sec. 2.3.1) that show pronounced vibronic progressions [127, 170], with 0-0 transitions located at 2.62 eV and 2.15 eV for TET and PEN, respectively (see absorption spectra of dissolved compounds in Fig. 4.3). Furthermore, the two materials show significantly stronger peaks at 4.47 eV and 4.11 eV, respectively, which have been assigned to β-bands [284, 285]. The TDMs of these transitions are polarized along the molecular long axis also for TET and PEN [127, 286]. For monomeric TET and PEN, the short-axis polarized β'-bands are predicted to be located at 5.88 eV and 5.71 eV, respectively [127, 174]. Absorbance spectra of dissolved compounds above ≈ 5 eV, however, are not accessible due to the solvent absorption.

The absorbance spectra of thin films of TET and PEN show a red-shifted $S_0 \rightarrow S_1$ 0-0 transition (p-band) to 2.38 eV and 1.87 eV, respectively. Furthermore, these transitions exhibit a DS (roughly 80 meV for TET [285, 287] and 120 meV for PEN [153], slightly depending on the polymorph [288]), which has been shown to largely originate from an admixture of CT states in the low-energy component [153, 195, 196]. The degree of CT admixture is roughly 30 % for TET and 50 % for PEN [195]. The β-band of crystalline TET has been reported at 4.43 eV [285] but is barely seen in the thin film absorbance spectrum due to the upright-standing orientation of TET molecules. The thin films of TET and PEN exhibit further transitions at higher energies, which might originate from the short-axis polarized β'-band [127, 174].

As alternant hydrocarbons [23, 171], acenes have a large singlet-triplet splitting, see Fig. 4.4. Since SF generally occurs from a relaxed S_1 state, literature values of S_1 (see Fig. 4.4) are used for calculation of the energy balance of SF (ΔE_{SF}) instead of those

Table 4.1: Unit cell parameters of selected TET and PEN structures (str.). The unit cell lengths were rounded to two decimal places and the unit cell angles to one decimal place independent of the reported precision. SC and TF abbreviate single crystal and thin film, respectively.

Material	Str.	a (Å)	b (Å)	c (Å)	α (°)	β (°)	γ (°)	CCDC ID	Ref.
TET	SC	6.06	7.84	13.01	77.1	72.1	85.8	TETCEN01	152
TET	SC	6.04	7.92	13.10	76.6	72.0	86.0	-	281
TET	TF	5.92	7.60	13.20	79.8	86.4	89.6	-	281
PEN	SC	7.90	6.06	16.01	101.9	112.6	85.8	PENCEN	149
PEN	TF	5.96	7.60	15.61	81.3	86.6	89.8	PENCEN10	277

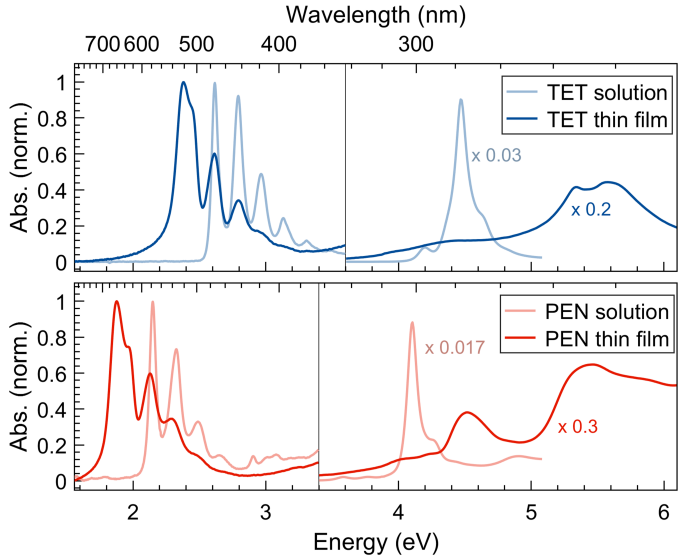


Figure 4.3: Absorbance spectra of TET and PEN in solution and as thin films. The solvents are dichloromethane for TET and chloroform for PEN. The spectra are normalized to the maximum of the $S_0 \rightarrow S_1$ transition (p-band) and the high energy part has further been arbitrarily scaled, see labels.

obtained from absorbance spectra. The energy balance ΔE_{SF} of the SF process then is 180 meV for TET and −110 meV for PEN.

Due to their simple chemical structure and low triplet energy, TET and PEN are well-known, prototypical SF compounds with SF time constants of approximately 80 ps [98, 206] and 80 fs [97, 292], respectively. The microscopic mechanisms of the SF process in TET and PEN, however, have been extensively studied due to observations contradicting basic SF mechanisms. In TET, the decay of singlet excitons is temperature independent below 200 K [64, 67, 98, 206], which is seemingly contradicting the endothermic energy balance of 180 meV. Different mechanisms have been suggested as an explanation of this observation. First, a coherent SF mechanism was proposed, i.e. the formation of adiabatic ^{1}(TT) states from dephasing of a photoexcited superposition of diabatic FE, CT and ^{1}(TT) states [50] (Sec. 2.4.4), in this case driven by entropic gain [56, 293]. However, a coherent SF mechanism in TET has been criticized for the necessity of drawing energy from a bath, which would not lead to a temperature-independent process [64, 98].

Therefore, an incoherent, adiabatic SF process has been proposed in Refs. 57 and 64, which is driven by nuclear movement through an avoided crossing along an intermolecular coordinate [64]. The nuclear reorganization leads to a state of dominant ^{1}(TT)-character and lower energy than that of S_1. The two triplets in this ^{1}(TT) state are then further thermally excited to separated triplets of higher total energy. This scenario was suggested to explain the temperature-independence, but also a red-shifted emission of TET observed at lower temperatures [64]. It was suggested that this emission originates from trapped excitons in the relaxed ^{1}(TT) state that cannot evolve back to S_1 nor produce separate triplets, and therefore (slowly) emit red-shifted photons through remaining FE character [64, 66]. Recently, a comprehensive study on SF in TET single crystals with temperatures ranging from 20 K to 500 K was reported [67]. In these investigations, the red-shifted emission was excluded as an intermediate for SF, and a temperature-dependence was found above

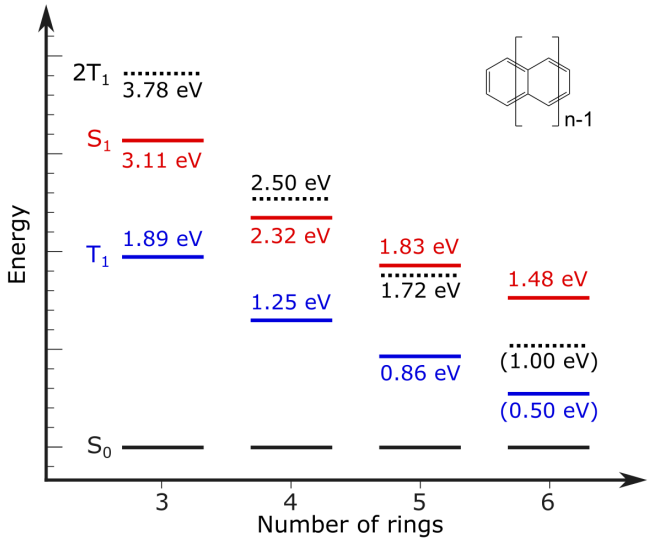


Figure 4.4: Energy levels of crystalline acenes as reported by Ref. 289 for anthracene ($n=3$), Ref. 290 for TET, Refs. 28, 107 for PEN and Refs. 58, 291 for hexacene ($n=6$). The dotted lines correspond to twice the T_1 energies for estimation of the ^{1}(TT) state energy. The energy of T_1 of hexacene is shown in parentheses since it has been extrapolated from those of lower acenes.

200 K. Based on these observations, the red-shifted emission was speculated to originate from crystal defects. For temperatures above 200 K the authors concluded on a direct, incoherent transition from S_1 to ^{1}(T...T) states via a thermally activated process [67].

In PEN, SF is exothermic and consequently faster than in endothermic SF systems [28, 97, 107]. However, as generally for any quantum mechanical process, it must not only be iso- or exothermic to be fast, but the coupling between the initial and the final state also has to be sufficiently strong. However, the direct coupling between a Frenkel exciton and ^{1}(TT) in PEN has early been realized to be too weak to explain the ultrafast SF in PEN, and additional mechanisms that enhance the coupling between these states have to be present [74, 294, 295]. Since the SF process is driven by intermolecular transfer of electrons, especially the role of CT states in the SF process has been debated [74, 294, 295]. While CT states in principle are able to strongly couple S_1 and ^{1}(TT) (Sec. 2.4.4), they first seemed to be too high in energy to actually mediate the SF process in crystalline PEN [294]. First proposed mechanisms explaining the ultrafast SF in PEN were the movement along an intermolecular coordinate leading to a crossing and enhanced direct coupling of S_1 and ^{1}(TT) without the involvement of CT states [294, 296], as well as a superexchange mechanism, in which CT states are not directly occupied, but required as virtual states for the SF process [75, 295] (Sec. 2.4.4).

While such mechanisms might indeed be responsible for SF in other materials [79, 80, 85, 297], later experimental studies on crystalline PEN contradicted these mechanisms and excluded them to be responsible for ultrafast SF in PEN, although also this conclusion has been debated temporarily [50, 57]. These experiments proved the direct excitation of a superposition of a Frenkel exciton (FE) and ^{1}(TT), corresponding to a coherent SF mechanism [50, 69, 74, 293] (Sec. 2.4.4). This superposition state has been calculated to originate from a strong coupling of both a symmetric FE state and the ^{1}(TT) state to a symmetric superposition of CT states [196]. Finally, the importance of vibronic coupling and thermodynamics in the coherent SF mechanism in crystalline PEN have

been emphasized in the last years [69, 71]. These studies demonstrated that a vibrational mode at 1150 cm^{-1} provides energetic resonance of S_1 and a vibrationally excited ^{1}(TT) state, called $TT_1^\star$. The energetic resonance was shown to be crucial for the coherent mixing of the two states and therefore for the ultrafast SF [69, 71].

4.2 Fluorinated pentacenes

Besides blends of well known compounds, also new materials have been studied in this work as neat thin films. These materials are partially fluorinated PENs (FPENs), which contrast the well-known perfluoro-PEN ($C_{22}F_{14}$, PFP) [78, 242, 298], and have been synthesized by the research group of Prof. H. F. Bettinger [121, 122, 299].

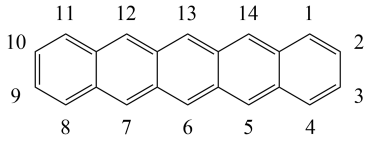


Figure 4.5: Labeling of substitution locants for PEN.

The locants for a nomenclature of substituted PENs are shown in Fig. 4.5. Four different FPENs have been studied in this work and are shown in Fig. 4.6. Among them, there is one difluoropentacene (F2PEN) with the fluorine atoms substituted at the locants numbered 2 and 3 (thus 2,3-F2PEN) and three tetrafluoropentacenes (F4PEN) with the fluorine atoms at various locants of the outermost benzene rings (2,3,9,10-F4PEN, 1,4,9,10-F4PEN and 1,4,8,11-F4PEN). From the higher electronegativity of fluorine compared to hydrogen atoms it can directly be derived from the chemical structures that the two asymmetric molecules (2,3-F2PEN and 1,4,9,10-F4PEN) have a dipole moment in their ground state, while the two symmetric molecules (2,3,9,10-F4PEN and 1,4,8,11-F4PEN) do not. The dipole moment of the F2PEN is, however, significantly larger than that of 1,4,9,10-F4PEN. The symmetric molecules further have a quadrupole moment that is different from that of PEN [121].

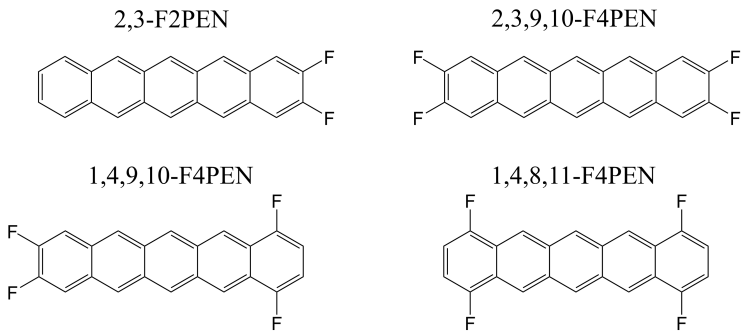


Figure 4.6: Chemical structures of different fluorinated PENs.

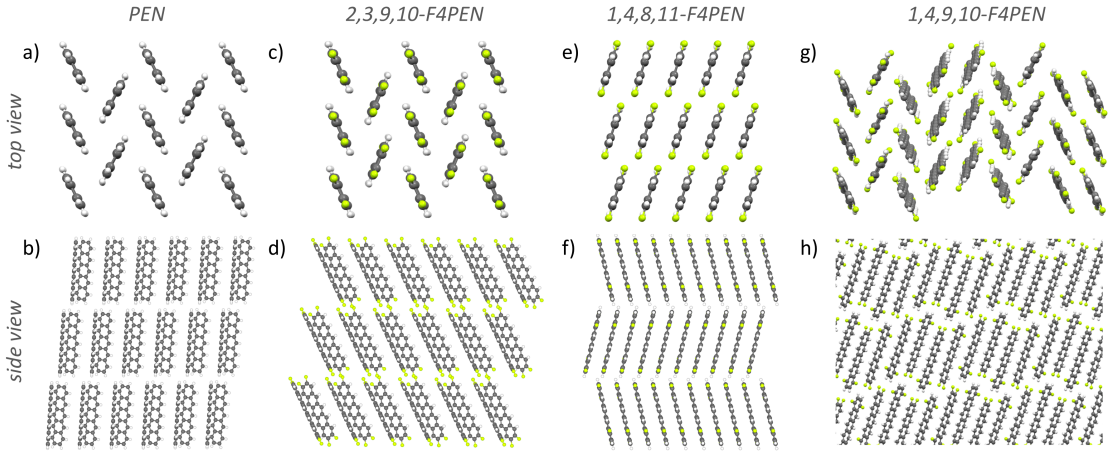


Figure 4.7: Orientation of molecules of different structures. Top view: view along the molecular long axes. Side view: view perpendicular to the molecular long axes. a,b) PEN [277] c,d) 2,3,9,10-F4PEN [121] e,f) 1,4,9,10-F4PEN [122] g,h) 1,4,8,11-F4PEN [122]. Note that the top view is no top view of the molecular planes. Screenshots taken from the Mercury software [300].

The synthesis and characterization of the three F4PEN compounds by Prof. H. Bettinger and co-workers has been published in Refs. 121 and 122. The latter reference contains a basic characterization of thin films of 2,3,9,10-F4PEN and 1,4,9,10-F4PEN as well as TA measurements, which were part of this work.

The crystal structures of PEN and FPENs [121, 122] are shown in Fig. 4.7. The different fluorination strongly impacts the crystallization, as the compounds exhibit very different intermolecular orientations. Like PEN, also 2,3,9,10-F4PEN forms a HB aggregate, yet with a slightly smaller HB angle than PEN ($\Phi = 50.9°$ instead of $\Phi = 54.3°$, see Figs. 4.7a and Fig. 4.7c), as well as a significantly larger inclination angle of $\chi \approx 33°$ [121] from the molecular plane normal (Fig. 4.7d) instead of $\chi \approx 25°$ for the PEN bulk polymorph [152] and $\chi \approx 6°$ for the PEN thin film polymorph [277] (Fig. 4.7b).

Table 4.2: Unit cell parameters of different PEN and FPEN structures. The unit cell lengths were rounded to two decimal places and the unit cell angles to one decimal place independent of the reported precision. For reasons of space, only the fluorination locants of FPENs are named.

Material	Str.	a (Å)	b (Å)	c (Å)	α (°)	β (°)	γ (°)	CCDC ID	Ref.
PEN	SC	7.90	6.06	16.01	101.9	112.6	85.8	PENCEN	149
PEN	TF	5.96	7.60	15.61	81.3	86.6	89.8	PENCEN10	277
2,3,9,10	SC	6.72	7.65	14.30	100.6	94.6	98.4	ZETQUN	121
1,4,9,10	SC	18.20	5.93	26.66	90.0	92.2	90.0	VUFNIW	122
1,4,8,11	SC	3.78	27.64	6.94	90.0	93.4	90.0	VUFKAL	122

The other symmetric F4PEN, 1,4,8,11-F4PEN has a crystal structure with slip-stacked face-to-face oriented molecules (Fig. 4.7e). The primitive unit cell of 1,4,8,11-F4PEN still includes two molecules, however, the translationally inequivalent molecules are located in different molecular planes, see Fig. 4.7f. Hence, there are no translationally inequivalent molecules within one molecular plane, as shown in Fig. 4.7e. The unit cell of the crystal structure of the asymmetric 1,4,9,10-F4PEN contains eight molecules that have very different orientations to each other, including HB-like arrangements, inclined long axes and face-to-face orientations, see Fig. 4.7g. The face-to-face oriented 1,4,9,10-F4PEN molecules are further slip-stacked along their long axes, leading to offsets along the molecular long axes, after each four molecules (Fig. 4.7h). The unit cell parameters of PEN and FPENs are summarized in Tab. 4.2.

Absorbance maxima of $S_0 \rightarrow S_1$ transitions (p-bands) of PEN and different FPENs diluted in dichloromethane have been reported at 2.15 eV (PEN [301]), 2.21 eV (2,3,9,10-F4PEN [121]), 2.18 eV (1,4,9,10-F4PEN [122]) as well as at 2.16 eV (1,4,9,10-F4PEN [122]). The T_1 state emission wavelengths of the F4PENs have been reported at 0.936 eV (2,3,9,10-F4PEN), 0.928 eV (1,4,9,10-F4PEN) and 0.934 eV (1,4,8,11-F4PEN) [122], denoting a difference between T_1 state energies of F4PENs on the order of 10 meV.

SF rates for any of these partially fluorinated PENs have been determined in this work for the first time, and some of them have been published in Ref. 122. However, two studies on perfluoro-PEN (PFP) have been published [78, 242]. PFP also forms a HB aggregate, but has a different molecular packing compared to PEN, since the HB angle is 90° and translationally equivalent neighbors have a slip-stacked face-to-face orientation [298]. The structural difference between PEN and PFP has been shown to strongly impact the SF process, and singlet excitons in PFP undergo SF with a time constant of 200 fs between translationally equivalent molecules [78, 242]. Furthermore, calculations have recently been performed of a 6,13-F2PEN dimer [123]. In this study, a pronounced impact of the fluorine atoms on vibronic coupling has been found.

4.3 Acene derivatives: anthradithiophene and rubrene

Besides TET and PEN, also two derivatives of acenes, rubrene ($C_{42}H_{28}$, RUB) and anthra-[2,3:6,7]dithiophene ($C_{18}H_{10}S_2$, ADT), are used in this work as SF materials in thin film blends. RUB has a TET backbone with four phenyl groups replacing the inner hydrogen atoms (Fig. 4.8). These phenyl groups lead to a different packing behavior and relative orientation of the TET backbones in RUB aggregates compared to crystalline TET [60].

Thin films of RUB tend to photo-oxidize [302] and are typically amorphous if produced by OMBD [303]. In single crystals, RUB forms a crystal structure with slip-stacked TET backbones and four molecules per unit cell, see Fig. 4.2d. ADT has an anthracene core with two fused sulfur-containing thiophene groups at both ends, leading to five linearly fused rings (ADT is a heteropentacene [304]) with a size of the conjugated system in

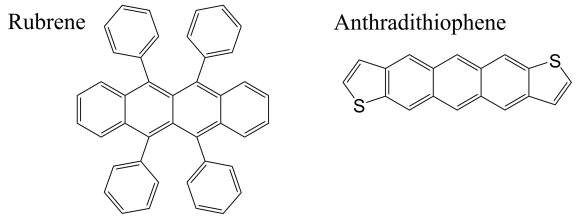


Figure 4.8: Chemical structures of acene derivatives studied in this work.

between those of TET and PEN (Fig. 4.8). Note that two isomers of ADT exist that differ in the symmetry regarding the position of the sulfur atoms [278]. The material used for the investigations in this work is a mixture of these two isomers. Like acenes, ADT forms a HB aggregate, as shown in Fig. 4.2c. The unit cell parameters of each one reported crystal structure of RUB and ADT are shown in Tab. 4.3.

Regarding the optical absorption of RUB shown in Fig. 4.9, both the $S_0 \rightarrow S_1$ 0-0 transition (p-band) (2.35 eV) and the β-band (4.12 eV) of dissolved RUB (Fig. 4.9) are red-shifted and broadened compared to TET (Fig. 4.3) [305, 306]. Main differences, however, occur between the thin film absorbance spectra of the two compounds. Since thin films of RUB are not crystalline they exhibit no DS of the $S_0 \rightarrow S_1$ transition (p-band), which is only slightly red-shifted compared to dissolved RUB to 2.33 eV [305, 306]. Furthermore, the RUB thin film spectrum clearly shows the β-band [302] in contrast to TET, which is a result of the amorphous growth of RUB thin films. The lower intensity ratio between β- and the p-band in thin films of RUB compared to dissolved RUB is probably no result from a preferred upright-standing of the RUB molecules but a distribution of oscillator strength due to different environments in the amorphous film, which leads to a broader band that is seemingly less intense. The thin film absorbance of RUB did not change over several days if stored dark and in vacuum. Upon illumination in air, degradation was found within few hours in agreement with Ref. 302.

Solution and thin film absorbance spectra of ADT ($S_0 \rightarrow S_1$ 0-0 transition at 2.54 eV and 2.29 eV, respectively [278]) are similar to those of acenes, and the same assignment of transitions can be assumed. ADT also exhibits a DS of the $S_0 \rightarrow S_1$ 0-0 transition, which is determined to 86 meV by a fit of two gaussian functions. The β-band is also absent in thin films of ADT, indicating an upright-standing growth of the molecules. It is noteworthy that the energies of all transitions are in between those of TET and PEN.

Table 4.3: Unit cell parameters of selected RUB and ADT single crystal structures. The unit cell lengths were rounded to two decimal places and the unit cell angles to one decimal place independent of the reported precision.

Material	a (Å)	b (Å)	c (Å)	α (°)	β (°)	γ (°)	CCDC ID	Ref.
RUB	26.86	7.19	14.43	90.0	90.0	90.0	QQQCIG11	279
ADT	5.92	7.77	13.99	86.6	78.3	86.4	AQAXOH	278

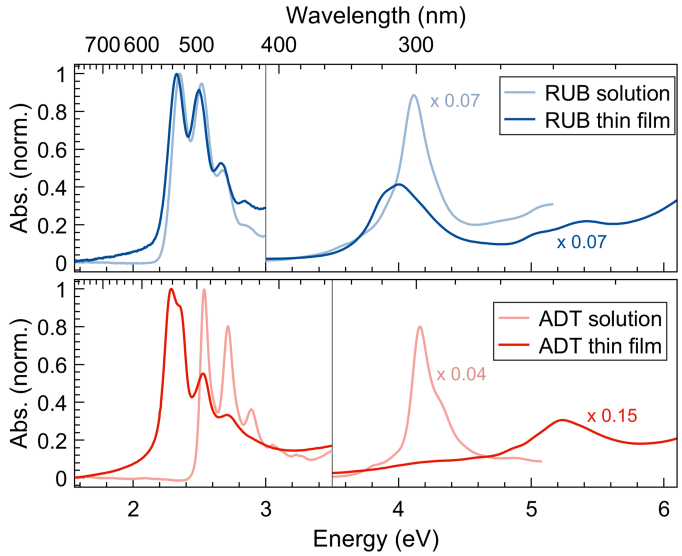


Figure 4.9: Absorbance spectra of RUB and ADT in solution and as thin films. The solvents are dichloromethane for RUB and chloroform for ADT. The spectra are normalized to the maximum of the $S_0 \rightarrow S_1$ transition (p-band) and partially further arbitrarily scaled, see labels.

The singlet and triplet energy levels of crystalline RUB have been reported as 2.27 eV (central energy between absorption and emission maximum in Ref. 305) and 1.15 eV, respectively [305, 307], which denotes a much smaller ΔE_{SF} for RUB (30 meV) compared to TET (180 meV [290]. RUB has frequently been reported to exhibit multiexponential exciton dynamics with very different timescales [96, 244, 306, 308, 309]. In particular, studies using TA spectroscopy suggested different assignments [60, 96, 308], such as an ultrafast (femtosecond) formation of an equilibrium between S_1 and ^{1}(TT), a vibrational relaxation within few picoseconds and a subsequent separation of triplets to ^{1}(T...T) on a timescale of 30 ps [60, 96] or more than one nanosecond [308].

Using TRPL, however, SF time constants are frequently reported on the order of a nanosecond [244, 303, 306, 309] with differences occurring from different crystallinities of the samples, especially amorphous films compared to single crystals [303]. Different interpretations of experimental results might especially explain the inconsistency between time constants obtained by TA spectroscopy and TRPL, since it has been suggested that the species observed after 30 ps are not separated triplets but an emissive ^{1}(TT) state [308].

Not only the lower triplet energy and thus the lower ΔE_{SF} introduces a fundamental difference between SF in TET and RUB, but also the different crystal structure of RUB with nearest neighbor molecules having a C_{2h} symmetry [60, 222, 223]. This symmetry has been recognized to lead to zero electronic coupling between FE and ^{1}(TT), and only coupling to symmetry-breaking vibrational modes leads to coherent excitation of a ^{1}(TT) contribution [60].

First indications on the SF exothermicity of ADT derivatives were given by calculations, which resulted in singlet and triplet energies of 2.20 eV and 0.81 eV, respectively [92, 118], denoting a strong exothermicity of $\Delta E_{SF} = -580$ meV. Later phosphorescence studies on ADT derivatives, however, showed a triplet energy of 1.08 eV with almost no difference between different derivatives [308] and a strong exothermicity has also been questioned due

to a slow SF process [310]. With the energy of the non-relaxed S_1 state of pristine ADT obtained from the thin film absorbance spectrum, this measured triplet energy corresponds to a much smaller exothermicity of $\Delta E_{SF} = -40\,\text{meV}$.

SF in pristine ADT has not been investigated to the best of the author's knowledge. However, studies on SF in a variety of solution-processable derivatives of ADT have been published [92, 118, 308, 310–312], reporting a SF process on a timescale between tens of picoseconds and one nanosecond with some variations between the different derivatives [308, 310, 312]. The slow timescales despite favorable SF energetics might be explained by differences in excimer formation in different ADT derivatives [92], as well as a high sensitivity of the electronic coupling on the arrangement of the participating chromophores [92]. However, these two factors might be strongly altered in polycrystalline ADT and no expectations for the SF rate can be drawn on the basis of ADT derivatives.

4.4 Phenacenes: picene and [6]-phenacene

Phenacenes are compounds with $n \geq 3$ fused benzene rings in a zig-zag manner [313], thus each [n]-phenacene is an isomer to the corresponding [n]-acene. The lowest-order phenacenes with $n > 3$ (Fig. 4.10) are further called chrysene ($C_{18}H_{12}$, CRY), picene ($C_{22}H_{14}$, PIC) and fulminene ($C_{26}H_{16}$, 6PH). Phenacenes have a remarkably high bandgap in view of the size of their conjugated system. PIC as well as 6PH are therefore used as inactive spacer materials in this work [52, 275].

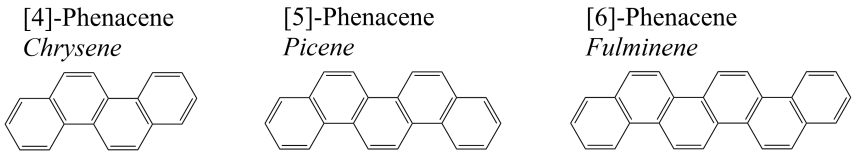


Figure 4.10: Chemical structures of CRY, PIC and 6PH.

Like acenes, phenacenes typically form a HB arrangement, see Fig. 4.2e and 4.2f for reported single crystal structures and Tab. 4.4 for the respective unit cells. The primitive unit cells of single crystal structures of CRY [156], as well as the 6PH thin film structure [314], contain four molecules with a pairwise HB-type orientation in contrast to PIC, which has only two molecules per primitive unit cell [155]. No molecular orientations of the single crystal structure of 6PH have been reported [315], but the unit cell parameters indicate four molecules per primitive unit cell that are all located within one molecular plane (see Tab. 4.4).

Absorbance spectra of PIC and 6PH in solution and as thin films are shown in Fig. 4.11. 0-0 transitions of different bands of dissolved PIC are found here at 3.30 eV, 3.79 eV, 4.35 eV and 4.83 eV and have been shown to correspond to the α- (short), p- (long), β'- (long) and β- (short) band, respectively, where the parenthesis gives the polarization with respect

Table 4.4: Unit cell parameters of selected CRY, PIC and 6PH single crystal structures. The unit cell lengths were rounded to two decimal places and the unit cell angles to one decimal place for higher reported precisions.

Material	Str.	a (Å)	b (Å)	c (Å)	α (°)	β (°)	γ (°)	CCDC ID	Ref.
CRY	SC	8.39	6.20	25.20	90.0	116.2	90.0	CRYSEN	156
PIC	SC	8.48	6.15	13.52	90.0	90.5	90.0	ZZZOYC01	155
6PH	SC	12.13	7.94	15.40	90.0	93.2	90.0	-	315
6PH	TF	8.4	6.2	32	90	98	90	-	314

to the molecular axes [170, 173, 316, 317]. These assignments and polarizations are in agreement to those of phenanthrene due to the same symmetry of the molecule (Sec. 2.3). For phenanthrene and PIC the optical band-gap is defined by the very weak α-band and the strongest absorption is the long-axis polarized β'-band.

Dissolved 6PH has a very similar absorbance spectrum to PIC with all peaks at slightly lower energy, at 3.24 eV, 3.65 eV, 4.22 eV and 4.72 eV. For assignment of these transitions, CRY can be used as a reference due to the same symmetry [170, 173, 318]. Therefore, the four peaks found in the absorbance spectrum of 6PH are likely the α- (oblique), p- (oblique), β- (long) and β'- (short) band, respectively. For CRY, and likely also for 6PH, the optical band-gap is again defined by the very weak α-band, but the strongest absorption is the long-axis polarized β-band [173].

Absorbance spectra of thin films of PIC and 6PH [273, 316] show a slight red-shift of the transitions and a very similar shape of the α-band compared to the respective solution spectrum with the 0-0 transition at 3.24 eV and 3.18 eV, respectively. The strongest absorption peak, which corresponds to long-axis polarized transitions for both PIC and 6PH has a weakened intensity due to upright standing molecules, and merges with the other two transitions to a broad absorption between $3.5 - 4.5$ eV. The α-band that defines the band-

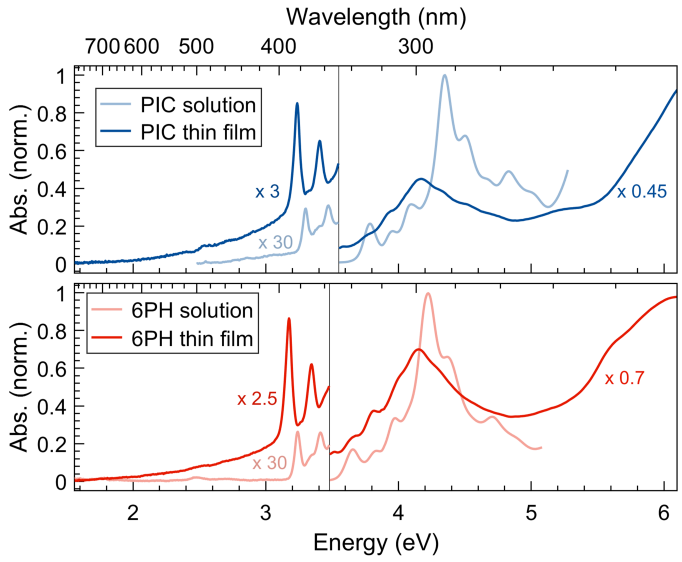


Figure 4.11: Absorbance spectra of PIC and 6PH in solution and as thin films. The solvents are dichloromethane for PIC and chloroform for 6PH. The spectra are normalized to the maximum of the band between 4 eV and 4.5 eV and partially further arbitrarily scaled, see labels.

gap of phenacenes is extremely weak for isolated molecules, but can easily be observed in thin films, see scaling of the low-energy part in Fig. 4.11. This observation has been explained by an aggregation-induced intensification in thin films of phenacenes [316, 317].

5. Results I: Singlet fission in fluorinated pentacenes

In this chapter, the impact of a modification of the partial charge distribution of molecules on the SF rate by altering the molecular arrangement and the coupling of electronic states is discussed. For this purpose, the photophysics of fluorinated PENs (FPENs) are examined and compared to those of PEN. The investigations presented in this chapter have been published in *The Journal of Physical Chemistry Letters* [299]. Parts of the investigations of this chapter have been published in Ref. 122. These investigations have been performed in collaboration with Prof. H. F. Bettinger's and Prof. G. Cerullo's research groups, see Apx. F for details on the contributions.

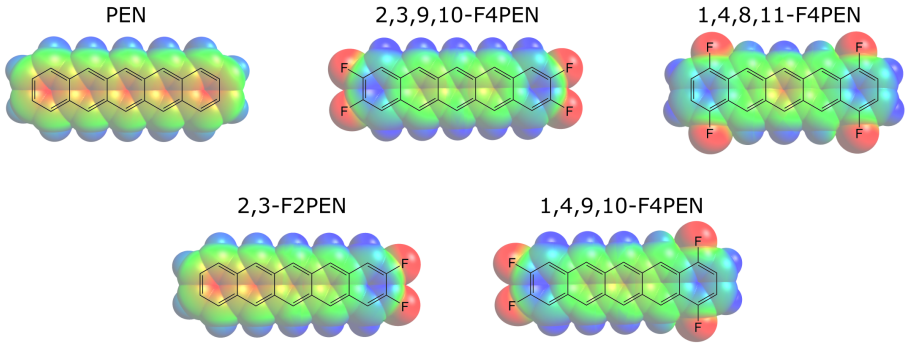


Figure 5.1: Chemical structures and electrostatic potential surfaces of PEN and the FPENs investigated in this work. Red and blue colors qualitatively indicate negative and positive partial charges, respectively, on a surface given by the van der Waals radii of the atoms. Calculated with the software Avogadro.

One of the most prominent approaches for studying SF (see Sec. 2.4.6) is the artificial variation of the electronic coupling between SF compounds by chemical modification, and measuring the impact on the SF process. Chemical modifications for the investigation of SF are based on

- covalently linking two chromophores to a dimer to alter their orbital overlap [76, 86–90]

- the attachment of bulky side-chains to the chromophore to alter the molecular arrangement in aggregates [49, 80, 319, 320]
- a substitution of carbon atoms of the chromophore backbone by heteroatoms to change the SF energetics [117–120]
- halogenation of chromophores to alter the molecular arrangement in aggregates and the coupling of states by a modification of the partial charge distribution [84, 85, 94, 99, 123, 242, 321]

In this chapter, the chemical modification of the last category is discussed, which has several advantages. The modification of the partial charge distribution (see Fig. 5.1) lead to altered Keesom-forces between molecules, which dictate the crystal structure formation and thus the relative arrangement of molecules [84, 85, 94, 99, 123, 242, 321, 322]. The variation of relative arrangement is therefore achieved while retaining a highly crystalline system with delocalized singlets [59, 94, 95] and a fixed relative arrangement of molecules [72]. In contrast to the attachment of bulky side-chains, partial halogenation allows to achieve a variety of scenarios for the molecular arrangement, ranging from HB aggregates to face-to-face stacking [84, 99, 121–123, 322]. In addition, different Keesom interactions between molecules might also impact the character of (contributions of FE, CT and ^{1}(TT)) and couplings between electronic states [78, 84, 85, 123, 323], e.g. by altering the energies of CT states, an aspect that is unique to this type of chemical modification.

In the following study, PEN was chosen as the parent compound and different fluorinated PENs (FPENs) have been synthesized by Prof. H. F. Bettinger's research group, namely 2,3-F2PEN, 2,3,9,10-F4PEN, 1,4,9,10-F4PEN and 1,4,8,11-F4PEN (see Sec. 4.2) [121, 122]. The photophysics of thin films of these five compounds is compared with respect to their structural properties and the impact of altered coupling of states due to the modified partial charge distribution.

5.1 Structural characterization

The thin films of PEN and FPENs have been structurally characterized by GIWAXS and XRR, see Sec. 3.2.1. For details on the preparation of the films for which data is shown in the following, see Tab. E.1.

GIWAXS measurements

GIWAXS data of a thin film of PEN is shown in Fig. 5.2 along with comparisons to calculated reflections based on reported unit cells (see Sec. 4.2 and Refs. 121 and 122). The strongest reflections in the reciprocal space map of PEN correspond to the thin film structure [277] (Fig. 5.2a), but also some reflections of the single crystal structure reported by Campbell [149] are observed (Fig. 5.2b). The simultaneous growth of two

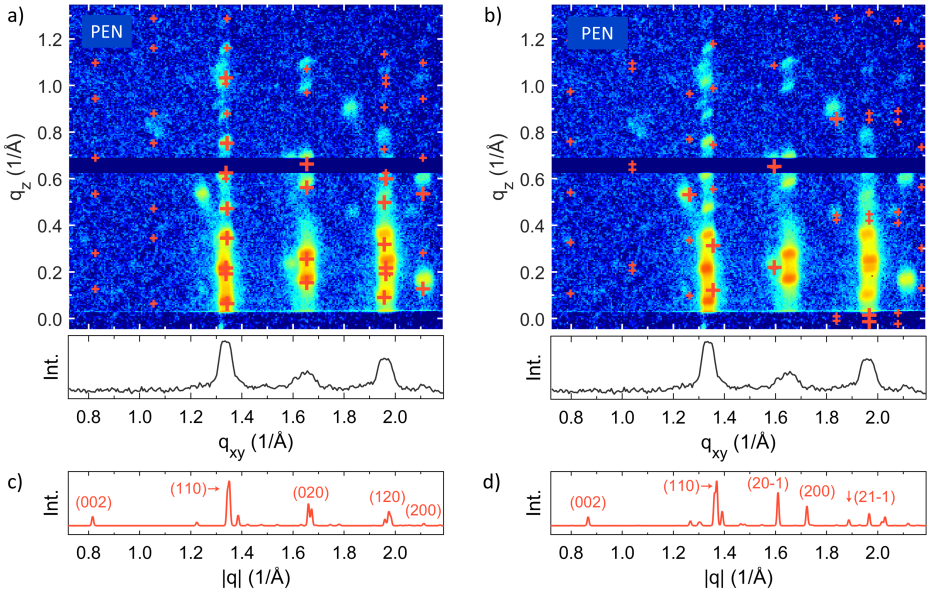


Figure 5.2: a,b) Reciprocal space maps of thin films of PEN [299] measured at the *Xeuss system* and calculated reflections from crystal structures a) PEN thin film [277] and b) PEN single crystal [149]) reported in literature. For the calculated reflections in both panels the respective crystal structure is oriented with $c^\star$ parallel to the substrate normal. Two different sizes are used for the markers to clarify the relative intensity of the calculated reflections. The in-plane scattering intensity as a function of q_{xy}, extracted by integrating between $q_z = 0 - 0.12\,\text{Å}^{-1}$, is shown below the reciprocal space map. c,d) Calculated powder diffractogram of the corresponding single crystal structures [149, 277].

different polymorphs in thin films of PEN has been reported before [324]. Both structures, however, are HB aggregates, leading to an extinction of (10ℓ) and (01ℓ) reflections between $q_{xy} = 0.7\,\text{Å}^{-1}$ and $q_{xy} = 1.2\,\text{Å}^{-1}$.

The reciprocal space map of 2,3-F2PEN (Fig. 5.3a) is similar to that of PEN with three pronounced series of reflections and no reflections below $q_{xy} = 1.2\,\text{Å}^{-1}$ at low q_z. Since the single crystal structure has not been reported yet for this compound, the reflections in this reciprocal space map are compared to calculated reflections of the PEN thin film structure [277]. The calculated reflections match well with the experimental reflections of 2,3-F2PEN, and it can be concluded that 2,3-F2PEN also crystallizes in a HB aggregate similar to PEN.

A large inclination angle χ of the molecular long axis from the substrate normal typically leads to a non-orthogonal angle γ between the in-plane crystal axes [281, 288] and thus to an in-plane splitting of peaks, as also seen for the PEN single crystal structure reported by Campbell [149] (see Fig. 5.2b). The fact that such a splitting is not observed for 2,3-F2PEN denotes a small γ and points towards a small χ, thus, almost upright-standing molecules.

2,3,9,10-F4PEN has been reported to crystallize in a HB aggregate with rather large inclination angles of the molecular long axes from the substrate normal ($\chi = 33°$) [121], see Fig. 4.7c and 4.7d. A reciprocal space map of a thin film of 2,3,9,10-F4PEN (Fig. 5.3b) shows several reflections whose intensities are slightly distributed over rings as observed

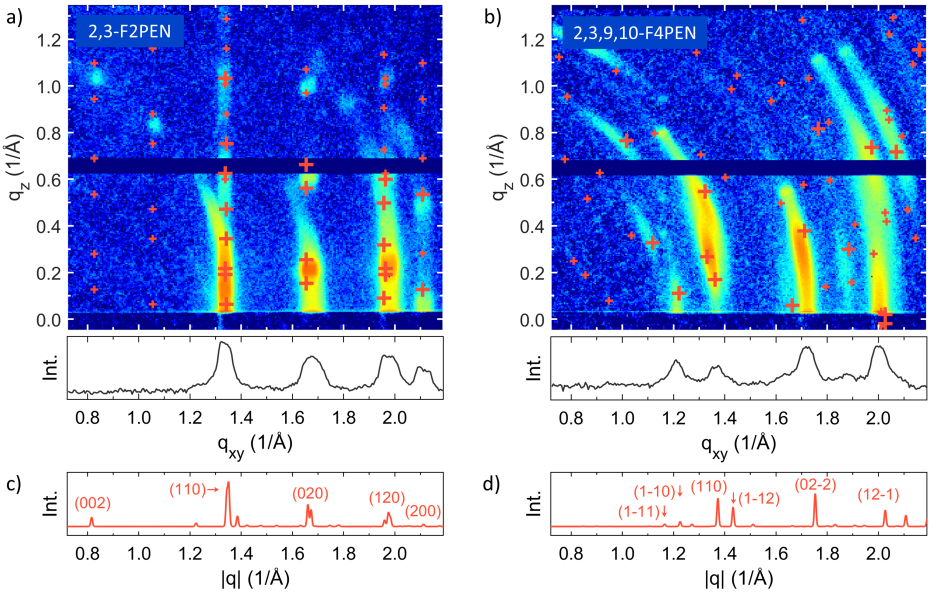


Figure 5.3: a,b) Reciprocal space maps of thin films of a) 2,3-F2PEN [299] and b) 2,3,9,10-F4PEN measured at the *Xeuss system* and calculated reflections from a) the PEN thin film structure [277] and b) the single crystal structure of 2,3,9,10-F4PEN [121]. For the calculated reflections in a) the unit cell is oriented with $c^\star$ parallel to the substrate normal, for those in b) the unit cell has been rotated from $c^\star$ parallel to the substrate normal around the crystal a and b axes by 6° and 12°, respectively. Two different sizes are used for the markers to clarify the relative intensity of the calculated reflections. The in-plane scattering intensity as a function of q_{xy}, extracted by integrating between $q_z = 0 - 0.12\,\text{Å}^{-1}$, is shown below the reciprocal space map. c,d) Calculated powder diffractogram of the corresponding single crystal structures [121, 277].

before for thin films of this compound [100]. The strongest reflections in the reciprocal space map can be described based on the reported unit cell [121] using two different crystallite orientations (see Apx. B.1). First, an orientation in which $c^\star$ is parallel to the substrate normal and second, an orientation, in which the unit cells are rotated around the crystal a and b axes by 6° and 12°, respectively, the latter is shown in Fig. 5.3b. The distribution of reflection intensity over rings indicates a variety of differently oriented crystallites and complicates the assignment of reflections. Still, a comparison between the in-plane scattering intensity as a function of q_{xy} in Fig. 5.3b with the calculated power diffractogram based on the single crystal structure [121] in Fig. 5.3d shows good agreement.

The asymmetrically fluorinated 1,4,9,10-F4PEN has been reported to exhibit a crystal structure with eight basis molecules [122] that have different orientations and are slip-stacked along the molecular long axes after each four molecules, as shown in Fig. 4.7. The reciprocal space map of a thin film of 1,4,9,10-F4PEN (Fig. 5.4a) shows several narrow reflections between $q_z = 0.4\,\text{Å}^{-1}$ and $q_z = 0.6\,\text{Å}^{-1}$ as well as three broad reflections and an overall broad scattering background below $q_z = 0.4\,\text{Å}^{-1}$. The complex diffraction pattern is likely a result of the complex crystal structure as indicated by the powder diffractogram in Fig. 5.4c. The in-plane scattering intensity as a function of q_{xy} is in agreement with the reported crystal structure [122], especially due to the pronounced (404) and (414)

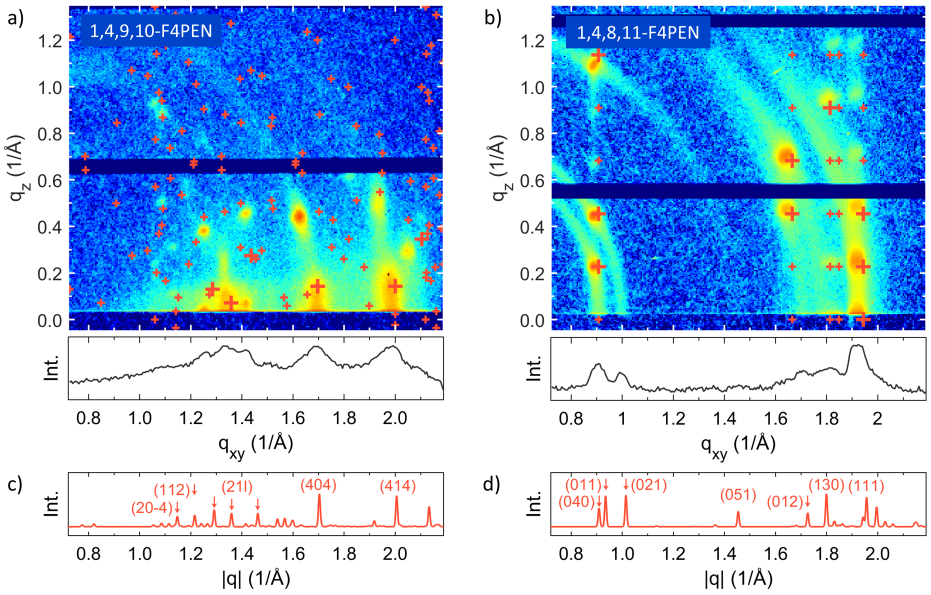


Figure 5.4: a,b) Reciprocal space maps of thin films of a) 1,4,9,10-F4PEN and b) 1,4,8,11-F4PEN [299] measured at the *Xeuss system* and calculated reflections from the single crystal structure of the respective compound [122]. For the calculated reflections in a) the unit cell has been rotated from $c^\star$ parallel to the substrate normal around the crystal b-axis by 31°. For the calculated reflections in b) the unit cell is oriented with $b^\star$ parallel to the substrate normal. Two different sizes are used for the markers to clarify the relative intensity of the calculated reflections. The in-plane scattering intensity as a function of q_{xy}, extracted by integrating between $q_z = 0 - 0.12\,\text{Å}^{-1}$, is shown below the reciprocal space map. c,d) Calculated powder diffractogram of the corresponding single crystal structures [122].

reflections, which correspond to scattering at planes parallel to the molecular long axes and thus upright-standing molecules (see Apx. B.1) [122]. The in-plane reflections between $q_{xy} = 1.2\,\text{Å}^{-1}$ and $q_{xy} = 1.5\,\text{Å}^{-1}$ can be identified to be mainly (21ℓ) reflections. For a detailed analysis of the reflections in the reciprocal space map of 1,4,9,10-F4PEN, see Apx. B.1. This analysis shows that the strongest reflections in this reciprocal space map correspond to at least two coexisting orientations of the known single crystal structure [122], but with slight deviations of the unit cell parameters.

1,4,8,11-F4PEN is the only FPEN studied in this work for which the molecules arrange face-to-face [122]. The reported single crystal structure contains two translationally inequivalent molecular planes (see Sec. 4.2) [122], which is unlikely to influence the photophysics, but impacts the diffraction pattern. A reciprocal space map of a thin film of 1,4,8,11-F4PEN is shown in Fig. 5.4b and exhibits several narrow reflections that clearly differ from the diffraction pattern of HB aggregates due to the appearance of reflections at $q_{xy} = 0.9\,\text{Å}^{-1}$. In the reported crystal structure, $b^\star$ is chosen to be parallel to the stacking direction of the molecular planes, and upon choosing $b^\star$ parallel to the substrate normal, the calculated reflections shown in Fig. 5.4b are obtained. These reflections can well explain all experimental reflections, which allows to conclude on upright-standing molecules in the thin film of 1,4,8,11-F4PEN [122].

XRR measurements

XRR data of PEN and the FPENs are shown in Fig. 5.5a. Thin films of PEN exhibit two series of BPs in the XRR data, which correspond to a thin film and the single crystal structure reported by Campbell [149, 277, 324]. Also in the GIWAXS data these two polymorphs are observed. For the lattice spacings $d_{\mathrm{ls}}^{\mathrm{exp}}$ between molecular planes and comparisons to plane distances $d_{\mathrm{ls}}^{\mathrm{calc}}$ of reported unit cells, see Tab. 5.1.

The thin film of 2,3-F2PEN exhibits two BPs, of which the one at larger q_z can be assigned to a higher-order reflection of that at smaller q_z. Based on the similarity of the reciprocal space maps and the XRR data of PEN and 2,3-F2PEN (see Figs. 5.2, 5.3a and 5.5), the two BPs are analogously assigned to (001) and (002) reflections, corresponding to a lattice spacing of 16.2 Å (see Tab. 5.1). From the lattice spacing d_{ls} between molecular planes, the inclination angle of the molecular long axis χ can be calculated by

$$d_{\mathrm{ls}} = l_{\mathrm{m}} \cdot \cos(\chi) - d_{\mathrm{id}} \tag{5.1}$$

with the molecular lengths l_{m} and the interdigitation d_{id} between different molecular planes (see Apx. B.2). Since χ is not known for 2,3-F2PEN, it is calculated here using Eq. 5.1 and the experimental lattice spacing. The molecular length l_{m} of a 2,3-F2PEN molecule can be approximated as the mean of the lengths of PEN and 2,3,9,10-F4PEN molecules, see corresponding column in Tab. 5.2. For an approximation of the interdigitation d_{id} of 2,3-F2PEN, other crystal structures can be used for comparison. It is roughly $d_{\mathrm{id}} = 0.6$ Å for the PEN thin film structure [277] ($\chi = 6°$), the PEN single crystal structure reported by Campbell [149] ($\chi = 21°$) and also for the crystal structure of 2,3,9,10-F4PEN [121] ($\chi = 33°$), see Tab. 5.2. Hence, for 2,3-F2PEN, the same interdigitation is assumed here for the calculation of χ. With these values, Eq. 5.1 yields $\chi \approx 0$ (see Tab. 5.2), corresponding

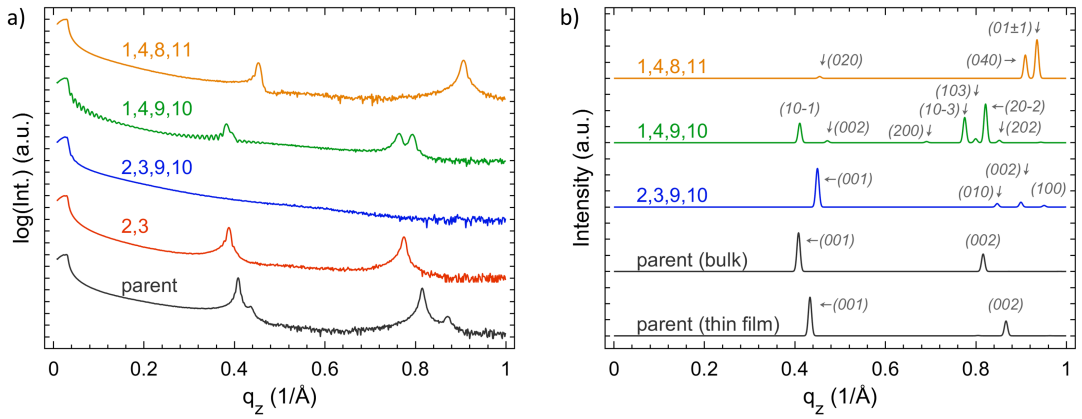


Figure 5.5: a) XRR data of PEN and the FPENs [122, 299]. b) Calculated powder diffractograms from reported crystal structures [121, 122, 277] and assignment of reflections (grey). Note that the vertical axis in a) is a logarithmic scale, while it is in linear scale in b).

Table 5.1: Assignment of BPs in the XRR data to lattice planes of reported structures. Note that $d_{\mathrm{ls}}^{\mathrm{exp}}$ and $d_{\mathrm{ls}}^{\mathrm{calc}}$ are calculated from the respective coprime (h,k,l) tuple and hence is the same e.g. for (001) and (002) reflections.

Compound	q_z (1/Å)	assignment	$d_{\mathrm{ls}}^{\mathrm{exp}}$(Å)	$d_{\mathrm{ls}}^{\mathrm{calc}}$(Å)	Ref.
PEN	0.408	(001) (TF)	15.4	15.40	277
PEN	0.815	(002) (TF)	15.4	15.40	277
PEN	0.436	(001) (SC)	14.4	14.46	149
PEN	0.870	(002) (SC)	14.4	14.46	149
2,3-F2PEN	0.387	(001)	16.2	-	-
2,3-F2PEN	0.774	(002)	16.2	-	-
1,4,9,10-F4PEN	0.383	(10-1)	16.4	15.30	122
1,4,9,10-F4PEN	0.764	(20-2)	16.4	15.30	122
1,4,9,10-F4PEN	0.793	(10-3)	15.8	16.21	122
1,4,8,11-F4PEN	0.453	(020)	27.7	27.64	122
1,4,8,11-F4PEN	0.906	(040)	27.7	27.64	122

to almost perfectly upright-standing molecules. Notably, already the reciprocal space map of the 2,3-F2PEN thin film gave an indication for a small χ as discussed before.

Thin films of 1,4,9,10-F4PEN exhibit three pronounced BPs in the XRR data, see Fig. 5.5a and Tab. 5.1. As mentioned before for the reciprocal space map of 1,4,9,10-F4PEN, it is shown in Apx. B.1 that in-plane reflections in the reciprocal space maps can be explained with at least two co-existing orientations of the single crystal structure [122], yet with slight deviations of the unit cell parameters. The two orientations would lead to the appearance of (10-1), (20-2) and (10-3) reflections in the XRR data (see Apx. B.1). Since the BP at 0.7642 $\mathrm{Å}^{-1}$ is likely a higher-order reflection of the BP at 0.3825 $\mathrm{Å}^{-1}$, they are assigned to the (20-2) and (10-1) reflection, respectively (see Tab. 5.1), although the corresponding lattice spacing deviates from the calculated lattice spacing [122] due to the noticed change of lattice parameters in Apx. B.1. Consequently, the third BP at 0.7925 $\mathrm{Å}^{-1}$

Table 5.2: Inclination χ of the long molecular axis with respect to the molecular plane normal calculated with Eq. 5.1. The starred d_{ls} of 2,3,9,10-F4PEN is a calculated value [121] since no BP is observed in the XRR data. For 2,3-F2PEN, χ is calculated from the experimental lattice spacing and the assumption $d_{\mathrm{id}} = 0.6$ Å (thus shown in parentheses, see main text). l_{m} of 2,3-F2PEN has been approximated as the mean of the lengths of PEN and 2,3,9,10-F4PEN. The latter have been calculated by taking the distance between the atoms at locants 2 and 10 in the crystal structures in Refs. 121 and 152, and by accounting for the van der Waals diameters of hydrogen and fluorine atoms of 2.2 Å and 2.9 Å, respectively [325].

Structure	d_{ls}(Å)	l_{m}(Å)	d_{id}(Å)	χ(°)	Ref.
PEN TF	15.4	16.1	0.6	6	277
PEN SC	14.4	16.1	0.6	21	149
2,3,9,10-F4PEN	14.0*	17.4	0.6	33	121
2,3-F2PEN	16.2	16.8	(0.6)	0	-

is assigned to the (10-3) reflection. All observations on the thin film structure of 1,4,9,10-F4PEN are therefore consistent with differently oriented crystallites in a similar structure as the single crystal structure, but with some deviations of the unit cell parameters.

1,4,8,11-F4PEN exhibits two BPs at $0.4532\,\text{Å}^{-1}$ and $0.9056\,\text{Å}^{-1}$ (Fig. 5.5a) that are in agreement with calculated lattice spacings of the reported crystal structure [122], see Tab. 5.1. The second-order BP is stronger for 1,4,8,11-F4PEN than the first-order BP, which is in agreement with the calculated powder diffractogram (Fig. 5.5b) and originates from translationally inequivalent molecular planes in this crystal structure [122].

5.2 Optical characterization

Optical characterization of the thin films of PEN and FPENs has been performed by UV-Vis absorbance spectroscopy, see Fig. 5.6a. For comparison, the absorption spectra of the compounds dissolved in chloroform have been measured and are shown as thin lines in Fig. 5.6a. The absorption spectra of the dissolved F4PENs are in agreement with previous reports, in which dichloromethane instead of chloroform was used as the solvent [121, 122]. Within the series studied here, the band gaps of dissolved compounds, always defined by p-bands as for PEN [121, 122], shift to larger energies with 2,3 or 9,10 fluorination and back to lower energies from 2,3,9,10-F4PEN over 1,4,9,10-F4PEN to 1,4,8,11-F4PEN, see circles in Fig. 5.6b. These trends have been calculated to originate from a HOMO stabilization [121] in the former case as well as a stronger LUMO than HOMO stabilization in the latter case [122].

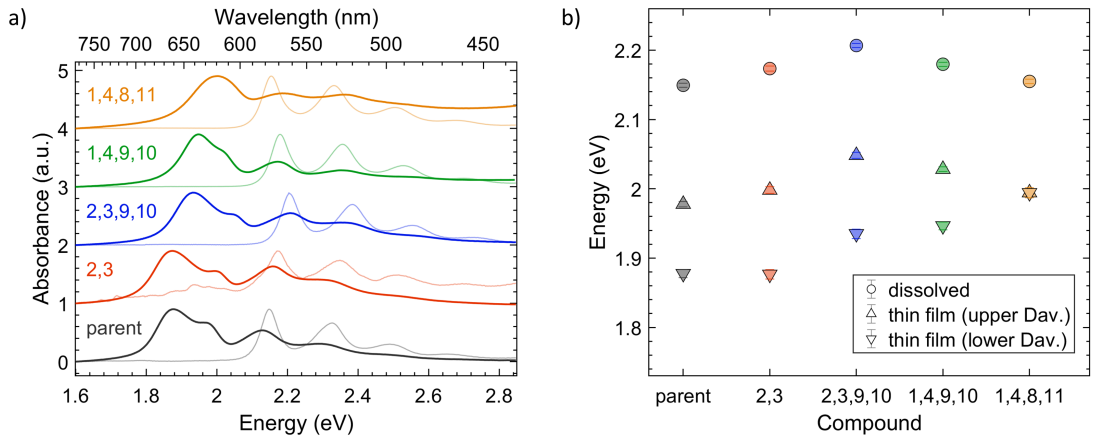


Figure 5.6: UV-Vis absorbance spectroscopy on PEN and FPENs [122, 299]. a) Absorbance spectra of thin films (thick lines) and solutions (thin lines). b) Energies of the 0-0 transitions as determined by fits of gaussian functions to the absorbance spectra in panel a). For details, see Apx. B.3. The compound labeling in both panels indicates the locants of fluorine substitution. The uncertainties of the peak positions are taken as 10 % of the full width at half maximum (FWHM) of the fitted gaussians and are on the order of the marker size.

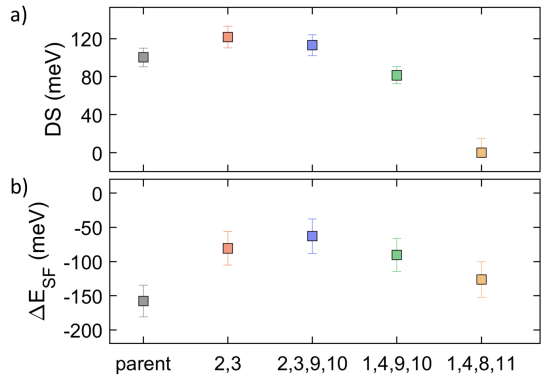


Figure 5.7: a) DS of the thin film 0-0 transitions, see Apx. B.3 for the fits. b) ΔE_{SF} based on the determined energies of the lower Davydov-component and reported triplet energies [28, 107, 122]. The triplet energy of 2,3-F2PEN has been approximated as described in the main text. The relative uncertainty of all triplet energies has been approximated to be 1 %. The compound labeling indicates the locants of fluorine substitution.

As expected from the structural characterization, the compounds exhibit very different absorption spectra in thin films, see thick lines in Fig. 5.6a. All compounds except 1,4,8,11-F4PEN show a pronounced DS of the 0-0 transition between 1.8 eV and 2.0 eV. 1,4,8,11-F4PEN does not exhibit a DS, since it has a crystal structure with only face-to-face oriented molecules. The spectral region of the DS has been fitted with gaussian functions (see Apx. B.3) in order to determine energetic positions of peaks as well as the absolute value of the DS. The results of these fits are shown in Fig. 5.6b. Note that these fits can give slightly different values for the DS than polarization-resolved absorption measurements on single crystals [288], most likely due to a deviation of the experimental absorption peak shapes from a gaussian function. Nevertheless, the qualitative trend between PEN and the FPENs should be captured by these fits.

The positions of the energetically upper Davydov component in the thin film spectra of FPENs show the same trend as observed for the band gaps of dissolved compounds, which indicates that the absolute difference in these energies is the solution-to-crystal shift. Therefore, the trend observed for the upper Davydov component is caused by the same stabilization of molecular orbitals as discussed before for the band gaps of dissolved compounds. The position of the energetically lower Davydov component, however, does not follow this trend. It is known for PEN that the position of the lower Davydov component is much more sensitive to intermolecular interactions than the position of the upper Davydov component [196]. Therefore, the different trend observed for the lower Davydov component compared to the upper Davydov component can be assigned to the influence of the modified partial charge distribution on the character and coupling of states [195, 196].

The different trends of the two Davydov components with fluorination lead to different DSs of the compounds, which is shown in Fig. 5.7a. 2,3,9,10-F4PEN, which has been shown to crystallize in a HB aggregate similar to PEN [121], has a slightly larger DS than PEN. 1,4,9,10-F4PEN, which crystallizes in a complex structure with different relative molecular orientations, exhibits an intermediate DS [122]. Finally, 2,3-F2PEN, which forms a similar HB aggregate as PEN, has the largest DS between the FPENs studied in this work, significantly larger than that of PEN. The origin of these differences in the DS of PEN and the FPENs will be discussed later on.

With T_1 energy levels reported in literature, the SF energy balance ΔE_{SF} (negative for exothermic SF, see Sec. 2.4) can be calculated from the energetic position of the lower Davydov-component for the thin films. Triplet energy levels are typically determined by phosphorescence of isolated molecules but can be approximated to be similar in thin films due to small gas-to-crystal shifts [234, 235]. The triplet energy of PEN has frequently been reported as 860 meV [28, 107], while those of F4PENs were recently determined to be close to each other around 930 meV [122]. The triplet energy of 2,3-F2PEN has not been reported yet, and it is approximated to lie in between those of PEN and 2,3,9,10-F4PEN at roughly 900 meV. With these triplet energies, the different values for ΔE_{SF}, as shown in Fig. 5.7b, are obtained. Due to the higher triplet energies, ΔE_{SF} of the FPENs is less negative than for PEN. Due to the continuous shift of the lower Davydov-component, ΔE_{SF} decreases slightly from 2,3,9,10-F4PEN over 1,4,9,10-F4PEN to 1,4,8,11-F4PEN.

5.3 TA spectroscopy

TA spectroscopy on thin films of PEN and the different FPENs has been conducted in two series of experiments, using different spectral ranges of the white light probe pulse, namely $470 - 780$ nm and $550 - 980$ nm. In the following, measurements of either series will be referred to as *Vis-probe* and *IR-probe* for clarity. In both series, an excitation wavelength of 620 nm (2.00 eV) has been used to excite the 0-0 transition of the p-band for all compounds, see Fig. 5.6. Furthermore, PEN has been measured in both series for comparison.

5.3.1 Feature assignment

The TA measurements are shown in Fig. 5.8, with those using *IR-probe* on the left side and those using *Vis-probe* on the right side. In the following, the assignment of spectral features observed in these measurements is discussed before the determination of decay constants (see Sec. 3.3.1) by GA.

For neat PEN the TA spectra (Fig. 5.8a and 5.8b) are consistent with previous reports [97] with the GSB of the energetically lowest electronic transition at 675 nm (1.84 eV, consistent with the steady-state absorption maximum at 1.88 eV) and the bleach of the high-energy Davydov component and vibronic progression at shorter wavelengths. At short delay times (i.e. 200 fs), SE of singlets is observed between 690 nm and 750 nm and singlet ESA below 530 nm. After 200 fs the singlet features disappear due to SF [97], and an increase in the $T_1 \rightarrow T_2$ ESA [97, 260, 326] is observed between 750 nm and 1000 nm, which peaks around 850 nm. The signal decays on the order of a nanosecond with a slight red-shift of the triplet ESA. The spectral features in TA measurements of thin films of 2,3-F2PEN, 2,3,9,10-F4PEN and 1,4,9,10-F4PEN (Figs. 5.8c, 5.8d and 5.8f, respectively) can be assigned based on the overall similarity to TA spectra of PEN, see Tab. 5.3. Like for PEN, also in these compounds singlet SE and ESA is observed at short delay times. The

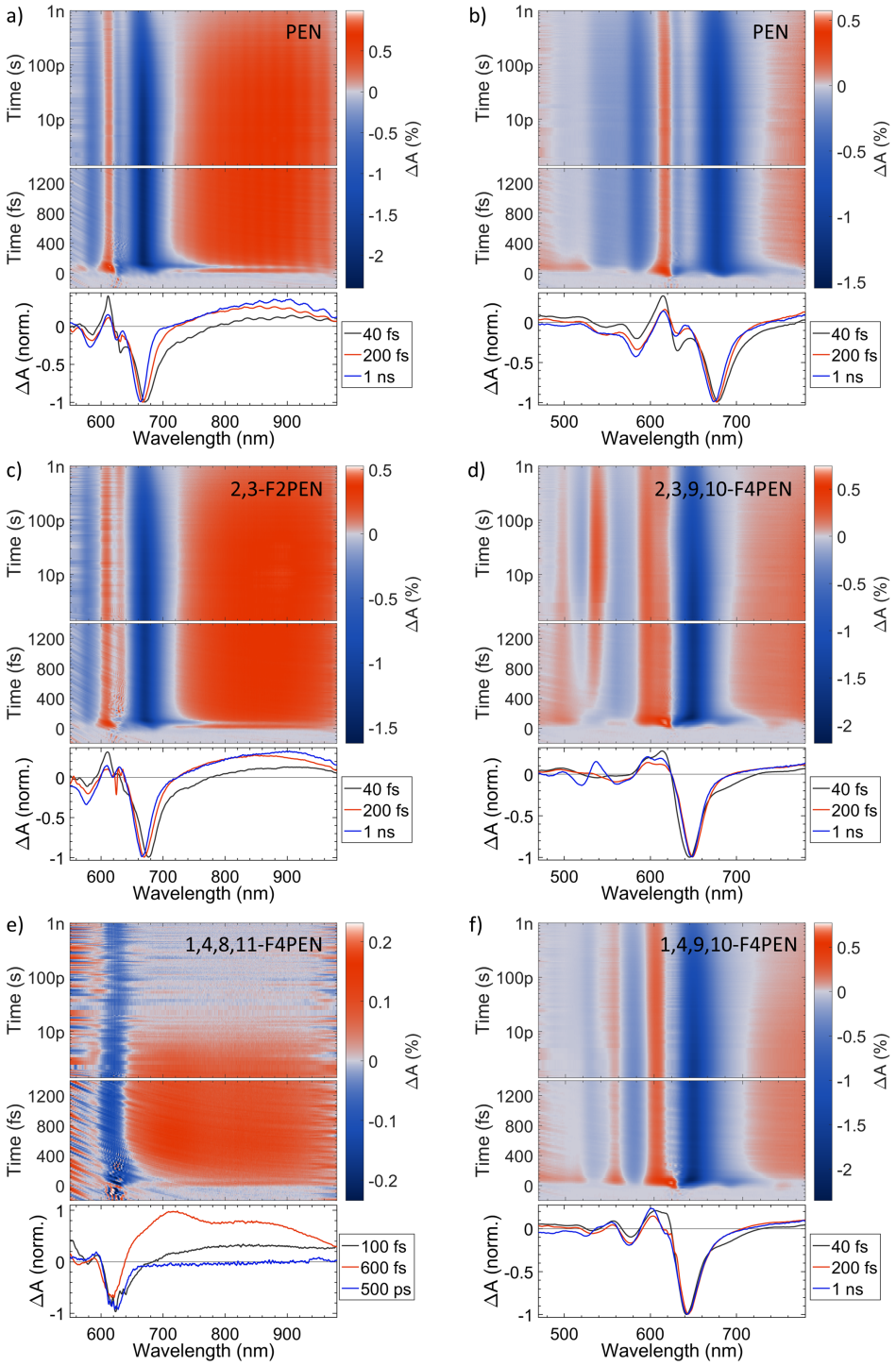


Figure 5.8: TA maps of PEN and different FPENs using *IR-probe* (left) and *Vis-probe* (right, see main text). For all measurements, an excitation wavelength of 620 nm, as well as a fluence of approximately $25 - 32\,\mu J/cm^2$ has been used, except for 1,4,8,11-F4PEN (panel e), which has been measured with a fluence of $8\,\mu J/cm^2$. Beneath each TA map, TA spectra extracted at different delay times of different compounds are shown. Data published in Refs. 122 and 299.

singlet features disappear within 200 fs, triplet ESA rises on a similar time scale and decays with the GSB on the order of a nanosecond, which is a clear indication that triplet-pair formation occurs also in these compounds.

For 2,3,9,10-F4PEN (Fig. 5.8d) and (weaker) for 1,4,9,10-F4PEN (Fig. 5.8f), new features evolve on the order of picoseconds around 540 nm (positive ΔA) and below 520 nm (towards negative ΔA). These additional evolutions of the spectral shapes are not fluence-dependent (see Apx. B.4). A photoinduced absorption around 540 nm has also been observed previously in TA measurements on PEN under oblique incidence angles of the probe pulse [260, 292]. For PEN, the feature was assigned to the $T_1 \rightarrow T_3$ ESA with a TDM along the long molecular axis [260, 326]. Based on the overall similarity of the TA spectra of PEN, 2,3,9,10-F4PEN and 1,4,9,10-F4PEN, the feature at 540 nm can be assigned to a $T_1 \rightarrow T_3$ ESA also for the FPENs [326]. The observation of this triplet ESA with a TDM along the long molecular axis [326] would agree with the large χ of 2,3,9,10-F4PEN as well as the orientational disorder of crystallites in the thin film (see Fig. 5.3), which both lead to a tilt of the molecular long axes towards the substrate plane. Also for 1,4,9,10-F4PEN, two different orientations of crystallites have been found, of which one orientation (the one leading to the (10-1) reflection observed in the XRR data, see Apx. B.1) indicates strongly inclined molecular long axes with respect to the substrate normal [122].

TA spectroscopy of 1,4,8,11-F4PEN (Fig. 5.8e) has been challenging due to a degradation of the sample, occurring for measurements both on encapsulated samples and samples in vacuum. Degradation of the sample during the TA measurement is seen from 1) an increasing reference transmission spectrum in the spectral range of the sample absorption, and 2) a decreasing TA signal between subsequent scans (see Apx. B.5). Only very low fluences allowed for scanning the whole temporal range few times with a signal that did not decrease by more than 70 % (see Apx. B.5). Importantly, since time traces of subsequent scans and those extracted from measurements using different fluences do not exhibit significant differences, the decreasing number of photoexcited molecules over time only lead to a decrease of the amplitude, but not to a qualitative change in the TA signal (see Apx. B.5). The decreasing signal between subsequent scans (see Sec. 3.3.1) has been corrected by normalizing to the first scan before averaging.

Table 5.3: Assignment of features in the TA spectra of PEN and the FPENs. For reasons of space, only the fluorination locants of FPENs are named.

Compound	GSB (nm)	SE (nm)	singlet ESA (nm)	triplet ESA (nm)	Fig.
PEN	675	690-750	<530	750-1000	5.8a,b
2,3	670	700-760	–	750-1000	5.8c
2,3,9,10	645	670-720	<520	>720	5.8d
1,4,9,10	640	670-720	<520	>720	5.8f
1,4,8,11	620	660	–	660-1000	5.8e

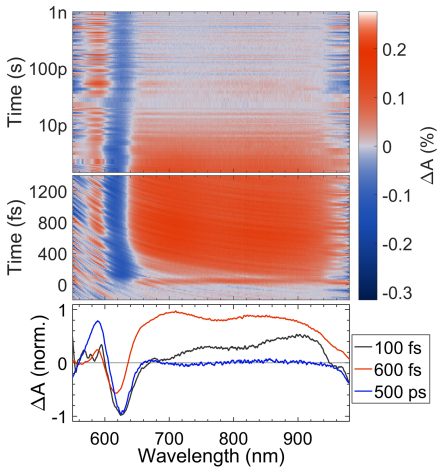


Figure 5.9: TA measurement on 1,4,8,11-F4PEN using *IR-probe*, an excitation wavelength of 530 nm and a fluence of 15 µJ/cm^2.

Thin films of 1,4,8,11-F4PEN exhibit slightly different TA spectra than thin films of PEN, thus complicating the assignment of spectral features. The negative ΔA signal at 620 nm can be assigned to a GSB based on the steady-state absorption spectra (Fig. 5.6a). Again, there is a broad, positive ΔA signal between 660 nm and 1000 nm, which is assigned to triplet ESA as in the case of PEN due to two reasons. First, it would be a large coincidence that a singlet ESA in this compound is in the same spectral range as the triplet ESA of other FPENs. Second, previously reported triplet phosphorescence does not indicate a large difference between the T_1 state of this compound and other FPENs [122], suggesting that also higher T_n states might have at least similar energies. In the TA map, a slight shift of the GSB is further observed, which might originate from a contribution of decaying SE (negative ΔA) around 660 nm.

Since both the rise of triplet ESA and the decay of SE occur within the first picosecond it can be concluded that also in this compound triplet-pairs are formed. Interestingly, however, the triplet ESA decays within few picoseconds in strong contrast to the previous cases, for which the decay was on the order of a nanosecond. After decay of the triplet ESA, a GSB persists on longer time scales than a nanosecond. Since the GSB is spectrally located exactly at the excitation wavelength, for which scattering of the pump pulse might impact the TA spectrum, an additional TA measurement has been performed on 1,4,8,11-F4PEN with an excitation wavelength of 530 nm, outside the spectral range of the *IR-probe* measurements. This measurement is shown in Fig. 5.9 and also exhibits the persistent GSB, proving that it is not an artifact from scattering of the pump pulse. The interpretation of the disappearing of the triplet ESA and the persistent GSB will be discussed later on.

5.3.2 Global analysis

A GA has been performed on all TA measurements with different fluences in order to determine time constants for evolutions between different species. In the following, the time constants mentioned with uncertainties are the mean value obtained from the fits of

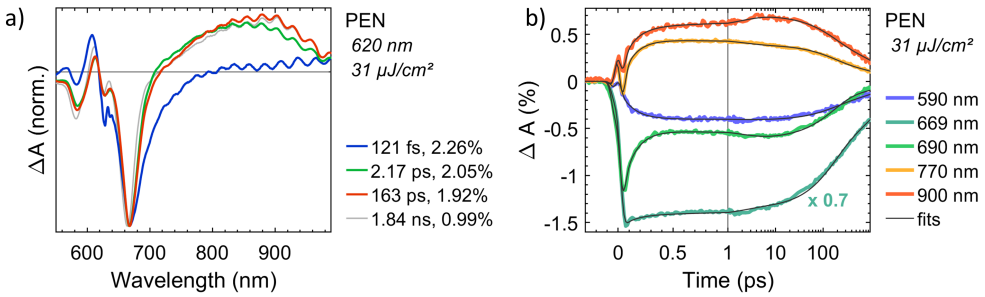


Figure 5.10: GA of a TA measurement on a PEN film with *IR-probe*. a) Normalized EAS. The legend gives the time constants for the decay into the following species, as well as the amplitude of the EAS before normalization. b) Comparison of selected time traces of the TA map to the result of the GA. The vertical solid line shows the change from linear to logarithmic scale. Data published in Ref. 299.

TA maps at different fluences. For PEN and most of the FPENs discussed in the following, modeling of the coherent artifact is found to be the dominant origin for uncertainties in the SF time constant. Therefore, the lower and upper uncertainty limits for the time constants and rates in this chapter correspond to the lowest and highest time constant obtained with different models and fluences that produced reasonable results. The GA results of TA measurements on PEN and the FPENs are shown and discussed in the following only for an intermediate fluence. For all GA results, see Apx. B.4.

PEN

The result of the GA for PEN at an intermediate fluence is shown in Fig. 5.10 for the TA measurement using *IR-probe* and in Fig. 5.11 for the TA measurement using *Vis-probe*. For a fit of the complete TA map, four (*IR-probe*) or five (*Vis-probe*) species were necessary. In both cases, the first species can be assigned to singlet excitons based on the absence of triplet ESA between 750 nm and 1000 nm, as well as the SE between 690 nm and 750 nm. All three to four following species exhibit the triplet ESA between 750 nm and 1000 nm and are therefore assigned to triplet excitons. A slight red-shift of the triplet ESA is observed between the second and the third EAS for the TA measurement using *IR-probe* in Fig. 5.10a. This red-shift has previously been assigned to the evolution from the ^{1}(TT) state to the ^{1}(T...T) state [308, 326]. Although the red-shift cannot be observed with the spectral range of the *Vis-probe* measurements, a similar decay time constant is obtained (Fig. 5.11a). Therefore, the time constants for conversion of the first to the second species (121 fs in Fig. 5.10a, 113 fs in Fig. 5.11a) are assigned to the formation of ^{1}(TT). For clarity [26], these time constants are called triplet-pair formation time constants in the following, although they have also been established as SF time constants in literature [97]. The time constants for conversion of the second to the third species (2.17 ps in Fig. 5.10a, 2.29 ps in Fig. 5.11a) are assigned to the formation of ^{1}(T...T).

The necessity of several species corresponding to ^{1}(T...T) with almost the same TA spectrum for a fit of the TA map corresponds to a non-exponential decay of the triplets.

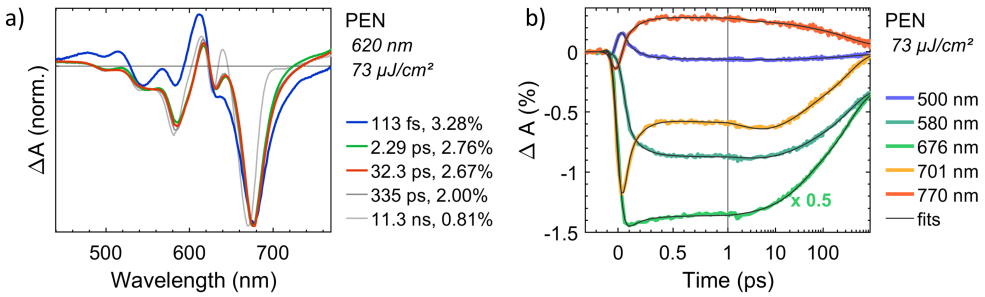


Figure 5.11: GA of a TA measurement on a PEN film with *Vis-probe*. a) Normalized EAS. The legend gives the time constant for the decay into the following species each, as well as the amplitude of the EAS before normalization. b) Comparison of selected time traces of the TA map to the result of the GA. The vertical solid line shows the change from linear to logarithmic scale. Data published in Ref. 122.

These non-exponential decays result from TTA, which is a process described by second-order rate equations [292, 327]. This interpretation is supported by the fluence-dependent TA measurements on thin films of PEN (see Apx. B.4), which show a tendency towards the necessity of less triplet species at lower fluences. Furthermore, these measurements show a faster decay of the overall signal at higher fluences (Apx. B.4) in agreement with the decay of triplets by TTA. The non-exponential, fluence-dependent decay of the triplet signal at longer delay times is also observed for most of the FPENs. Since the decay of triplets is not in the scope of this work, the respective EAS are only shown in grey in Fig. 5.10a and in the following.

Some FPENs discussed in the following exhibit a slight fluence-dependence of the triplet-pair formation time constant obtained by GA. These trends, however, are a result of the fact that the GA has been performed on the whole accessible delay time range, which includes the fluence-dependent, non-exponential triplet decay at long times. The fitting of the different non-exponential triplet decays at different fluences slightly influences the obtained triplet-pair formation time constants. Nevertheless, the time traces of TA measurements with different fluences in Apx. B.4 show that only long-time dynamics after SF are fluence-dependent, while the fast dynamics are clearly not. Furthermore, the time traces of the GA shown in the following demonstrate that the obtained time constants describe the TA data well.

The average triplet-pair formation time constant in PEN, based on the TA measurements at different fluences, is $124\,^{+4}_{-37}$ fs using *IR-probe* and $112\,^{+2}_{-13}$ fs using *Vis-probe*. Previous studies reported a triplet-pair formation time constant for thin films of PEN of 80 fs, based on fits of time traces of the triplet ESA [97]. Analogously extracted time traces in this work (see Apx. B.4) show a strong wavelength-dependence, which results, in combination with excluding the coherent artifact from the fit, in large uncertainties of the determined time constant. These uncertainties cover the time constant range from 80 fs

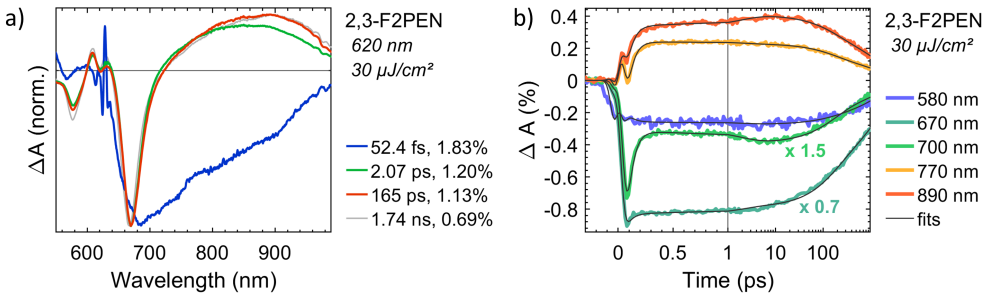


Figure 5.12: GA of TA data of a 2,3-F2PEN film with *IR-probe*. a) Normalized EAS. The legend gives the time constants for the decay into the following species, as well as the amplitude of the EAS before normalization. b) Comparison of selected time traces of the TA map to the result of the GA. The vertical solid line shows the change from linear to logarithmic scale. Data published in Ref. 299.

to 150 fs and are thus consistent with both the previously reported time constant [97] and the results obtained by GA in this work.

2,3-F2PEN

A GA of TA data of 2,3-F2PEN is shown in Fig. 5.12. Four species were necessary to fit the TA map of this measurement. Based on the similarity of the EAS to those of PEN, including the red-shift of the triplet ESA, the first, second and third EAS are analogously assigned to S_1, ^{1}(TT) and ^{1}(T...T), respectively. The fourth species is spectrally similar to the third and originates from the non-exponential triplet decay due to TTA. The time constant of the triplet-pair formation converting singlets into triplet-pairs (52 fs in Fig. 5.12a) is smaller than in PEN and close to the time-resolution of the system, as also visible from the fast dynamics of time traces shown in Fig. 5.12b. Therefore, within the rise-time of the signal some singlets already decayed into triplet-pairs, which complicates the fit of a pure singlet EAS in the GA and explains the low signal-to-noise ratio and strange shape of the EAS assigned to singlets in Fig. 5.12a. The average time constant of triplet-pair formation in 2,3-F2PEN obtained by GA of TA data at different fluences is $57\,^{+12}_{-9}$ fs.

2,3,9,10-F4PEN

Fig. 5.13 shows a GA of the TA data of 2,3,9,10-F4PEN. Five EAS are required for the GA. The first EAS can be assigned to singlets based on the spectral features described before. All following species exhibit the $T_1 \rightarrow T_2$ ESA above 720 nm and can therefore be assigned to triplet-pairs. The decay time of the first species (87 fs in Fig. 5.13a) is the time constant of triplet-pair formation and its average over TA measurements at different fluences is $86\,^{+7}_{-9}$ fs.

As noticed before, the spectral evolution from the second to the third EAS is restricted to the region between 490 nm and 560 nm, which is likely connected to the $T_1 \rightarrow T_3$

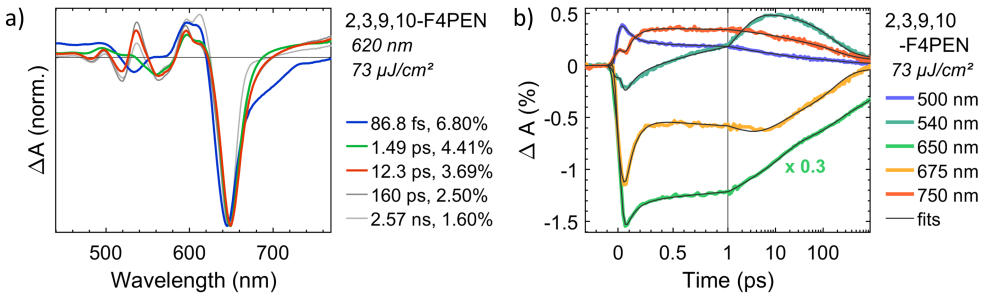


Figure 5.13: GA of a TA measurement on a 2,3,9,10-F4PEN film with *Vis-probe*. a) Normalized EAS. The legend gives the time constants for the decay into the following species, as well as the amplitude of the EAS before normalization. b) Comparison of selected time traces of the TA map to the result of the GA. The vertical solid line shows the change from linear to logarithmic scale. Data published in Ref. 122.

ESA [260, 326]. Based on the similar time scale of this evolution to the second evolution in PEN, this evolution between triplet-pair species is again assigned to the formation of ^{1}(T...T) from ^{1}(TT) [122]. The evolution of the $T_1 \rightarrow T_3$ ESA during the conversion from ^{1}(TT) to ^{1}(T...T) [326] cannot be observed in PEN and 2,3-F2PEN, most likely since it corresponds to a TDM oriented along the long molecular axis, which is perpendicular to the substrate plane with upright-standing molecules [260, 326]. The fourth and fifth EAS are spectrally similar to the third and again originate from the non-exponential triplet decay due to TTA.

1,4,9,10-F4PEN

Five species were necessary in the GA of TA data of 1,4,9,10-F4PEN shown in Fig. 5.14. In analogy to 2,3,9,10-F4PEN, the first, second and third species can be assigned to S_1, ^{1}(TT) and ^{1}(T...T), respectively. Thus, the decay time of the first species (87 fs in Fig. 5.14a) is the triplet-pair formation time constant, with an average from GA of TA

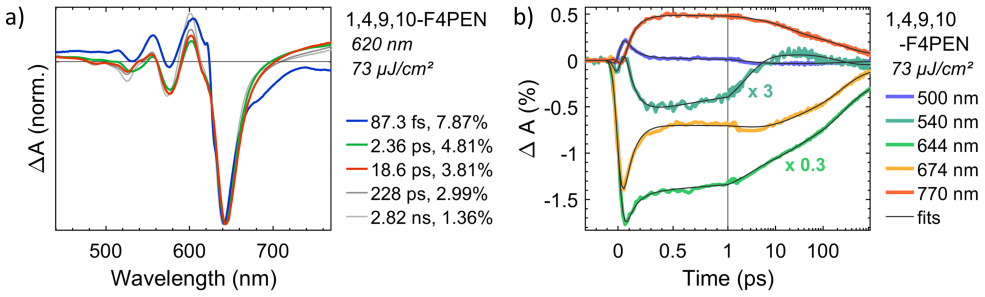


Figure 5.14: GA of a TA measurement on a 1,4,9,10-F4PEN film with *Vis-probe*. a) Normalized EAS. The legend gives the time constants for the decay into the following species, as well as the amplitude of the EAS before normalization. b) Comparison of selected time traces of the TA map to the result of the GA. The vertical solid line shows the change from linear to logarithmic scale. Data published in Ref. 122.

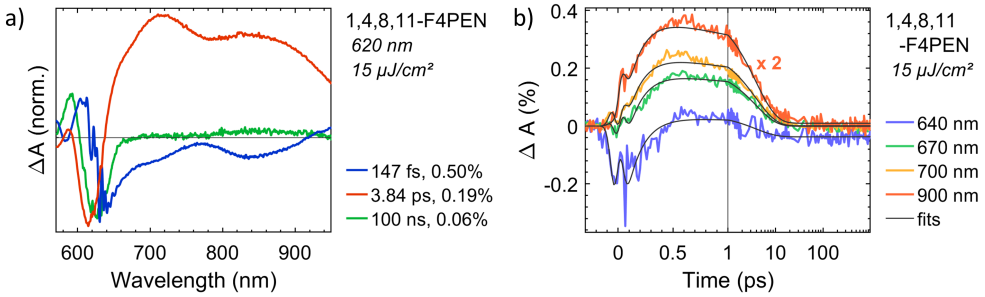


Figure 5.15: GA of a TA measurement on a 1,4,8,11-F4PEN film with *IR-probe*. a) Normalized EAS. The legend gives the time constants for the decay into the following species, as well as the amplitude of the EAS before normalization. b) Comparison of selected time traces of the TA map to the result of the GA. The vertical solid line shows the change from linear to logarithmic scale. Data published in Ref. 299.

data at different fluences of $89\,^{+28}_{-28}$ fs. As for 2,3,9,10-F4PEN, an additional evolution in the spectral region between 490 nm and 560 nm is observed for the conversion from ^{1}(TT) to ^{1}(T...T) [308, 326].

1,4,8,11-F4PEN

A GA of TA data of 1,4,8,11-F4PEN (Fig. 5.15) was complicated by the low TA signal, which originates from the low fluence used to prevent sample degradation. Three species were necessary for a fit of the complete TA map. The decay time of the last species was fixed to very long delay times (100 ns in Fig. 5.15a), since no decay could be observed within one nanosecond. Based on the features described before, the first (blue in Fig. 5.15a) and the second (red) species can be assigned to singlets and triplets, respectively. The third EAS (green) shows the GSB at 620 nm and no signal above 680 nm, thus no triplet ESA. The singlet decay time constant (147 fs in Fig. 5.15a) is the time constant with which the triplet ESA appears, with an average over the TA measurements at different fluences of $140\,^{+18}_{-10}$ fs. The average time constant of the decay of the triplet species is $3.9\,^{+0.4}_{-0.4}$ ps. The origin of this decay is discussed later on.

5.4 Discussion

In the previous section the TA data was presented, features and EAS obtained by GA were assigned and time constants for the decay of species were determined. Until here, the time constant τ_1 corresponding to the formation of ^{1}(TT) was discussed as the triplet-pair formation time constant. In the following discussion, triplet-pair formation rates $r_{\mathrm{tp}} = 1/\tau_1$ are mentioned instead of time constants. The molecular arrangement, DS, ΔE_{SF} and triplet-pair formation rates r_{tp} of PEN and the FPENs are summarized in Tab. 5.4. In the following, the observations by TA spectroscopy are discussed with regard to the structural and optical properties of the films.

Table 5.4: Structure, χ, DS, ΔE_{SF} and triplet pair formation rates of PEN and the FPENs studied in this work. For reasons of space, only the fluorination locants of FPENs are named. FTF abbreviates face-to-face oriented molecules.

Compound	structure	χ (°)	DS (meV)	ΔE_{SF} (meV)	τ_1 (fs)	r_{tp} (1/ps)	Ref.
PEN	HB	6	100	-158	118	8.5	277
2,3	HB	0	122	-81	57	17.5	–
2,3,9,10	HB	33	113	-63	86	11.6	121
1,4,9,10	HB/FTF	–	82	-91	89	11.2	122
1,4,8,11	FTF	–	0	-126	140	7.1	122

5.4.1 Impact of face-to-face arrangement of molecules

Before the comparison between the different HB aggregates, first the photophysics of 1,4,8,11-F4PEN are discussed in the following, since it is the only compound, for which all molecules in the crystal structure are face-to-face oriented [122]. The determined r_{tp} in thin films of this compound is the lowest of all compounds studied here. For the discussion of the triplet-pair formation in 1,4,8,11-F4PEN the comparison with PFP can be helpful, since it has been shown for PFP that triplet-pair formation also occurs between face-to-face oriented molecules [242]. SF in PFP is significantly slower than in PEN with a timescale of 200 fs [78]. PFP and 1,4,8,11-F4PEN therefore suggest the face-to-face orientation of PEN derivatives to be detrimental for the formation of a triplet-pair, in agreement with similar observations in the literature [92, 99, 229].

The exact orientation of the face-to-face oriented molecules is likely to be crucial for r_{tp} and large variations in the SF rate are theoretically predicted upon laterally shifting face-to-face oriented PEN molecules due to the altered orbital overlap [229]. The displace-

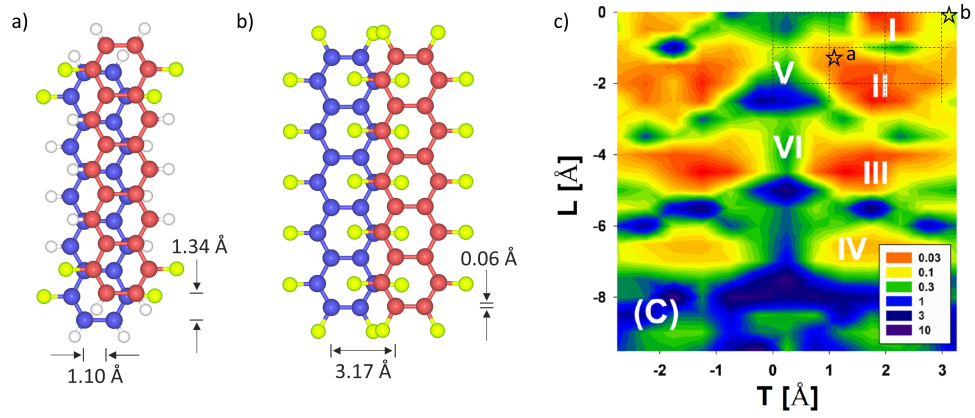


Figure 5.16: Impact of face-to-face stacking displacements on the SF rate. a,b) Displacements of the face-to-face oriented molecules in the a) 1,4,8,11-F4PEN [122] and b) PFP [298] crystal structure. c) Calculated SF time constants in Ref. 229 (legend values in ps) for displaced, face-to-face oriented PEN molecules. The star symbols indicate the displacements of the two compounds shown in panels a) and b). Panel c) reprinted (adapted) with permission from Ref. 229. Copyright (2014) American Chemical Society.

ments of translationally equivalent molecules of 1,4,8,11-F4PEN and PFP are shown in Fig. 5.16a and 5.16b and compared to the theoretically calculated SF rate map shown in Fig. 5.16c [229]. The small displacement along both the molecular short and the molecular long axis for 1,4,8,11-F4PEN results neither in a pronounced minimum or a maximum of the calculated SF rate for PEN. The calculated SF rate corresponding to the large displacement of PFP molecules along the short molecular axis is far from a maximum and clearly lower than the calculated SF rate corresponding to the displacement of 1,4,8,11-F4PEN. Therefore, this calculation would be in qualitative agreement with the experimental finding that r_{tp} in 1,4,8,11-F4PEN is larger than in PFP. It is important to highlight that the SF rate map for displacements shown in Fig. 5.16c is calculated for PEN and might differ for PFP and 1,4,8,11-F4PEN. Based on the same pattern of HOMO and LUMO of the three molecules (see Apx. B.6) it is, however, likely that a calculated SF rate map for displacements of these FPENs would exhibit a similar pattern and thus lead to the same conclusion.

Finally, also the different ΔE_{SF} of the two compounds might have an impact. PFP has a much lower ΔE_{SF} (calculated $-310\,\mathrm{meV}$ in Ref. 78), contrasting the higher ΔE_{SF} of PEN ($-160\,\mathrm{meV}$) and 1,4,8,11-F4PEN ($-130\,\mathrm{meV}$) [28, 107, 122]. This lack of correlation between r_{tp} and ΔE_{SF} indicates that the face-to-face geometry is the dominant source for the smaller r_{tp} of 1,4,8,11-F4PEN and PFP compared to PEN.

In contrast to PEN and the other FPENs, a decay of the triplet ESA on the order of picoseconds is observed for 1,4,8,11-F4PEN. After this decay, a GSB persists on a time scale longer than one nanosecond, which denotes at least a fraction of photoexcited molecules that are in a long-lived state that does not lead to triplet ESA in the TA spectrum. One explanation for the persistent GSB would be a second species of excitons in an environment where they cannot form triplet-pairs and radiative or non-radiative relaxation to the ground state is slow. However, XRD does not indicate any polymorphism but a highly crystalline film with large crystallites (9.7 nm extracted from the reciprocal space maps in Fig. 5.4b using the Scherrer formula [158]), i.e. few grain boundaries. It is therefore concluded that the long-lived GSB does not originate from trapped excitons at defects.

Since no triplet ESA is observed at longer delay times, the long-lived GSB corresponds to a singlet state, which is different from the photoexcited singlet state that formed the triplet-pair. The face-to-face orientation of 1,4,8,11-F4PEN molecules leads to the formation of an H-aggregate [153] with a dark singlet state (S_1^-) below the observed bright state (S_1^+) at 2.00 eV, thus in energetic proximity to the expected triplet-pair energy of 1.87 eV [122]. Even if the energy of the dark state is lower than the triplet-pair energy, an exothermic conversion from ^{1}(TT) to the dark state with a time constant of 3.9 ps would be remarkably slow [23].

However, this time constant agrees very well with typical time constants for excimer formation [328–330], which has been found for various other face-to-face oriented chromophores [91–93, 194, 328–330]. Therefore, a scenario shown in Fig. 5.17 is proposed, which would be consistent with all observations. The rise of the triplet ESA can be as-

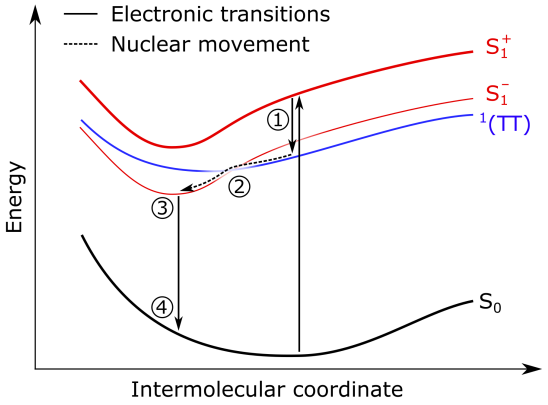


Figure 5.17: Sketch of the proposed scenario for the photophysics of 1,4,8,11-F4PEN upon excitation of S_1.

signed to the formation of ^{1}(TT) from S_1^+ on a time scale of 140 fs (step 1 in Fig. 5.17), which is much faster than the above mentioned typical time scale for excimer formation and thus explains why the excimer is not formed along the S_1^+ PES. After the formation of ^{1}(TT), the system evolves along an intermolecular coordinate on the ^{1}(TT) PES [294] towards an avoided crossing region or a conical intersection with the S_1^- PES and transitions onto the latter (step 2). This step corresponds to the observed disappearance of triplet ESA with a timescale of 3.9 ps. On the PES of S_1^-, the system subsequently relaxes into an excimer configuration (step 3). Since SF is highly endothermic in this configuration, the excimer cannot undergo SF and relaxes back to S_0 (step 4). PL of such an excimer was not observed above 1.3 eV (see Apx. B.3), which indicates that it relaxes non-radiatively due to the low oscillator strength of the $S_1^- \rightarrow S_0$ transition.

5.4.2 Altered coupling of electronic states

The slower triplet-pair formation in 1,4,8,11-F4PEN likely originates from the different molecular arrangement compared to the HB aggregates. Comparing the HB aggregates with each other, however, no correlation between χ and r_{tp} is observed (see Tab. 5.4). Therefore, the differences between r_{tp} of the HB aggregates might directly originate from the modification of the partial charge distribution [78, 84, 85, 123, 323]. There are several mechanisms how a modification of the partial charge distribution can impact the triplet-pair formation rate, which are summarized in Fig. 5.18. As a central parameter, influences on the coupling between FE and CT states (called FE-CT coupling in the following), will be discussed in the following before presenting an analysis of the correlation between the FE-CT coupling and the triplet-pair formation rate.

Origins of enhanced FE-CT coupling

CT states are known to be important intermediate states in the SF processes of different materials [55, 62, 76, 79, 196, 331]. For PEN, CT states are even admixed in the S_1 state by approximately 50 % [153, 195, 197, 234] due to a strong FE-CT coupling, and have been shown to be crucial for the ultrafast, coherent SF process in PEN [51, 71, 196, 293]. Due to this admixture, CT states have further been shown to largely determine the energy

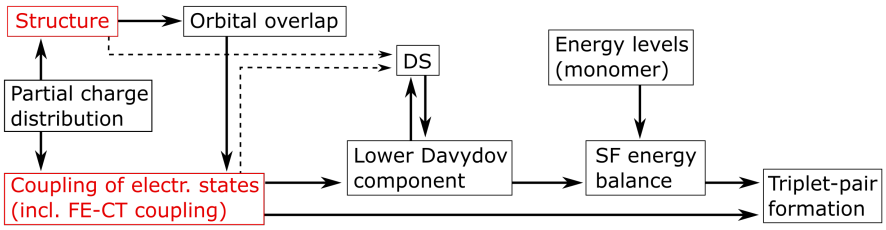


Figure 5.18: Flow diagram of possible impact mechanisms of intermolecular interactions on the triplet-pair formation in HB aggregates. Weak influences are shown as dotted lines. The two directly altered parameters by the partial charge distribution are colored in red.

of the energetically lower Davydov component, and thus the DS of acenes, which has been calculated to be negligibly small (and even to change its sign) without the contribution of CT states [153, 195, 196] (see Sec. 2.3.2). Therefore, theory predicts a close relation between the DS and the strength of FE-CT coupling in acenes [153, 195, 196, 288], for which also experimental indications have been found [52]. Due to the similarity of the molecular arrangement and the optical properties, a similar relation can be expected for the FPENs forming HB aggregates.

The DS of the only compound with a large permanent dipole in the ground state, 2,3-F2PEN, is clearly the largest among PEN and the FPENs studied in this work, see Tab. 5.4. As mentioned above, this indicates that the FE-CT coupling is enhanced compared to PEN [195, 196]. A reason for this enhancement might be the attracting partial charges of neighboring molecules, which are likely to facilitate the transfer of electrons to neighboring molecules (Fig. 5.19). This would reduce the CT state energy and enhance the FE-CT coupling [78, 123]. Such attracting partial charges on neighboring molecules are also present for 2,3,9,10-F4PEN, whose DS is in between those of PEN and 2,3-F2PEN. 1,4,9,10-F4PEN exhibits a significantly smaller DS than PEN, which might originate from a superposition of absorption spectra of molecules at the different sites in the crystal, including the molecules with face-to-face orientations that do not lead to a DS. Although the impact of a modification of the partial charge distribution on the FE-CT coupling seems likely [78, 123] and there is no correlation between χ and r_{tp}, it cannot be excluded

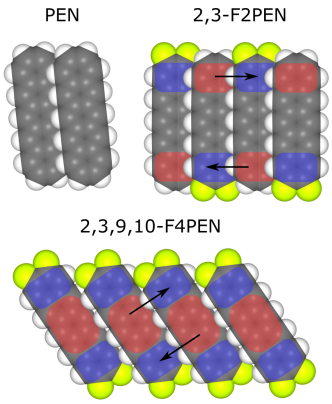


Figure 5.19: Sketch of intermolecular orientations and molecular charge distributions of PEN, 2,3-F2PEN and 2,3,9,10-F4PEN. Neighboring molecules are meant to represent translationally inequivalent molecules in the HB aggregate, but are shown with the same orientation for simplicity. Red and blue areas show negative and positive partial charges, respectively (see Fig. 5.1). Arrows indicate the possible pathways of electron transfer to neighboring molecules. White spheres represent hydrogen atoms, citreous spheres fluorine atoms and dark spheres carbon atoms.

that the different crystal structures with the different inclination angles χ and HB angles have a significant impact on the FE-CT coupling and r_{tp} [288].

Correlation between FE-CT coupling and triplet-pair formation rate

An altered FE-CT coupling can impact the triplet-pair formation in two ways (Fig. 5.18). First, due to its impact on the lower Davydov component it alters ΔE_{SF}. Second, it has a direct impact due to the superexchange coupling of the CT state to the ^{1}(TT) state [50, 196]. These two contributions are difficult to distinguish experimentally. The measured r_{tp} in comparison to the respective DS and ΔE_{SF} is shown in Fig. 5.20. Since the DS and ΔE_{SF} are both affected by the FE-CT coupling (see Fig. 5.18) these figures give information about the impact mechanism of FE-CT coupling on r_{tp}.

It is directly apparent from Fig. 5.20a that the compound with the largest DS (2,3-F2PEN) and a permanent dipole also exhibits the largest r_{tp}, which indicates that the large FE-CT coupling concluded from the large DS also facilitates the triplet-pair formation [50, 196]. This interpretation is further supported by r_{tp} and the DS of 2,3,9,10-F4PEN, which both are in between those of PEN and 2,3-F2PEN and thus strengthen the correlation between the two observables. Only 1,4,9,10-F4PEN does not follow the trend observed in Fig. 5.20a. However, this compound also crystallizes in a complex crystal structure with both, HB and face-to-face arrangements of molecules. Singlet excitons on different molecules in the film have several differently oriented neighboring molecules, with which the triplet-pair formation rates differ, and for which the fastest is more likely to occur. Singlet exciton diffusion before the triplet-pair formation might even increase the importance of this effect. Therefore, for 1,4,9,10-F4PEN in Fig. 5.20a, the DS is an average value of all sites in the crystal, while r_{tp} likely over-represents the triplet-pair formation at one of the different sites in the crystal.

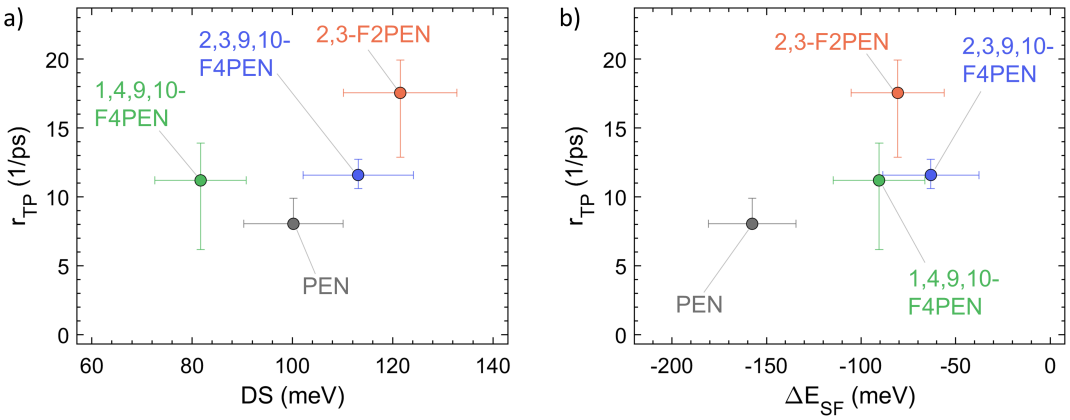


Figure 5.20: Relation between r_{tp} and a) the DS, b) ΔE_{SF} as reported in Tab. 5.4. ΔE_{SF} is the SF exothermicity as defined in Eq. 2.31. It has been calculated based on fits of absorption spectra of the thin films as well as triplet energies reported in literature [28, 107, 122]. The triplet energy of 2,3-F2PEN is interpolated to lie in between PEN and 2,3,9,10-F4PEN.

A similarly clear correlation between r_{tp} and ΔE_{SF} as between r_{tp} and the DS cannot be seen in Fig. 5.20b. In particular 2,3-F2PEN with the large r_{tp} has an intermediate ΔE_{SF}. However, the triplet energy used for calculation of this value was assumed to lie in between that of PEN and 2,3,9,10-F4PEN, and ΔE_{SF} is strongly sensitive to this value.

Importantly, both dependencies of r_{tp} on the DS and ΔE_{SF} rely on the FE-CT coupling, see Fig. 5.18. Therefore, not only an enhancement of FE-CT coupling by the modification of the partial charge distribution (see discussion before), but also a clear correlation between the FE-CT coupling and r_{tp} can be concluded for the HB aggregates. The relative importance of the two impact mechanisms of FE-CT coupling (indirect over ΔE_{SF} or direct, see Fig. 5.18) cannot be examined based on these measurements. It is, however, likely that the altered FE-CT coupling not only changes ΔE_{SF}, but also directly affects r_{tp}, since the couplings between CT and TT states rely on similar electron transfer integrals as the FE-CT coupling (see Sec. 2.4.4). In contrast to ΔE_{SF}, a direct impact of altered FE-CT coupling on r_{tp} due to the modified partial charge distribution would denote a unique handle for varying the SF process.

5.5 Conclusion

The photophysics of four different FPENs (2,3-F2PEN, 2,3,9,10-F4PEN, 1,4,9,10-F4PEN and 1,4,8,11-F4PEN) with various crystal structures have been investigated using TA spectroscopy on thin films and compared to PEN. For all compounds, a triplet ESA was observed and time constants for its rise, corresponding to the formation of triplet-pairs, were determined.

The triplet-pair formation rate (r_{tp}) was discussed with regard to the molecular arrangement, the DS and the SF energy balance (ΔE_{SF}), which relate to different parameters impacting the triplet-pair formation. The comparison between observations on PEN and the different FPENs gave information about the importance of the mechanisms connected to these three observables. A decreased r_{tp} was observed in 1,4,8,11-F4PEN with face-to-face oriented molecules, similar to the decrease observed previously for face-to-face oriented PFP molecules [78] and for other compounds [92, 94, 99]. The experimentally observed triplet-pair formation rates between the translationally equivalent molecules of 1,4,8,11-F4PEN and PFP were shown to qualitatively agree with calculated SF rates for face-to-face oriented PEN dimers reported in literature [229]. After triplet-pair formation in 1,4,8,11-F4PEN, excimer formation impedes a separation of the triplets.

Upon comparing r_{tp} of the HB aggregates, no correlation to χ, which connects to the molecular arrangement, but a clear correlation to the DS was observed. The DS and the triplet-pair formation rate increase from PEN over 2,3,9,10-F4PEN to 2,3-F2PEN. This strongly indicates that the increase in r_{tp} originates from an altered coupling of electronic states. The FE-CT coupling is known to be crucial for the DS and the triplet-pair formation in acenes [196]. It seems likely that the Keesom interaction of attracting

partial charges on neighboring molecules are the origin of the enhanced FE-CT coupling and triplet-pair formation rate [78, 123].

To conclude this chapter, by the modification of the partial charge distribution, fluorination of PEN allows to alter the arrangement and the coupling of states while retaining a highly crystalline structure. In going from HB aggregates to face-to-face oriented molecules, a slower triplet-pair formation was observed as calculated for PEN before and also observed for other compounds [78, 92, 94, 99, 229]. Furthermore, between different HB aggregates strong differences in the triplet-pair formation were found and were assigned to enhanced coupling of states by the partial charges on neighboring molecules. More generally, this study highlights the impact of halogenation on the triplet-pair formation. Molecular design with an exclusive view on state energies may lead to ideal SF energetics, but the photophysical processes that occur in crystalline aggregates can significantly be impacted by different intermolecular couplings [84, 85, 123]. This study shows that the possibility of specifically addressing the coupling of states is a powerful handle, beyond the modification of orbital overlap [84], to impact the triplet-pair formation as the first step of SF.

6. Results II: Singlet fission in blends with spacer molecules

In this chapter the impact of a reduced number of nearest neighbors of a given SF molecule (Fig. 6.1) on the SF process in TET and ADT is studied. These investigations have been performed in collaboration with Prof. C. J. Bardeen's research group (UC Riverside, USA), Prof. R. Tempelaar (Northwestern University, USA) and Prof. D. R. Reichman (Columbia University, USA), see Apx. F for a detailed overview of contributions. The investigations presented in this chapter have been published in *Nature Communications* [271].

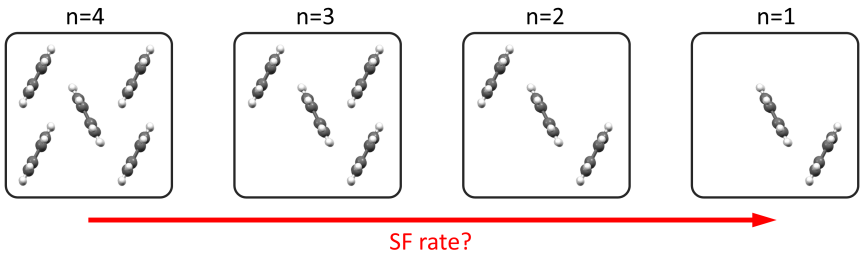


Figure 6.1: In a HB aggregate, a molecule has four nearest neighbors. The impact of replacing neighbors of a given molecule by weakly interacting, high-bandgap spacer molecules on the SF rate is investigated in this chapter.

As described in Sec. 2.4.5, different effects can impact the SF rate in spacer blends. Among these parameters are the continuous change in the crystal lattice and the CT-character of S_1. Interestingly, for PEN, the SF rates in PEN:spacer blends were found to be insensitive to such changes [52], which was explained by a hot-spot mechanism, ultrafast hopping of excitons to low-energy sites at which SF is as fast as in neat PEN [52, 231].

In contrast, a decreased singlet decay rate has been observed in amorphous blends of RUB with spacer materials and explained by a continuous increase in intermolecular distances [275]. Furthermore, already in the 1970s, the increase of fluorescence time constants and decrease of singlet decay rates in mixed single crystals of TET and a spacer material [105] was explained by the replacement effect, i.e. the reduction of the SF rate due to a reduced number of neighboring SF chromophores (see Sec. 2.4.5), and enhanced triplet fusion.

Table 6.1: Unit cell parameters of neat films and blends based on unit cells reported in Refs. 155 and 314, see Tab. 4.4. The column labeled Fig. 6.2 indicates in which panel of the figure calculated reflections based on the respective unit cell are shown. Note that the a and b parameters (and accordingly the α and β angles) of 6PH and PIC have been switched compared to the original publication [155, 314] for reasons of comparison.

Film type	Fig. 6.2	a (Å) ±0.1	b (Å) ±0.1	c (Å) ±0.1	α (°) ±2	β (°) ±2	γ (°) ±0.5
neat 6PH	b,f	6.22	8.37	32.0	98	90	90
25% TET:6PH	d	6.18	8.33	31.0	96.5	90	90
40% TET:6PH	e	6.17	8.25	30.5	96	90	90
neat PIC	c	6.23	8.37	13.5	90.5	90	90
17% TET:PIC	g	6.27	8.39	27.0	90.5	90	90
33% TET:PIC	h	6.24	8.27	27.0	90.5	90	90
50% TET:PIC	i	6.27	8.22	27.0	90.5	90	90

These observations reveal a systematic, opposite behavior of exothermic (PEN) and endothermic (TET, RUB) SF materials in spacer blends. They suggest that, besides the mechanisms proposed in literature (see above), also different SF pathways in these compounds might play a role in the different concentration-dependence of the respective SF rate [26]. While there is an agreement in literature that SF in PEN is a coherent process [26, 69, 71, 74], the SF pathway in TET and RUB is debated [56, 59, 60, 64, 67, 70, 96]. Recent studies indicated that at least in TET the SF process is incoherent [67], which would pose a fundamental difference to SF in PEN.

A direct comparison of the results of previous studies regarding the SF pathway is complicated by the different employed systems (polycrystalline film [52], single crystal [105], amorphous film [275]). Therefore, polycrystalline spacer blends with TET were prepared in the present study in analogy to those containing PEN in Ref. 52. Investigation of the SF rate in these directly comparable systems, differing only in the energy balance of the SF process, allows an investigation of the microscopic origin for the different concentration-dependence of their SF rates.

6.1 Structural characterization

In Fig. 6.2, GIWAXS data of the blends and neat films are shown in comparison to calculated reflections based on different unit cells shown in Tab. 6.1. For details on the preparation of the TET:6PH and TET:PIC blends for which data is shown also in the following, see Tabs. E.2 and E.3. The crystal structure of the thin film of TET is clearly that of the thin film polymorph [281], see cross markers in Fig. 6.2a. Also the reciprocal space maps of neat PIC and 6PH (Figs. 6.2b and 6.2c) are consistent with previously reported unit cell parameters [155, 314].

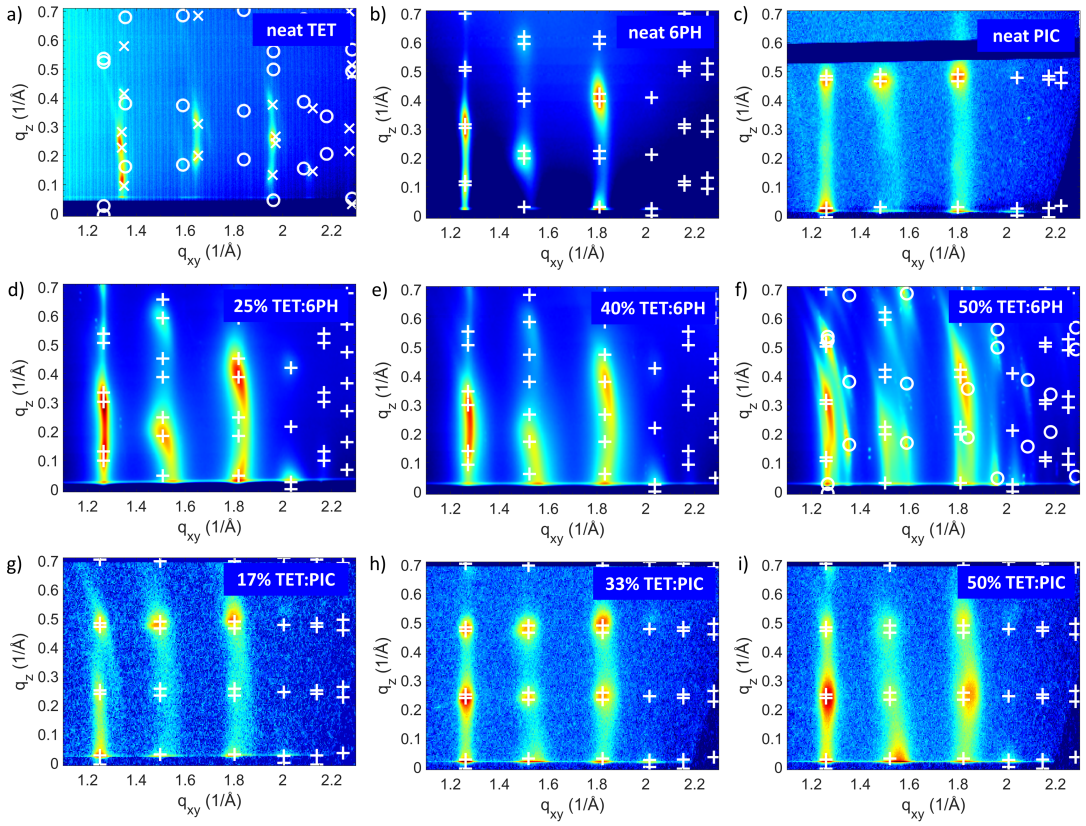


Figure 6.2: Reciprocal space maps of TET:6PH blends, TET:PIC blends and the neat compounds, see labeling in the panels. Crosses (circles) correspond to calculated reflections based on the unit cell of the TET thin film (bulk) phase [281]. The plus markers correspond to calculated reflections based on the unit cells listed in Tab. 6.1 and are based on unit cells reported in Refs. 155 and 314. The reciprocal space maps have been measured a) at *Diamond*, b,d-f) at *Soleil*, c,g-i) at the *Xeuss-system*. For growth parameters see Tabs. E.2 and E.3. Published in Ref. 271.

Reciprocal space maps of TET:6PH blends are shown in Figs. 6.2d-f. The reflections at 25 % and 40 % TET concentration are similar to neat 6PH, but are slightly shifted (see Tab. 6.1) and smeared out. For the blend with 50 % TET concentration a phase separation between a TET bulk polymorph and a mixed phase similar to the 6PH crystal structure is observed. This observation indicates limited intermixing, as observed before for mixtures of PEN and PIC [332, 333]. In limited intermixing, which is investigated in more detail below, phase separation between a mixed and a neat phase occurs above a certain concentration. Typically, the shorter molecules form the neat phase due to a more favorable substitution of longer molecules by shorter molecules in a crystal than vice versa [332]. The same is observed here as the TET molecule is significantly shorter than a 6PH molecule.

Reciprocal space maps of TET:PIC blends, shown in Figs. 6.2g-i, exhibit a similar reflection pattern as the reciprocal space map of neat PIC. Towards higher TET concentrations, the reflections exhibit a slight in-plane shift, see corresponding a and b unit cell

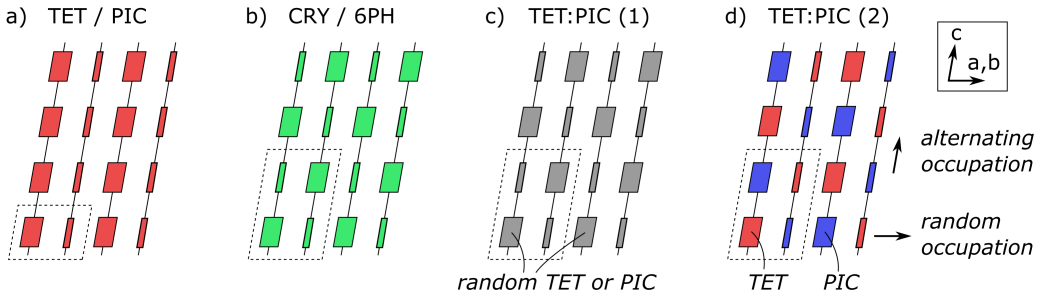


Figure 6.3: Possible origins for the reflections at $q_z = 0.25\,\text{Å}^{-1}$ in the reciprocal space maps of TET:PIC (see Figs. 6.2g-i). Large and small colored trapezia correspond to the two translationally inequivalent molecules in the ab-plane of a HB aggregate. As a guide to the eye, the molecules are connected by lines along the c-axis. Dotted trapezia indicate primitive unit cells. a,b) Sketch of reported crystal structures with two [152, 155] and four [156, 314] molecules per unit cell. c,d) Sketch of two scenarios for explanation of the intermediate reflections in the reciprocal space maps of TET:PIC. The unit cells are doubled by an alternating rotation (c) or by an alternating occupation (d).

parameters in Tab. 6.1. Furthermore, additional reflections appear at $q_z = 0.25\,\text{Å}^{-1}$. These reflections can be reproduced by calculated reflections based on a unit cell that is doubled along the c-axis, see the lattice parameter c in Tab. 6.1. A doubled unit cell along the c-axis implies that the molecules in subsequent molecular planes are not translationally equivalent anymore.

For a discussion of possible origins of this doubled unit cell in the TET:PIC blends, it is instructive to refer to the neat materials. While the crystal structures of TET [152] and PIC [155] contain only two molecules in the unit cell (Fig. 6.3a), molecules in subsequent planes of CRY and 6PH are rotated by 90° around their long axes [156, 314], as shown in Figs. 4.2e and 6.3b. Based on these crystal structures, the doubled unit cell observed for the TET:PIC blends can be explained by the two scenarios shown in Figs. 6.3c and 6.3d. Either, molecules in subsequent molecular planes are alternatingly rotated around the long axes as for neat CRY and 6PH (Fig. 6.3c), or the lattice sites of subsequent molecular planes are alternatingly occupied by TET and PIC (Fig. 6.3d). The identification of either case would require an analysis of the relative intensities of reflections and is beyond the scope of this work. Importantly, independent of the doubled unit cell, the absence of new in-plane reflections and the persistence of those corresponding to the PIC unit cell is strong evidence for an in-plane solid solution, i.e. a random occupation along in-plane directions.

XRR data of the neat films and blends are shown in Fig. 6.4a and 6.4b. The BP positions for neat films of 6PH and PIC agree with the unit cells used for comparison to the reciprocal space maps (Tab. 6.1). For the blends, BPs are observed at similar positions as for the spacer materials. At 50 % and 75 % TET concentration in the TET:6PH and TET:PIC system, respectively, a contribution of a neat TET phase can be observed, which denotes limited intermixing above 50 % TET concentration in both systems, consistent with the observations in the reciprocal space map of the TET:6PH blend with 50 % TET in Fig. 6.2f.

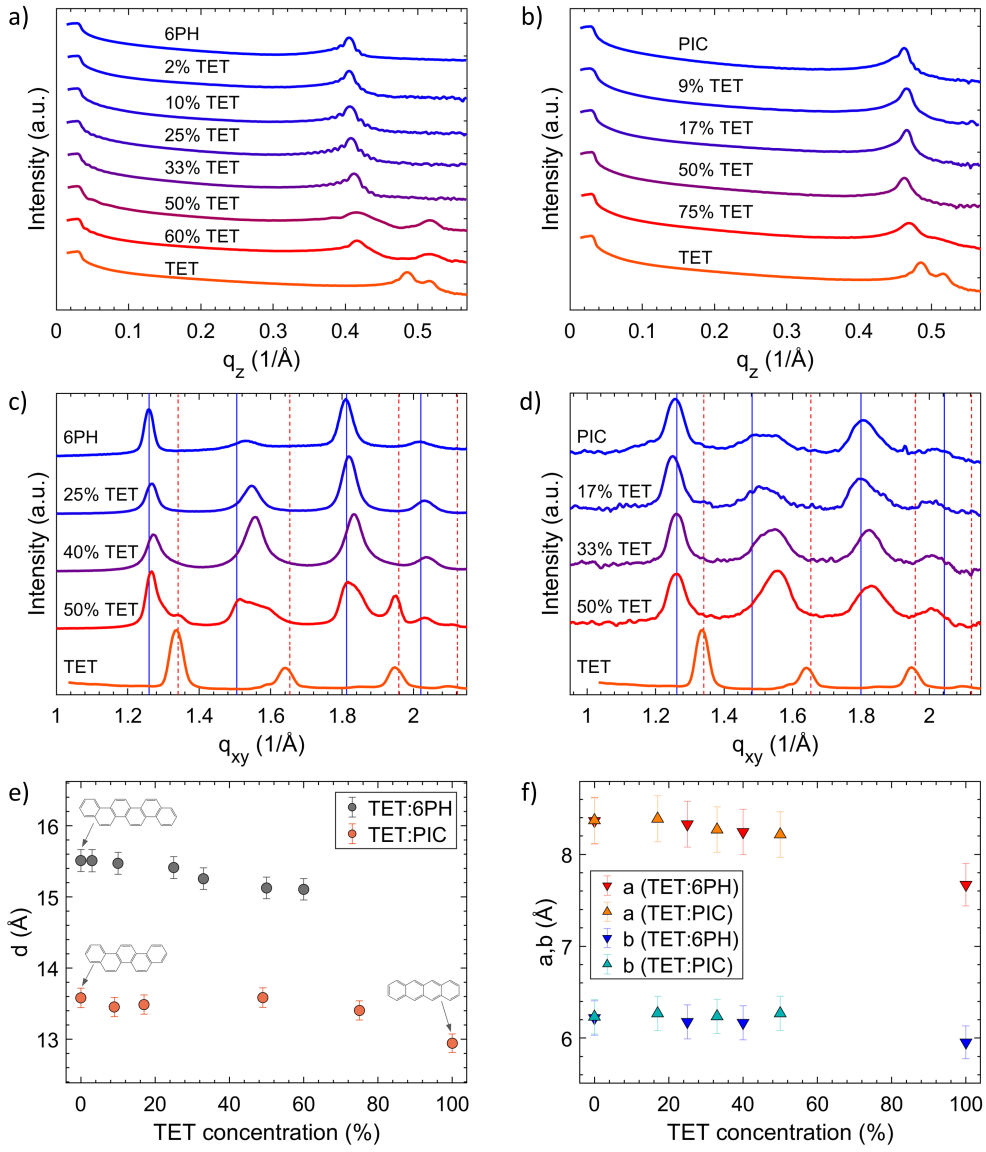


Figure 6.4: Crystal lattice parameters of TET:6PH and TET:PIC blends. a,b) XRR scans on TET:6PH and TET:PIC blends. c,d) In-plane scattering intensity as a function of q_{xy} of TET:6PH and TET:PIC blends. Blue vertical lines indicate the position of in-plane BPs corresponding to neat 6PH (c) or neat PIC (d) films [155, 314], see Tab. 6.1. Dotted vertical lines correspond to BPs of the thin film phase of TET [281]. e) Extracted lattice spacings from a). f) Extracted in-plane unit cell parameters from c) and d). For growth parameters see Tabs. E.2 and E.3. Data published in Ref. 271.

The in-plane scattering intensity as a function of q_{xy} of the neat films and blends is shown in Fig. 6.4c and 6.4d. For TET concentrations below the critical concentration for limited intermixing, the positions of the in-plane BPs in both mixed systems are close to the corresponding reflexes of the respective spacer compound with only slight shifts in position. Furthermore, no TET BPs are observed, supporting the conclusion of complete intermixing for TET concentrations below 50 % in both systems.

The out-of-plane lattice spacing (Fig. 6.4e) and the in-plane unit cell parameters (Fig. 6.4f) of the films have been extracted by analyzing the BP positions in the XRR data and the in-plane scattering intensity, respectively. Since TET and PIC molecules have approximately the same length, no significant shift in the out-of-plane lattice spacing is observed between 50 % TET and neat PIC (Fig. 6.4e). The 6PH molecule is significantly longer than TET, and a slight decrease in the out-of-plane lattice spacing is observed from neat 6PH to 50 % TET.

For both TET:6PH and TET:PIC blends, the in-plane unit cell parameters (Fig. 6.4f) remain almost constant with changes in the TET concentration and only exhibit a small difference to TET. Importantly, the changes of the in-plane unit cell parameters between the blends (≈ 0.12 Å in TET:6PH, ≈ 0.22 Å in TET:PIC) are significantly smaller than between the two TET polymorphs (0.32 Å) and include an almost constant unit cell angle γ, contrasting the 3° difference in γ between the two TET polymorphs [230, 281]. Therefore, structure-induced variations in the SF rate as observed between the two TET polymorphs [230] are expected to be significantly less pronounced. Furthermore, the structural changes are also much smaller compared to those in PEN:PIC blends (≈ 0.3 Å [52]).

6.2 Optical characterization

Absorbance spectra of TET:6PH and TET:PIC blends are shown in Fig. 6.5. With decreasing TET concentration, a shift of the TET absorption to higher energies is observed in both cases, and accompanied by a decrease in the DS and the intensity of the lower Davydov component. Such a behavior has been observed before in PEN:spacer blends [52, 104] and is again consistent with the formation of a solid solution in the blends.

PL spectra of TET:6PH and TET:PIC blends are shown as filled areas in Fig. 6.5. The PL spectra are extracted from TRPL spectroscopy measurements discussed later on, and correspond to the spectral distribution of all photons emitted until a time difference of 100 ns after photoexcitation. The PL spectrum of neat TET is consistent with previous reports [206] and exhibits a broad peak at 2.32 eV as well as a shoulder at lower energies that has been assigned to a 0-1 vibronic transition [206]. The PL spectra of the blends at low TET concentration (2 % TET concentration for TET:6PH, 9 % TET concentration for TET:PIC) exhibit a narrow peak at 2.52 eV as well as a more pronounced 0-1 vibronic transition. This indicates that the emission of monomeric TET molecules (TET molecule only surrounded by spacer molecules) dominates in these blends. The PL spectra of

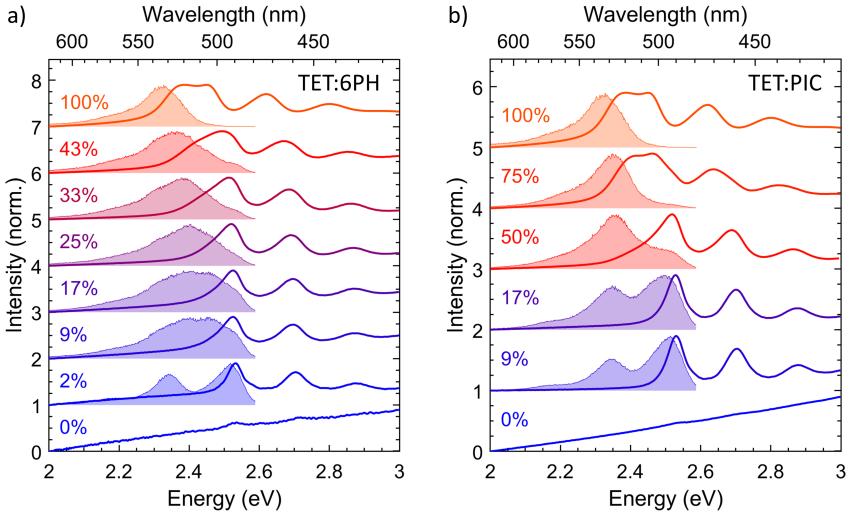


Figure 6.5: Thin film absorbance (solid lines) and quasi-steady-state PL (filled area) of TET:6PH (a) and TET:PIC (b) blends. The PL intensity is the integrated emission until 100 ns. Data published in Ref. 271.

TET:6PH blends at higher TET concentration are broad and featureless, indicating a superposition of PL spectra of a variety of emitting species. For TET:PIC blends at higher TET concentration (17 % and 50 %) the PL spectra appear to be a superposition of mainly two contributions with a similar PL spectrum to monomeric and neat TET.

In order to investigate the composition of the PL spectra of TET:6PH and TET:PIC blends in more detail they have been fitted with a superposition of five spectra, corresponding to the emission spectra of different LECs, see Fig. 6.6a-c. For this fit the PL spectra are assumed to be composed of PL spectra of five different LECs of a TET molecule in the HB aggregate (see Sec. 2.2 and the insets in Fig. 6.6c), namely those with no TET neighbor (LEC_0, monomeric TET), one to three TET neighbors, as well as four TET neighbors (LEC_4, bulk TET). The experimental PL spectra of the blends are therefore fitted with a superposition

$$\begin{aligned} I_{\mathrm{PL}}(c,E) = A_0(c)\cdot I_0(E) \;+\; A_4(c)\cdot I_4(E) \;+\; A_1(c)\cdot I_4(E-\Delta E_1) \\ +\; A_2(c)\cdot I_4(E-\Delta E_2) \;+\; A_3(c)\cdot I_4(E-\Delta E_3) \end{aligned}$$

with the TET fraction c, the PL spectrum $I_n(E)$ of LEC_n (n TET neighbors of a TET molecule), the amplitudes A_n as well as spectral shifts E_n. The PL spectra of the LECs with one to three TET neighbors are assumed to have the same spectral shape as those of the TET bulk emission $I_4(E)$ except for spectral shifts ΔE_n as free parameters in the fit routine, see Fig. 6.6c. Based on the small structural changes observed between the blends, the shifts are assumed to be independent of the TET concentration. Hence, each LEC_n is assumed to exhibit the same photophysics in the different blends, including the same SF rate examined later on. Furthermore, the spectral shifts are restricted in the

fit to keep their relative spectral ordering ($\Delta E_1 < \Delta E_2 < \Delta E_3 < 0$). The results of these decompositions are shown in Figs. 6.6a and 6.6d for TET:6PH and in Figs. 6.6b and 6.6e for TET:PIC. Clearly, the relative contribution of the five emitting species is varied between the blends. The variation is more continuous in TET:6PH than in TET:PIC, for which in particular the contribution of LEC_2 is weak.

If all LECs of the solid solution would contribute to the experimental PL spectrum of a given concentration with an intensity according to their binomial occurrence ($A_n(c) \propto B_n(c)$, see Sec. 2.2.2), a spectral decomposition as shown in Fig. 6.6f would be expected. However, the LECs are expected to exhibit different SF rates [105], and a large SF rate decreases the probability of emission before SF. This effect reduces the relative number of emitted photons for those LECs with more TET neighbors (faster SF), and a stronger contribution of LECs with few TET neighbors (slower SF) would be expected compared to the binomial distribution.

Surprisingly, the opposite trend is observed for TET:6PH and TET:PIC in Fig. 6.6d and 6.6e, since the contribution of LECs with more neighbors is larger compared to the binomial distribution. This observation can be explained by fast hopping of singlet excitons from LECs with few TET neighbors to those with more TET neighbors [52, 231],

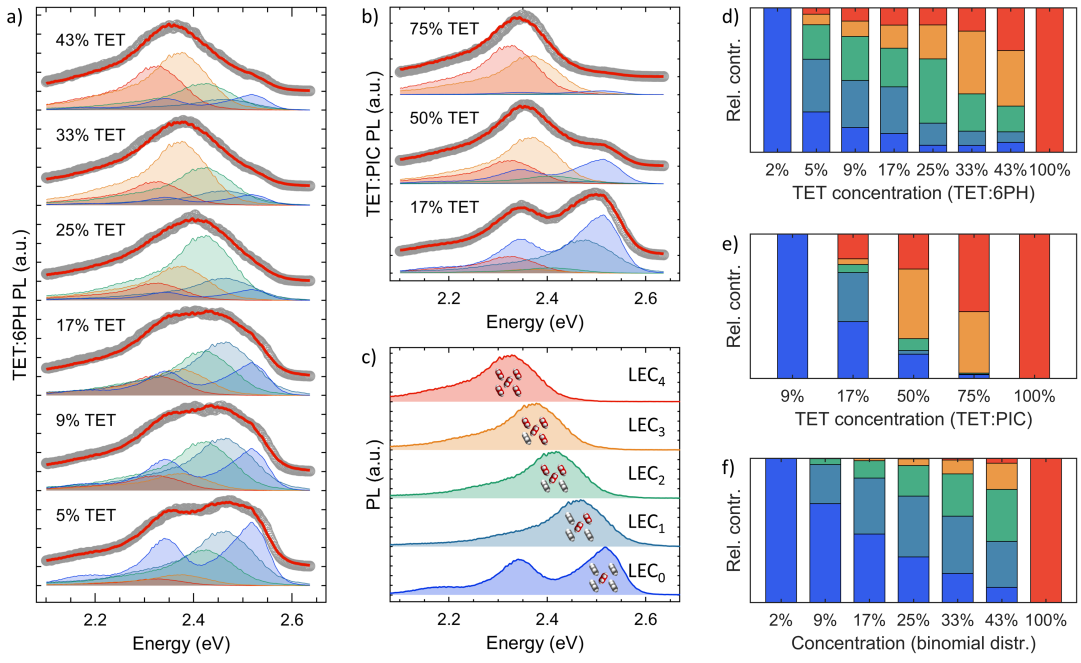


Figure 6.6: Spectral decomposition of the PL spectra shown in Fig. 6.5. a,b) PL spectra (grey) and fits (red) of a superposition of different spectra (colored areas) for a) TET:6PH and b) TET:PIC blends. The single contributions are offset and scaled for better visibility. c) PL spectra used for the superposition, for details see main text. d,e) Relative coefficients of the spectra in the fitted superposition. For a reasonable relative contribution relating the monomer to the bulk spectrum, the spectra have been normalized accounting for areas of gaussians fitted to the main peak of the respective spectrum. Data published in Ref. 271.

which increases the relative contribution to the PL spectrum of the latter. It is, however, important to note that the hopping of singlet excitons does not end at LEC_4 for all TET concentrations but a distribution is observed after this hopping that also includes other LECs. Since the hopping is expected to occur on ultrafast timescales [52], the SF rate at different LECs can be investigated by time-resolved measurements.

To conclude on the structural and optical characterization, TET forms a solid solution in thin films with both 6PH and PIC below a TET concentration of 50 %. The solid solution is concluded from the observation of continuously changing unit cell parameters as well as a continuous change of the position and relative intensity of the two Davydov components in the absorbance spectra. Above 50 % TET concentration, phase-separated TET was observed and indicated limited intermixing for both TET:6PH and TET:PIC [332, 333]. Since limited intermixing can strongly complicate the photophysics of the blends, only the time-resolved measurements on the blends with a TET concentration below 50 % are used for discussion of the effect of a reduced number of nearest neighbors on SF in TET. Quasi-steady state PL spectra could be decomposed into five contributions from the different LECs of TET molecules in the spacer blends. The decomposition showed that hopping of excitons to low-energy sites is present in the blends but does not only result in singlet excitons at LEC_4.

6.3 TRPL spectroscopy

In order to investigate the photophysics of TET:6PH and TET:PIC blends, TRPL spectroscopy has been performed, which is frequently used in literature for studying SF in emissive materials [67, 206, 231, 275, 306]. Since SF rates at different LECs can differ, solid solutions generally exhibit multiexponential population dynamics. In order to investigate what population dynamics can be expected for such samples, simulations are presented in the following before the discussion of the TRPL spectroscopy measurements.

6.3.1 Simulation of the fluorescence decays

The spectral decomposition shown in Fig. 6.6 demonstrated that different LECs contribute to the emission. With a replacement effect (see Sec. 2.4.5), the SF rate $k_{n\geq 0} = \frac{n}{4}\, k_4$ of LEC_n is reduced with respect to the SF rate of LEC_4. Therefore, the overall fluorescence decay is a superposition of fluorescence decays of the single LECs,

$$\mathrm{PL}(c,t) = \sum_{n=0}^{4} C_n(c)\, \mathrm{e}^{-k_n t} \tag{6.1}$$

with the coefficients C_n. Note that these coefficients are different from the amplitudes A_n used for the decomposition of the PL spectra, since long-lived LECs (small k_n) lead to a larger integrated emission intensity and therefore a larger amplitude $A_n \propto C_n/k_n$.

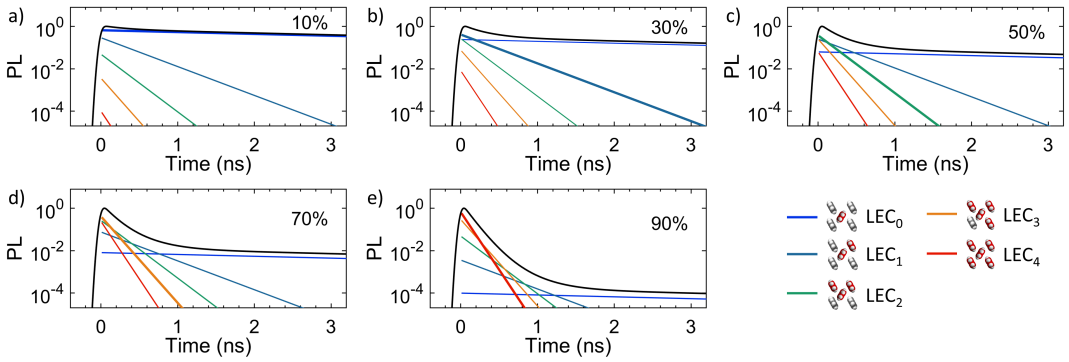


Figure 6.7: Simulations of the overall fluorescence decay based on the superposition of the fluorescence decays of different LECs. The decay time constant of the LECs are linearly scaled between that of bulk TET ($12.5\,\mathrm{ns}^{-1}$ [206]) and monomeric TET ($0.2\,\mathrm{ns}^{-1}$ [270]). The coefficients C_n of the single decays are based on a binomial distribution ($C_n(c) = B_n(c)$, see Sec. 2.2.2) with the respective concentration. The black line is the sum of all single contributions, convolved with a gaussian function with a width of 0.04 ns to simulate an IRF for better comparability to the experimental data.

The overall fluorescence decay was simulated for different TET concentrations based on Eq. 6.1, taking five different LECs with concentration-dependent coefficients C_n into account (Fig. 6.7). In the simulations, the decay rates k_n of the LECs were linearly scaled between that of bulk TET ($12.5\,\mathrm{ns}^{-1}$ [206]) and monomeric TET ($0.2\,\mathrm{ns}^{-1}$ [270]) and their coefficients $C_n(c)$ are based on a binomial distribution $B(c)$ (Sec. 2.2.2). At low TET concentrations (Fig. 6.7a), the intensity of the PL contributions with a fast decay (LECs with a large number of TET neighbors) is too low to significantly contribute to the overall dynamics, and the overall fluorescence decay is almost monoexponential with a decay time constant given by that of the monomeric decay. At high TET concentrations (Fig. 6.7e), Eq. 6.1 yields a multiexponential fluorescence decay, in which both the components with a fast and a slow decay can be observed.

Besides the evolution from a mono- to a multiexponential fluorescence decay with increasing TET concentration, a continuously increasing slope at short times of the fluorescence decay can be observed in the simulations in Fig. 6.7. This slope corresponds to an initial decay rate k_{init} and will be used for a quantitative analysis of the experimental fluorescence decays later on. Therefore, it will be briefly discussed for the simulations in the following.

The initial decay rate k_{init} equals the absolute value of the derivative of the logarithmic fluorescence decay at time zero,

$$k_{\mathrm{init}}(c) = \left| \frac{\partial}{\partial t} \ln(\mathrm{PL}(c, t=0)) \right| = \frac{\sum_{n=0}^{4} C_n(c)\, k_n}{\sum_{n=0}^{4} C_n(c)} = \sum_{n=0}^{4} C_n(c)\, k_n \tag{6.2}$$

and therefore corresponds to the coefficient-weighted average of the decay rates of the five LECs. Note that Eq. 6.2 is valid for any superposition of exponential decays and is not based on any assumptions on C_n or k_n.

The simulations in Fig. 6.7 show how k_{init} is varied with the concentration, since the relative contributions of the LECs are changed. At low TET concentration (Fig. 6.7a), the initial slope is small due to a dominant contribution of LEC_0 (large C_0) in Eq. 6.2. At intermediate TET concentrations, the contribution of LECs with a faster decay lead to an increase of k_{init}, until it is dominated by LEC_4 at high TET concentrations (large C_4). Therefore, the simulations illustrate that the initial fluorescence decay rate k_{init} is dominated by the SF rate of the LEC with the largest coefficient C_n. Therefore, k_{init} is used in the data analysis of the following experimental fluorescence decays to examine the SF rate of the dominant LEC in each blend.

6.3.2 Experimental fluorescence decays

Fluorescence decays obtained by TRPL spectroscopy measurements on the TET:6PH and TET:PIC blends are shown in Fig. 6.8. Neat TET exhibits a sub-nanosecond initial decay, followed by a longer-lived tail that decays on the order of tens of nanoseconds. These two contributions have been assigned to emission of photoexcited singlets before SF and after triplet fusion, respectively, and thus are prompt and delayed fluorescence (see Sec. 3.3.2) [206]. Since the triplet fusion rate depends on the spin-states of the triplet-pair the delayed fluorescence is magnetic-field dependent [82], see Apx. C.1.

In blends with a low TET concentration a fluorescence decay is found that is almost monoexponential over tens of nanoseconds. Since in these blends almost all TET molecules are isolated by spacer molecules and cannot undergo SF, this decay corresponds to the

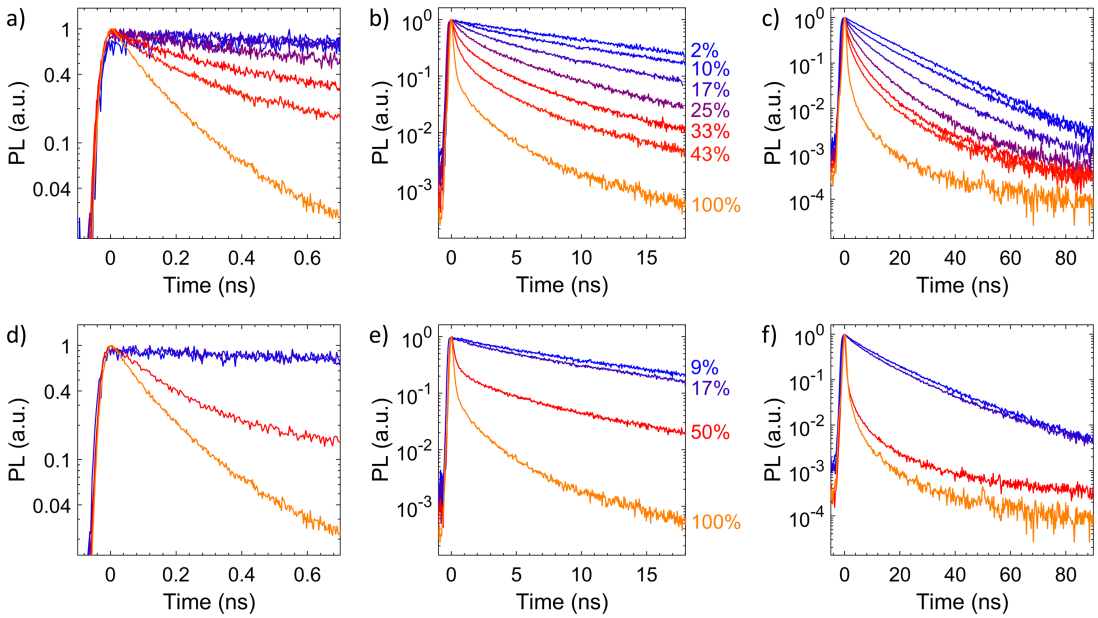


Figure 6.8: Fluorescence decays obtained by TRPL spectroscopy measurements on TET:6PH (a-c) and TET:PIC (d-f) blends with different time-windows. The percentages shown in panel b) and e) are the TET concentrations of the blends and analogously apply to the other panels of each row. Data published in Ref. 271.

decay of singlet excitons due to radiative decay, ISC and IC and is therefore not magnetic-field dependent (see Apx. C.1). The fluorescence decays of blends with intermediate TET concentration exhibit a multiexponential decay similar to that of neat TET, but with an enhanced long-lived tail. Magnetic-field effects (Apx. C.1) are found to decrease with decreasing TET concentration, which indicates that the enhanced long-lived tail in the blends originates rather from emission of monomeric TET (LEC_0, as observed in the spectral decomposition in Fig. 6.6) than from enhanced triplet fusion [105].

If only TET monomers would lead to a long-lived fluorescence and all other LECs would undergo SF as fast as neat TET, one would expect a superposition of a very fast decay due to SF and a very slow decay stemming from monomers. For the blends with intermediate TET concentration, however, a clear difference from such a superposition can be observed, since the fast, initial decay (Figs. 6.8a and 6.8d) exhibits a decreased slope, as discussed for the simulations in Fig. 6.7. According to Eq. 6.2, the initial decay rate k_{init} is mostly determined by the component with the largest coefficient C_n. Since the spectral decomposition in the previous section (Fig. 6.6) provided strong indication that for different blends, different LECs exhibit the largest C_n, the decrease of k_{init} can only originate from different decay rates k_n of singlets at different LECs (LEC_1 to LEC_4).

6.3.3 Analysis of the initial decay rate

For a quantitative analysis of $k_{\mathrm{init}}(c)$, an exponential function has been fitted to the short times in Figs. 6.8a and 6.8d, as shown in Fig. 6.9a. A quantitative analysis of the later times is difficult due to the unknown impact of triplet fusion in the blends with high TET concentration. A kinetic fit accounting for both, SF and triplet fusion rates as established for homogeneous films in literature [269, 275, 306] would be highly complicated here, since the different LECs with different kinetic rates and hopping via energy transfer between the LECs would need to be included. In Ref. 231 a kinetic model for disordered systems is presented, which, however, includes only two LECs, of which one is incapable of undergoing SF and can only transfer energy to the other LEC. For a system with five LECs, of which four are capable of SF, a much more complex model would be required. Such a model would be interesting, also in view of the triplet fusion rates of the different LECs, but is beyond the scope of this study.

Fitting only the initial decay as shown in Fig. 6.9a is frequently applied in literature for determination of SF rates [67, 105, 206]. In particular the singlet decay rates in Ref. 105, to which the results of this work will be compared later on, have been determined only by the initial decay rate. In this publication [105], the measured fluorescence decays are not shown but it is referred to a study on fluorescence decays of neat TET single crystals [217]. There, excitation pulses with $\approx 10\,\mathrm{ps}$ full width at half maximum (FWHM) as well as a monoexponential fit of the fluorescence decay until 300 ps are used to evaluate the SF time constant, which results in a similar analysis like in the present work to obtain $k_{\mathrm{init}}(c)$.

The fit results of k_{init} of the different blends are shown in Fig. 6.9b. As mentioned before, investigations of blends at TET concentrations higher than 50 % were impeded by the limited intermixing of the compounds. The two systems, TET:6PH and TET:PIC show very similar dynamics. For the blends with 50 % TET concentration k_{init} is approximately half the SF rate of bulk TET. Towards lower TET concentration, it dramatically decreases until the fast, initial decay that is significantly different from the monomeric decay rate can no longer be observed below 20 % TET concentration.

This behavior of $k_{\text{init}}(c)$, including the decrease from neat TET to 50 % TET concentration as well as the dramatic drop to 20 % TET concentration, is discussed in the following with regard to the physical origin described by Eq. 6.2. SF does not occur for monomeric TET, and the fluorescence rate (see Sec. 3.3.2) of monomeric TET can be taken from the blends at low TET concentration ($k_0 = 0.077 \pm 0.005$ ns, $1/k_0 = 13 \pm 1$ ns in both systems). This monomeric decay is significantly slower than reported singlet lifetimes of dissolved TET (3.8 – 4.8 ns [269, 270, 334]). However, the singlet lifetime of dissolved TET originates to a large extent from fast ISC [270], which can be expected to slow down in aggregates [67, 177]. Indeed, subtracting the ISC rate given in Ref. 270 from the fluorescence decay rate in Ref. 270 results in a singlet lifetime of 11.2 ns, which is not only close to the monomeric decay found in this work, but also to the 11.6 ns singlet lifetime found for a dissolved TET derivative [335]. Since the monomeric rate is a constant contribution for all blends, it has been subtracted from all other k_{init} in Fig. 6.9b and is neglected in the following models.

Without a replacement effect, it is $k_{n\neq 0} = k_4$ and for a binomial distribution ($C_n(c) = B_n(c)$, see Sec. 2.2.2), Eq. 6.2 yields a curve of $k_{\text{init}}(c)$ that exhibits much faster initial decays, see upper grey line in Fig. 6.9b. This model describes the impact of monomeric TET ($k_0 = 0$) on $k_{\text{init}}(c)$. The strong deviation of experimental values from

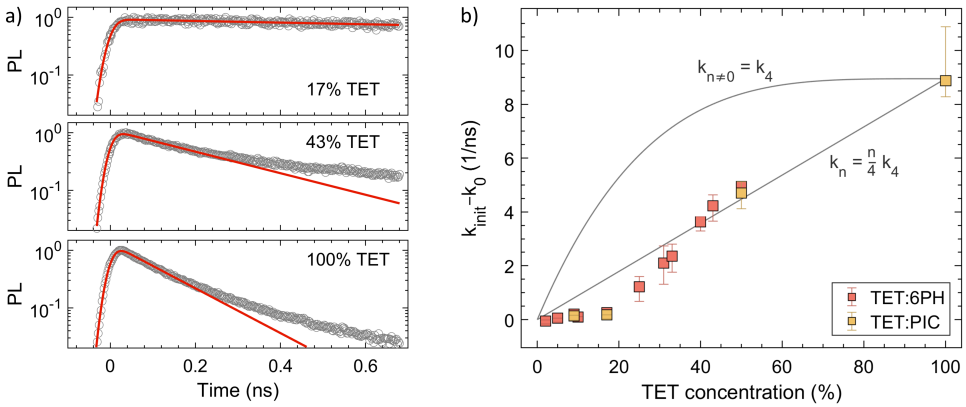


Figure 6.9: Examples of fitted functions (a) and comparison of resulting decay rates (b) of the initial fluorescence decays. The fitted functions are monoexponential functions convolved with a gaussian IRF. The decay rate of monomeric TET in panel b) has been subtracted from all other data points. Data published in Ref. 271.

this model shows that other LECs contribute significantly to the decrease of k_{init}, i.e. it is $k_{n\geq 0} < k_4$.

With an ideal replacement effect, it is $k_n = \frac{n}{4}\, k_4$. In this case, the initial decay rate (Eq. 6.2) is for a binomial distribution

$$k_{\text{init}}(c) = \sum_{n=0}^{4} B_n(c)\, k_n = \frac{k_4}{4} \sum_{n=0}^{4} \binom{4}{n} \cdot c^n \cdot (1-c)^{4-n} \cdot n = c \cdot k_4 \tag{6.3}$$

due to the linearity of the expected value of a binomial distribution. Therefore, an ideal replacement effect for binomially distributed excitons leads to a linear decrease of k_{init} with the TET concentration, see lower grey line in Fig. 6.9b. Notably, the simulated replacement effect factors in Ref. 105 are close to the reciprocal of the TET concentration, which confirms

$$\frac{k_4}{k_{\text{init}}(c)} = \frac{1}{c} \tag{6.4}$$

as obtained from Eq. 6.3. This linear model excellently matches the experimentally determined k_{init} around 50 % TET concentration. Around 20 % TET concentration there is a deviation, as the experimental values decrease stronger than the model. Despite the slight remaining deviation, the origin of which will be discussed in the following, this model matches well with the experimentally determined rates and strongly suggests the replacement effect to be primarily responsible for the slower k_{init} in the blends.

6.3.4 Effects in addition to the replacement effect

Finally, effects are discussed that might be responsible for the reduction of the SF rate in addition to the replacement effect ($k_n < \frac{n}{4}\, k_4$) in blends with a low TET concentration.

First, the effect of exciton hopping as observed using the PL spectra might be considered. Due to the lower energy of those LECs with more TET neighbors (see Sec. 2.4.5), the preferential hopping direction is towards those LECs. This shifts the exciton population away from the initial binomial distribution. Since the LECs with more TET neighbors also exhibit higher SF rates, k_{init} should increase with exciton hopping, i.e. the experimental k_{init} would be expected to lie above theoretically calculated values. Similarly, the reduced SF endothermicity due to the shift of S_1 to higher energies in the blends (see Fig. 6.5) should lead to larger SF rates. Since the opposite is observed and experimental values tend to be smaller than the theoretical models, both the exciton migration and the altered SF energy balance can be excluded to be responsible for the SF rates smaller than $k_n = \frac{n}{4}\, k_4$ of some LECs.

Second, the SF rates smaller than $k_n = \frac{n}{4}\, k_4$ of some LECs might be explained by altered electronic state characters and couplings due to the slightly altered unit cell parameters [52] and altered state energies such as the increased energy observed for S_1 in the blends (Fig. 6.5). In particular the CT-character of S_1, which is connected to the DS in

acenes [195, 196], has been found to be reduced in spacer blends with PEN [52]. A similar, but less pronounced, decrease of the CT-character is observed for TET:spacer blends (see Apx. C.2) and might be the origin of the additional reduction of the SF rate in blends with low TET concentration [196] besides the replacement effect.

To conclude on the experimental observations on TET:6PH and TET:PIC blends, TRPL spectroscopy on the blends revealed a strongly decreased initial singlet decay rate, which has been used as an experimental handle for quantitative analysis of the SF rate. A stronger decrease of k_{init} in the blends than expected from the impact of TET monomers (Fig. 6.9b), as well as the approximately linear decrease of k_{init} indicated that the replacement effect is primarily responsible for the observed behavior, although deviations below 30 % TET concentration indicated the presence of other influences such as a reduced CT-character of S_1 [52, 95, 153, 196].

6.4 Comparison to previously reported spacer blend systems

To the best of the author's knowledge, three studies on the concentration-dependent SF rate in other spacer blends have been reported before [52, 105, 210, 275], which will be compared in the following to the results of the present work.

In Ref. 105, a slower fluorescence decay was obtained in TET single crystals by doping with up to 50 % spacer material. The spacer molecules were anticipated to act as reflectors for triplets created by SF and to restrict geminate triplets to closer proximity compared to neat TET. This triplet exciton caging enhances the triplet fusion rate which slows down the fluorescence decay by back-donation of population to the singlet state. The singlet decay rate measured in Ref. 105 was found to decrease more strongly with increasing spacer concentration than expected from the replacement effect, and the authors assigned this observation to enhanced triplet fusion leading to a longer fluorescence lifetime. However, recent studies on triplet fusion in TET indicated a rate of $k_{\mathrm{tf}} \approx 0.1\,\mathrm{ns}^{-1}$ [82], which is two orders of magnitude slower than SF. This makes an impact of the triplet fusion rate on k_{init} as proposed in Ref. 105 unlikely. In the present work, this can be further substantiated by the before discussed magnetic field effect on the fluorescence decay. A pronounced effect would be expected if the triplet fusion rate increased due to triplet caging, which is not observed in the data (see Apx. C.1). This gives further evidence that the impact of triplet fusion on k_{init} can be neglected. Nevertheless, the observed decrease in the singlet decay rate in Ref. 105 as well as the proposed impact of the replacement effect are largely consistent with the results of the present study.

In Ref. 275, TRPL measurements on amorphous thin film blends of RUB and several spacer materials with RUB concentrations below 50 % are reported and analyzed using a kinetic model. In this model a homogeneous sample with uniformly distributed RUB

molecules is assumed and the impact of increasing average distance between the molecules is investigated. The SF rates of the samples are found to decrease with decreasing RUB concentration and with increasing average distance similar to the replacement effect observed here. The amorphous nature of the samples in Ref. 275, however, does not lead to a replacement of nearest neighbors but rather a continuous increase in their distance. Thus, the systems investigated in Ref. 275 provide a complementary aspect compared to the data of this work, in which intermolecular distances are almost constant and the change in the SF rate is dominated by the replacement effect.

In Ref. 52, blends of PEN with PIC as spacer molecule have been investigated, which form solid solutions like the systems of the present work. The focus of this study was laid on the impact of the increase of intermolecular distances due to an expansion of the unit cell on the SF rate. Calculations on the expected impact of this expansion yield a dramatic decrease in the SF rate. However, experimentally, a SF rate was found that was almost independent of the PEN concentration. The discrepancy between calculations and experiment was explained by ultrafast hopping of excitons to low-energy sites in the crystal at which SF is as fast as in neat PEN [52], compare the hot-spot mechanism (Sec. 2.4.5). It is interesting to note that this hot-spot mechanism is also present in TET:spacer blends (see Sec. 6.2), but a fundamentally different behavior of the SF rate is observed. While the SF rate in TET:spacer blends decreases with the number of nearest neighbors, it is almost independent of this number in PEN:spacer blends. One possible explanation for this observation is that the exciton hopping rate in PEN is much larger than in TET. This would allow the majority of excitons to reach sites with four nearest neighbors (LEC_4), independent of the concentration of PEN molecules, before they undergo SF. However, the SF rate of neat PEN is three orders of magnitude larger than the SF rate of neat TET, giving an exciton in PEN on average three orders of magnitude less time to reach LEC_4 than in TET. Thus, in order to explain the robustness of SF, the exciton hopping rate would have to be significantly larger in PEN than in TET, which is unlikely based on the similarity of the investigated systems [336]. It is more likely that also in PEN LECs with numbers of nearest neighbors ranging from 1 to 4 contribute to the SF and that the relative weight of a given LEC contribution changes with the mixing ratio as it does in TET blends. Importantly, the fact that the SF rate is independent of the mixing ratio then indicates that the number of nearest neighbors has no impact on the SF rate in PEN. This hints towards a fundamental difference between the mechanisms of SF in TET and PEN, which motivated theoretical calculations on model systems. These calculations were performed by Prof. R. Tempelaar (Northwestern University, USA) and Prof. D. R. Reichman (Columbia University, USA) and are compared to experimental data in the following.

6.5 Calculations on the impact of vacancies on singlet fission in acenes

In order to investigate the different behavior of TET and PEN in spacer blends, calculations on model systems have been performed by Prof. R. Tempelaar (Northwestern University, USA) and Prof. D. R. Reichman (Columbia University, USA). For the calculation of SF rates, 2x2 supercells of PEN and TET (8 molecules) with periodic boundary conditions were used [71, 337]. Investigation of the effect of the number of nearest neighbors was achieved by taking out one to four molecules of this supercell, as depicted in Fig. 6.10. The molecules were taken out by maximizing the distance between the vacancies, which means that for the configuration with only four remaining molecules in the supercell, each unit cell contains only one molecule (Fig. 6.10). Since zero to four molecules can be taken out of the supercell with this model, five different systems were calculated. For comparison of the calculated SF rates to experimental SF rates, the average number of nearest neighbors n_{AvNN} (see Sec. 2.2.2) is used. This number is 4, 3.429, 2.667, 1.6 and 0 for the five calculated systems (see Fig. 6.10), and four times the concentration for solid solutions due to the linear expectation value of binomial distributions (see Sec. 2.2.2).

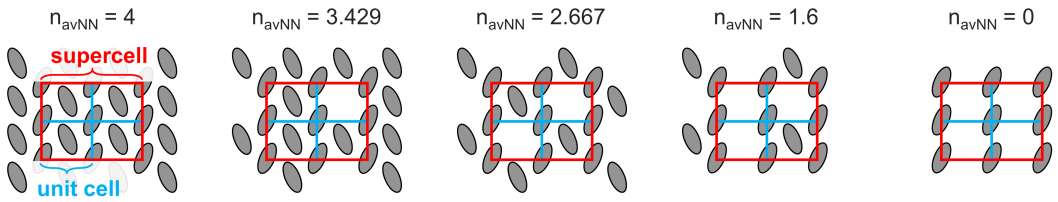


Figure 6.10: Sketch of the configurations, for which calculations have been performed. n_{avNN} is the average number of translationally inequivalent nearest neighbors of remaining molecules in the 2x2 supercell. For example, $n_{\mathrm{avNN}} = 1.6$ is calculated by (1+1+1+1+4)/5.

The time-dependent population (dynamics) of ^{1}(TT) states was calculated using Markovian Redfield theory in the secular approximation as described in Ref. 337 and is shown for the five systems in Fig. 6.11a. Two parameters were extracted from each dynamics, first, the initial (coherent) ^{1}(TT) population at time zero, and second, the SF rate obtained from a fit of an exponential function to the dynamics. These extracted parameters are shown in Fig. 6.11b in the upper and lower panel, respectively. The behavior of these two parameters with varying concentration are compared to each other and to the replacement effect.

The calculations show that the vacancies in the PEN supercell lead to a fluctuating initial ^{1}(TT) population around 12 %. The SF rate exhibits the same fluctuations and does not show a linear decrease as expected from the replacement effect. On the contrary, the initial ^{1}(TT) population in the TET supercells is much weaker on the order of 1 % and slightly increases with decreasing TET concentration. The calculated SF rates are close to the expected linear decrease from the replacement effect and exhibit a completely opposite trend compared to the initial ^{1}(TT) population.

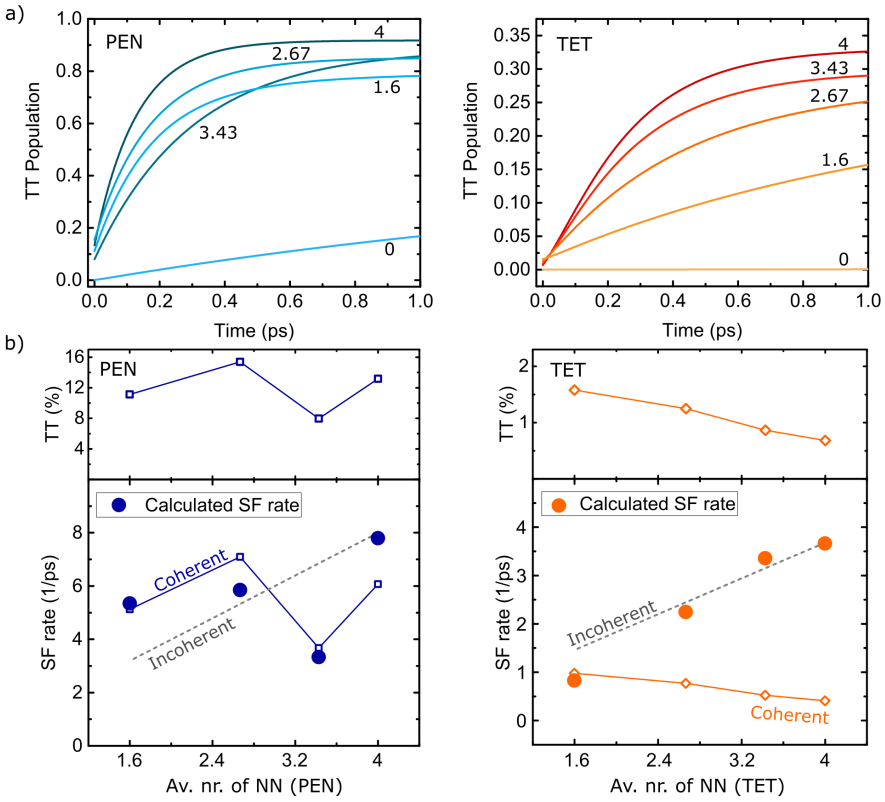


Figure 6.11: Calculations performed by Prof. R. Tempelaar (Northwestern University, USA) and Prof. D. R. Reichman (Columbia University, USA). a) Population of the ^{1}(TT) state calculated for different n_{AvNN} (labels at each line) of PEN (left) and TET (right). b) Extracted parameters (coherent TT contribution and SF rate) from the dynamics in panel a). The SF rate is a fit of an exponential function to each dynamics. The coherent TT contributions are the population of ^{1}(TT) at time zero and are arbitrarily scaled and labeled *Coherent* in the lower panel of (b). The dotted line labeled *Incoherent* in the lower panel is the expected decrease from the replacement effect (Eq. 6.3). Modified from Ref. 271.

These calculations support several conclusions. In PEN, the coherent ^{1}(TT) contribution is directly related to the SF rate, while in TET it is clearly not. This relation demonstrates that the SF mechanism in PEN is coherent, but is incoherent in TET. Notably, this identification of an (in)coherent SF process in calculations would not be that straightforward without the calculated vacancy-dependence. Another important finding is that the coherent ^{1}(TT) contribution, and therefore the SF rate in PEN, is not sensitive to the introduction of vacancies but rather fluctuates due to other effects (see Sec. 2.4.5). In TET, however, for which SF is incoherent, the SF rate follows a linear decrease that represents the replacement effect. It is further noteworthy that the calculated SF rate in TET decreases faster with decreasing average number of nearest neighbors than expected from the replacement effect, which might relate to the strong decrease between 40 % ($n_{\mathrm{AvNN}} = 1.6$) and 20 % ($n_{\mathrm{AvNN}} = 0.8$) concentration in the experimental data in Fig. 6.9b. However, the method, by which the vacancies are introduced (see Fig. 6.10) does not allow to examine if this trend continues for $n_{\mathrm{AvNN}} = 1.6$ and $n_{\mathrm{AvNN}} = 0$.

6.6 Discussion

The different sensitivity of SF to the spacer concentration in TET:spacer and PEN:spacer blends, as observed in the present work and a previously reported study [52], respectively, can be explained based on the calculations discussed in the previous section.

SF in PEN is known to occur via a coherent mechanism (see Sec. 2.4), which means that strong coupling between the FE and ^{1}(TT) state leads to an admixture of ^{1}(TT) to the photoexcited S_1 state and SF occurs from dephasing of this superposition [50, 293]. The coherent mixing is observed in the calculations in Fig. 6.11 as the instantaneous ^{1}(TT) population, and occurs in PEN by vibronic coupling between a vibrationally excited ^{1}(TT) state (called TT* or T*T, see Fig. 6.12a) and S_1 without vibrational excitation [26, 71].

Since the SF rate of PEN is directly connected to the admixture of ^{1}(TT) states to S_1 [50, 293], the observed insensitivity of the initial ^{1}(TT) contribution against vacancies in Fig. 6.11 leads to a robust SF regarding the PEN concentration in spacer blends, as observed experimentally in Ref. 52. This insensitivity can be rationalized since the fate of the singlet exciton is already determined by the photoexcited ^{1}(TT) admixture. The coherent SF process is not a stochastic transition to any target state (see Sec. 2.4.4), but the target state is predetermined upon photoexcitation. As a direct consequence, a lower number of PEN neighbors of the photoexcited LEC does not decrease the SF rate as long as at least one of its neighbors is a SF molecule (Fig. 6.13a).

The SF mechanism in TET has been extensively discussed in the last years [56, 57, 59, 64, 67, 70, 206]. The calculations in Fig. 6.11 support an incoherent SF process (see Sec. 2.4) in TET [67], since the SF rate does not follow the concentration-dependence of the weak instantaneous ^{1}(TT) population. The incoherent SF mechanism is a stochastic transition to another PES after several attempts (Fig. 6.12b). Therefore, upon creating vacancies, or, analogously, replacing TET molecules by spacer molecules in the blends, the

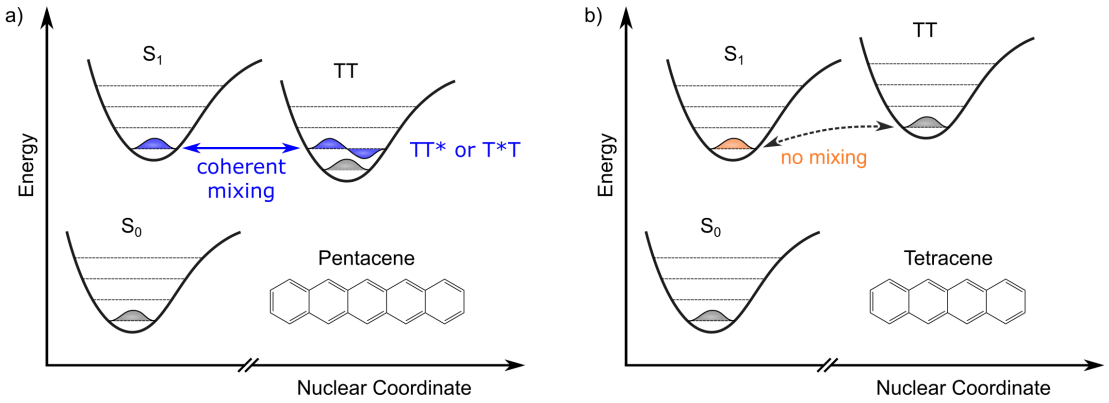


Figure 6.12: SF mechanisms in a) PEN and b) TET. Coherent mixing between the vibrational ground state of S_1 and a vibrationally excited state of ^{1}(TT), called TT* or T*T, leads to the coherent SF mechanism in PEN. In TET, no such mixing is possible due to the endothermicity of the SF process. Modified from Ref. 271.

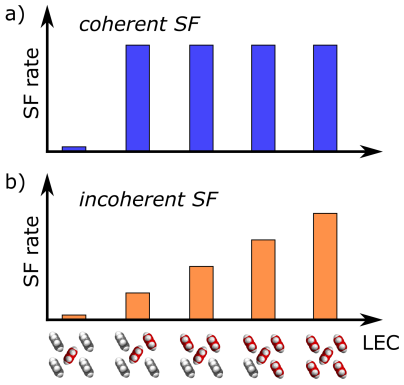


Figure 6.13: SF rates of different LECs depending on the SF mechanism. a) Coherent SF with a SF rate that is independent of the LEC as long as at least one neighbor is a SF molecule. b) Incoherent SF with a SF rate that scales linearly with the number of SF molecules as nearest neighbors. In both cases, the SF rate is zero if there is no SF molecule as nearest neighbor. The LECs shown at the coordinate of panel (b) also apply to panel (a).

replacement effect decreases the SF rate (Sec. 2.4.5 and Fig. 6.13b). A possible reason for the faster decrease than expected from the replacement effect observed both in experiment and theory might be the decreasing CT character of S_1 that leads to a reduced SF rate even between the remaining molecules [52, 94, 196]. A reduced CT character upon reducing the cluster size was also observed in recent calculations on PEN [95]. Taking molecules out of the cluster can be anticipated to lead to a similar effect for TET. This decrease of CT character might reduce the coupling between S_1 and ^{1}(TT) and thus contribute to the decreasing SF rate in addition to the replacement effect.

As prototypical, directly comparable systems, TET:spacer and PEN:spacer blends showed in combination with calculations of model systems that the coherent and incoherent SF mechanisms exhibit a different sensitivity to the replacement of nearest neighbors of a given SF molecule. Notably, although the two chosen SF compounds are prototypical compounds for exo- and endothermic SF, their different behavior does not originate from the energy balance, but from the SF mechanism. Therefore, for example, for RUB [60, 96] and a well-know derivative of TET [65], in both of which SF is endothermic (see Sec. 4.3), but a contribution of a coherent mechanism has been observed, no replacement effect on the SF rate would be expected. On the contrary, for hexacene [61], in which the SF process is partially incoherent although the energy balance is highly exothermic, a reduced number of nearest neighbors should reduce the SF rate.

6.7 Comparison with anthradithiophene blends

The above finding that only incoherent SF processes are sensitive to vacancies has motivated a study on spacer blends with ADT, for which a SF rate has not yet been reported, but which should exhibit SF energetics in between those of TET and PEN, see Sec. 4.3. Therefore, ADT:6PH blends were grown with the aim to investigate if the SF rate in these blends decreases as observed for TET, or if it is robust against the introduction of spacer molecules as observed for PEN [52].

The structural and optical characterization of ADT:6PH blends is shown in Fig. 6.14. ADT exhibits a broad (002) BP (Fig. 6.14a) that might originate from two different

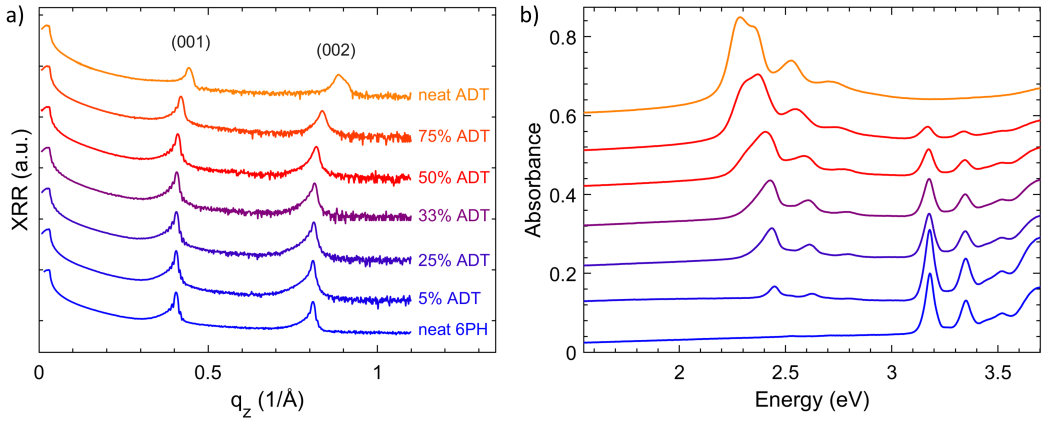


Figure 6.14: XRR data (a) and UV-Vis absorbance spectra (b) of ADT:6PH blends. In both panels the curves are offset for better visibility. The legend in a) also applies to b).

polymorphs. With increasing spacer concentration the BP becomes more narrow and shifts continuously towards lower q_z consistent with the longer 6PH molecule compared to ADT. Since no contributions from neat phases are present in the blends, XRR indicates complete intermixing of the two compounds and no limited intermixing as observed for the TET:spacer blends. In the absorbance spectra (Fig. 6.14b) the 6PH absorption bands above 3 eV only decrease in intensity in the blends, but the absorption band around 2.4 eV, corresponding to the $S_0 \rightarrow S_1$ transition of ADT, exhibits pronounced changes. In agreement with the spectral changes of TET:6PH and other spacer blends reported earlier [52, 104], the energetically lower Davydov component loses intensity and shifts to higher energies. This observation is in agreement with the shifting BP in XRR and provides evidence that the ADT:6PH blends are solid solutions.

TCSPC data and steady-state PL spectra of ADT:6PH blends are shown in Fig. 6.15. The steady-state PL spectrum of ADT exhibits two peaks, a narrow one at 2.24 eV and a broad one at 1.99 eV. Due to its energetic proximity to the lowest absorption peak of ADT at 2.28 eV, the former PL peak likely corresponds to bulk emission of ADT in analogy to TET [206]. The latter PL peak might be emission of formed excimers [92, 186] (and is called excimer emission in the following), but a detailed investigation of this emission is beyond the scope of this study. In the blends, the excimer emission becomes weaker with respect to the bulk emission until a pronounced vibronic 0-1 transition is visible for 5 % ADT, indicating the emission of isolated molecules. The TCSPC data of neat ADT and blends with ADT concentrations above 33 % exhibit fast initial decays and a long-lived contribution that might originate from triplet fusion. In the blends with 33 % and 25 % ADT concentration the initial decay rate is strongly decreased and the decay becomes almost monoexponential at 5 % ADT.

Only fits of a sum of three exponential functions (tri-exponential fits) to the TCSPC decay curves (black lines in the panels of Fig. 6.15) have been found to satisfactorily describe the TCSPC data. A fit of a gaussian function to the rising edge of the IRF

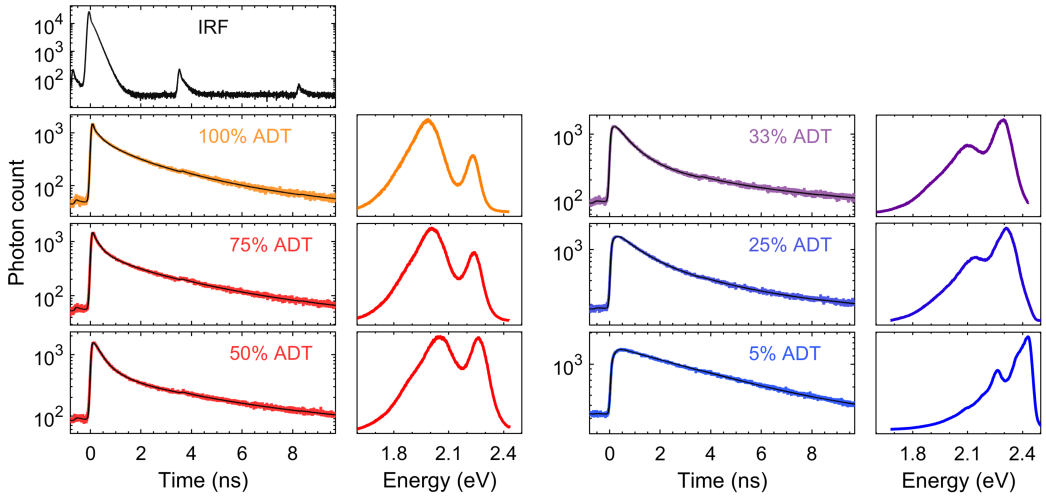


Figure 6.15: TCSPC and steady-state PL on ADT:6PH blends. For each blend the TCSPC decay curve (left) and a steady-state PL spectrum (right) are shown. The solid black line in the TCSPC-panels are tri-exponential fits to the data. The two measurements were performed at the same spot of the sample (Sec. 3.3.2). Note that the spectral shape of the PL spectrum of 5 % ADT concentration might be affected at high photon energies by the filter of the excitation at 2.64 eV.

(see topmost panel in Fig. 6.15) yields a FWHM/2 of 45 ps, see Apx. C.3. The falling edge of the IRF, however, differs significantly from a gaussian function, which makes the convolution with the experimentally determined IRF (instead of an ideal gaussian function as used for TRPL spectroscopy before) necessary in these fits.

The resulting time constants of these fits are shown in Fig. 6.16. Neat ADT exhibits a decay rate of the dominant component (largest amplitude) of approximately 25 ns^{-1}, which corresponds to a time constant of 40 ps. Since this singlet decay rate is much higher than typical rates for IC or ISC it is assigned to SF in ADT and the slow component to delayed fluorescence from triplet fusion in analogy to the fluorescence decay in TET [206]. With decreasing ADT concentration from 100 % to 30 %, the decay rate of the dominant, faster component decreases approximately linearly, see the grey line in Fig. 6.16. At 25 % ADT concentration the fast and slow components have similar amplitudes and their amplitudes swap for 5 % ADT concentration, for which the slow component dominates with a time constant of 4.5 ± 0.3 ns. In the discussion of TET:spacer blends the SF rates have been analyzed using the initial fluorescence decay rate of TRPL spectroscopy measurements. The analogon of k_{init} is here the highest rate obtained from the fits of tri-exponential functions (blue markers in Fig. 6.16), independent of its intensity.

Below 30 % ADT concentration, the largest decay rate does not further decrease but stagnates around 7 ns^{-1} (140 ps). This observation differs from the TET:spacer systems but is likely related to the different employed technique and analysis. In particular the non-gaussian falling edge of the IRF leads for long-lived components to an (artificial) increase of the emission intensity withing the first hundreds of picoseconds (see Apx. C.3).

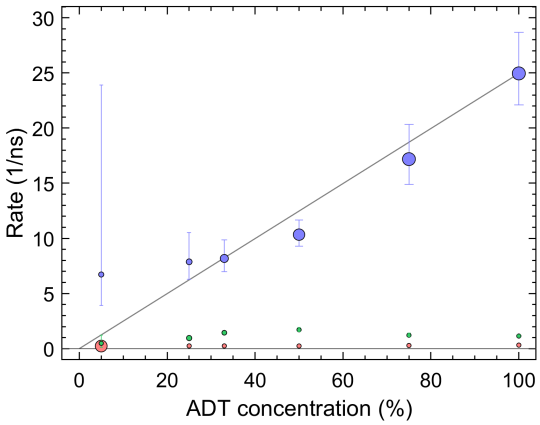


Figure 6.16: Decay rates obtained from tri-exponential fits to the TC-SPC data on ADT:6PH blends (see Fig. 6.15). The marker size corresponds to the relative amplitude of the respective component. A minimum marker size prevents a complete disappearing of markers.

The fast decays with low amplitudes at low ADT concentrations are superimposed with this artificial increase due to the long-lived components. The superposition might lead to systematic uncertainties exceeding the statistical uncertainties shown in Fig. 6.16. Therefore, an interpretation of the large decay rates below 30 % ADT concentration would require measurements with a higher time-resolution, which are beyond the scope of this work. Importantly, however, the relative amplitude of the fast components at higher ADT concentrations are sufficiently large to dominate over the artificial increase due to long-lived components (see Apx. C.3) and the linear decrease of SF rates above 30 % ADT concentration is considered to be trustworthy.

Since SF has not yet been examined in pristine ADT, the timescale of the neat ADT film deserves brief discussion. Using the photon energy of bulk emission of ADT at 2.24 eV and a reported T_1 energy of ADT derivatives of 1.08 eV measured by triplet phosphorescence [308], the SF energy balance of crystalline ADT would be $\Delta E_{\mathrm{SF}} = -80\,\mathrm{meV}$, which denotes a slightly exothermic SF process. A surprisingly slow SF process has been observed before in several ADT derivatives [92, 118, 308, 310–312], which has led to questioning a SF exothermicity [310]. Similarly, SF in pristine ADT occurs with a time constant 40 ps, which is only twice as fast as SF in TET and still more than two orders of magnitude slower than SF in PEN. This observation suggests that the SF process is rather endothermic in ADT [310], and hence that the energy of T_1 in ADT is 1.12 eV or higher.

Regarding the concentration-dependence of the SF rate in ADT:6PH blends, the absence of limited intermixing allowed to examine the complete range of mixing ratios. The linear decrease of the SF rate in ADT:6PH blends with decreasing ADT concentration is reminiscent of the SF rate in TET:spacer blends in Fig. 6.9b and the calculations in Fig. 6.11b. Thus, by revealing a replacement effect for SF in ADT as for SF in TET, the ADT:6PH blends provide indication of an incoherent SF process in ADT.

To conclude this chapter, the impact of a reduced number of SF molecules on the SF rate in spacer blends has been studied for three systems of polycrystalline spacer blends (TET:6PH, TET:PIC and ADT:6PH). In all systems, a pronounced replacement effect

has been found [105], contrasting previous observations of analogous spacer blends with PEN [52]. In combination with calculations on model systems, these findings allowed to conclude that the different concentration-dependence of the SF rate in spacer blends of TET and PEN originates from the different SF mechanisms (incoherent and coherent) in these systems. Most importantly, this demonstrates that spacer blends can serve as a tool to investigate the role of electronic coherences in SF, which were so far only accessible via 2DES.

7. Results III: Singlet heterofission

In this chapter homofission, heterofission and FRET is investigated in blends of PEN and TET in dependence of the mixing ratio and the excitation wavelength. The investigations presented in this chapter have been published in *Angewandte Chemie International Edition* [338]. They have been performed in collaboration with Prof. G. Cerullo's research group, see Apx. F for details on the contributions.

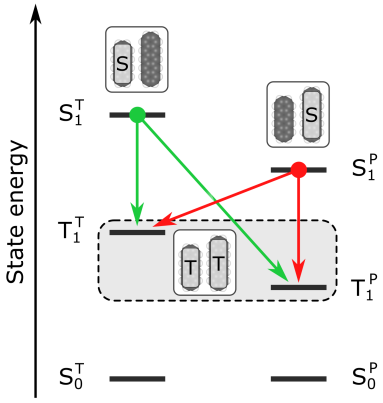


Figure 7.1: Energy level diagram of electronic states of TET and PEN molecules with the two possible heterofission processes, compare Fig. 2.21. The two heterofission processes are the heterofission of TET singlets (green) and the heterofission of PEN singlets (red). Both processes result in the same ^{1}(TT) state (grey dashed box), which is composed of one TET triplet and one PEN triplet. The superscripts T and P denote electronic states of TET and PEN molecules, respectively. Note that the relative state energies are arbitrarily scaled.

In the previous chapter, SF compounds have been mixed with spacer compounds, whose excited states are not involved in the SF process. In this chapter, two SF compounds are mixed in a polycrystalline blend, which opens up the possibility for heterofission [78, 90, 106, 107, 339] as a competing decay channel to homofission. As discussed in Sec. 2.4.5, heterofission describes the creation of two triplets via SF that are located on two chemically distinct molecules rather than on two molecules of the same type, see Fig. 7.1.

Reports of heterofission in literature are in general scarce [23, 78], although it has been found in two different systems involving PEN and TET chromophores [90, 106, 107, 339]. First, intermolecular heterofission has been observed for PEN-doped TET single crystals in the 1970s using magnetic-field dependent steady-state PL spectroscopy [106, 107]. Second, heterodimers of TET and PEN have been synthesized in recent years and intramolecular heterofission could be detected by TA spectroscopy [90, 339].

These studies motivate the investigation of intermolecular heterofission of thin film blends using time-resolved techniques. Therefore, PEN:TET blends have been prepared in this work, with which the impact of several phenomena on the singlet exciton lifetime can

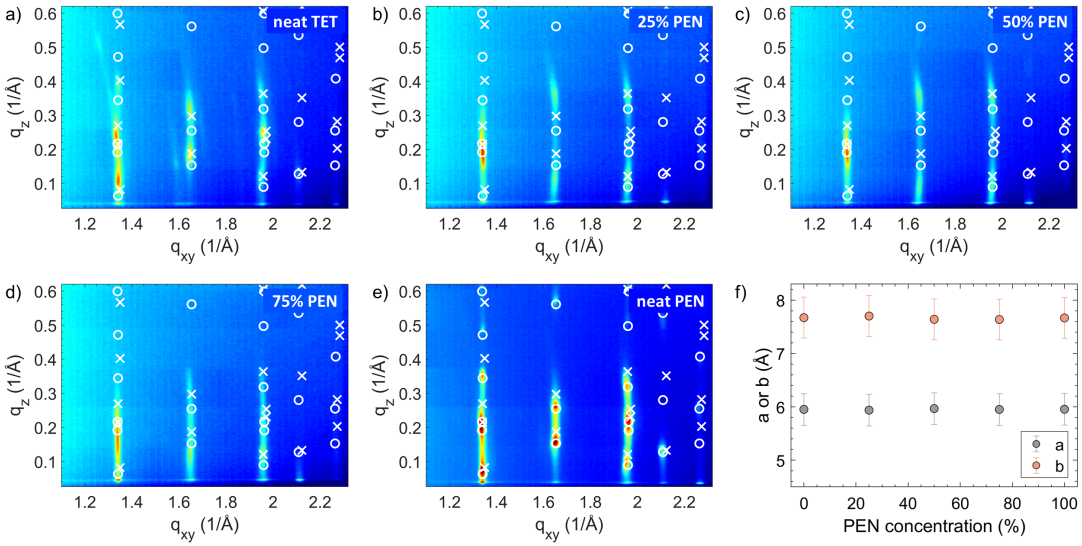


Figure 7.2: a-e) Reciprocal space maps of blends of PEN and TET measured at *Diamond*. For the mixing ratio see the labeling in the respective top right corner. White crosses (circles) correspond to calculated reflections based on the unit cell of the TET [281] (PEN [277]) thin film phase. f) In-plane unit cell parameters calculated from the BP position of the in-plane scattering intensity. Data published in Ref. 338.

be investigated, including homofission, heterofission, energy transfer and the replacement effect (see Sec. 2.4.5).

At low PEN concentrations, the photophysics of the PEN:TET blends should correspond to that of the PEN-doped TET single crystals reported in the 1970s [106, 107] and thus allow to determine the PEN heterofission (red arrows in Fig. 7.1) time constant, which has so far not been reported. With PEN concentrations exceeding the doping level, the competition between homo- and heterofission of PEN singlets, as well as the competition between energy transfer and heterofission of TET singlets (green arrows in Fig. 7.1) can be investigated.

7.1 Structural characterization

Before presenting time-resolved measurements on PEN:TET blends, their structural and optical characterization is briefly discussed in the following. For details on the preparation of the PEN:TET blends for which data is shown in the following, see Tab. E.5. In particular the optical and structural properties have been found to be independent of the film thickness by comparing 20 nm and 80 nm thick films.

Reciprocal space maps of PEN:TET blends measured by GIWAXS are shown in Fig. 7.2. The reciprocal space maps of neat TET (Fig. 7.2a) and neat PEN (Fig. 7.2e) have been discussed before, see Sec. 6.1 and Sec. 5.1, respectively. The reciprocal space maps of all blends are similar to those of neat TET and neat PEN, in particular since the diffraction

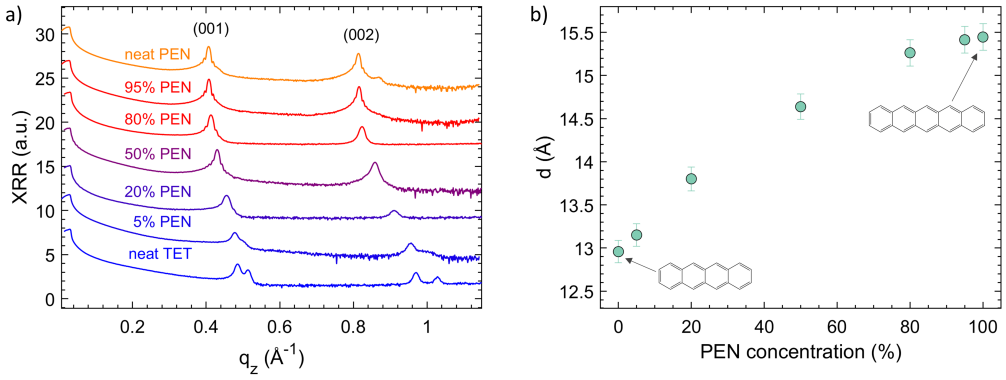


Figure 7.3: a) XRR data blends of PEN and TET. The curves of 20 % and 80 % PEN have a higher background since they have been measured on glass substrates. b) Lattice spacings extracted from the XRR data in a) using the (002) BPs. For XRR data with two (002) BPs, the one at lower q_z (thin film polymorph [281]) has been taken. Data published in Ref. 338.

rods remain at the same q_{xy} position. In-plane unit cell parameters of neat compounds and blends have been extracted from the in-plane scattering intensity ($q_{xy} \approx 0$) and are shown in Fig. 7.2f. Clearly, the in-plane parameters do not significantly change, which can be rationalized by the same width of the two molecules along their short axes.

A peculiar observation is the shifted intensity along the q_z-direction, particularly observed for the 25 % and 50 % PEN blends at $q_{xy} = 1.65\,\text{Å}^{-1}$. This observation can be explained by a relative shift of adjacent molecular planes, which affects the q_z-position of oblique reflections (i.e. $q_{xy} \neq 0$ and $q_z \neq 0$), but leaves the position in q_{xy} unaltered. A significant impact of a changed relative position of molecules in different molecular planes on the photophysics is unlikely, since the intermolecular distances between molecules in different molecular planes are much larger and there is only orbital overlap between molecules in the same molecular plane (see Sec. 2.2). In addition, the changing intensity distribution along the q_z-direction is a strong indication for the intermixing of the two compounds, since a phase separation would lead to a superposition of the diffraction pattern of the neat compounds.

XRR data of blends of PEN and TET are shown in Fig. 7.3a. All blends exhibit BPs corresponding to a lattice spacing in between those of the two neat materials. The bulk phases of PEN and TET (corresponding to the BPs at $q_z = 0.87\,\text{Å}^{-1}$ for PEN, at $q_z = 1.03\,\text{Å}^{-1}$ for TET) are not present in the blends except for a slight contribution in the blend with 5 % PEN concentration. The continuous shift of the BPs in the blends excludes a co-crystal and is, in particular together with the reciprocal space maps, strong indication for a solid solution (see Sec. 2.2). The lattice spacing extracted from these BPs (see Fig. 7.3b) is no linear function of the mixing ratio [340], but tends to be larger than the linear interpolation between the neat materials. This observation can be rationalized by less strain between neighboring lattice planes upon substitution of longer by shorter molecules than vice versa. Thus, the substitution with TET molecules at high PEN

concentrations affects the lattice spacing less than the substitution with PEN molecules at low PEN concentrations.

7.2 Optical characterization

Steady-state absorption spectra of PEN:TET blends are shown in Fig. 7.4a. Clearly, the absorption spectra of the blends are no superposition of the absorption spectra of the neat compounds, but the shape of the absorption bands corresponding to PEN and TET are strongly altered. This is in good agreement with the structural characterization, which already indicated the intermixing of PEN and TET in the blends. The PEN (TET) $S_0 \rightarrow S_1$ 0-0 transition shifts to higher (lower) energies in the blend, which originates from the reduced (increased) polarizability of the molecular environment from the replacement of neighbors by TET (PEN) molecules [104].

The behavior of the PEN DS is similar as for other PEN spacer blends [52, 104], since the energetically lower Davydov component strongly looses intensity with respect to the energetically higher Davydov component upon decreasing PEN concentration, as observed before [52]. The DS of PEN has been fitted with two gaussian functions, and the resulting peak positions are depicted in Fig. 7.4b. The energetically lower Davydov component clearly shifts stronger with the PEN concentration than the energetically higher Davydov component. Therefore, the absolute value of the DS, shown in Fig. 7.4c, decreases with decreasing PEN concentration, which indicates reduced CT interactions between PEN molecules [52, 196]. In the 5 % PEN blend, only a single peak is observed, which denotes the majority of PEN molecules to be surrounded by TET molecules. The optical band gap of these PEN monomers is determined to 2.02 eV (Fig. 7.4b).

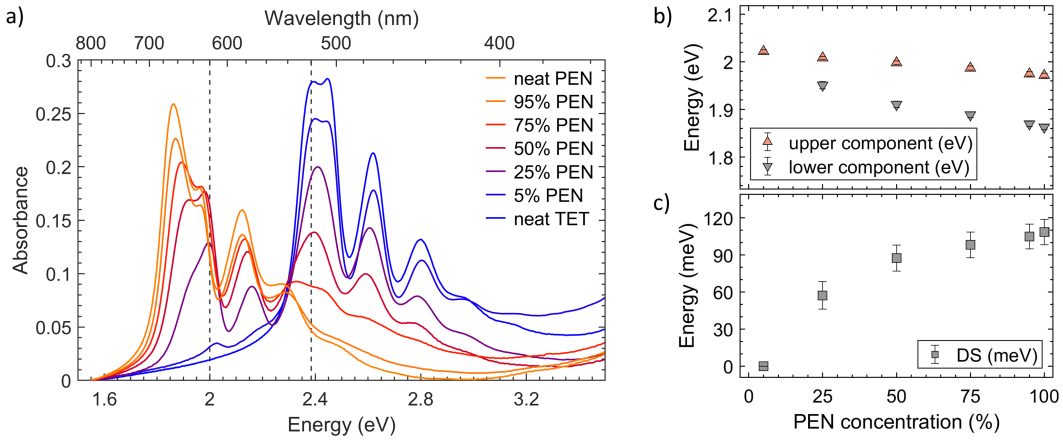


Figure 7.4: a) UV-Vis absorbance measurements on blends of PEN and TET. The two vertical dashed lines indicate the excitation wavelengths used for TA measurements. b,c) Peak positions and DS of $S_0 \rightarrow S_1$ 0-0 transition of PEN obtained from fits of gaussian functions. The uncertainties of peak positions in a) have been estimated as 10 % of the FWHM and are within the order of the marker size. Panel a) published in Ref. 338.

The $S_0 \rightarrow S_1$ 0-0 transition of TET is superimposed with the vibronic progression of PEN, which complicates an unambiguous analysis of the DS of TET. Nevertheless, it decreases faster, as it is not even visible in the blend containing 75 % TET (25 % PEN) anymore, for which the distortion from underlying PEN absorption should still be weak. The faster decrease of the TET DS with increasing PEN concentration can be explained by the smaller CT-character of S_1 of TET compared to that of S_1 of PEN [195].

To conclude on the structural and optical characterization, the PEN:TET blends investigated in this study are solid solutions with almost no change of in-plane lattice parameters due to the similar in-plane lattice parameters of the neat compounds and the same width of the two molecules along their short axes. The absorption spectra indicate altered intermolecular interactions between PEN and between TET molecules in the blends with respect to the neat materials. This observation is consistent with absorption spectra of other solid solutions [52, 104] and originates from reduced CT interactions [195, 196].

7.3 TA spectroscopy of the neat compounds

The photophysics of PEN:TET blends have been examined using two different excitation wavelengths λ_{exc}. Using $\lambda_{exc} = 620\,nm$, only PEN molecules in the blends can be excited, see vertical dotted line in Fig. 7.4a. In contrast, with $\lambda_{exc} = 520\,nm$ both PEN and TET molecules in the blends can be excited. As a basis for the discussion of TA measurements of PEN:TET blends, TA spectra of the neat compounds are discussed first.

TA maps and extracted spectra of measurements on neat PEN and TET are shown in Fig. 7.5. The TA measurement of neat PEN excited with $\lambda_{exc} = 620\,nm$ (Fig. 7.5a) was already discussed in Sec. 5.3 [97]. A TA measurement on the same film using $\lambda_{exc} = 520\,nm$ is shown in Fig. 7.5b. In both measurements, the negative ΔA signal at 675 nm can be assigned to a GSB of the energetically lowest excited state, singlet ESA at short delay

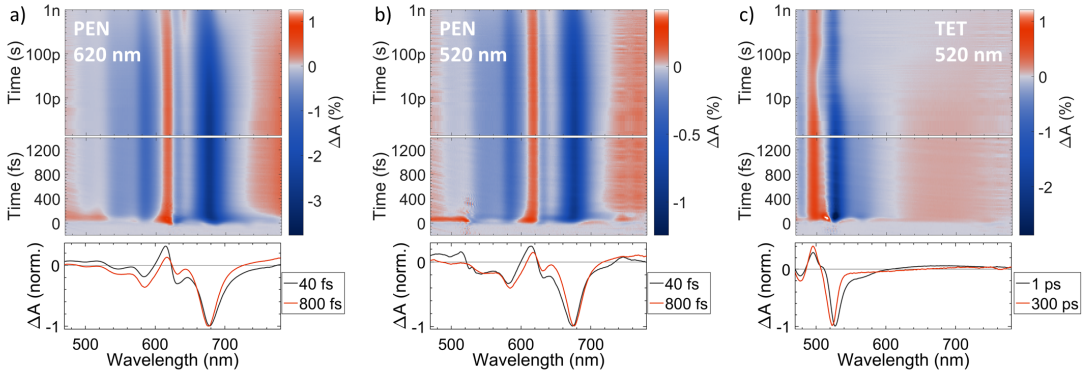


Figure 7.5: TA maps and spectra of thin films of a,b) neat PEN and c) neat TET. For the excitation wavelength, see label. The pump fluences were a) $73\,\mu J/cm^2$, b) $22\,\mu J/cm^2$ and c) $20\,\mu J/cm^2$. Data published in Ref. 338.

times before SF contributes a positive ΔA signal below 530 nm [97], and triplet ESA is observed at longer delay times after SF above 700 nm (see Sec. 5.3) [326].

A TA measurement of neat TET with $\lambda_{exc} = 520$ nm is shown in Fig. 7.5c and is consistent with literature [98, 206]. The negative ΔA signal observed at 530 nm can be assigned to a GSB of TET molecules. The signal shifts to 520 nm for longer delay times due to a disappearing contribution from SE [98, 206]. The SE contributes a pronounced signal at 570 nm that can be assigned to the 0-1 transition [206]. The 0-0 SE transition has been reported to peak at 530 nm [206] and is therefore superimposed with the GSB. The decay of SE, as well as the change in the shape and the position of the ESA above 700 nm are signatures of SF in TET.

In TET, SSA complicates the determination of the SF time constant at high pump fluences [64, 206], see Apx. D.1 for details. Note that, since it also depopulates the singlet state, the impact of the fluence-dependence due to SSA on the determination of the SF rate in TET is different from that due to TTA in PEN. However, for the investigation of the photophysics of the blends, SSA is strongly suppressed compared to neat TET by two reasons. First, the diffusion constant of TET singlets should be strongly decreased in the blends, since the PEN molecules serve as barriers [105]. Second, it will be shown that the photophysical processes in this study occur on a time scale that is much faster than TET homofission and should easily outcompete SSA.

7.4 TA spectroscopy without excitation of tetracene

TA measurements on the PEN:TET blends have been performed with two different excitation wavelengths ($\lambda_{exc} = 620$ nm and $\lambda_{exc} = 520$ nm) and will be discussed separately in Secs. 7.4 and 7.5. In this section, the results of TA measurements using $\lambda_{exc} = 620$ nm are presented and discussed. Since the blend with 5 % PEN concentration exhibits distinctively different photophysics, it is discussed in more detail separately later on in this section.

7.4.1 Feature assignment and global analysis

The excitation with $\lambda_{exc} = 620$ nm corresponds to a photon energy below the optical band gap of TET (see Fig. 7.4a). Therefore, only PEN molecules in the blends are excited with this excitation wavelength, which excludes contributions in the TA signals from decay channels (FRET, homo- and heterofission) of TET singlets. For PEN singlets, five different decay channels exist, namely radiative decay, IC, ISC, homo- and heterofission. However, radiative decay, IC, and ISC typically occur on the order of tens of nanoseconds and can be excluded to impact the dynamics observed in these TA measurements [178, 270, 341]. Therefore, only homo- and heterofission constitute efficient decay channels of PEN singlets in the blends.

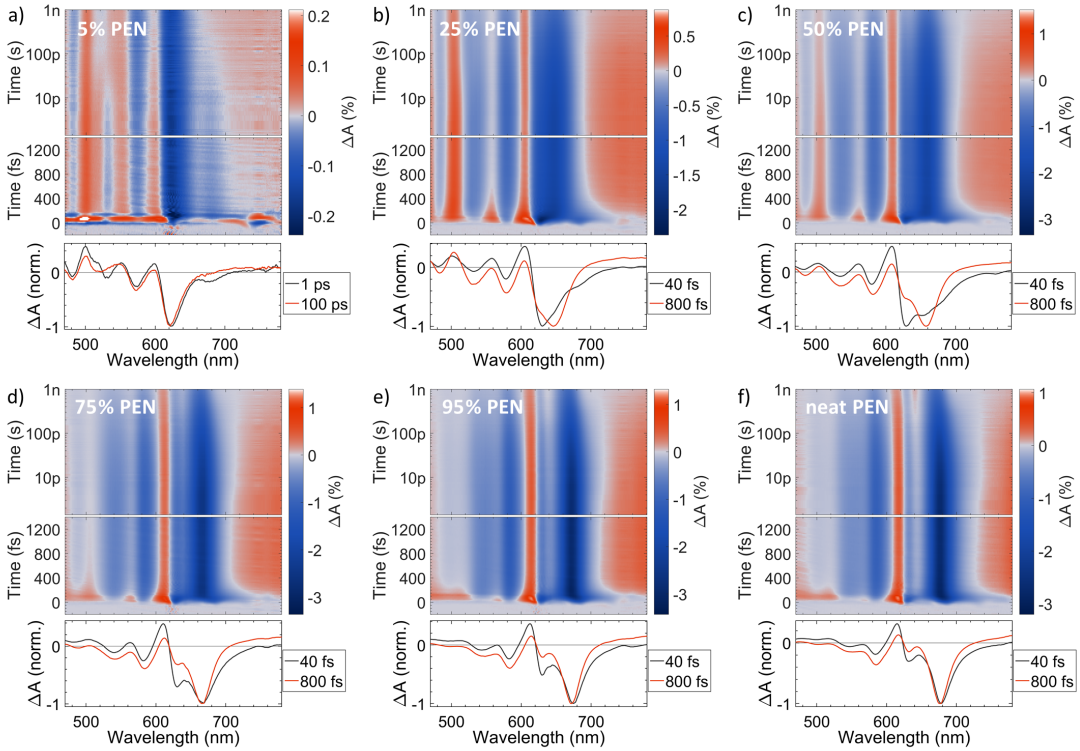


Figure 7.6: TA maps and spectra of TET:PEN blends with $\lambda_{exc} = 620\,nm$, $73\,\mu J/cm^2$ pump fluence and different PEN concentrations. The TA spectra shown in the respective lower panel have been normalized for better comparison. Data published in Ref. 338.

Results of TA measurements on PEN:TET blends performed with $\lambda_{exc} = 620\,nm$ are shown in Fig. 7.6. Except for the blend with 5 % PEN concentration, all blends exhibit a similar spectral pattern with analogous features as discussed for neat PEN above. These blends also exhibit fast dynamics within the first hundreds of femtoseconds as well as a long-lived signal that decays on the order of nanoseconds. Due to the overall similarity of the spectral features of the blends to those of neat PEN (in particular the rise of triplet ESA at wavelengths above 700 nm), the fast dynamics can be assigned to homofission of PEN singlets in the blends.

Spectral differences between the blends and neat PEN are a shift of the PEN GSB to shorter wavelengths in agreement with the steady-state absorption spectra (Fig. 7.4a), as well as the occurrence of features in the spectral region of TET absorption between 450 nm and 520 nm. The origin of the latter will be discussed in more detail below. Furthermore, a change in the shape of the GSB of PEN is observed in the TA spectra of the blends, in particular for those with 50 % PEN and 25 % PEN concentration. This change might originate from the photoexcitation of singlets at high-energy LECs, followed by hopping to low-energy sites [52].

The PEN GSB in the TA measurement on the blend with 5 % PEN concentration (Fig. 7.6a) at 620 nm is more narrow than those of the blends with higher PEN concentration, again in agreement with the steady-state absorption spectrum (Fig. 7.4a) that

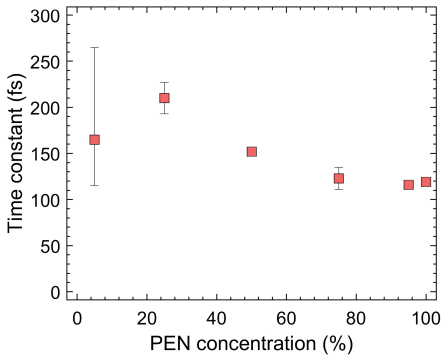


Figure 7.7: Time constants for PEN homofission in TET:PEN blends, obtained from GA of the measurements conducted with $\lambda_{exc} = 620\,nm$ (Fig. 7.6). The uncertainties are derived from the impact of a different modeling (number of species and coherent artifacts) in the GA. Data published in Ref. 338.

indicated isolated PEN molecules. Additionally, a feature of negative ΔA is observed at 680 nm, which corresponds to an energy difference of 176 meV to the position of the PEN GSB. This energy difference suggests that the feature at 680 nm can be assigned to the 0-1 transition of SE of the isolated molecules, since the energy difference between the 0-0 and 0-1 transition in absorption spectra of dissolved PEN (see Sec. 4.1) is 177 meV, and a similar energy difference can be expected for emission spectra [153].

Triplet ESA is observed above 700 nm, which strongly indicates that SF also occurs in this blend. In contrast to the blends with higher PEN concentration, the blend with 5 % PEN concentration exhibits an additional evolution on the order of 30 ps in the TA map in Fig. 7.6a. This evolution involves a spectral change in the region between 510 nm and 540 nm, a decay of the SE, as well as an increase of the triplet ESA. The time constant and the origin of this evolution will be discussed in more detail later on.

In order to obtain time constants for the changes of spectral signatures seen in the TA maps, they have been analyzed by a GA (see Sec. 3.3.1 and Apx. D.2). The resulting time constants for the ultrafast conversion of singlets into triplets are shown in Fig. 7.7. The uncertainties in these time constants are derived from the impact of a different modeling (number of species and coherent artifacts) in the GA. From neat PEN to 25 % PEN concentration, the time constant of PEN homofission increases from (113 ± 5) fs to (210 ± 17) fs. Yet, this slight increase is still consistent with the robust SF observed for PEN:spacer blends in Ref. 52 (see Ch. 6), since it is significantly less pronounced than expected for incoherent SF (theoretically 452 fs for 25 % PEN concentration, see Ch. 6). The GA on the 5 % PEN blend results in three distinct species that evolve with time constants of $(165\,^{+100}_{-50})$ fs and (26 ± 3) ps into each other. Both evolutions include a rise in the triplet ESA and thus correspond to SF. The origin of these two time constants will be discussed later on.

7.4.2 Thermal artifacts

In TA spectra of PEN:TET blends shown in Fig. 7.6, spectral features between 450 nm and 520 nm are observed. Since neither neat PEN (Fig. 7.6f) nor a PEN:PIC blend with 25 % PEN concentration measured for comparison (see Figs. 7.8c and 7.8d) show such features, they have to be related to the presence of TET molecules. These features can be assigned to thermal artifacts as evaluated in the following. It can be excluded that these features arise

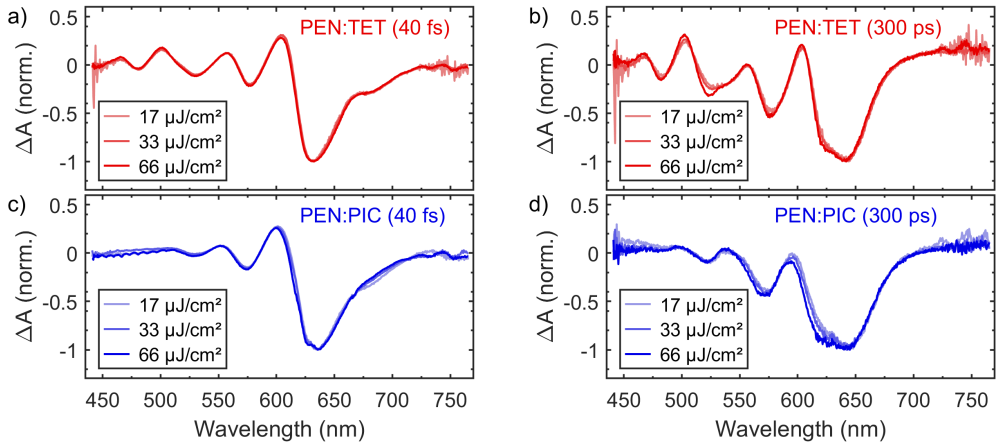


Figure 7.8: TA spectra at 40 fs and 300 ps of 25 % PEN blends mixed with TET (a,b) and PIC (c,d) at different delay times and pulse energy. Published in Ref. [338].

from the direct one- or two-photon excitation of TET molecules, since first, the photon energy corresponding to $\lambda_{exc} = 620$ nm is well below the band gap of TET molecules, and second, the TA measurements are not fluence-dependent (see Figs. 7.8a and 7.8b).

For both PEN and TET, a thermal artifact in TA spectra has been reported due to local heating of the sample by the pump pulse [97, 98, 260, 261]. This increase in temperature leads to a changed absorption of the molecules that are still in the ground state after photoexcitation of the sample. Since the TA signal is the (normalized) difference in absorption of the sample with and without previous photoexcitation, this thermally changed absorption leads to a thermal artifact in TA spectra. A proper description of the thermal artifact requires temperature-dependent absorption spectra [98, 260]. However, if the change in absorption upon increasing temperature can be approximated to be a small shift (with respect to the width of spectral features) to higher energies, the thermal artifact resembles the derivative of the steady-state absorption.

Using the derivative of the steady-state absorption spectra, the shapes of thermal artifacts are simulated for different PEN:TET blends and compared to the respective TA spectra in Fig. 7.9. Please note that in the following, features around 610 nm [260] and between 450 nm and 520 nm are of particular interest.

The simulated thermal artifacts of the PEN:TET blends agree well with both, positive and negative features in the relevant wavelength ranges of the TA spectra of PEN:TET blends, see Figs. 7.9a-c, and are at 610 nm in good agreement with a report on neat PEN [260], in which this feature was assigned to the thermal artifact. In order to further support the assignment of these features to a thermal artifact, it was also simulated for the PEN:PIC blend with 25 % PEN concentration discussed above (see Fig. 7.8), as well as for neat TET (Figs. 7.9e and 7.9f). Consistent with the experimental TA spectrum, the simulated thermal artifact of the PEN:PIC blend with 25 % PEN concentration (Fig. 7.9e) does not exhibit strong features between 450 nm and 520 nm. For neat TET (Fig. 7.9f) the photoinduced absorptions at 460 nm and 495 nm can be well explained by the simu-

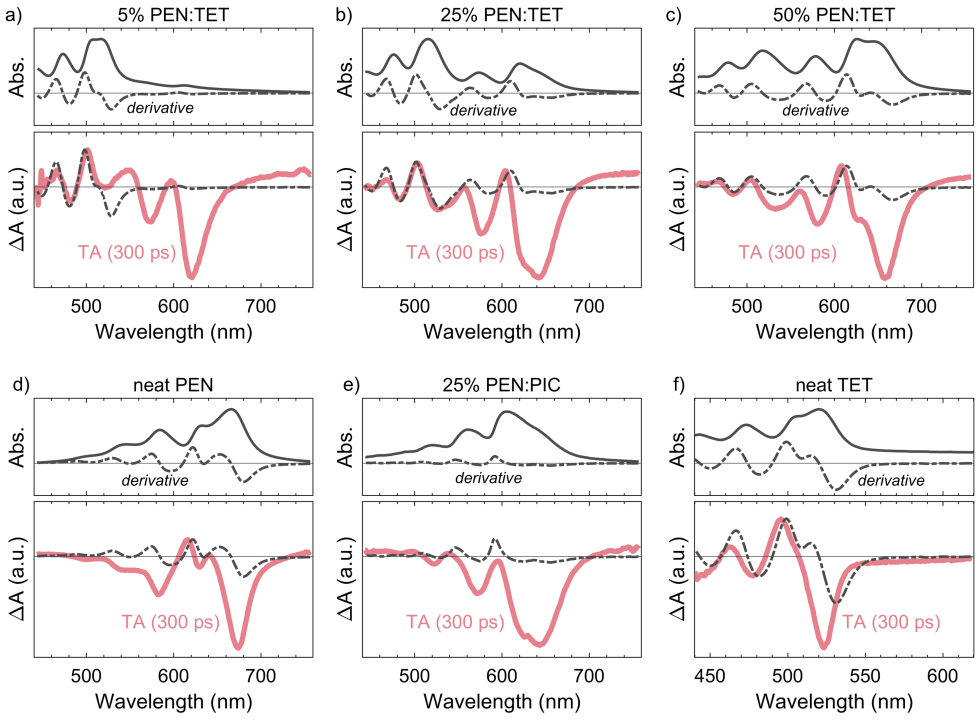


Figure 7.9: Comparison of measured TA spectra to simulated thermal artifacts for selected films (see label). The simulated thermal artifacts are arbitrarily scaled derivatives (dotted black line) of the steady-state absorption spectrum (solid black line), see respective upper panel. The TA spectra in the lower panels are extracted at delay times of 300 ps. The excitation wavelengths were $\lambda_{exc} = 620$ nm for a-e) and $\lambda_{exc} = 520$ nm for f). For details, see text. The derivatives in each lower panel (except for e)) were normalized to the largest positive features. Data published in Ref. 338.

lated thermal artifact. Furthermore, the simulated thermal artifact predicts a significant negative signal at 530 nm, as already noticed before [98]. Slight deviations of the shown simulated thermal artifacts can be explained by a larger shift of the absorption spectrum or a change of its shape with increasing temperature [98, 260].

This model for thermal artifacts assumes the heat to be instantaneously distributed homogeneously over the sample [260] independent of the excitation wavelength and therefore is a function solely of the steady-state absorption spectrum. As a noteworthy result, independent of the excited compound in a blend, the thermal artifact predominantly occurs at the spectral region of the absorption of the excess compound. Consequently, even without excitation of TET ($\lambda_{exc} = 620$ nm), the thermal artifact in the PEN:TET blends with 5 % and 25 % PEN concentration is only significant in the spectral region of the steady-state absorption of TET (Fig. 7.9a).

7.4.3 5% pentacene blend

The photophysics of the 5 % PEN blend are more complex than those of the blends with 25 % PEN concentration or higher. The special nature of the 5 % PEN blend originates

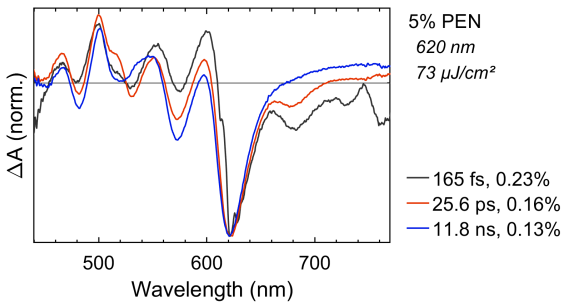


Figure 7.10: EAS and corresponding time constants obtained by GA of a TA measurement on a 5 % PEN blend with $\lambda_{exc} = 620\,nm$ and $73\,\mu J/cm^2$ pump fluence. The percentages indicated for each EAS in the legend correspond to the amplitude of the EAS before normalization. Data published in Ref. 338.

from the presence of isolated PEN molecules (monomers), which are surrounded by TET molecules, see simulation of a solid solution with 5 % concentration in Fig. 2.5. According to a binomial distribution (see Sec. 2.2.2), 81 % of the PEN molecules in a 5 % PEN blend are isolated, while 19 % have at least one PEN neighbor. Due to this large number of well separated PEN monomers, the 5 % PEN blend fundamentally differs from the other blends. After excitation with $\lambda_{exc} = 620\,nm$, most PEN singlets are located on monomers and cannot undergo homofission. These PEN singlets have been proposed in Refs. 106 and 107 to undergo heterofission. Therefore, the TA measurement on this blend is examined in more detail in the following.

A GA on the TA measurement of the 5 % PEN blend using $\lambda_{exc} = 620\,nm$ shown in Fig. 7.6a, could be performed using three species and its result is shown in Fig. 7.10. As already mentioned above, the decay time constants of the first two species are $\tau_1 = (165\,^{+100}_{-50})\,fs$ and $\tau_2 = (26 \pm 3)\,ps$, respectively. For the following discussion, TA spectra at different delay times extracted from the TA map in Fig. 7.6a are shown in Fig. 7.11a. In order to demonstrate the quality of the GA, time traces were extracted at different wavelengths (see arrows in Fig. 7.11a) and are compared to the fit result of the GA at the respective wavelength in Fig. 7.11b.

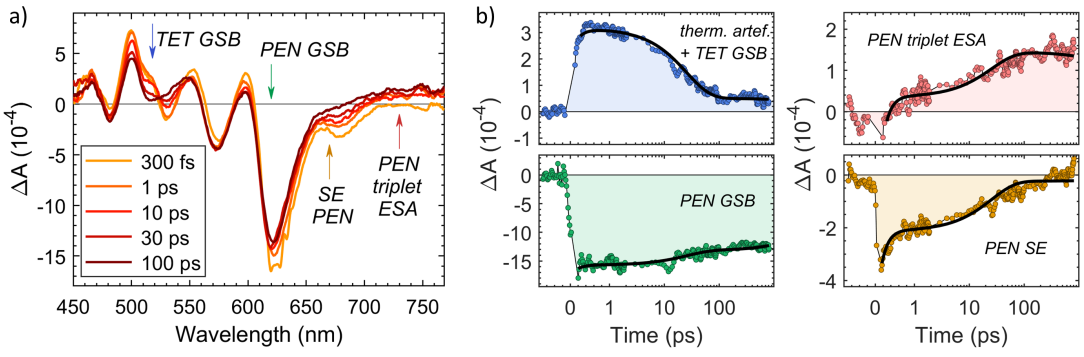


Figure 7.11: TA spectra (a) and time traces (b) of the TA measurement on the 5 % PEN blend using $\lambda_{exc} = 620\,nm$ and $73\,\mu J/cm^2$ pump fluence. The position and colors of the arrows in panel a) indicate the wavelengths of the time traces shown in b). In panel b), the black lines are the results of a GA on this TA measurement, the time-axis changes from linear to logarithmic scale at 1 ps and data points affected by a coherent artifact are not shown. Modified from Ref. 338.

The analysis of this TA measurement is divided into examinations of the two spectral regions above and below 550 nm. First, the spectral region at longer wavelengths is discussed. The evolution from the first to the third EAS in this spectral region in Fig. 7.10 is analogous to the observations for blends with higher PEN concentration (Fig. 7.6b-f). The EAS of the second species is in between that of the first and the third species and there is a clear build-up of a photoinduced absorption (>700 nm) that can be assigned to ESA of PEN triplets [97, 326]. Furthermore, also the shift of the signal to lower ΔA between 550 nm and 610 nm has been observed for the other blends in Fig. 7.6b-f. Therefore, it can be concluded from the spectral region above 550 nm that also in the case of the 5 % PEN blend, PEN singlets decay into PEN triplets.

The dynamics at the wavelengths corresponding to the PEN triplet ESA and the PEN SE shown in Fig. 7.11b can well be described by the biexponential dynamics with the two time-constants τ_1 and τ_2 obtained by the GA. The rise of PEN triplet ESA, decay of PEN SE and a persistent GSB on time scales that are too fast for ISC [178] denotes the presence of two distinct SF channels of PEN singlets that produce PEN triplets. Based on the similar timescale as observed in blends with higher PEN concentration, τ_1 can be assigned to homofission of those PEN molecules in the 5 % PEN blend with a PEN neighbor [52]. Consequently, the second SF process, corresponding to τ_2, is ascribed to the PEN monomers and thus to heterofission of PEN singlets (red arrows in Fig. 7.1) as observed in the 1970s [106, 107].

There are several indications for the assignment of τ_2 to heterofission, even beyond the biexponential build-up of the triplet ESA. First, regarding the spectral shape in Fig. 7.11a, SE of isolated PEN molecules at 680 nm is very pronounced at a delay time of 300 fs, hence after the homofission of PEN dimers with τ_1, but completely absent after the second process at a delay time of 100 ps. Thus, the process corresponding to τ_2 involves the decay of singlets on isolated PEN molecules. Two other processes besides heterofission can lead to a decay of these singlets, first, radiative relaxation of the PEN singlets, and second, energy transfer from PEN monomers to PEN dimers. Radiative relaxation of PEN monomers in PIC has been reported with a much larger time constant $\tau = 1.17$ ns [341] and can further be excluded since the PEN GSB does not decay with τ_2, hence the PEN molecules are still in an excited state. Energy transfer to PEN dimers would result in a strong red-shift of the PEN GSB, thus approaching a similar shape as observed for blends with higher PEN concentrations (Fig. 7.6). This is clearly not the case in Fig. 7.11a, since the GSB even exhibits a slight blue-shift, which strongly indicates that also PEN monomers remain in an excited state.

Until here, the discussion of spectral features and dynamics was entirely based on observations with probe wavelengths longer than 550 nm. These observations already give strong indication that the process connected to τ_2 is heterofission of PEN singlets on isolated PEN molecules proposed in the 1970s [106, 107]. For heterofission, one would further expect that a TET GSB rises with τ_2 at wavelengths shorter than 550 nm shown in Fig. 7.12a.

As discussed in Sec. 7.4.2, the spectral region of the TET absorption in the TA spectra of the 5 % PEN blend is strongly affected by a thermal artifact. A simulated thermal artifact, as described before, exhibits remarkable agreement with the shape of the TA spectrum of the 5 % PEN blend at 1 ps delay time, i.e. at much shorter delay times than τ_2 but longer than τ_1, see Fig. 7.12b. This indicates that, except for the thermal artifact, there is no contribution of TET molecules to the signal at these delay times. The difference between the thermal artifact and the TA spectrum at 1 ps delay time can be explained by ESA of PEN singlets. Within τ_2, a strong change is observed in the spectral region of the TET absorption with an isosbestic point at 525 nm [342] that indicates the transition between two species (Fig. 7.12a). This spectral change includes the build-up of a bleach at 514 nm (see respective time trace in Fig. 7.11b), which points towards the formation of excitons on TET molecules via processes other than direct photoexcitation (the reader is reminded that the excitation energy is below the band-gap of TET). These excitons are likely triplets produced by the heterofission of PEN singlets.

However, there are two surprising features in this spectral region. First, the TET GSB is surprisingly weak compared to the PEN GSB, and second, a positive ΔA signal at 530 nm appears simultaneously. These two observations might be explained by a combination of the following effects. One possible reason might be the anatomy of the adiabatic ^{1}(TT) state formed by coupling of the diabatic ^{1}(TT) state to diabatic CT states (CT^{ab} and CT^{ba}, see Fig. 2.19 and Ref. 196). In a homofission process, CT^{ab} and CT^{ba} are approximately degenerate. However, in a heterofission process, the degeneracy is lifted, since one electron transfer direction (TET → PEN or PEN → TET) is preferred. This means, that the contribution of CT^{ab} and CT^{ba} to the adiabatic ^{1}(TT) state will differ, resulting in a polarity of the adiabatic ^{1}(TT) state. This net dipole will result in a Stark effect [343] on the surrounding TET molecules, i.e. a shift of their absorption [344] and a derivative-like feature in the TA spectrum in analogy to the thermal artifact.

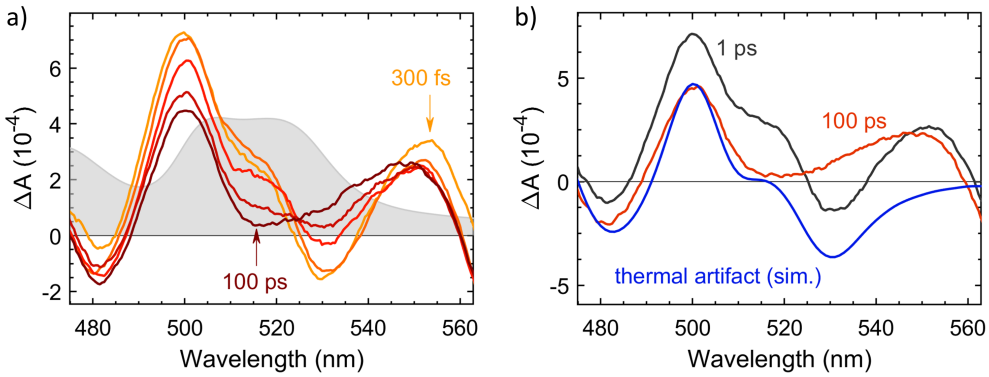


Figure 7.12: a) TA spectra shown in Fig. 7.11a in the region of the 0-0 transition of the TET absorption (shown in grey). b) TA spectra at 1 ps and 100 ps delay time in comparison to the simulated thermal artifact also shown in Fig. 7.9a. Modified from Ref. 338.

Finally, also the subsequent diffusion of TET triplets created by heterofission might reduce the build-up of a TET GSB, if it leads to energy transfer of the TET triplets to other PEN monomers. The diffusion length of TET triplets within 26 ps is approximately 2 nm with the diffusion constant reported in Ref. 345, and other PEN molecules might exist within this distance for a significant fraction of TET triplets.

In summary for the 5 % PEN blend with $\lambda_{exc} = 620$ nm, the probe wavelengths longer than 550 nm already give sufficient indication for heterofission. Additionally, also the spectral region at shorter wavelengths is consistent with this scenario, and the heterofission process of PEN singlets surrounded by TET molecules, as proposed in Refs. 106 and 107, can be concluded to be unambiguously observed. This heterofission of singlets on PEN monomers occurs with a time constant of $\tau_2 = 26$ ps.

7.5 TA spectroscopy with excitation of tetracene

The previously discussed TA measurements on PEN:TET blends were performed with an excitation wavelength of $\lambda_{exc} = 620$ nm. For PEN concentrations of 25 % or higher, PEN homofission was found to outcompete all other decay channels. In a blend with 5 % PEN concentration, heterofission of PEN singlets as proposed before [106, 107] has been observed, and a time constant of 26 ps for this process was extracted.

In the following, TA measurements on the same blends, but with $\lambda_{exc} = 520$ nm, are presented and discussed. This excitation wavelength corresponds to a photon energy above the optical band gap of TET, see Fig. 7.4a. Therefore, both PEN and TET molecules in the sample are excited with a wavelength of $\lambda_{exc} = 520$ nm, which opens up the decay channels of FRET from TET to PEN, as well as heterofission of TET singlets (green arrows in Fig. 7.1). Due to the multitude of decay channels of TET singlets, as well as the concomitant excitation of TET and PEN molecules, the photophysics of the PEN:TET blends with an excitation wavelength of $\lambda_{exc} = 520$ nm is complex. Since the complexity is even intensified in the 5 % PEN blend due to the presence of PEN monomers, which undergo PEN heterofission, the corresponding measurement is again discussed separately in this section. In the following, the discussion of origins of signatures in the TA data therefore only relates to blends with PEN concentrations of 25 % or higher.

7.5.1 Feature assignment and global analysis

The results of the TA measurements performed with $\lambda_{exc} = 520$ nm are shown in Fig. 7.13. For high PEN concentrations the measurements are very similar to those with $\lambda_{exc} = 620$ nm, including an ultrafast evolution of the TA spectra with a rise of triplet ESA above 700 nm assigned to SF, as well as a long-lived TA signal that decays on the order of nanoseconds. With lower PEN concentration, a negative ΔA signal is observed at short times at 525 nm, which can be assigned to a GSB of TET singlets created by direct photoexcitation (see Figs. 7.13a-c). In agreement with the concentration of TET

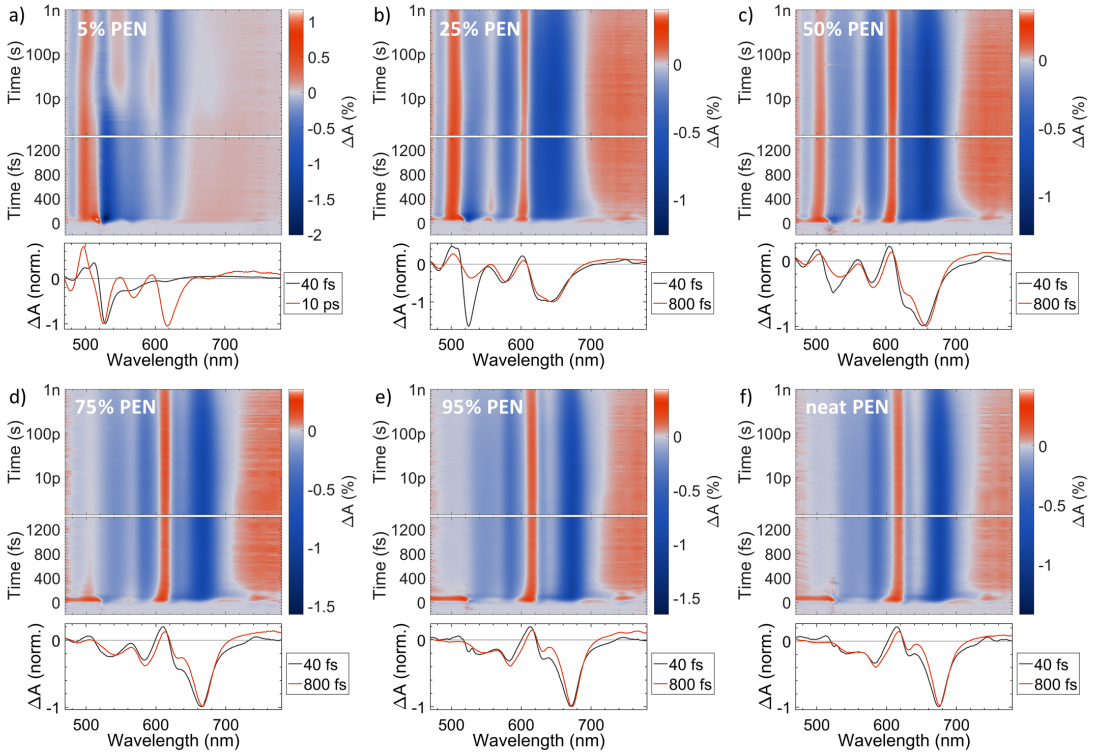


Figure 7.13: TA maps of TA measurements of TET:PEN blends with $\lambda_{exc} = 520\,nm$, $20\,\mu J/cm^2$ pump fluence and different PEN concentrations. The TA spectra shown in the respective lower panel have been normalized for better comparison. Data published in Ref. 338.

molecules in the blends, this GSB is weak in the 50 % PEN blend (see TA spectrum at a delay time of 40 fs in Fig. 7.5c) and strongly increases in intensity when going to the 5 % PEN blend (Fig. 7.13a).

Furthermore, the lifetime of the TET GSB increases between these blends (see time traces in Apx. D.2). While the TET GSB decays in the 50 % PEN blend within few hundreds of femtoseconds, the decay is prolonged to several hundreds of femtoseconds in the 25 % PEN blend and to several picoseconds in the 5 % PEN blend. Additionally, the decay of the TET GSB is accompanied by a rise of a PEN GSB, seen most pronounced for the 5 % PEN blend at 620 nm (see time traces in Apx. D.2).

There are two possible explanations for the decay of the TET GSB and the rise of the PEN GSB, namely FRET from TET to PEN as well as heterofission of TET singlets. Note that as mentioned before, the following discussion only relates to those blends with 25 % PEN concentration or higher. For the discussion of a distinction of the two decay channels of TET singlets (FRET and TET heterofission), it is useful to compare TA spectra at long delay times (300 ps) with an excitation wavelength of $\lambda_{exc} = 620\,nm$ and $\lambda_{exc} = 520\,nm$, which are shown in Fig. 7.14. If FRET is responsible for the decay of TET singlets with an excitation wavelength of $\lambda_{exc} = 520\,nm$, PEN singlets are created, which subsequently decay into two PEN triplets as observed using $\lambda_{exc} = 620\,nm$. Therefore,

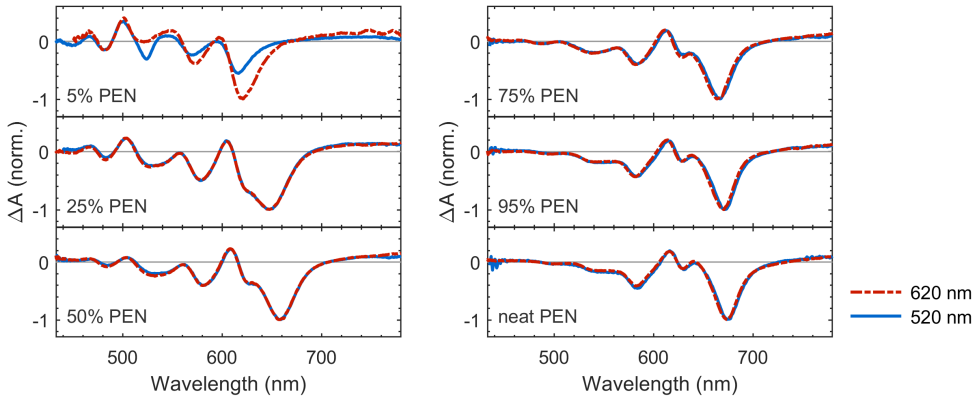


Figure 7.14: TA spectra of TET:PEN blends with different PEN fractions and different wavelengths at long delays (300 ps). For reasonable comparison (see Sec. 7.4.2), the TA spectra have been scaled to have the same amplitude at 500 nm. Data published in Ref. 338.

the TA spectra at long delay times with an excitation wavelength of $\lambda_{exc} = 620$ nm and $\lambda_{exc} = 520$ nm should be the same in this case.

In contrast, if TET heterofission is responsible for the decay of TET singlets created by excitation with $\lambda_{exc} = 520$ nm, these TA spectra at long delay times might differ, since TET heterofission creates a TET triplet and a PEN triplet, while with $\lambda_{exc} = 620$ nm, only PEN homofission was observed (for blends with 25 % PEN concentration or higher) and hence only PEN triplets are created. Note that this difference due to TET heterofission is only observed if TET triplets do not undergo subsequent Dexter energy transfer (Sec. 2.3.3) to PEN and thus again lead to two PEN triplets per photoexcited TET singlet, as depicted in Fig. 7.15.

The TA spectra with $\lambda_{exc} = 620$ nm and $\lambda_{exc} = 520$ nm shown in Fig. 7.14 are the same for all blends except the one with 5 % PEN concentration. Therefore, the final state of the system in these blends is independent of the excitation of TET or PEN molecules. As discussed above, this means that photoexcited TET singlets create two PEN triplets, either by FRET followed by PEN homofission or by TET heterofission followed by heteromolecular Dexter energy transfer (see Fig. 7.15). Since these two cases can only be distinguished by the dynamics at short delay times, the time constants extracted from the TA data using $\lambda_{exc} = 520$ nm are discussed in the following.

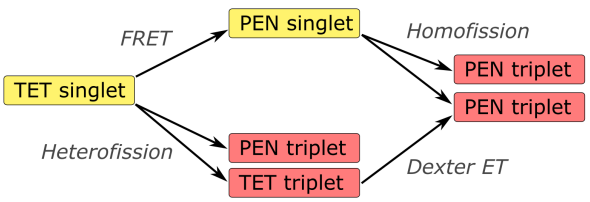


Figure 7.15: Scheme illustrating decay pathways of a TET singlet to two PEN triplets.

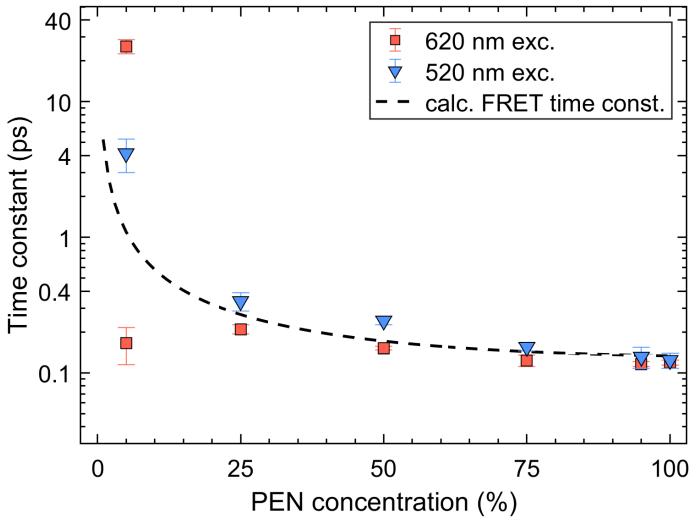


Figure 7.16: Time constants for the conversion of the initially excited singlets to triplets, determined by GA of the TA measurements with an excitation wavelength of $\lambda_{exc} = 620\,nm$ (red circles) and $\lambda_{exc} = 520\,nm$ (blue triangles). See Apx. D.2 for the GA results. Data published in Ref. 338.

The time constants for the conversion of photoexcited singlets in the blends into triplets have been obtained by a GA (see Apx. D.2). The TA data on the blends with 25 % PEN concentration or higher could again be fitted with two spectrally distinct species that can be assigned to singlets and triplets, as before. In Fig. 7.16, the time constants for the conversion between the two species are shown in comparison to the time constants of the GA on TA measurements with $\lambda_{exc} = 620\,nm$ (Fig. 7.7). For blends with 25 % PEN concentration or higher, the time constants for excitation with $\lambda_{exc} = 520\,nm$ are systematically higher than for excitation with $\lambda_{exc} = 620\,nm$.

Importantly, with $\lambda_{exc} = 520\,nm$, these time constants do not reflect a single process, but the decay of TET and PEN singlets with different relative contributions to the total signal due to the changing relative number of photoexcited TET and PEN molecules. At high PEN concentrations, for which few TET molecules are present and can be excited, the larger time constants result from excitation of higher vibronic sublevels of S_1 in PEN and SF only after vibrational relaxation. For lower PEN concentrations, and in particular for 25 % PEN, the time constant for excitation with $\lambda_{exc} = 520\,nm$ reflects predominantly the conversion of TET singlets to PEN triplets, as discussed before. Since the evolutions from singlets to triplets in blends with 25 % PEN concentration or higher are more than two orders of magnitude faster than TET homofission [98, 206], the latter can be excluded to constitute an efficient decay channel in these blends.

After these considerations, the open question as discussed before and depicted in Fig. 7.15 remains, which is, if the fast conversion of TET singlets into PEN triplets in blends with 25 % PEN concentration or higher is due to FRET followed by PEN homofission, or if it is due to heterofission of TET singlets followed by heteromolecular Dexter energy transfer of the created TET triplet to PEN.

7.5.2 Calculation of the Förster resonance energy transfer rate

While the heterofission rate of TET singlets is difficult to anticipate, the FRET rate of TET singlets to PEN can be approximated. In order to examine if FRET can be responsible for the decay of TET singlets, its rate has been calculated. The formula for the FRET rate as given in Sec. 2.3.3 includes, besides physical constants, the radiative rate of the donor molecule k_{rad} in the absence of an acceptor, the distance R of donor and acceptor molecule, the orientation-factor κ of their TDMs, the refractive index n as well as the overlap J between donor emission and acceptor absorption spectra. Before considering the HB aggregate, first the Förster radius R_{F} of a TET donor and a PEN acceptor with $\kappa = 1$ in vacuum ($n = 1$) is determined. With J calculated from the spectral overlap of TET emission and PEN absorption shown in Fig. 7.17a, a Förster radius of $R_{\mathrm{F}}^{\mathrm{vac}} = 54.7\,\text{Å}$ is obtained with Eq. 2.29 [346].

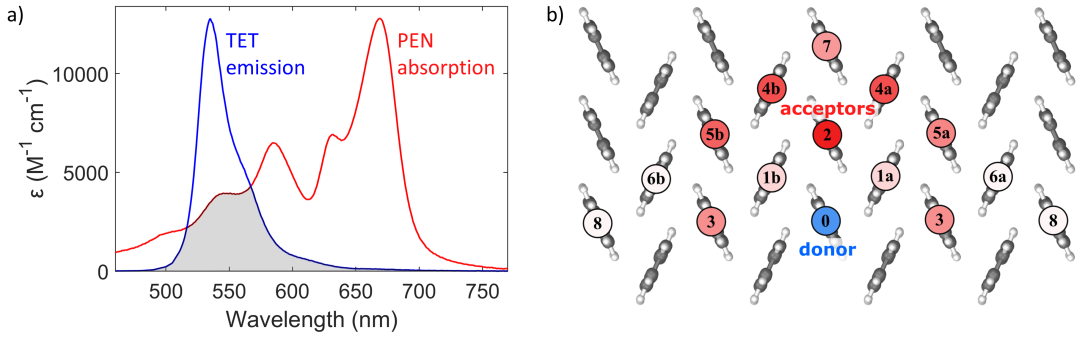


Figure 7.17: Calculation of the FRET rate from PEN to TET [338]. a) Overlap between TET emission and PEN absorption that determines J (see Sec. 2.3.3). The amplitude of the emission has been calculated from the absorbance of a film with 20 nm thickness and the molecular density. The emission spectrum is shown normalized to the absorption [204], but is normalized to unit area for calculation of the Förster radius [110]. b) Relative orientation of acceptor molecules in a HB arrangement with respect to an arbitrary donor molecule. The color intensity of the acceptor indicates the ordering in coupling strength κ_i^2/R_i^6 see main text and Apx. D.3. The targets can be point-mirrored to the lower half.

The FRET rate k_{ET} in an aggregate is the sum of the FRET rates $k_{\mathrm{ET},i}$ to all acceptor molecules with index i. The FRET rate to an acceptor molecule in a HB aggregate is given by

$$k_{\mathrm{ET},i} = k_{\mathrm{rad}} \frac{\kappa_i^2}{n(c)^4} \left(\frac{R_{\mathrm{F}}^{\mathrm{vac}}}{R_i} \right)^6 , \tag{7.1}$$

see Sec. 2.3.3. In the blends, the sites of the HB aggregate are statistically occupied by donors and acceptors, which can be accounted for by multiplying the rate with the concentration of acceptor (PEN) molecules c,

$$k_{\mathrm{ET}} = c \sum_i k_{\mathrm{ET},i} = c \cdot k_{\mathrm{rad}} \cdot n(c)^{-4} \cdot (R_{\mathrm{F}}^{\mathrm{vac}})^6 \cdot \sum_i \frac{\kappa_i^2}{R_i^6} . \tag{7.2}$$

The acceptor-dependent factors κ_i^2/R_i^6 can be calculated for the 24 nearest neighbors of a donor molecule in a reported PEN crystal structure [277], see Fig. 7.17b and Apx. D.3. Their sum is determined for this work as

$$\sum_{i=1}^{24} \frac{\kappa_i^2}{R_i^6} = 1.03 \cdot 10^{-4} \text{Å}^{-6}, \tag{7.3}$$

to which the translationally equivalent neighbors along the molecular short axes (labeled 2 in Fig. 7.17b) contribute 80 % of the total value. For the radiative rate of a TET molecule the literature value of $k_{\text{rad}} = 0.0435\,\text{ns}^{-1}$ is used [270]. The concentration-dependent refractive index is assumed to be linear between those of TET (n=1.6 [283]) and PEN (n=2 [347]). Inserting the values for neat PEN yields a FRET rate of TET singlets surrounded by PEN molecules of

$$k_{\text{ET}}^{\text{PEN}} = 0.0435\,\text{ns}^{-1} \cdot \frac{1}{16} \cdot \left(54.7\,\text{Å}\right)^6 \cdot 1.03 \cdot 10^{-4} \text{Å}^{-6} = 7.52\,\text{ps}^{-1}. \tag{7.4}$$

The largest contribution to an uncertainty in this value is the Förster radius determined from the spectral overlap in Fig. 7.17a. The PEN absorption is relatively flat in the region of TET emission, but both change in the blends (see Fig. 7.4a). The sixth power, with which the Förster radius contributes to the FRET rate, further enhances this relative uncertainty, but a relative uncertainty of $k_{\text{ET}}^{\text{PEN}}$ below one order of magnitude is reasonable to assume.

The obtained FRET rate equals a time constant of $1/k_{\text{ET}}^{\text{PEN}} = 133\,\text{fs}$. This demonstrates that FRET from TET to PEN molecules in HB aggregates can indeed occur on the order of the PEN homofission time constant and can easily outcompete TET homofission. With decreasing PEN concentration, the FRET time constant increases due to the decreasing number of acceptor molecules in the proximity of a donor molecule. The concentration-dependent FRET rate (shown as the black dotted line in Fig. 7.16) agrees well with the increase of the time constants of the conversion of photoexcited singlets to triplets using $\lambda_{\text{exc}} = 520\,\text{nm}$.

The good agreement of calculated FRET rates with the observed time constants for the conversion of singlets to PEN triplets indicates that the FRET + PEN homofission channel in Fig. 7.15 is responsible for the decay of TET singlets. This assignment can be further substantiated by considering that Dexter energy transfer rates are in general slower than FRET rates [345, 348]. Therefore, a Dexter energy transfer that follows heterofission would lead to additional, slower dynamics in the TA data, but the observed dynamics are monoexponential (see Apx. D.2) on ultrafast timescales that agree with FRET and PEN homofission. With the TA spectra shown in Fig. 7.14 and the calculation of the FRET rate, it can therefore be concluded that in blends with 25 % PEN concentration or higher, TET singlets undergo FRET to PEN, and PEN triplets are produced by PEN homofission.

7.5.3 5% pentacene blend

As for the TA measurements using $\lambda_{exc} = 620\,nm$, also for $\lambda_{exc} = 520\,nm$ the 5 % PEN blend is examined in more detail in the following. The TA measurement of this blend, shown in Fig. 7.13a, exhibits a pronounced spectral change on a timescale of several picoseconds. The spectral change includes a decay of a TET GSB and a rise of a PEN GSB, indicating the same FRET + SF process that has been observed for blends with 25 % PEN concentration or higher. However, in contrast to the latter, the blend with 5 % PEN concentration exhibits clear differences in the TA data obtained with $\lambda_{exc} = 620\,nm$ and $\lambda_{exc} = 520\,nm$ at longer delay times, see Fig. 7.14.

The GA on this measurement is shown in Fig. 7.18. The TA data could be fitted with four species that evolved into each other with time constants of $\tau_1 = (334 \pm 19)\,fs$, $\tau_2 = (4.15 \pm 0.31)\,ps$ and $\tau_3 = (113 \pm 18)\,ps$. Again, the quality of the GA is demonstrated for time traces extracted at different wavelengths, see Fig. 7.19a and 7.19b. The EAS shown in Fig. 7.18 exhibit distinctively different spectral features. The first and the second EAS include a pronounced TET GSB at 530 nm and only differ in a slight contribution of a PEN GSB at 620 nm in the second EAS. In the third EAS, the PEN GSB is stronger than the TET GSB, and a PEN SE at 680 nm is observed. Finally, the fourth EAS is similar to the third EAS but does not include the PEN SE.

Since the PEN GSB contribution in the first EAS is vanishingly small, direct photoexcitation of PEN plays a minor role due to the much larger fraction of TET molecules. The first and the second process with τ_1 and τ_2 likely correspond to FRET of TET singlets to PEN as for blends with higher PEN concentration. Some TET singlets are created with PEN acceptors in their environment, and directly undergo FRET to PEN. Since τ_1 is in good agreement with the FRET calculations (Fig. 7.16) it is assigned to FRET of TET singlets to PEN.

Some TET singlets, however, do not have a PEN molecule as neighbor and first diffuse to sites with accessible PEN acceptors. The second time constant τ_2 is therefore likely to be related to diffusion-limited FRET of TET singlets to PEN. It is shown in Apx. D.4 that this assignment is reasonable based on a reported singlet diffusion constant for TET [345]. During the diffusion of TET singlets, TET homofission is in principle possible and might lead to TET triplets. However, the diffusion-limited FRET within τ_2 is still more than one order of magnitude faster than TET homofission, and the relative number of TET

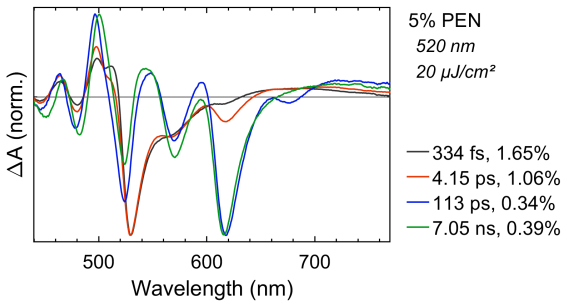


Figure 7.18: EAS and corresponding time constants obtained by GA of a TA measurement on a 5 % PEN blend with $\lambda_{exc} = 520\,nm$ and $20\,\mu J/cm^2$ pump fluence. The percentages indicated for each EAS in the legend correspond to the amplitude of the EAS before normalization. Data published in Ref. 338.

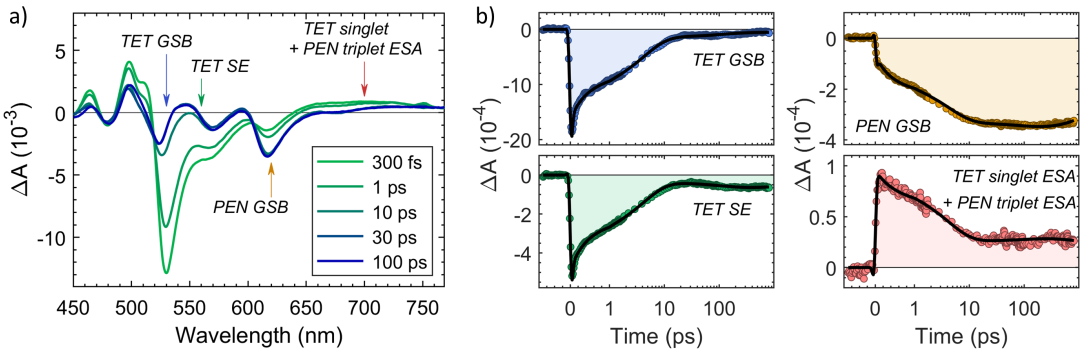


Figure 7.19: TA spectra (a) and time traces (b) of the TA measurement on the 5 % PEN blend using $\lambda_{exc} = 520\,nm$ and $20\,\mu J/cm^2$ pump fluence. The position and colors of the arrows in a) indicate the wavelengths of the time traces shown in b). In b), the black lines are the results of a GA on this TA measurement, the time-axis changes from linear to logarithmic scale at 1 ps and data points affected by a coherent artifact are not shown. Modified from Ref. 338.

triplets created by the latter should be small. Nevertheless, these TET triplets might be responsible for the differences observed between the TA spectra using $\lambda_{exc} = 620\,nm$ and $\lambda_{exc} = 520\,nm$ at delay times of 300 ps in Fig. 7.14.

After FRET of TET singlets to PEN (direct or diffusion-limited), the singlets that have been transferred to PEN monomers and dimers are expected to undergo PEN heterofission and PEN homofission, respectively. Since the FRET rate to PEN monomers and dimers might differ, the resulting PEN singlets might not be distributed between dimers and monomers as they are upon photoexcitation using $\lambda_{exc} = 620\,nm$. This effect might also contribute to the differences observed in Fig. 7.14. The PEN homofission is too fast for a distinction from the FRET process, and the corresponding PEN triplets are already included in the third EAS, as seen by the PEN triplet ESA above 700 nm in Fig. 7.18. The heterofission of PEN singlets with a time constant of 26 ps determined using $\lambda_{exc} = 620\,nm$ is too slow to significantly influence this EAS.

Indeed, the PEN SE in the third EAS in Fig. 7.18 shows that PEN singlets at monomers still exist. The fourth EAS, however, clearly does not show PEN SE, indicating that heterofission of PEN singlets occurred. The time constant τ_3 corresponding to this process is significantly higher than observed with $\lambda_{exc} = 620\,nm$. This is, however, likely an artifact from the fit routine that preferably optimizes evolutions corresponding to larger amplitudes. The diffusion-limited FRET process from TET to PEN corresponding to τ_2 can be expected to exhibit multiexponential dynamics, since the diffusion time before FRET differs for different TET singlets. Therefore, in particular for the time trace corresponding to the PEN GSB in Fig. 7.19b, the GA is not ideal, which likely impacts τ_3.

To conclude the photophysics of the 5 % PEN blend using $\lambda_{exc} = 520\,nm$, the biexponential dynamics of the TET singlets likely correspond to direct and diffusion-limited FRET. The observed differences in TA spectra between $\lambda_{exc} = 620\,nm$ and $\lambda_{exc} = 520\,nm$ at longer delay times can be explained by TET homofission during the diffusion of TET

singlets as well as the different distribution of PEN singlets between monomers and dimers after FRET. As mentioned before, the multitude of contributing processes, including TET singlet diffusion, TET homofission, FRET from TET to PEN, as well as homofission and heterofission of PEN singlets complicates the analysis of SF rates upon excitation with $\lambda_{exc} = 520\,nm$. Nevertheless, these measurements are consistent with FRET + SF as the dominant decay channel for TET singlets.

7.6 Conclusion

The photophysics of PEN:TET blends have been investigated using TA spectroscopy with two different excitation wavelengths, $\lambda_{exc} = 620\,nm$ and $\lambda_{exc} = 520\,nm$, which correspond to photon energies below and above the band gap of TET, respectively. The possible decay channels for TET and PEN singlet excitons on the sub-nanosecond timescale are shown in Fig. 7.20. Determined time constants for these processes are summarized in Tab. 7.1. Due to the distinctively different behavior of the 5 % PEN blend, it was examined in more detail.

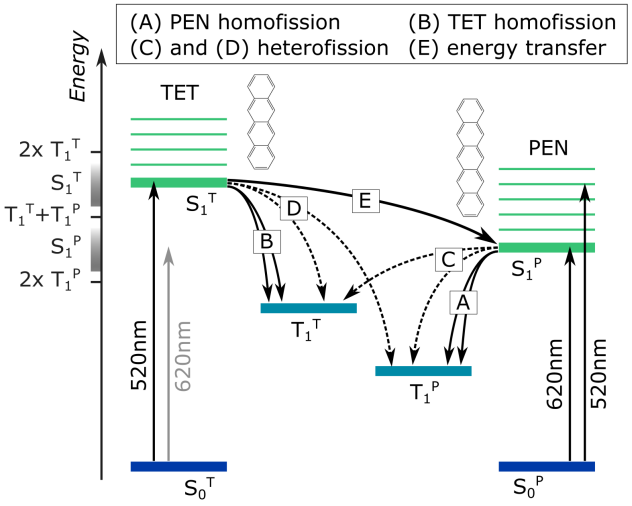


Figure 7.20: Possible ultrafast (sub-nanosecond) electronic processes involving excited states of TET and PEN, compare Fig. 7.1. Dotted arrows indicate heterofission processes. Uppercase letters T and P denote electronic states of TET and PEN molecules, respectively. Published in Ref. 338.

Above 25 % PEN concentration and with $\lambda_{exc} = 620\,nm$, the time constant of PEN homofission increases slightly with decreasing PEN concentration from 110 fs (neat PEN) to 210 fs (25 % PEN). This slight increase is significantly less than expected due to the replacement effect for incoherent SF and is thus consistent with the robust SF observed for PEN:spacer blends in Ref. 52 (see Ch. 6). Using $\lambda_{exc} = 520\,nm$, a decrease of the TET GSB and a rise of the PEN triplet ESA was observed within $130 - 400\,fs$ for the blends with 25 % PEN concentration or higher. Indications were found that FRET from TET to PEN outcompetes heterofission of TET singlets, followed by the same PEN homo- and heterofission processes as observed using $\lambda_{exc} = 620\,nm$. This conclusion was supported by calculations of FRET rates from TET to PEN in the blends.

For the 5 % PEN blend and $\lambda_{exc} = 620\,nm$, biexponential dynamics corresponding to SF of PEN singlets have been observed. The processes were assigned to homofission at

Table 7.1: Time constants of the photophysical processes observed in the blends. The time constants are labeled as in Fig. 7.20, and thus correspond to PEN homofission (τ_A), TET homofission (τ_B), PEN heterofission (τ_C), TET heterofission (τ_D) and FRET from TET to PEN (τ_E). n.a. refers to processes which cannot be observed due to the excitation wavelength, multiexponential (m.e.) denotes the convoluted nature of the signal with $\lambda_{exc} = 520\,nm$, and X indicates processes that are outcompeted by others. *This time constant has a large uncertainty (-50/+100 fs).

	$\lambda_{exc} = 620\,nm$		$\lambda_{exc} = 520\,nm$	
	5 % PEN	> 5 % PEN	5 % PEN	> 5 % PEN
τ_A	165 fs*	110 − 210 fs	m.e.	130 − 400 fs
τ_E	n.a.	n.a.		
τ_B	n.a.	n.a.		X
τ_C	26 ps	X		X
τ_D	n.a.	n.a.	X	X

PEN dimers and heterofission at PEN monomers. The heterofission of PEN singlets to TET and PEN triplets has been proposed already in the 1970s [106, 107] and the results in this work denote the first observation using time-resolved spectroscopy, which allowed to extract a time constant for the process of 26 ps. Excitation of the 5 % PEN blend with $\lambda_{exc} = 520\,nm$ led to biexponential dynamics of TET singlets, which was assigned to a combination of direct and diffusion-limited FRET from TET to PEN.

The heterofission time constant of 26 ps can further be discussed in view of the energy balance of this process, which is given by $\Delta E = E(T_1^P) + E(T_1^T) - E(S_1^P)$, see Fig. 7.20. The PEN singlet energy in blends with 5 % PEN concentration can be obtained from the narrow absorption peak in Fig. 7.4 and has been determined to $E(S_1^P) = 2.02\,eV$. The triplet states $E(T_1^P) = 0.86\,eV$ [28] and $E(T_1^T) = 1.25\,eV$ [290] are less sensitive to the molecular environment (see Sec. 2.4.5) and can be taken from literature. This gives an endothermic heterofission process by $\Delta E = 90\,meV$, which is half the endothermicity of TET homofission ($\Delta E = 180\,meV$) [290]. Therefore, regarding the endothermicity, the observed time constant for heterofission of 26 ps is in good agreement with the time constant of TET homofission of 80 ps [98, 206]. The slower time constant compared to that of intramolecular heterofission (1 ps) observed in covalently bound oligoacenes [90, 108] likely results from the weaker coupling in the molecular aggregates.

The endothermicity of the heterofission process of PEN singlets further rationalizes its absence in blends with higher PEN concentration, for which most PEN molecules have another PEN neighbor. In these blends, the exothermic, coherent PEN homofission efficiently outcompetes the heterofission of PEN singlets. For TET singlets, it can be concluded from the presented data that FRET efficiently outcompetes heterofission. The heterofission of TET singlets is exothermic by 200 meV, which is an even larger exothermicity than that of PEN homofission. This demonstrates the importance of additional parameters such as the coherent admixture of ^{1}(TT) states to S_1 or orbital overlap for a fast SF process.

7.7 Comparison with rubrene blends

The presented study on heterofission in PEN:TET blends was motivated by its observation in single crystals in the 1970s [106, 107]. It showed that heterofission in PEN:TET blends is only efficient for PEN singlets surrounded by TET molecules, but is outcompeted by PEN homofission if there are PEN neighbors due to the ultrafast, coherent SF process originating from the exothermicity of SF in PEN [71, 74]. This result motivated the investigation of RUB:TET blends, for which homofission of the compound of lower band gap (RUB) is endothermic. These investigations of RUB:TET blends are briefly presented in the following. For details on the preparation of the RUB:TET blends for which data is shown in the following, see Tab. E.6.

7.7.1 Optical microscopy

Before the discussion of the structural and optical characterization, optical microscopy images of the blends are shown in Fig. 7.21 to illustrate the multifaceted features observed for the thin films. Neat TET exhibits bright, circular features containing holes, and these features are also observed in between other features in all blends (see in particular the 50 % RUB blend). In going from neat TET to blends containing 20 % RUB, dark spots appear and increase slightly in size. With 50 % RUB concentration the number of these dark spots decreased again. A strong change in the morphology of the films occurs for the blend with 80 % RUB concentration, which exhibits dendrites in addition to the darker spots. Also the blend with 90 % RUB concentration exhibits these dendrites, but on a larger scale. The formation of dendrites by neat RUB has been observed before [349]. Finally, neat RUB forms large, dark clusters in the microscopy image.

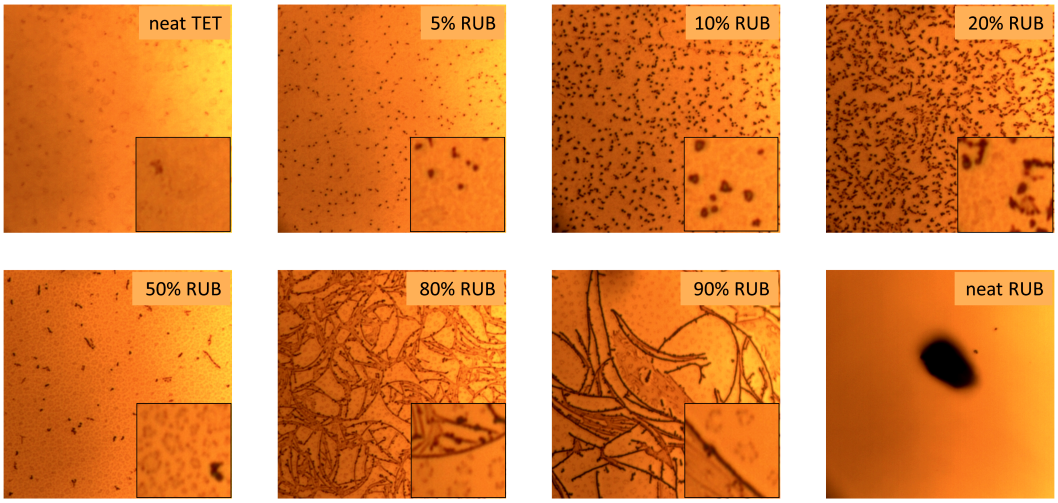


Figure 7.21: Microscopy images ($40 \times 40\,\mu m$, measured with a 50x objective) of RUB:TET blends. The insets show images measured with a 100x objective and are scaled to correspond to a magnification by a factor of four compared to the respective outer image.

7.7.2 Structural and optical characterization

Reciprocal space maps of neat TET and a selection of RUB:TET blends are shown in Fig. 7.22. Note that the reciprocal space maps shown here are measured with a different q_{xy}-range than those shown before. For blends with low RUB concentration, local maxima of the scattering intensity are observed at $q_{xy} = 0.18\,\text{Å}^{-1}$ and $q_z = 0.49\,\text{Å}^{-1}$ that likely correspond to (001)-reflections of rotated crystallites of a bulk TET polymorph ($|q| = 0.519\,\text{Å}^{-1}$ [281]). The presence of RUB molecules apparently leads to a tilt of the molecular planes of TET crystallites with respect to the substrate. Between 5 % and 10 % RUB concentration the tilt seems to increase slightly, but the reflections are absent for 50 % RUB concentration, for which only a small, non-rotated fraction of TET crystallites is observed.

Interestingly, a similar reflection appears again with $|q| = 0.55\,\text{Å}^{-1}$ for 80 % RUB concentration, yet with an in-plane maximum, see Fig. 7.22e. If the reflection also originates from the interference of photons scattered at different molecular planes, it would denote crystallites with a molecular plane stacking parallel to the substrate. The $|q|$-value of this reflection is slightly larger than the length of the reciprocal (001)-vector of the TET bulk crystal structure, see corresponding circle in Fig. 7.22e.

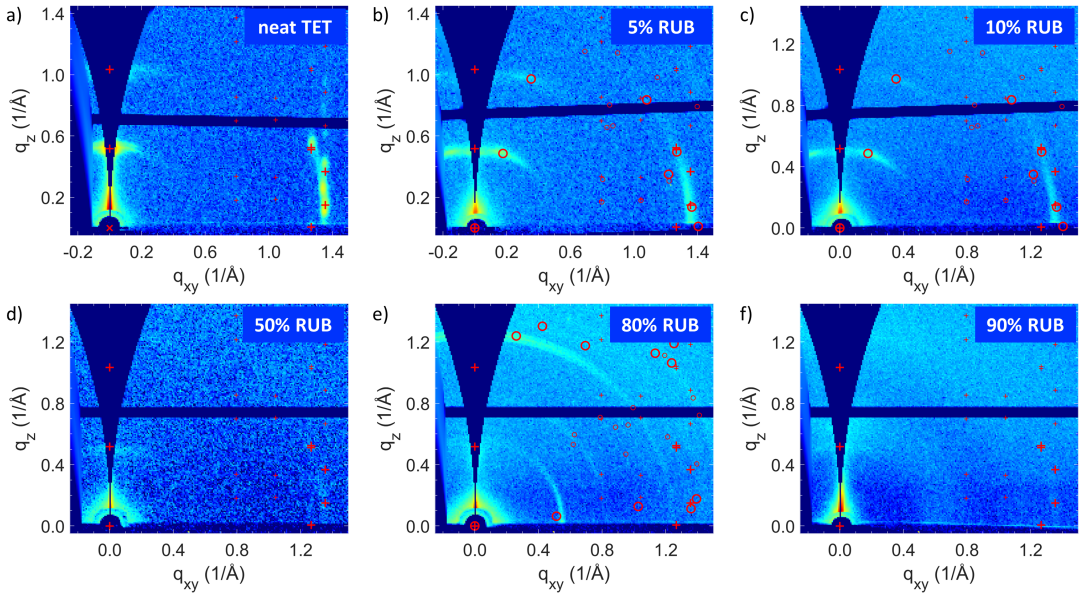


Figure 7.22: Reciprocal space maps of RUB:TET blends with different RUB concentrations (see labeling in the panels) measured at the *Xeuss-system*. The measurements were performed on blends of a different series than used for the other measurements. Plus symbols correspond to calculated reflections based on the unit cell of the TET bulk phase [281]. Circles correspond to calculated reflections based on the same, but rotated unit cell with the rotations as follows. b,c) Rotated clockwise around the crystal a-axis by 20°. e) Rotated counterclockwise around the crystal a-axis by 80° and around the crystal b-axis by 45°. Two different sizes are used for the markers to clarify the relative intensity of the calculated reflections.

Another reflection distributed onto a ring corresponding to $|q| = 1.27\,\text{Å}^{-1}$ is observed, which agrees with the reciprocal (111)-vector of the TET bulk crystal structure, see corresponding circle at $q_{xy} = 0.25\,\text{Å}^{-1}$ and $q_z = 1.25\,\text{Å}^{-1}$. In the reciprocal space map of the blend with 90 % RUB concentration, these reflections disappeared again, and only very weak, broad rings are observed. Note that these broad rings might correspond to similar structures as observed in the other blends, but with a much smaller crystallite size. Neat RUB did not show any features in the reciprocal space map.

In summary, the GIWAXS data of all RUB:TET blends are consistent with phase-separated TET crystallites of different orientations and sizes, since all features in the reciprocal space maps of the blends can be explained by calculated reflections based on tilted crystallites of the TET bulk phase. The microscopy images are in general consistent with this scenario, as the dendrites observed in blends with 80 % and 90 % RUB concentration have been observed before for thin films of neat RUB [349], thus indicating the presence of RUB molecules that behave similar as in neat RUB aggregates.

However, despite the phase separation, the presence of mixed domains, including the incorporation of dilute amounts of molecules of either compound in domains dominated by the other compound, cannot be excluded. One indication for such mixed domains could be the blend with 50 % RUB concentration, which clearly differs in both the microscopy image (50 % RUB in Fig. 7.21) and the reciprocal space map (Fig. 7.22d) from the blends

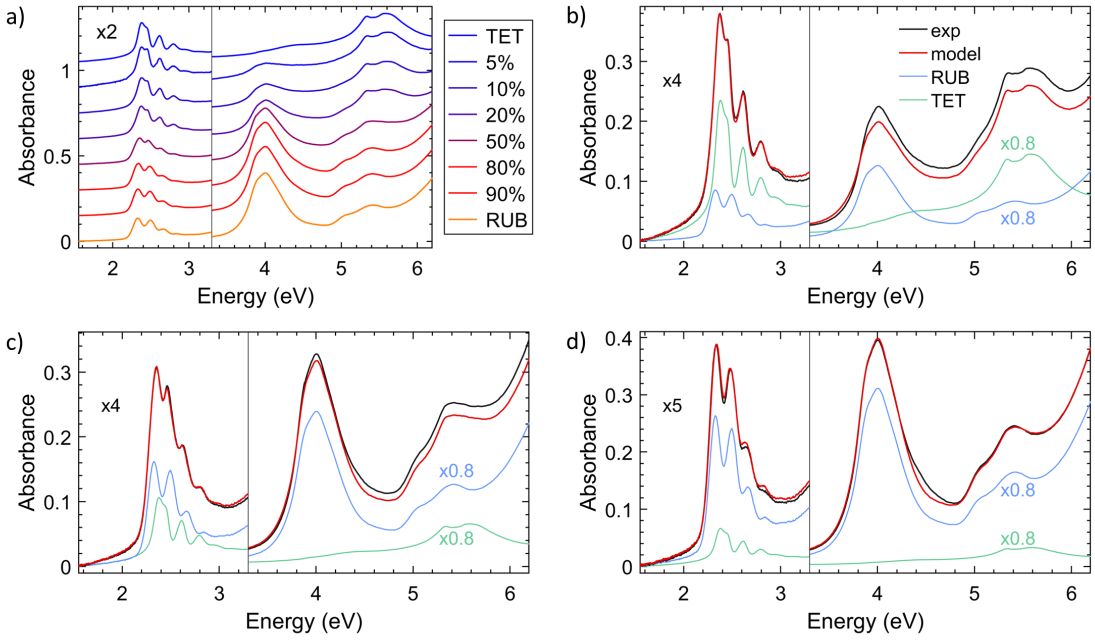


Figure 7.23: a) UV-Vis absorption spectra of RUB:TET blends with different concentrations. b-d) Analysis of three absorption spectra shown in a). A superposition (model) of the absorption spectra of RUB and TET with different amplitudes is compared to the measured absorption spectra of the blends. The legend in b) also applies to c) and d). The low-energy parts of the absorption spectra have been multiplied with the factors shown in the respective panel.

containing more RUB or more TET. For simplicity, in the following RUB and TET domains refer to RUB-dominated and TET-dominated domains. This is not meant to exclude incorporation of dilute amounts of molecules of the respective other compound.

Also the UV-Vis absorption spectra (Fig. 7.23) are consistent with such a phase separation of RUB and TET domains, as will be discussed in the following. Since the optical band gap of RUB is only slightly smaller than the band gap of TET, the $S_0 \rightarrow S_1$ transitions of the two compounds overlap in the blends, which complicates the determination of changes in the absorption spectra of the two compounds with varying mixing ratio. However, the position of the optical transitions of RUB and TET above 3.5 eV is markedly different. The intensity of the RUB absorption band at 4 eV increases with increasing RUB concentration and the intensity of the TET absorption band at 5.6 eV decreases without notable changes of the shapes of these bands in the blends.

Comparisons between absorption spectra of a selection of blends and superpositions of the absorption spectra of the neat compounds are shown in Figs. 7.23b-d. The good agreement of experimental and model spectra is due to the absence of spectral shifts or changes of the shape of the absorption bands corresponding to RUB and TET. This indicates that the presence of the respective other compound has little impact on the optical properties of TET and RUB in the blends, as one would expect for a phase separation of the two compounds.

7.7.3 Fluorescence decays

The phase separation in RUB:TET blends makes the discussion of their photophysics slightly more complex compared that of the model system PEN:TET. The interfaces between the RUB and TET domains, as well as potential incorporation of molecules of the respective other compound (for simplicity not explicitly mentioned in the following) still allow for heterofission. However, since most of the molecules are located within the bulk of these domains, heterofission should be strongly mediated by exciton diffusion to these interfaces. During the diffusion, homofission (depending on the domain, in which the singlet exciton was created) can lead to a decay of the singlets before reaching the interface, thus, preventing heterofission. Therefore, even though the RUB:TET system was chosen to study heterofission in blends of two endothermic SF materials, it complements the PEN:TET study not only in terms of SF energetics, but also in terms of mixing behavior.

The results of TCSPC and steady-state PL measurements on RUB:TET blends are shown in Fig. 7.24. The PL spectra of neat TET and RUB are consistent with previous reports, with peaks at 2.32 eV [206] and 2.21 eV [306], respectively. While the fluorescence of neat TET decays very fast, the fluorescence of neat RUB is relatively long-lived, which is in agreement with previous observations [244, 275, 303, 306, 309]. The blends with low RUB concentration exhibit a fast decay and a PL spectrum similar to that of TET. The PL spectrum of the blend with 50 % RUB concentration seems to be a superposition of those of neat TET and neat RUB, in particular due to the shoulder at 2.35 eV (assigned

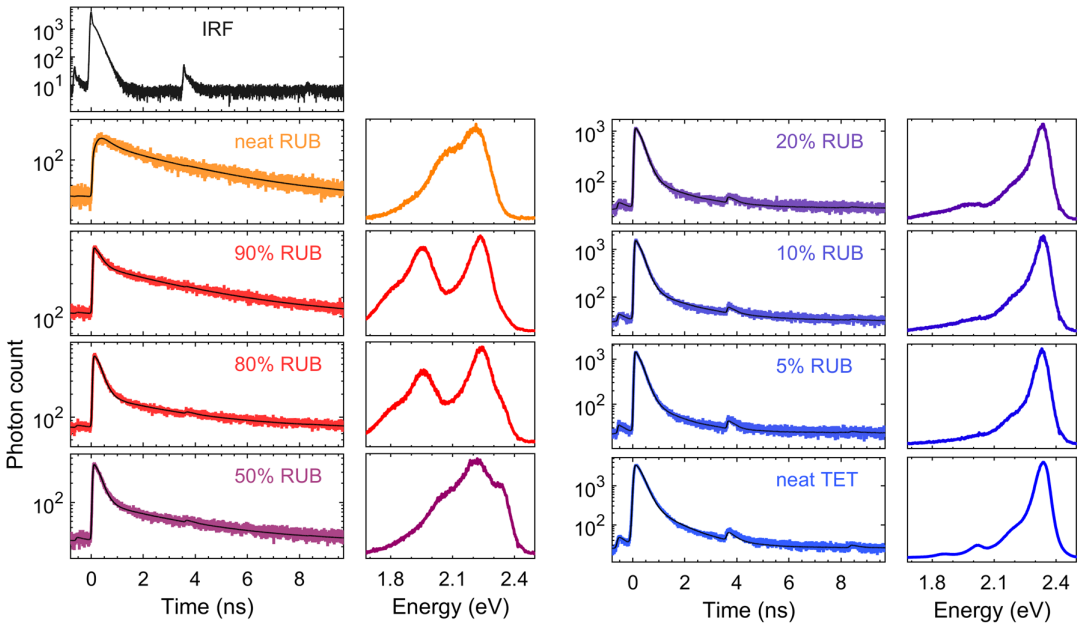


Figure 7.24: TCSPC and steady-state PL on RUB:TET blends. For each blend the TCSPC decay curve (left) and a steady-state PL spectrum (right) are shown. The two measurements were performed at the same spot of the sample (Sec. 3.3.2). The solid black line in the TCSPC-panels are biexponential fits to the data. Note that the neat TET measurement was performed on a film with 80 nm thickness, see Tab. E.6.

to TET) and the peak at 2.21 eV (assigned to RUB). For higher RUB concentration, a long-lived component appears and the PL spectrum exhibits an additional peak at 1.95 eV. The origin of this feature will be discussed later on.

The TCSPC data could be fitted with biexponential functions. The resulting rates of the slow and the fast component are shown in Fig. 7.25. As expected from the TCSPC data in Fig. 7.24, the fast component has a significantly larger amplitude and dominates for neat TET and low RUB concentrations. The rate of the dominant component for neat TET is of similar magnitude as the SF rates obtained from the TRPL spectroscopy measurements in Ch. 6. With increasing RUB concentration, the decay rate of the fast component is remarkably constant and slightly larger than that of neat TET. For neat RUB, the decay rate of the fast component is one half of the decay rate of neat TET.

The overall fluorescence decay corresponds to the decay of excitons from emissive states into dark states or the ground state. Note that based on the observed timescales, a contribution from radiative decay, IC and ISC can be excluded to contribute significantly to the overall decay rates in the neat compounds and the blends [178, 270, 306]. In TET, the emissive state is S_1, and the fluorescence decay rate has been assigned to the direct transition to ^{1}(T...T) [67]. For RUB, an ultrafast equilibration between S_1 and ^{1}(TT) has been reported [60, 96] (see Sec. 4.3). Since the ^{1}(TT) state in RUB is emissive, only the conversion from ^{1}(TT) to ^{1}(T...T) leads to a decay of the fluorescence [308], and the PL spectrum of RUB is a superposition of emission from S_1 and from ^{1}(TT) [308]. Due to

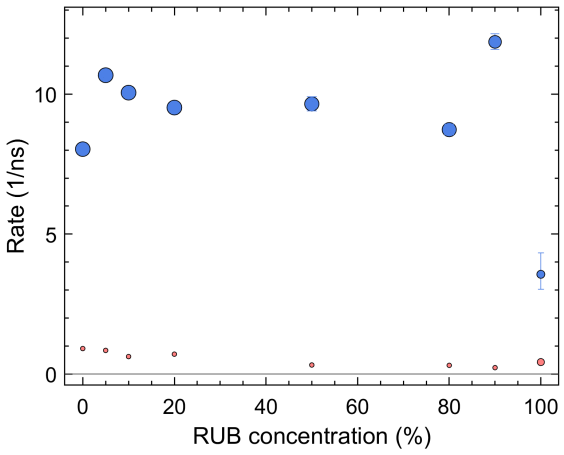


Figure 7.25: Fluorescence decay rates obtained from biexponential fits to the TCSPC data on RUB:TET blends (see Fig. 7.24). The marker size corresponds to the relative amplitude of the respective component. A minimum marker size prevents a complete disappearing of markers. Most uncertainties are smaller than the marker size.

the emission from the ^{1}(TT) state, the fluorescence decay of RUB is much slower than for TET, but this cannot be interpreted as a slower formation of ^{1}(TT). Since the emission from ^{1}(TT) is generally weaker than from S_1 [308], the PL intensity of RUB is significantly lower compared to that of TET, which will become important at a later stage of the discussion. In the blends, additional to homofission in RUB and TET domains, also (diffusion-mediated) FRET from TET to RUB, as well as (diffusion-mediated) heterofission at the interfaces might impact the fluorescence decay and are discussed in the following.

The steady-state PL spectra give information about the time-integrated contributions of RUB and TET to the overall emission of the blends. However, in blends with RUB concentrations up to 20 %, RUB emission is not visible in the steady-state PL spectra, although the excitation wavelength should excite both TET and RUB. This can be explained by the before mentioned weaker PL intensity of RUB compared to that of TET, which means that the contribution of TET emission to the steady-state PL spectrum of blends is expected to be much stronger than the contribution of RUB emission already without photophysical processes transferring excitation energy between the compounds. However, another contribution to the low intensity of RUB emission in these blends might be diffusion-mediated heterofission of RUB singlets at the interfaces between RUB domains and the TET domains. In particular if the dark spots observed in the microscopy images are RUB domains, their relatively small size might assist this process. The diffusion-mediated heterofission of RUB singlets will be discussed in more detail later on.

Besides the RUB emission, the photophysics in the blends with low RUB concentrations up to 20 % can also be discussed regarding the decay of the TET singlets, whose emission is well observed. The decay rate of the TET singlets in all blends is slightly larger than in neat TET (Fig. 7.25), which corresponds to a slightly reduced TET singlet lifetime. The decreased lifetime might either result from FRET from TET domains to RUB domains, or from heterofission of TET singlets at the interfaces between TET domains and RUB domains. In principle, these two processes could be distinguished by the relative intensity of RUB emission compared to TET emission in these blends. However, as discussed above,

the strong emission from TET singlets, which is superimposed with the weak RUB emission in the steady-state PL spectra, prevents a clear conclusion. Nevertheless, the reduced TET singlet lifetime is an interesting result and most likely related to photophysics at the interfaces between TET domains and RUB domains.

For the blend with a RUB concentration of 50 %, both, TET and RUB emission are observed in the steady-state PL spectra (Fig. 7.24). The contribution of RUB emission is surprisingly strong compared to the blend with 20 % RUB concentration. An enhanced FRET rate from TET to RUB is unlikely to be the reason for this observation, since this would lead to a larger decay rate of the fast component in the fits of the TCSPC data (Fig. 7.25), which is not observed. Since the stronger RUB emission apparently does not originate from enhanced FRET of the TET singlets, its origin might lie in the behavior of the photoexcited RUB singlets.

As discussed above, a possible origin of the absence of RUB emission in the blends with 20 % RUB concentration and less is heterofission of RUB singlets at the interface to TET domains, which, importantly, is diffusion-mediated. Larger RUB domains in the 50 % RUB blend would decrease the efficiency of diffusion to the interface, thereby reducing heterofission of RUB singlets and enhancing RUB emission. However, the amorphous arrangement of RUB molecules, leading to a lack of corresponding features in the GIWAXS images, makes experimental evidence for this interpretation challenging. Nevertheless, the appearance of RUB emission in the 50 % RUB blend is surprising, and is further indication for heterofission in the blends with 20 % RUB concentration and less.

In the blends with 80 % and 90 % RUB concentration, the contribution of TET emission at 2.32 eV to the steady-state PL spectra becomes even smaller, and the RUB emission at 2.21 eV dominates (Fig. 7.24). For the 80 % RUB blend, the decay rate of the fast component in Fig. 7.25 is even slightly smaller than for the blends with a lower RUB concentration, which indicates a smaller FRET rate, consistent with the large TET crystallites observed by narrow rings in GIWAXS (Fig. 7.22). A smaller FRET rate compared to that in the 50 % RUB blend supports the above discussion, which indicated heterofission in the blends with 20 % RUB concentration and less based on the absence of an enhanced FRET rate in the 50 % RUB blend. For the 90 % RUB blend only a very weak shoulder corresponding to TET emission is observed. The slightly larger decay rate of the fast component in Fig. 7.25 indicates a faster FRET of TET singlets to RUB domains, again consistent with the very small TET crystallites observed by broad rings in GIWAXS (Fig. 7.22) and the weak TET emission in the steady-state PL spectrum.

In the steady-state PL spectra of the blends with 80 % and 90 % RUB concentration, a strongly red-shifted peak appears at 1.95 eV (Fig. 7.24). This peak is not observed in steady-state PL spectra of neat TET [64], amorphous RUB [306], or crystalline RUB [305]. However, the analysis of TRPL data of neat RUB in the Supporting Information of Ref. 308 revealed a PL component that was assigned to emission from the ^{1}(TT) state located at 1.97 eV. Therefore, the red-shifted peak observed here in the steady-state PL spectra

of the blends with 80 % and 90 % RUB concentration is likely emission from ^{1}(TT) in the RUB domains, possibly in the dendrites observed in the microscopy images of these blends (Fig. 7.21). The appearance of enhanced emission from ^{1}(TT), as well as the overall different shape of the steady-state PL spectra of these blends compared to neat RUB can be explained based on the strong anisotropy of PL spectra in crystalline RUB [305], which are markedly different from those of amorphous RUB [306]. It is likely that the RUB molecules arrange differently in the dendrites [349] compared to those in the neat film and thus lead to a different spectral shape, although GIWAXS reflections corresponding to RUB domains were not observed for any film (Fig. 7.22), which indicates that both the dendrites and the neat RUB film are amorphous.

In summary of the steady-state PL spectra and TCSPC data of RUB:TET blends, the phase separation into RUB-dominated and TET-dominated domains complicates the interpretation of these data. Nevertheless, some conclusions can be drawn. For all blends, the decay rate of the fastest component is increased compared to neat TET, which indicates a reduced lifetime of TET singlets. The reduction can be explained by FRET from TET domains to RUB domains, in particular for the blends with higher RUB concentrations, for which a strong RUB emission is observed in the steady-state PL spectra. A strong emission from the ^{1}(TT) state in RUB is observed in blends with dendrites in the microscopy images, which is likely related to a different molecular arrangement of RUB molecules. The absence of RUB emission in blends with low RUB concentrations might indicate heterofission of RUB singlets at interfaces to TET domains, but a clear conclusion requires further investigations (e.g. by TA spectroscopy), which were beyond the scope of this study.

To conclude this chapter, heterofission of singlets to two triplets residing on chemically distinct chromophores has been investigated in blends of SF materials. In solid solutions of PEN and TET, the endothermic heterofission of PEN singlets surrounded by TET molecules, as proposed before [106, 107], has been observed using time-resolved spectroscopy, and a time constant of 26 ps for this process was extracted. For PEN singlets with one or more neighboring PEN molecules, ultrafast homofission outcompetes the heterofission process. Exothermic heterofission of TET singlets is outcompeted by FRET from TET to PEN, followed by the homo- or heterofission of PEN singlets. In addition, RUB:TET blends were investigated to complement the study of PEN:TET blends by mixing two endothermic SF materials. A phase separation into RUB domains and TET domains complicated the analysis, but indications for FRET from TET to RUB domains, as well as heterofission of RUB singlets at interfaces to TET domains were found. This study demonstrates that intermolecular heterofission can be an efficient decay channel of singlets in blends of two SF materials, which makes them alternative model systems for studying the impact of heteromolecular CT states on SF and the SF process in general.

8. Conclusion and Outlook

Intermolecular interactions of prototypical SF materials have been varied in this work to examine their impact on the SF process [49, 84–87]. The variation has been achieved either by partial fluorination of the SF materials (Ch. 5) or by mixing them with other compounds (Chs. 6 and 7). A summary of the main findings as well as an outlook are given in the following. A scheme of the SF process including the ^{1}(TT) state, as well as an overview of the studies in this work are shown in Fig. 8.1.

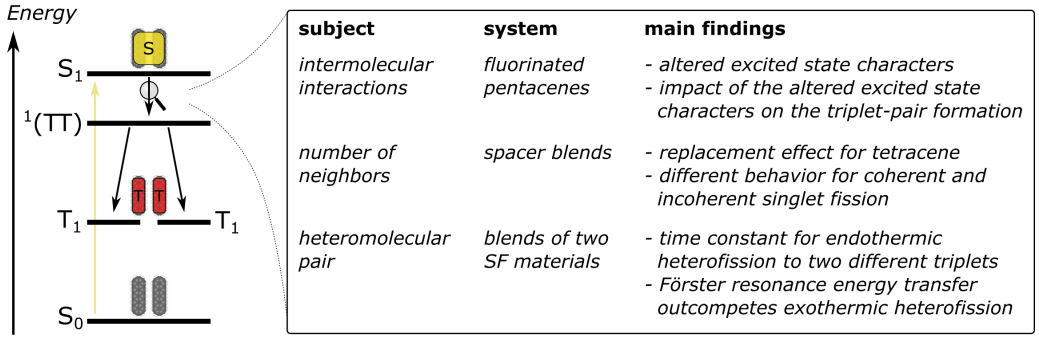


Figure 8.1: Scheme illustrating the investigations and summary of the main findings of this work.

8.1 Conclusion

SF in partially fluorinated PENs was investigated in Ch. 5 with the aim to examine the impact of altered molecular arrangements and coupling of electronic states [122, 299]. Among the large variety of crystal structures obtained by fluorination, in particular a compound with a face-to-face arrangement of molecules exhibited distinctively different photophysics [94, 99, 229]. In this compound, the triplet-pair formation was slower than in PEN, and instead of a subsequent spatial separation of the two triplets, the formation of a dark singlet excimer was observed.

However, also among different HB aggregates achieved by fluorination, large differences in the triplet-pair formation rate were found. In particular for an asymmetrically fluorinated PEN with a permanent dipole, the triplet-pair formation rate increased by a factor of

two with respect to that in PEN, which was assigned to an enhanced coupling of electronic states due to the interaction of partial charges on neighboring molecules [84, 85, 123]. Consistent with this observation, the DS of S_1, which is well-known to be an experimentally accessible measure of the CT character that drives the triplet-pair formation [196], was increased in this fluorinated PEN. The comparison between four different HB aggregates confirmed the correlation between the DS and the triplet-pair formation rate and further highlighted the impact of partial charges on the coupling of electronic states.

By strongly altering the molecular arrangement and the coupling of electronic states within one class of materials, this study has shown that fluorination is a powerful tool to influence key parameters of SF while retaining a highly crystalline structure. The latter is important to allow for strongly delocalized states [94], which are known to play a fundamental role in SF [59, 71, 94, 243, 294], but are not present in dissolved dimers and amorphous aggregates of compounds with substituted bulky side-chains [94].

In Ch. 6, the impact of a reduced number of SF molecules on the SF rate in spacer blends was investigated [271]. Previous studies on spacer blends with PEN exhibited a surprisingly robust SF that was independent of the mixing ratio [52]. In the present work, analogous spacer blends with TET were characterized and SF rates were determined. In strong contrast to PEN-based blends, these blends exhibited a pronounced replacement effect, i.e. a SF rate that linearly decreases with the reduced number of SF molecules [105].

The difference between the spacer blends containing PEN and TET was explained by their different SF mechanisms. In PEN, SF is a coherent process [50, 74], which is driven by the admixture of triplet-pair states in the photoexcited singlet state. With a reduction of the number of neighboring SF molecules, this admixture does not change, and SF does not depend on the concentration of the spacer material. For TET, SF is a stochastic, incoherent process [67], and a replacement of neighboring SF molecules directly reduces the SF rate [105]. These conclusions were supported by theoretical calculations performed by Prof. R. Tempelaar (Northwestern University, USA) and Prof. D. R. Reichman (Columbia University, USA), and demonstrate fundamental properties of coherent and incoherent SF mechanisms. Therefore, this study has shown that spacer blends can serve as tools to investigate the role of electronic coherences in SF [271].

In Ch. 7, blends of two SF materials (PEN and TET) were prepared to investigate the photophysical processes in the presence of a heterofission decay channel, i.e. the conversion of singlets into two triplets located on different types of molecules [338]. Exothermic, coherent homofission was found to outcompete the endothermic heterofission of PEN singlets in blends exceeding the doping regime. In a blend with low PEN concentration, however, the heterofission of PEN singlets as proposed in the 1970s [106, 107] was observed in the time-domain, which allowed to determine a time constant of 26 ps for this process. The exothermic heterofission of TET singlets was found to be outcompeted by FRET. Therefore, a similarly fast heterofission of TET singlets as PEN homofission could

be excluded, which demonstrates the importance of other parameters beyond the energy balance, such as the coherent admixture of ^{1}(TT) states to S_1, to achieve ultrafast SF.

The first time-resolved observation of the endothermic, intermolecular heterofission [106, 107] demonstrates the feasibility to examine heterofission time constants in thin film blends. Due to the asymmetric nature of the ^{1}(TT) state involved in heterofission, heterostructures of two SF materials might serve as promising, alternative model systems for investigations of the SF process [78, 338] compared to neat SF materials.

To conclude, fluorination of compounds, spacer blends as well as blends of two SF materials have been demonstrated to provide powerful tools for impacting the SF process in various ways to examine key parameters [49, 84–87]. The experimental investigation of effects that strongly alter the SF process leads to a better understanding of the microscopic mechanisms guiding this process and contributes to the development of guidelines for the synthesis of high-efficiency SF materials [37–43].

8.2 Outlook

The presented results offered new insights into the process of SF. Based on these results, new questions and ideas arose, which are outlined in the following and which could be the focus of follow-up studies.

The investigations on the photophysics of FPENs showed that the partial charge distribution can have a significant impact on the SF rate. Therefore, interesting future work might focus on

- the analogous partial fluorination of TET.
- the photophysics of FPENs with a permanent dipole pointing along the molecular short axis, as synthesized recently [350].
- the role of partial charges in the SF process in PEN:PFP blends [78].

The finding that coherent and incoherent SF lead to differences in the sensitivity of the SF rate on spacer concentrations in spacer blends can be used as a tool to examine the SF mechanism in less investigated SF materials. Besides, mechanisms impacting SF in spacer blends might be further investigated by

- TET:spacer blends with spacer materials that do not lead to limited intermixing, but intermixing throughout all concentrations.
- a kinetic model for the evaluation of complete time traces of TRPL measurements on spacer blends, including triplet fusion and hopping between different sites [231].
- spacer blends with SF materials, for which SF is exothermic and incoherent (such as hexacene [61]), or endothermic and coherent (such as RUB [60]).

- using spacer materials with different polarizabilities, which would differently shift the energy of S_1 and would allow to study the importance of the energetic resonance of S_1 and the vibrationally excited ^{1}(TT) state.

Finally, the time constant of intermolecular heterofission in PEN:TET blends has been reported using TA spectroscopy in this work. Despite the variety of conclusions that were drawn based on PEN:TET blends, the microscopic mechanism and prerequisites for such a heterofission process are yet largely unclear. Future research might therefore examine

- heterofission time constants of the singlets on the compound with a smaller band gap in analogous solid solutions to PEN:TET blends, such as ADT:TET blends or PEN:ADT blends.

- systems, in which heterofission of singlets at the compound with lower band gap is exothermic, while homofission is endothermic. In such a system, heterofission might outcompete homofission.

- the nature of the coupling between S_1 and the electronically coupled ^{1}(TT) state after heterofission, e.g. by calculations. In particular asymmetric contributions of CT states to the SF process [351] might be a new aspect compared to homofission.

A. Appendix: Techniques and materials

A.1 Description of molecular orientations in the unit cell

Besides their unit cell parameters, different HB aggregates can be compared by the orientation of the two translationally inequivalent molecules with respect to the unit cell. This orientation can be described by three Euler angles, named Θ, χ and φ as depicted in Fig. A.1 [154]. The three angles describe the orientation of a single molecule. The difference $\Delta\Theta = \Theta_2 - \Theta_1$ between the Θ angles of the two translationally inequivalent molecules corresponds to the difference in pointing direction. Only $\Delta\Theta \approx 0$ denotes coplanar long axes and a well-defined HB aggregate. Furthermore, the angle between the two molecular plane normals is here defined as the HB-angle Φ [154].

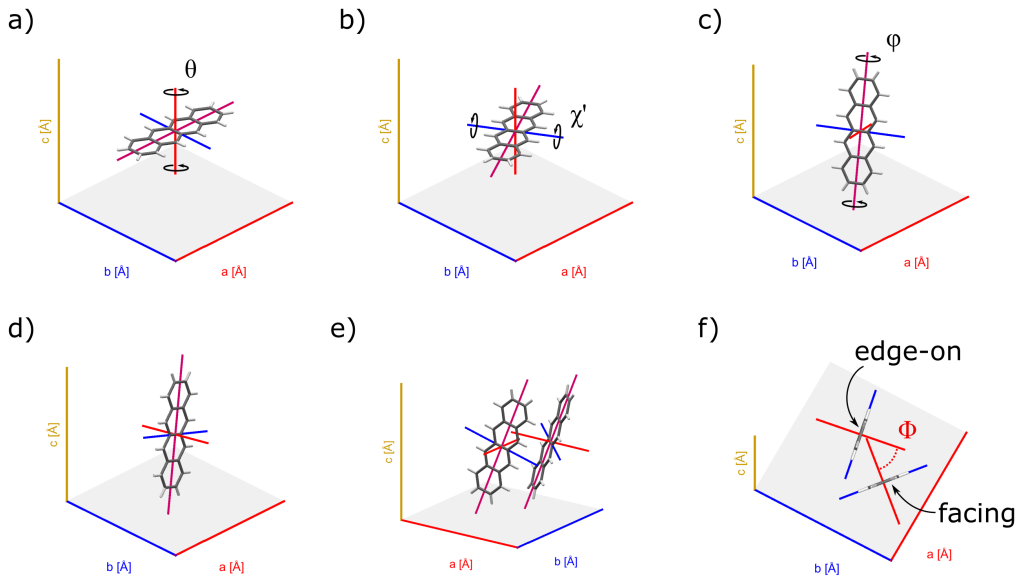


Figure A.1: Three-angle-description of molecular orientation [154]. (a) Rotation around the normal of the molecular plane. (b) Rotation around the short axis of the molecule. (c) Rotation round the long axis of the molecule. (d) Final orientation of one molecule. (e) HB arrangement (f) HB-angle Φ, view of panel e) along the long axes of the molecules.

Acenes

The angles χ_i and φ_i for each molecule, and $\Delta\Theta$ and Φ for both molecules have been calculated in this work for selected crystal structures reported in literature and are shown in Tab. A.1.

The HB-angle ($\Phi \approx 50-56°$) and the inclination angles ($\chi \approx 20-25°$) of the shown single crystal structures of TET, PEN and hexacene ($n=6$) are very similar. Furthermore, also the tilt angles of the two translationally inequivalent molecules, one rather facing the HB-plane ($\varphi_2 \approx 70-75°$), one rather oriented edge-on ($\varphi_1 \approx 14-23°$) are reported consistently between the structures. The molecular Euler angles of the single crystal structure of anthracene ($n=3$) [352], however, are different, as the inclination angle is lower and both molecules have the same tilt around their long axes. Furthermore, a high $\Delta\Theta$ denotes a strong deviation from an ideal HB aggregate, since the two long axes are not oriented parallel. The different angles might be a result from the short length of the molecules making them prone to rotational Coulomb interactions. The HB-angle is, however, yet remarkably similar to those of crystal structures of higher acenes.

For thin films of PEN (PENCEN10 in Tab. A.1), smaller inclination angles ($\chi \approx 6°$) have been found in strong contrast to the single crystal polymorphs [277], however, still with a similar HB-angle. For TET, a similar thin film structure with high inclination angles has been calculated [230], however, experimentally only unit cell parameters [281] and no atom positions have been reported yet.

Table A.1: Molecular orientation angles and lattice spacings of acenes with n benzene rings calculated from selected reported structures (str.) of acenes from the Cambridge Crystallographic Data Centre (CCDC [280]). The angles are defined in the main text, d is the lattice spacing between two HB-planes. All angles are given in degree (°), d is given in Å.

n	CCDC ID	Str.	χ_1	χ_2	φ_1	φ_2	$\Delta\Theta$	Φ	d	Ref.
3	ANTCEN	SC	30.8	30.8	37.9	37.9	28.2	51.4	9.19	[352]
4	TETCEN	SC	20.9	22.2	17.0	70.1	3.2	50.9	12.24	[149]
4	TETCEN01	SC	21.3	23.6	14.3	70.6	4.9	51.7	12.07	[152]
5	PENCEN	SC	20.4	22.1	16.3	74.5	5.2	52.7	14.46	[149]
5	PENCEN01	SC	24.9	25.5	22.0	73.4	0.4	51.8	14.05	[152]
5	PENCEN02	SC	24.4	25.2	21.5	72.8	0.6	52.1	14.11	[353]
5	PENCEN10	TF	5.6	6.0	51.9	76.3	2.7	54.3	15.40	[277]
6	ZZZDKE01	SC	25.1	25.8	21.9	73.3	0.4	51.6	16.28	[354]

Phenacenes

The definition of a long axis for phenacenes is not as straightforward as for acenes. For the following calculations, the line connecting every second carbon ring has been taken as the long axis. This choice slightly impacts the angles, but not the qualitative trends. In Tab. A.2, molecular orientations of selected crystal structures of CRY and PIC are shown. The inclination angles χ are slightly smaller, the HB-angles Φ slightly larger compared to those of acenes. In contrast to acenes, both molecules of the HB arrangement have exactly the same angle φ describing the tilt around their long axes. Thus, there is no distinction between one HB-plane-facing and one edge-on molecule, but both exhibit an intermediate angle.

Table A.2: Molecular orientation angles and lattice spacings of phenacenes with n benzene rings calculated from selected reported structures (str.) of phenacenes from the Cambridge Crystallographic Data Centre (CCDC [280]). The angles of CRY are those of only two out of four molecules in the unit cell, the other two molecules in this unit cell, however, are very similar. All angles are given in degree (°), d is given in Å.

n	CCDC ID	Str.	χ_1	χ_2	φ_1	φ_2	$\Delta\Theta$	Φ	d	Ref.
4	CRYSEN	SC	12.5	12.5	20.6	20.6	17.4	58.1	22.61	[156]
5	ZZZOYC01	SC	14.7	14.7	34.9	34.9	12.0	57.8	13.51	[155]

A.2 Calculation of growth rates from the molar mixing ratio

The growth rate r_i of a compound indexed by i is given by

$$r_i = \frac{V_i\ \Delta N_i}{A\ \Delta t} \tag{A.1}$$

with the volume V_i of one single molecule of compound i and the flux of molecules ΔN_i through an area A within time interval Δt. It has the dimension thickness per time. The *molar ratio* $x \in [0, \infty)$ of a binary mixture ($i \in \{1, 2\}$) is given by

$$x = \frac{\Delta N_1}{\Delta N_2} = \frac{1}{v}\,\frac{r_1}{r_2}\,, \qquad v = \frac{V_1}{V_2}\,. \tag{A.2}$$

The *molar fraction* $p_1 \in [0, 1]$ of compound 1 is connected to the *molar ratio* x by

$$x = \frac{p_1}{1 - p_1}, \qquad p_1 = \frac{x}{1 + x}\ . \tag{A.3}$$

Single growth rates

The growth rates r_i of the compounds can be expressed using the definition of the total growth rate

$$R = r_1 + r_2 \tag{A.4}$$

as

$$r_1 = \frac{xv}{1 + xv}\,R\,, \qquad r_2 = R - r_1 = \frac{1}{1 + xv}\,R\,. \tag{A.5}$$

Uncertainty

From Eq. A.2 and A.3 follows

$$p_1 = \frac{r_1}{r_1 + vr_2}\ . \tag{A.6}$$

The partial derivatives with respect to the two growth rates are

$$\frac{\partial p_1}{\partial r_1} = \frac{vr_2}{(r_1 + vr_2)^2}\ , \tag{A.7}$$

$$\frac{\partial p_1}{\partial r_2} = -\frac{vr_1}{(r_1 + vr_2)^2}\ . \tag{A.8}$$

The propagation of systematic uncertainties Δr_1 and Δr_2 into the uncertainty of the molar fraction Δp_1 therefore is

$$\Delta p_1 = \frac{vr_2\Delta r_1 + vr_1\Delta r_2}{(r_1 + vr_2)^2}\ . \tag{A.9}$$

Two types of uncertainties will be used in the following. (A) an uncertainty of a percentage ϕ of the value of r_i, thus $\Delta r_i^A = \phi r_i$, which also includes an uncertainty from the linear scaling factor (see Sec. 3.1). (B) an uncertainty Δr^B that is independent of r_i and the same for r_1 and r_2, e.g. due to underlying drifts in the QCM measurement. With Eq. A.2, r_2 can be expressed by r_1 and with Eq. A.5, r_1 by R. One obtains (see Fig. A.2)

$$\Delta p_1^A = \frac{2x}{(x+1)^2}\,\phi\,, \tag{A.10}$$

$$\Delta p_1^B = \frac{(1+xv)^2}{v(x+1)^2}\frac{\Delta r^B}{R}\,, \tag{A.11}$$

with the relation between p_1 and x from Eq. A.3

$$x = \frac{p_1}{1-p_1}\,.$$

Type (A) uncertainty of the molar fraction p_i dominates for blends with a concentration towards 50 %, as illustrated in Fig. A.2. For blends with a concentration towards 0 % or 100 % (doped films), the type (B) uncertainty dominates.

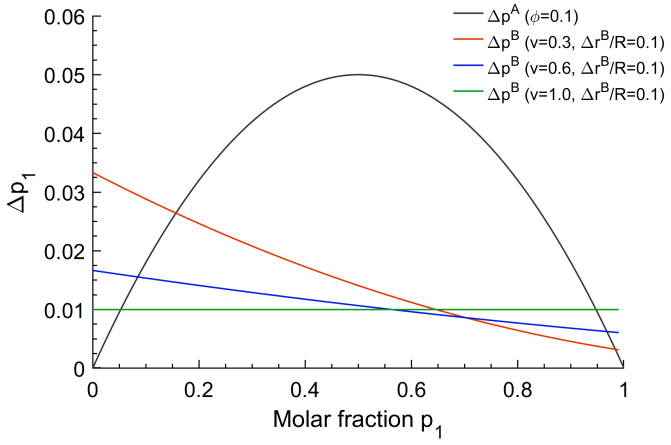


Figure A.2: Propagated uncertainty of the molar fraction as a function of the molar fraction.

B. Appendix: Fluorinated pentacenes

B.1 Orientation of crystallites in reciprocal space maps

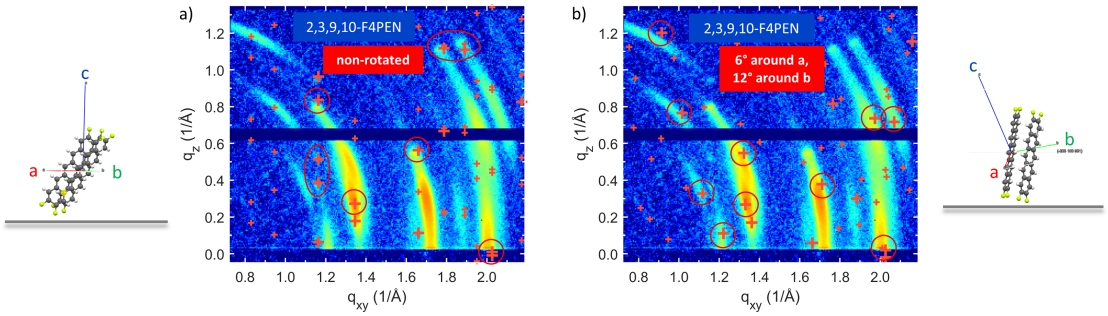


Figure B.1: a,b) Reciprocal space map of a thin film of 2,3,9,10-F4PEN measured at the *Xeuss system* and calculated reflections from a crystal structure of this compound with different orientations [121]. a) Orientation of the crystal structure with the $c^\star$ direction along the substrate normal. b) Orientation of the crystal structure obtained upon rotation from $c^\star$ pointing along the substrate normal around the crystal a and b axes by 6° and 12°, respectively. Two different sizes are used for the markers to clarify the relative intensity of the calculated reflections. Circles show the reflections that the respective orientation primarily reproduces. Next to each reciprocal space map, views parallel to the substrate on the two basis molecules and the crystal axes are shown.

The reciprocal space map of a thin film of 2,3,9,10-F4PEN is shown in Fig. B.1 in comparison to calculated reflections of the same crystal structure but different orientations to the substrate. All experimental reflections can be explained with two orientations. In the first orientation, $c^\star$ is parallel to the substrate normal, see Fig. B.1a. In the second orientation the crystal structure is tilted around the crystal a and b axes by 6° and 12°, respectively. In this case, the molecules are standing rather upright on the substrate. Importantly, a thin film phase with a smaller inclination angle χ would lead to a different diffraction pattern, and both orientations are consistent with the reported single crystal structure ($\chi \approx 33°$ [121]).

The reciprocal space map of a thin film of 1,4,9,10-F4PEN is shown in Fig. B.2 in comparison to calculated reflections of the single crystal structure [122] with different ori-

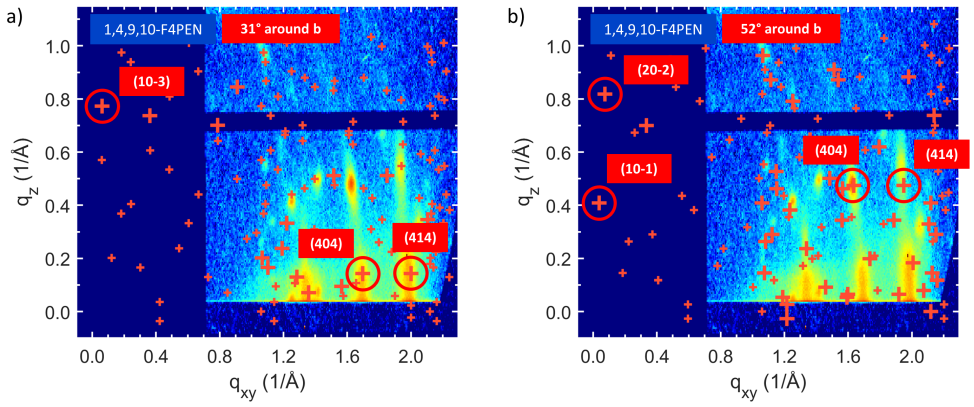


Figure B.2: Reciprocal space maps of a thin film of 1,4,9,10-F4PEN measured at the *Xeuss system* and calculated reflections from a crystal structure of this compound with different orientations [122]. The orientations are obtained by rotations of the crystal structure starting from an orientation with the $c^\star$ direction along the substrate normal. a) Rotation of the crystal structure around the crystal b-axis by 31°. b) Rotation of the crystal structure around the crystal b-axis by 52°. Two different sizes are used for the markers to clarify the relative intensity of the calculated reflections. Reflections discussed in the text are marked by circles and labeled.

entations to the substrate. Two orientations are necessary to explain the strongest reflections. The orientation shown in Fig. B.2a is obtained by rotation of the crystal structure around the crystal b-axis by 31° starting from the $c^\star$ direction along the substrate normal. This orientation brings the strongest reflections of the single crystal structure [122], (404) and (414), close to $q_z = 0$, which explains the strong in-plane reflections observed in the reciprocal space map. The orientation shown in Fig. B.2b is obtained by rotation of the crystal structure around the crystal b-axis by 52° starting from the $c^\star$ direction along the substrate normal. The two strongest reflections of the crystal structure, (404) and (414), are shifted away from $q_z = 0$ towards higher q_z, and can explain the experimental reflections at higher q_z. The complex diffraction pattern, however, does not suggest the two orientations to be exclusive, and further orientations might be present. Notably, the two mentioned orientations locate the (10-3), (10-1) and (20-2) reflections close to the $q_{xy} = 0$-line (see Figs. B.2a and B.2b) and should be observable in the XRR data.

It is further noteworthy that for the single crystal structure a rotation of 26° and 57° instead of 31° and 52° ideally transforms the (001) plane into the (10-1) and the (10-3) plane, respectively [122]. These ideal rotations, however do not reproduce the position of the strong (404) and (414) reflections in the reciprocal space map. The reason for the 5° mismatch each is most likely the slight deviation of the unit cell parameters. The two identified orientations correspond to different planes of the crystal structure being parallel to the substrate, see Fig. B.3. (10-1) planes are parallel to the molecular planes in this crystal structure, while (10-3) planes only connect every next nearest-neighbor package of four molecules. The (404) plane producing strong in-plane reflections is aligned with the molecular long axes.

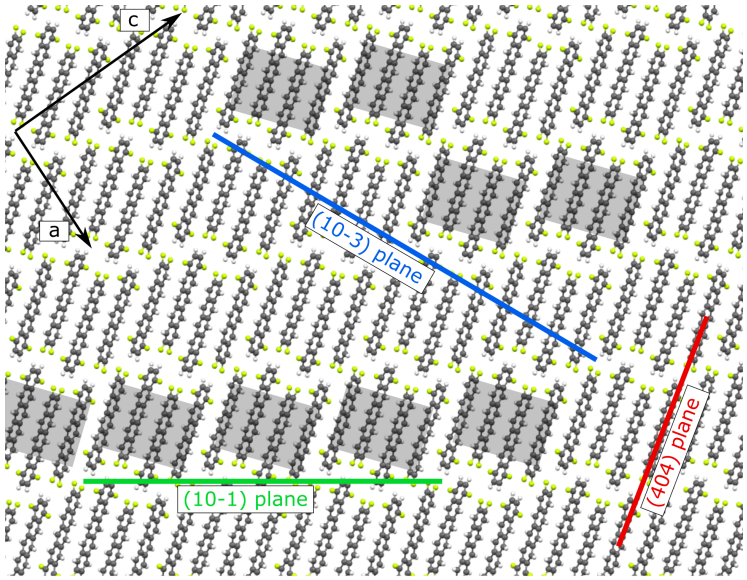


Figure B.3: View along the b*-direction on the reported crystal structure of 1,4,9,10-F4PEN. Black arrows indicate the unit cell axes a and c, colored lines indicate the orientation of crystal planes. Some groups of four molecules are colored in grey to clarify their alignment with respect to the molecular planes.

B.2 Relation between molecular length and lattice spacing

The relation between molecular lengths l_m and lattice spacings d_ls,

$$d_\mathrm{ls} = l_\mathrm{m} \cdot \cos(\chi) - d_\mathrm{id} \tag{B.1}$$

with the inclination angle from the substrate normal χ and an interdigitation d_id between different molecular planes, is sketched in Fig. B.4.

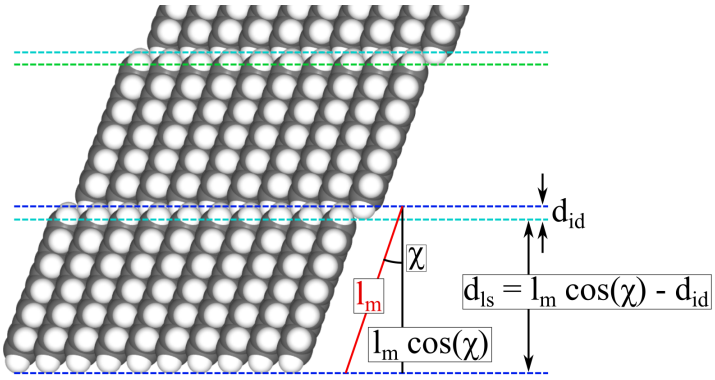


Figure B.4: Side view of translationally equivalent molecules in a PEN bulk structure [149] to demonstrate the calculation of the lattice spacing d_ls from the molecular length l_m, the inclination angle χ and the interdigitation d_id.

B.3 Davydov-splitting fits and photoluminescence spectra

Fits of the DS

Fit results of the DS of thin films of PEN and FPENs are shown in Fig. B.5.

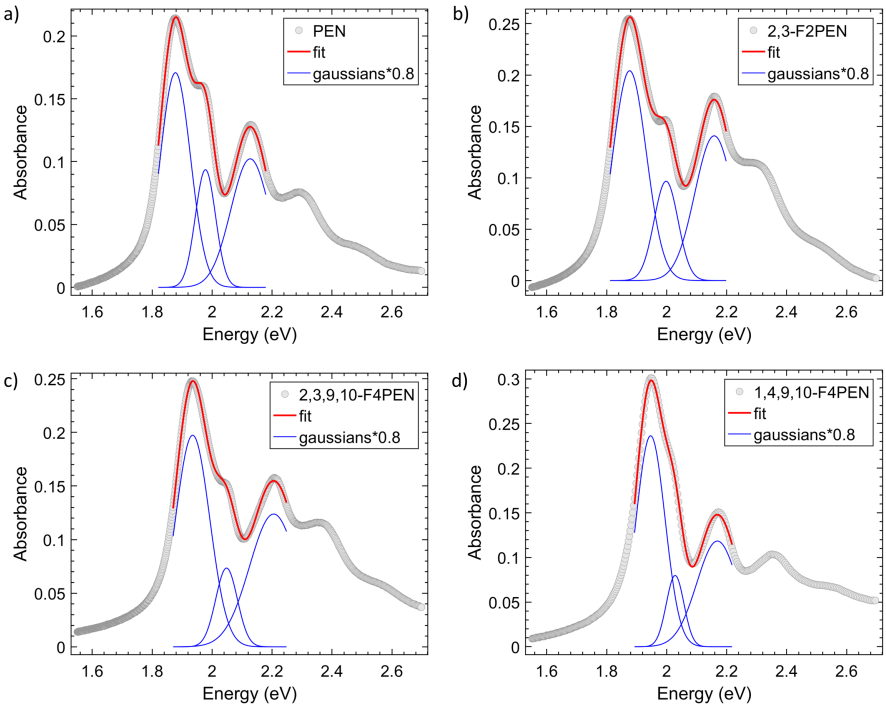


Figure B.5: Fits of the DS of different FPENS. a) PEN: 101 meV, b) 2,3-F2PEN: 125 meV, c) 2,3,9,10-F4PEN: 115 meV, d) 1,4,9,10-F4PEN: 82 meV. The single gaussians are scaled to 80 % for better visibility.

Steady-state PL spectra

Steady-state PL spectra of thin films of PEN and FPENs are shown in Fig. B.6. The PL spectra of 2,3-F2PEN, 2,3,9,10-F4PEN (Fig. B.6a) are similar to that of PEN, although slightly shifted in accordance with their absorption spectra. The PL spectrum of 1,4,9,10-F4PEN (Fig. B.6a) exhibits an additional shoulder at 1.85 eV, which likely originates from the different molecular orientations in the crystal structure of this compound [122].

No steady-state PL was observed for 1,4,8,11-F4PEN with an excitation wavelength of 633 nm (Fig. B.6b). The increase of the PL spectra towards lower energies is a background from the detector. With 532 nm excitation wavelength a strong PL signal is observed with a maximum above the band-gap of thin films of 1,4,8,11-F4PEN. Upon repeating measurements on the same spot this signal continuously increased in intensity, strongly suggesting it to be connected to the photodegradation of the sample. Since the energy of its maximum is close to that of the 0-0 transition of dissolved 1,4,8,11-F4PEN (Fig. B.6b), the emission observed with 532 nm excitation wavelength can be assigned to emission from

isolated 1,4,8,11-F4PEN molecules. These isolated molecules most likely originate from the degradation of the sample upon illumination (see Sec. B.5).

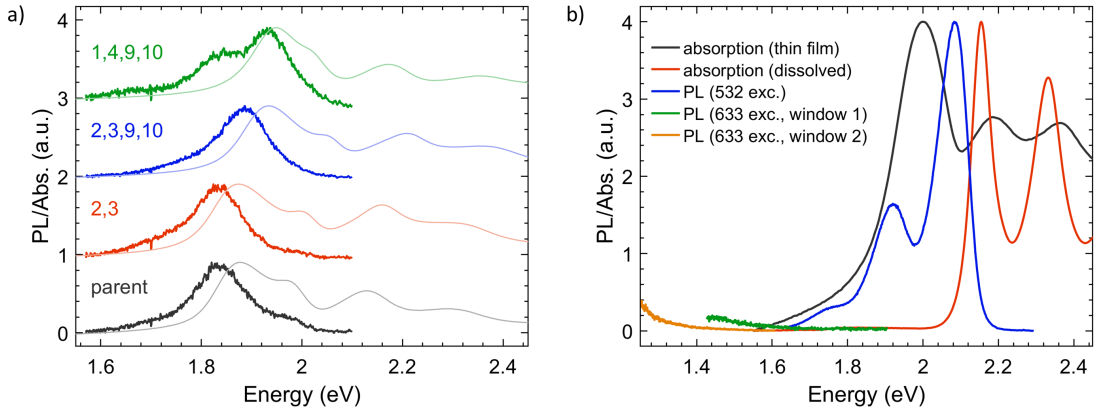


Figure B.6: a) Normalized PL spectra (thick lines) of PEN and FPENs with 633 nm excitation wavelength in comparison to the respective absorption spectra (thin lines). b) PL spectra of 1,4,8,11-F4PEN with two different excitation wavelengths. PL spectroscopy has been performed with a LabRam HR 800 spectrometer (HORIBA Jobin Yvon, France) as well as a frequency-doubled Nd:YAG laser and a He:Ne laser for 532 nm and 633 nm excitation wavelength, respectively. All samples were kept in nitrogen atmosphere during the measurement.

B.4 Fluence-dependent TA spectroscopy

TA maps of thin films of PEN and FPENs measured at different fluences are shown in Fig. B.7 for *Vis-probe* measurements and in Fig. B.8 for *IR-probe* measurements.

EAS obtained from GA of TA measurements on thin films of PEN and FPENs are shown in Fig. B.9. As described in the main text, EAS that are similar to previous ones are shown in grey. Comparisons between time traces and fits extracted from the GAs for each measurement are shown in Fig. B.10. Comparisons between time traces of TA measurements with different fluences are shown in Fig. B.11.

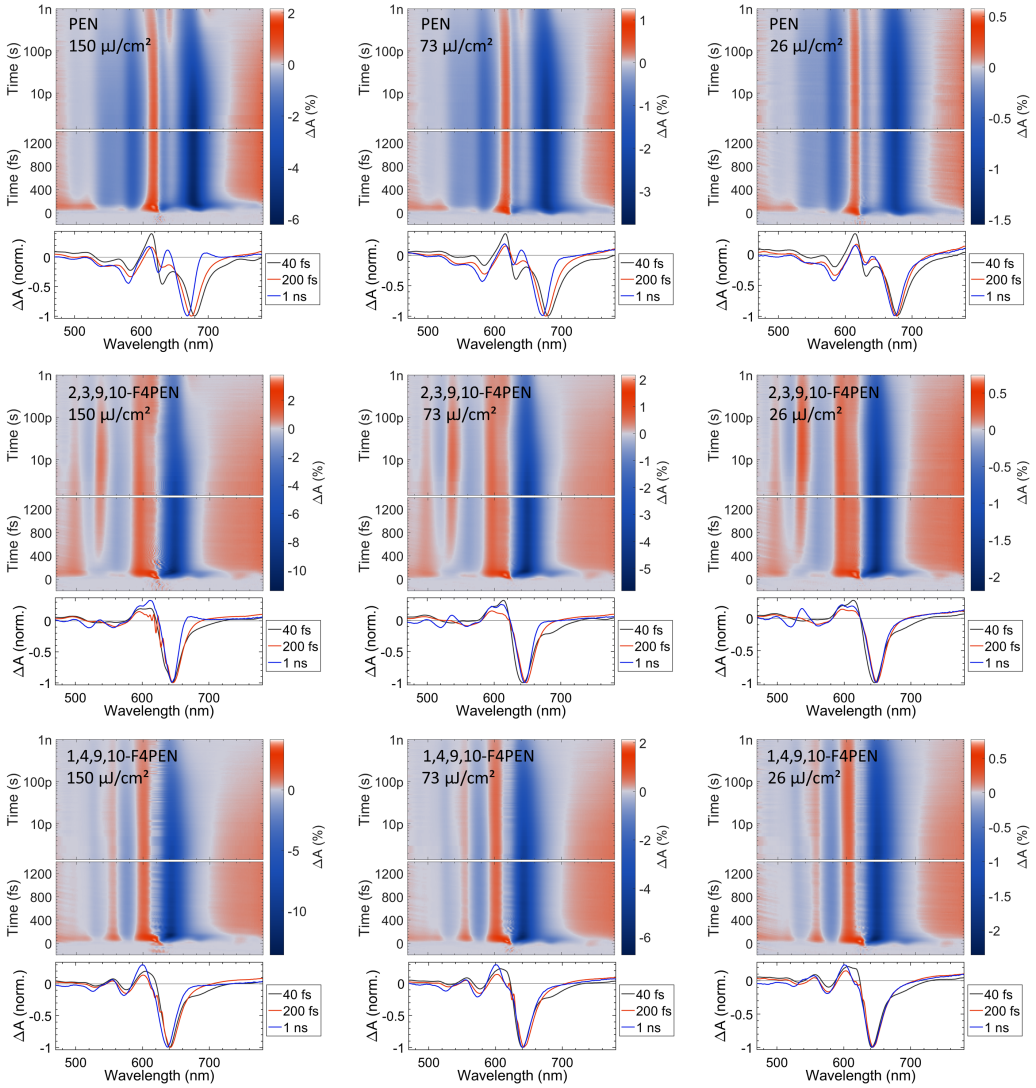


Figure B.7: TA maps of PEN and different FPENs using *Vis-probe*. For all measurements, an excitation wavelength of 620 nm has been used. The fluences are shown in the respective panel. Beneath each TA map, TA spectra extracted at different times of different compounds are shown. Parts of the data published in Ref. 299.

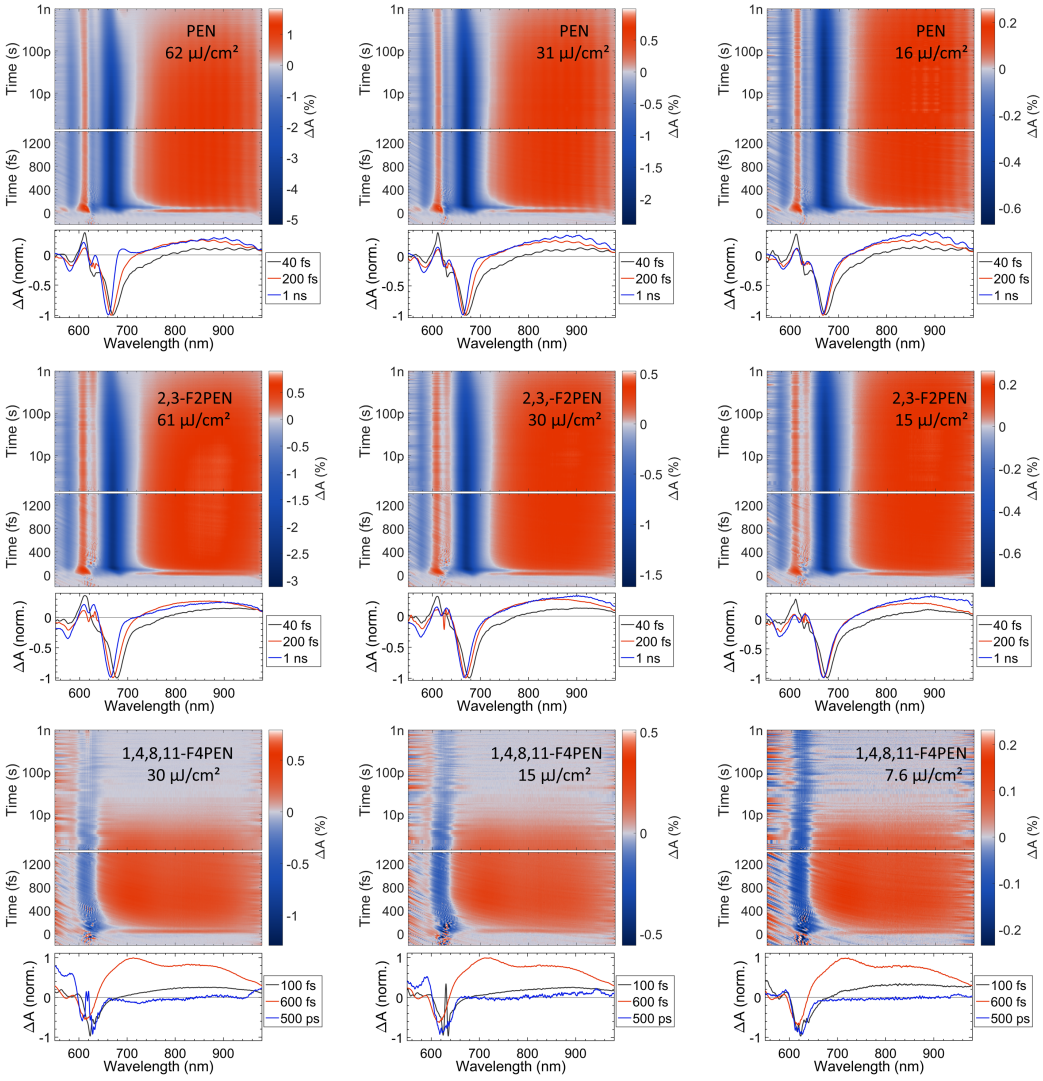


Figure B.8: TA maps of PEN and different FPENs using *IR-probe*. For all measurements, an excitation wavelength of 620 nm has been used. The fluences are shown in the respective panel. Beneath each TA map, TA spectra extracted at different times of different compounds are shown. Parts of the data published in Ref. 122.

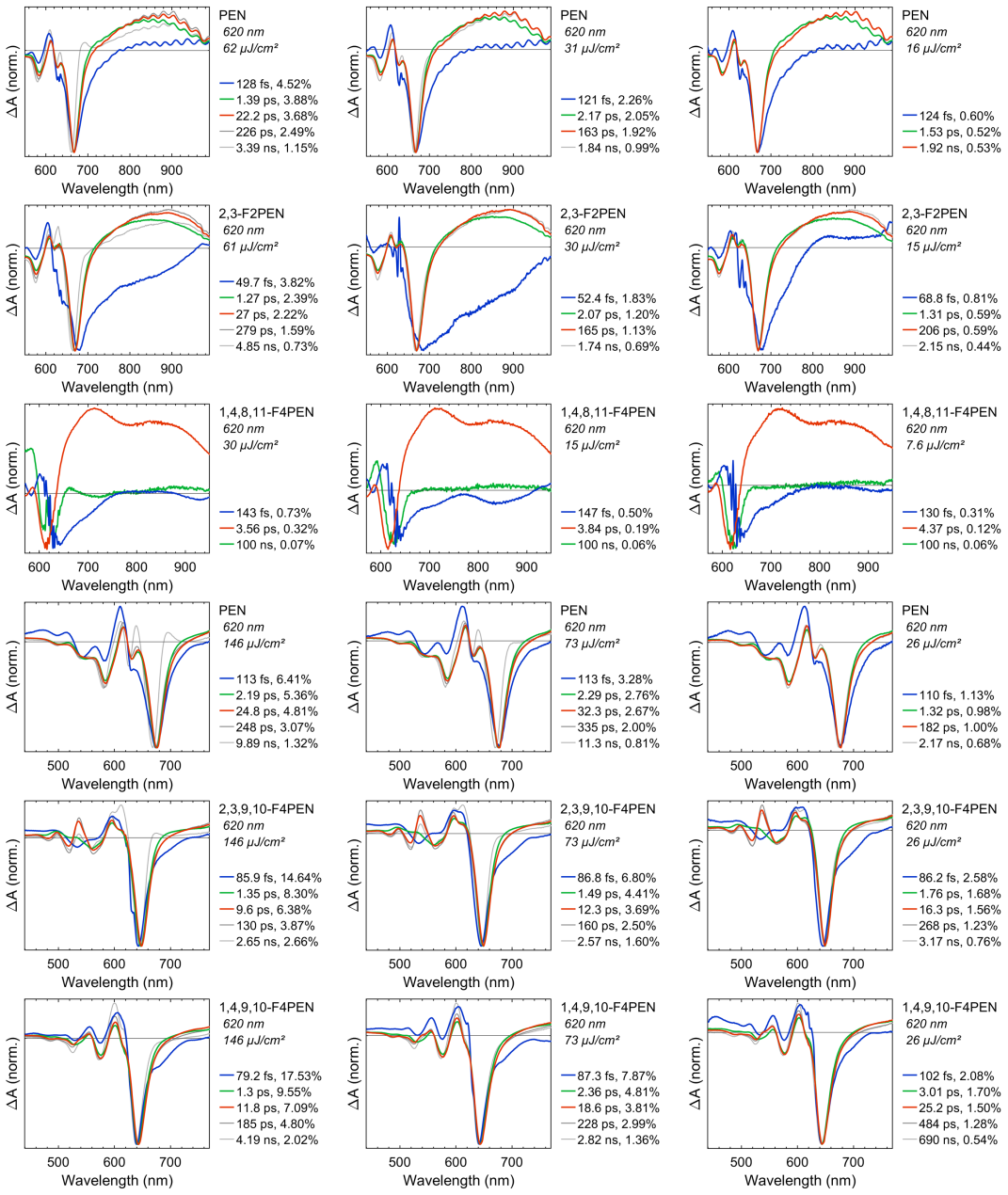


Figure B.9: Normalized EAS and corresponding time constants of a GA of TA measurements on thin films of PEN and FPENs using *IR-probe* (top three rows) and *Vis-probe* (bottoms three rows). The legend gives the time constant for the decay into the following species each, as well as the amplitude of the EAS before normalization. Parts of the data published in Refs. 122 and 299.

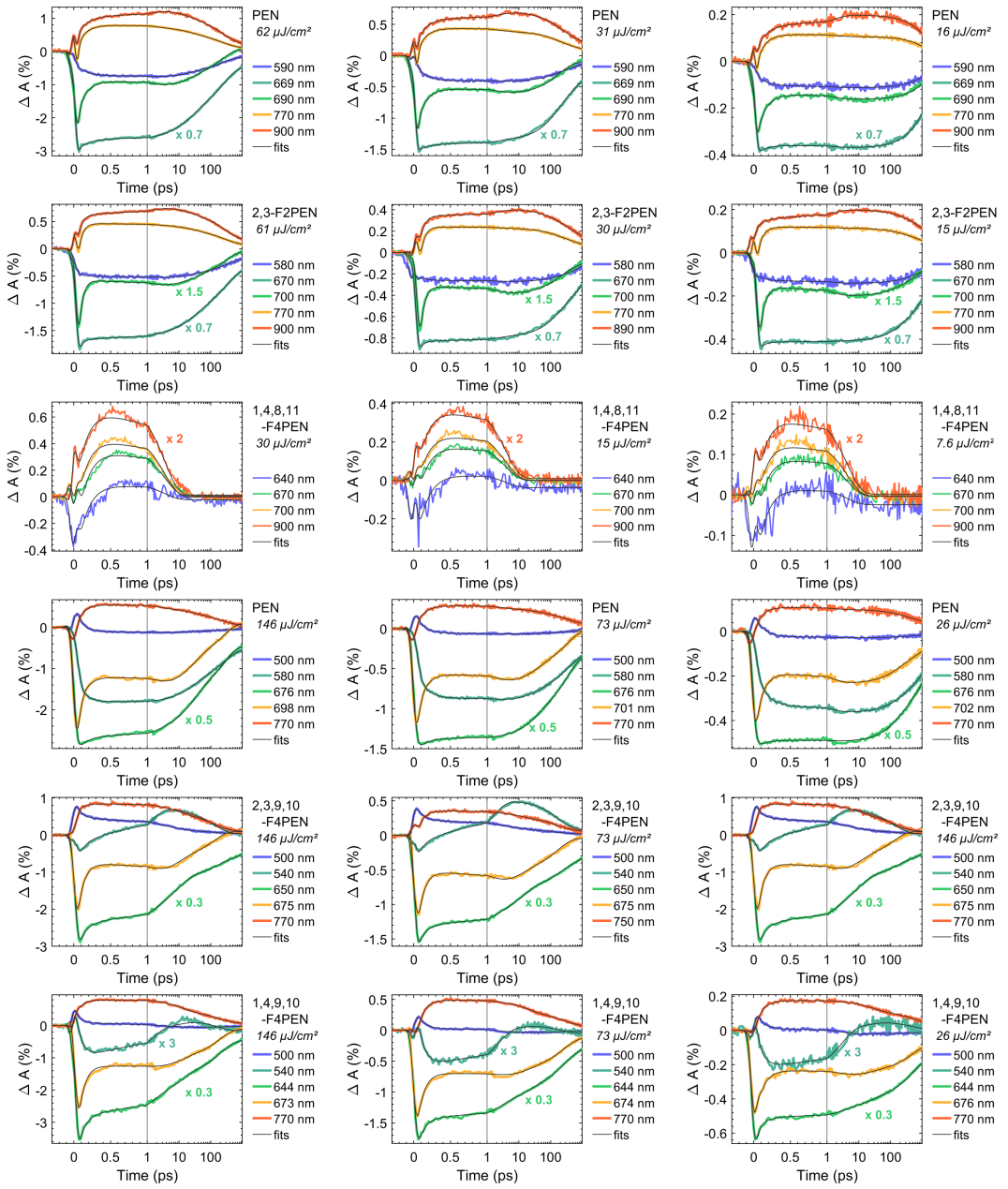


Figure B.10: Comparison of selected time traces of TA measurements on thin films of PEN and FPENs using *IR-probe* (top three rows) and *Vis-probe* (bottoms three rows) to the result of the GA. The vertical solid line shows the change from linear to logarithmic scale. Parts of the data published in Refs. 122 and 299.

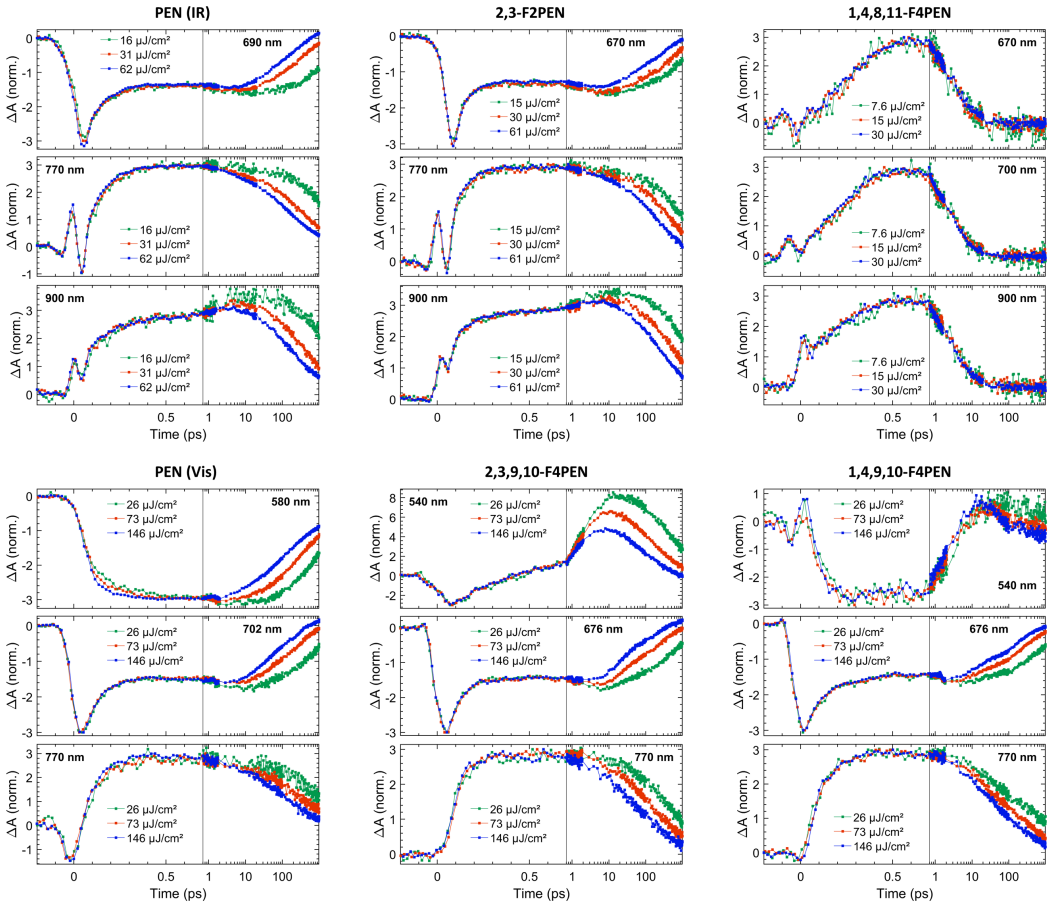


Figure B.11: Comparison of different time traces of TA measurements on thin films of PEN and FPENs using *IR-probe* (top three rows) and *Vis-probe* (bottoms three rows) and different fluences (see respective legend).

Fits of time traces of TA measurements on PEN

Fits of time traces of a TA measurement on PEN are shown in Fig. B.12. The time constant of these fits have large uncertainties. Spectral shifts might have significant impact on different time traces, which then do not exhibit the same time constant anymore. Furthermore, the coherent artifact around zero delay time prevents a simple convolution with a gaussian IRF and time traces can only be fitted starting at longer delay times. Fluctuations of the fit result due to a variation in the included data points can be used to determine the errorbars for a fit of a time trace (see errorbars in Fig. B.12d). There are, however, still significant variations between different time traces that are larger than the uncertainty within each fit.

A time constant of 80 fs has previously been reported for PEN using a time trace at 860 nm [97]. This time trace exhibits much larger time constants in this work. Time traces at 770 nm, however, are consistent with a time constant of 80 fs [97]. Is is further noteworthy that the average time constant over different time traces and fluences is 121 ± 28 fs, which is close to the fit result using a GA ($124\,^{+4}_{-37}$ fs).

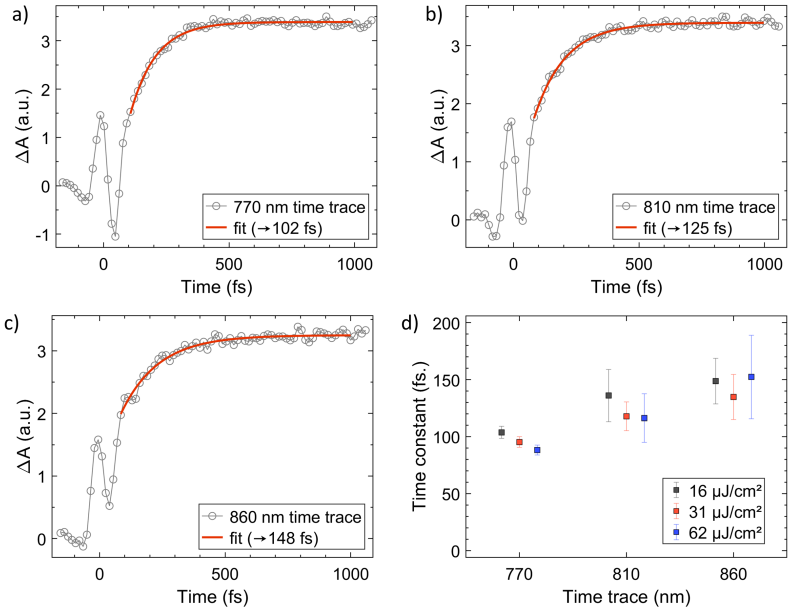


Figure B.12: a-c) Fits of time traces (wavelength see labeling) of a TA measurement on PEN conducted with a fluence of 31 µJ/cm^2. d) Time constants for different fluences as obtained from fits of time traces at different wavelengths. Note that the horizontal axis is not scaled and points of different fluences are horizontally offset for clarity.

B.5 Degradation of samples during TA measurements

Thin films of 1,4,8,11-F4PEN degraded during TA measurements, leading to an increasing reference transmission spectrum in the spectral range of the sample absorption as well as a continuous decrease of the TA signal between subsequent scans (see Fig. B.13).

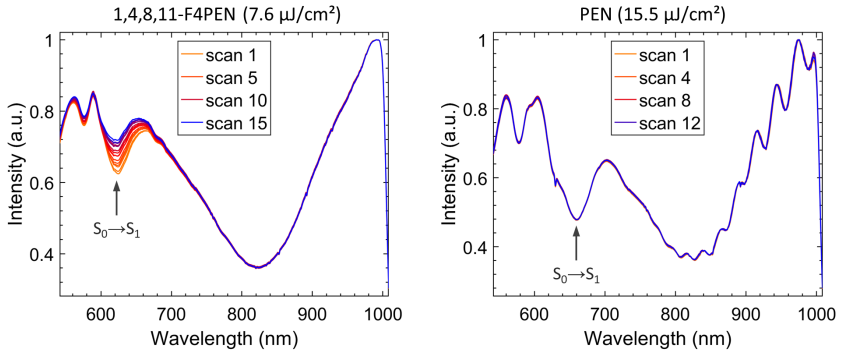


Figure B.13: Reference transmission spectra of subsequent scans of a TA measurement on a thin film of 1,4,8,11-F4PEN and PEN.

In order to account for and examine the impact of this degradation the single scans were scaled to the same intensity as the first scan before averaging the scans to the final TA map, see Fig. B.14a for the scaling factors. In Fig. B.14b, time traces extracted from TA maps are shown, for which a different number of scans have been averaged. Even though the signal decreased down to 40 % in this measurement the dynamics are not affected. All analyses were performed on TA maps with three scaled and averaged scans.

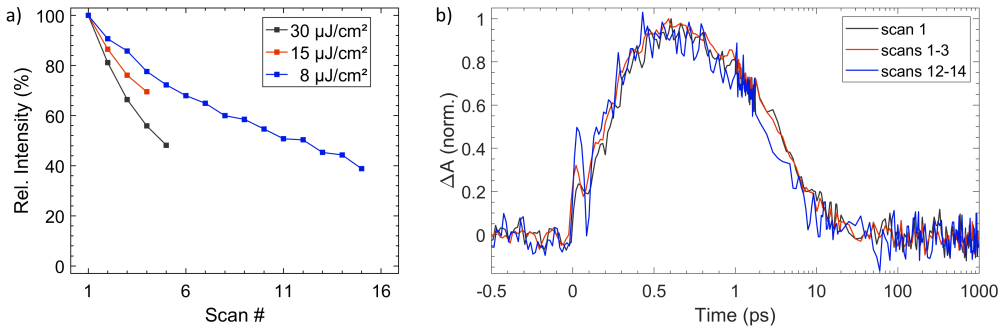


Figure B.14: Analysis of the degradation during TA measurements on 1,4,8,11-F4PEN. a) TA signal intensity integrated over the ESA and scaled to the first scan. b) Normalized time traces taken at 750 nm of TA measurements on 1,4,8,11-F4PEN with a fluence of 8 µJ/cm^2 and averaged for different numbers of scans (see legend).

B.6 Quantum chemistry calculations of molecular orbitals

Molecular orbitals of selected molecules, calculated using the ZINDO method, are shown in Fig. B.15. The molecular orbitals of PEN and PFP qualitatively agree with calculations in literature [126]. The pattern of HOMO and LUMO on the carbon atoms is the same for all three molecules.

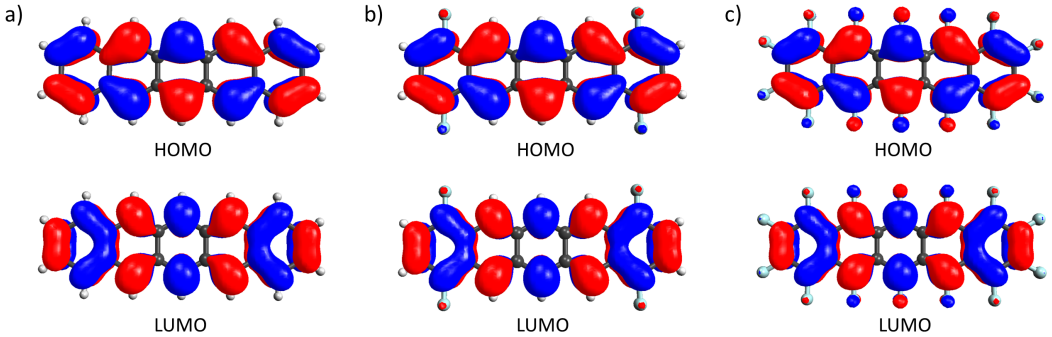


Figure B.15: HOMO and LUMO calculated using the ArgusLab software and ZINDO method of a) PEN, b) 1,4,8,11-F4PEN and c) PFP.

C. Appendix: Spacer blends

C.1 Magnetic field dependence of fluorescence decays

Magnetic-field-dependent fluorescence decays of TET:6PH blends are shown in Fig. C.1. Differences in the fluorescence decays originate from triplet fusion [82]. Since the magnetic-field effect is weaker in blends with low TET concentration, it can be concluded that the enhancement of the slower fluorescence decay does not originate from an enhanced triplet fusion rate but from TET monomers in the blends.

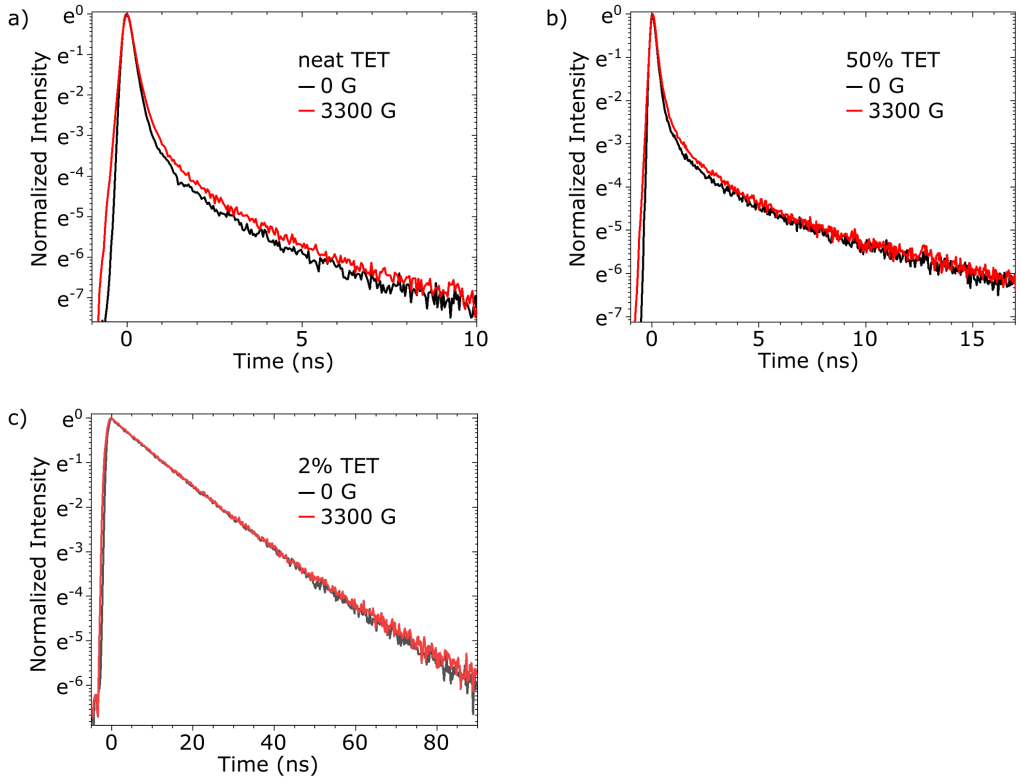


Figure C.1: Magnetic field dependence of fluorescence decays of different TET:6PH blends [271].

C.2 Davydov splitting

Fits of the absorption spectra of TET:spacer blends are shown in Fig. C.2. The reduced DS of the blends compared to the DS of neat TET (Fig. C.2c) indicates a reduced CT character of S_1 [195, 196].

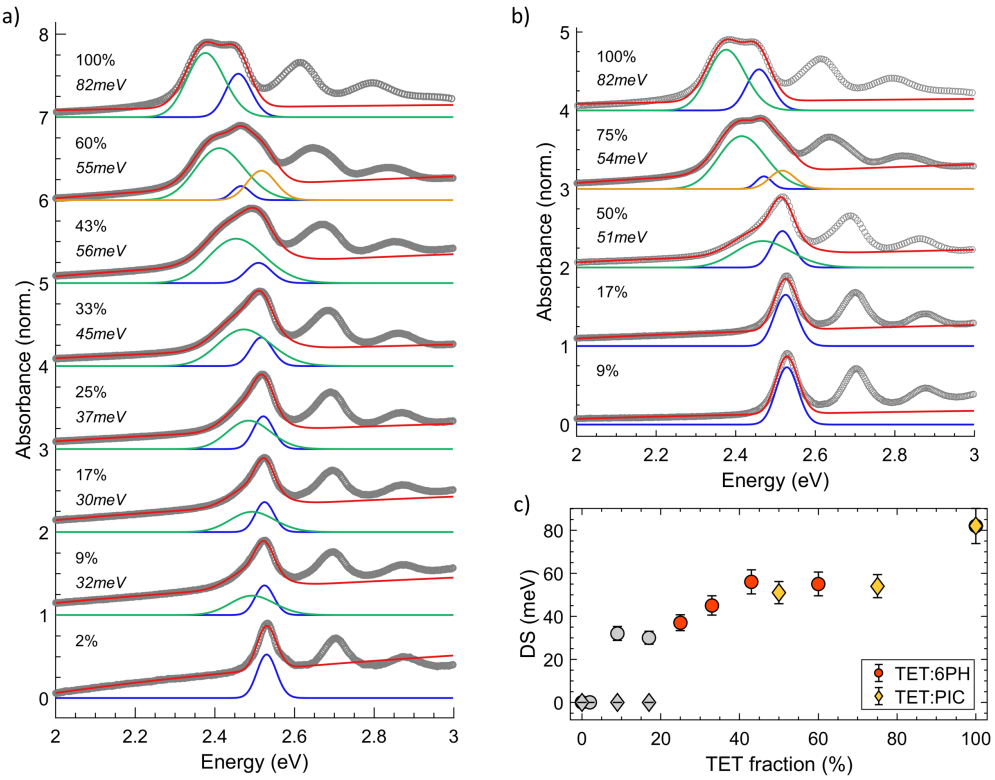


Figure C.2: a,b) Fits of the absorption spectra of TET:6PH blends (a) and TET:PIC blends (b) [271]. The fit function is the sum of gaussian functions and a first-order polynomial. The percentage and the energy shown for each spectrum denote the TET concentration and the DS, respectively. The DS is determined as the difference in position of the blue and the green gaussian. For blends with a phase separation (see Sec. 6.1, an additional gaussian (orange) was necessary in the fit. c) DSs extracted from the fits. Grey symbols indicate values for which the DS is not clearly observed.

C.3 Details on TRPL measurements

A fit of a gaussian function to the IRF for TCSPC measurements is shown in Fig. C.3.

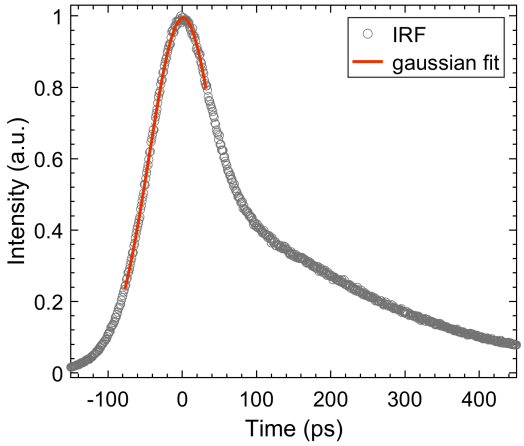


Figure C.3: Fit of a gaussian function to the IRF of the TCSPC measurements. The fit resulted in a FWHM/2 of 45 ps.

A comparison of TCSPC data of ADT:6PH blends to the cumulative IRF is shown in Fig. C.4. The cumulative IRF corresponds to a fluorescence decay that was observed for very long-lived species. The slow increase of the cumulative IRF at short times demonstrates that the corresponding increase in the TCSPC data of the blends is artificial.

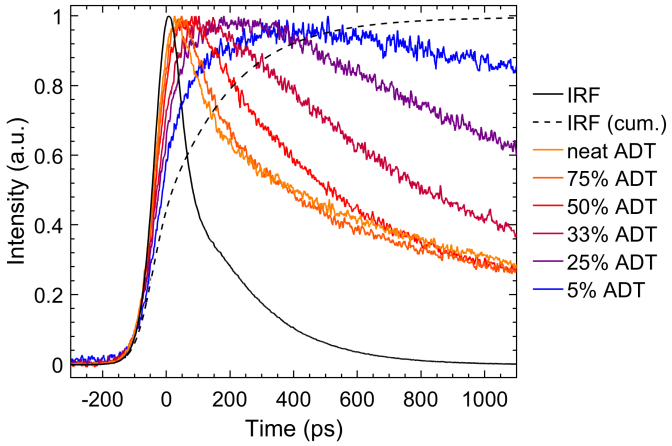


Figure C.4: TCSPC data on ADT:6PH blends. The decay curves have been set to zero below −200 ps, normalized and smoothed for better comparison. The dotted, black line is the cumulative IRF and corresponds to the dynamics one would obtain without any decay. The prolonged rise is an artifact that only occurs for long-lived species.

D. Appendix: Blends of pentacene and tetracene

D.1 Fluence-dependence of TA measurements on tetracene

TA measurements on neat TET with different pump fluences are shown in Fig. D.1. At low fluences, SF is observed by the decay of the 0-1 vibronic transition of the SE around 570 nm and a shift of the ESA at wavelengths above 620 nm to longer wavelengths. At higher fluences, the photoexcited singlet excitons can decay via SSA, leading to a faster decay of the SE, but no faster shift of the ESA.

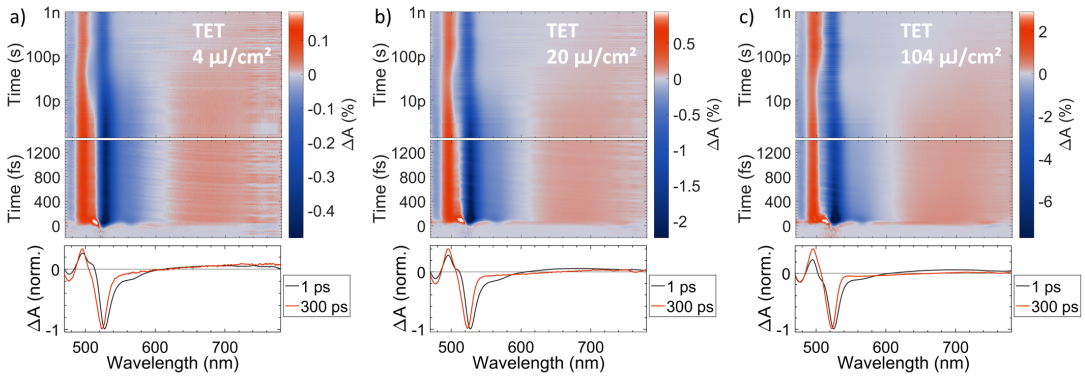


Figure D.1: TA measurements on neat TET with different pump fluences (see label).

D.2 Global analysis results

EAS obtained from GA of TA measurements on PEN:TET blends are shown for excitation wavelengths of $\lambda_{exc} = 620\,nm$ and $\lambda_{exc} = 520\,nm$ in Fig. D.2. Comparisons between time traces and fits extracted from the GAs for each measurement are shown in Fig. D.3.

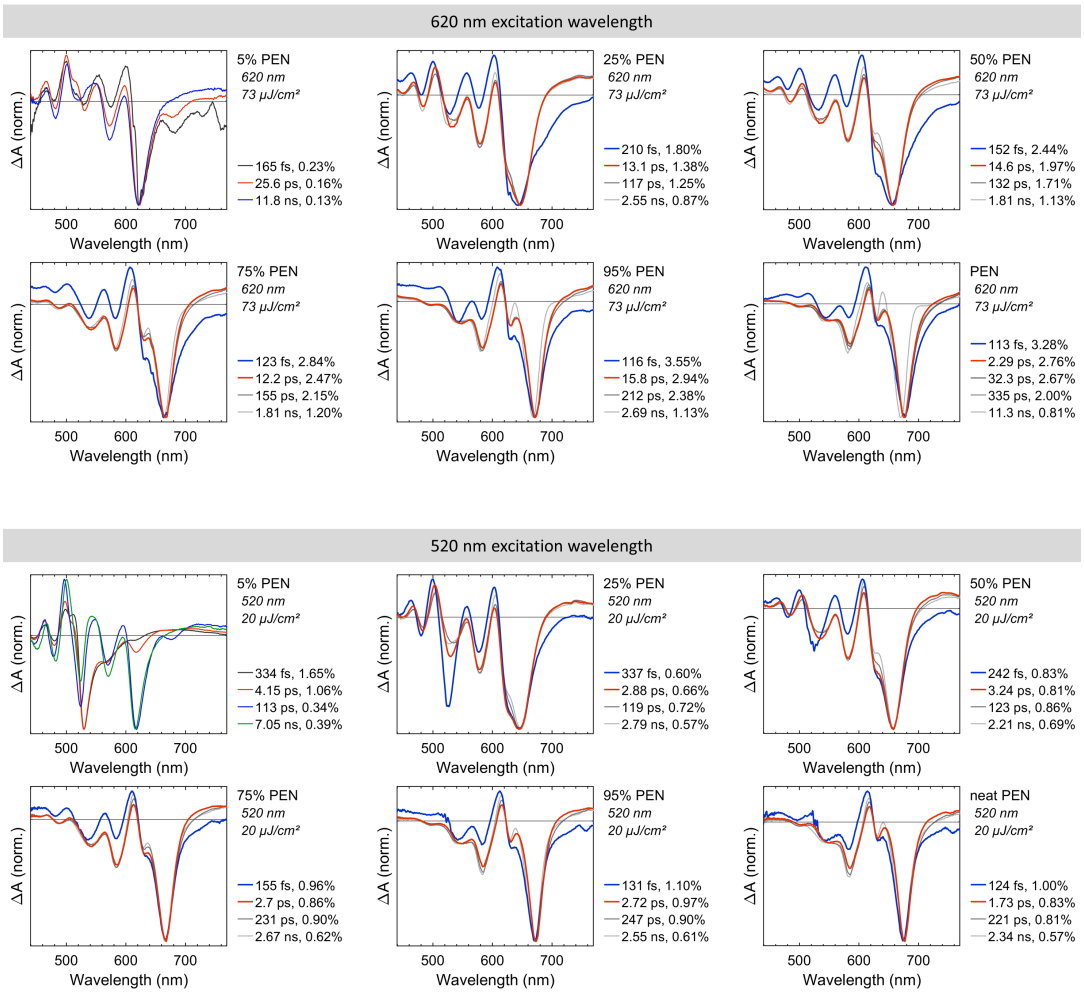


Figure D.2: EAS and corresponding time constants obtained by GA of the TA measurements with $\lambda_{exc} = 620\,nm$ and $73\,\mu J/cm^2$ pump fluence (top two rows), as well as with $\lambda_{exc} = 520\,nm$ and $20\,\mu J/cm^2$ pump fluence (bottom two rows). Data published in Ref. 338.

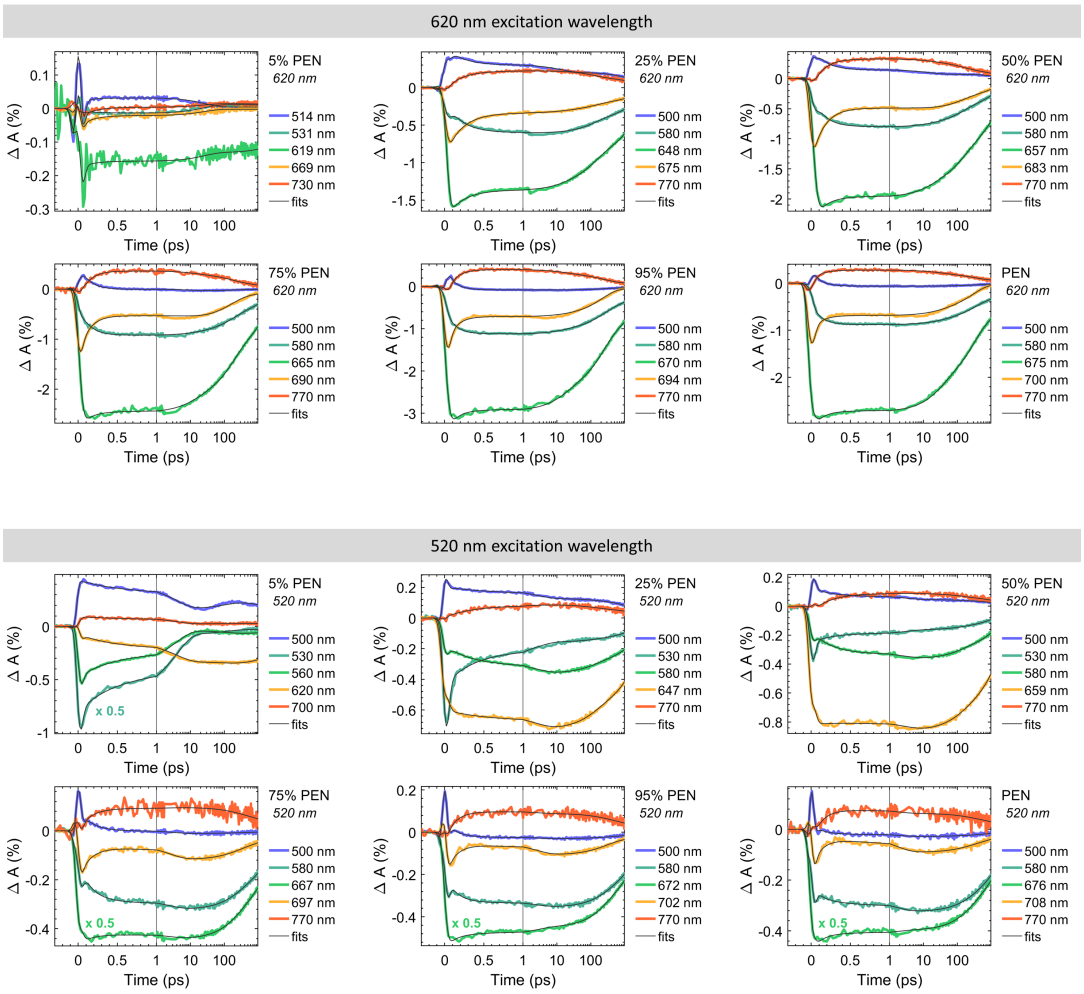


Figure D.3: Comparison of selected time traces of TA measurements on PEN:TET blends and neat PEN with $\lambda_{exc} = 620\,nm$ and $73\,\mu J/cm^2$ pump fluence (top two rows), as well as with $\lambda_{exc} = 520\,nm$ and $20\,\mu J/cm^2$ pump fluence (bottom two rows) to the result of the GA. The vertical solid line shows the change from linear to logarithmic scale. Data published in Ref. 338.

D.3 Förster resonance energy transfer rate

In order to calculate the sum

$$\sum_{i=1}^{24} \frac{\kappa_i^2}{R_i^6} \tag{D.1}$$

mentioned in the main text, the distances R_i acceptor molecules i as well as the orientation-factor κ_i of their TDMs to a donor molecule as shown in Fig. 7.17b have been calculated. These values have been calculated for a TET bulk [152] and a PEN thin film [277] structure, see Fig. D.4. For both compounds and structure types (bulk / thin film) most of the κ_i^2 are similar. For the calculation of the FRET rate in Fig. 7.16, the PEN thin film structure [277] has been used. The sum in Eq. D.1 is in this case $1.032 \cdot 10^{-4} \text{Å}^{-6}$. By far, the fastest FRET occurs between translationally equivalent molecules along the shortest primitive unit cell vector. FRET to these neighbors accounts for 80 % of the total sum in Eq. D.1.

Pentacene

target	κ^2	d [Å]	κ^2 d^{-6} [Å^{-6}]	relative
1a	0.006	4.819	4.791 E-07	1.00
1b	0.005	4.835	3.914 E-07	0.82
2	1.838	5.958	4.109 E-05	85.77
2'	1.817	5.958	4.062 E-05	84.79
3	0.146	7.596	7.601 E-07	1.59
3'	0.136	7.596	7.080 E-07	1.48
4a	1.725	9.723	2.042 E-06	4.26
4b	1.724	9.698	2.072 E-06	4.33
5a	0.796	9.67	9.735 E-07	2.03
5a'	2.127	9.67	2.601 E-06	5.43
5b	2.133	9.637	2.663 E-06	5.56
5b'	0.804	9.637	1.004 E-06	2.10
6a	1.027	11.787	3.830 E-07	0.80
6b	1.044	11.767	3.933 E-07	0.82
7	1.838	11.916	6.420 E-07	1.34
7'	1.817	11.916	6.347 E-07	1.32
8	0.146	15.192	1.188 E-08	0.02
8'	0.136	15.192	1.106 E-08	0.02

Tetracene

target	κ^2	d [Å]	κ^2 d^{-6} [Å^{-6}]	relative
1a	0.013	5.125	7.174 E-07	1.50
1b	0.004	4.773	3.383 E-07	0.71
2	1.704	6.057	3.451 E-05	72.03
2'	1.49	6.057	3.017 E-05	62.98
3	0.252	7.838	1.087 E-06	2.27
3'	0.248	7.838	1.070 E-06	2.23
4a	1.261	10.155	1.150 E-06	2.40
4b	1.693	9.626	2.128 E-06	4.44
5a	0.761	10.251	6.558 E-07	1.37
5a'	1.047	10.251	9.023 E-07	1.88
5b	1.903	9.547	2.513 E-06	5.25
5b'	0.753	9.547	9.945 E-07	2.08
6a	0.873	12.353	2.457 E-07	0.51
6b	0.94	11.923	3.272 E-07	0.68
7	1.704	12.113	5.395 E-07	1.13
7'	1.49	12.113	4.717 E-07	0.98
8	0.252	15.675	1.699 E-08	0.04
8'	0.248	15.675	1.672 E-08	0.03

Figure D.4: Calculated orientation factors and distances of acceptor molecules as shown in Fig. 7.17b for a bulk PEN and a thin film TET structure [152, 277]. The targets with a prime denote donor-target combinations, for which the orientation factor differs if the donor/target assignment is displaced to a molecule translationally inequivalent to molecule 0 (e.g. 1a). Published in Ref. 338.

D.4 Diffusion-limited energy transfer rate

In order to justify the assignment of dynamics observed in the TET:PEN blend with 5 % PEN concentration to the diffusion of TET excitons before FRET from TET to PEN, an average time $\langle t_{\mathrm{ET}} \rangle$ for the entire process in this blend will be estimated in the following.

A diffusion constant of $D = 3 \times 10^{-2}\,\mathrm{cm^2 s^{-1}}$ has been reported for TET [345]. Each molecule (TET or PEN) in the blend occupies an in-plane area of approximately $22.6\,\mathrm{Å}^2$ [277], which corresponds to an average in-plane distance d_{nn} between nearest-neighbors of

$$d_{\mathrm{nn}} = \sqrt{22.6\,\mathrm{Å}^2} = 4.75\,\mathrm{Å} \tag{D.2}$$

Assuming normal diffusion [355], a hopping time constant t_{TT} from a TET molecule to another TET molecule can be calculated by

$$t_{\mathrm{TT}} = \frac{d_{\mathrm{nn}}^2}{2D} = \frac{(4.75\,\mathrm{Å})^2}{2 \cdot 3.3 \times 10^{-3}\,\mathrm{cm^2 s^{-1}}} = 37.7\,\mathrm{fs}\,. \tag{D.3}$$

As a first approximation, the hopping time from TET to PEN t_{TP} is in the following assumed to equal t_{TT}, i.e. the exciton created at TET hops within t_{TT} through the crystal, and after each hop it has a chance corresponding to the concentration c to reside on a PEN molecule. The effect of $t_{\mathrm{TP}} \neq t_{\mathrm{TT}}$ will be discussed later on. The average number of hops $\langle n \rangle$ until residing on a PEN molecule can be calculated by

$$\langle n \rangle = \sum_{n=1}^{\infty} n \cdot p_n(c)\,, \tag{D.4}$$

with the number of hops n and the probability $p_n(c)$ to encounter a PEN molecule for the first time at hop n. This probability is given by

$$p_n(c) = c \cdot (1-c)^{n-1}\,, \tag{D.5}$$

with the probability $(1-c)^{n-1}$ of hopping $n-1$ times to a TET molecule and the probability c to hop to a PEN molecule. Therefore, the average number of hops required to reach a PEN molecule is

$$\langle n \rangle = \sum_{n=1}^{\infty} n \cdot c \cdot (1-c)^{n-1} = \frac{c}{1-c} \sum_{n=1}^{\infty} n \cdot (1-c)^n = \frac{c}{1-c} \cdot \frac{1-c}{c^2} = \frac{1}{c} \tag{D.6}$$

using the derivative of the geometric series. Hence, within the approximation $t_{\mathrm{TP}} = t_{\mathrm{TT}}$, the average diffusion-limited FRET time $\langle t_{\mathrm{ET}} \rangle$ is in the 5 % PEN blend

$$\langle t_{\mathrm{ET}} \rangle = \langle n \rangle \cdot t_{\mathrm{TT}} = \frac{1}{c} \cdot t_{\mathrm{TT}} = \frac{1}{0.05} \cdot 37.7\,\mathrm{fs} = 754\,\mathrm{fs}\,. \tag{D.7}$$

If $t_{\mathrm{TP}} = t_{\mathrm{TT}}$ cannot be assumed, a kinetic Monte Carlo simulation would be necessary to determine the average time for diffusion-limited FRET [105]. However, with knowledge of t_{TP}, at least the sign of a correction to the above result of $\langle t_{\mathrm{ET}} \rangle$ can be obtained.

The FRET rate of an isolated TET exciton surrounded by only PEN molecules in a HB aggregate is calculated in the main text (Sec. 7.5) to be 133 fs. Each of the two nearest neighbors in the HB aggregate contributes 40 % to this value (see Apx. D.3), which means that the hopping time constant t_{TP} from a TET molecule to a PEN molecule would be

$$t_{\mathrm{TP}} = \frac{133\,\mathrm{fs}}{0.4} = 333\,\mathrm{fs}\,, \tag{D.8}$$

i.e. approximately ten times larger than t_{TT}. Note that this value is not experimentally determined and might have large uncertainties (see discussion in Sec. 7.5). Nevertheless, a larger t_{TP} than t_{TT} would increase $\langle t_{\mathrm{ET}} \rangle$, since in this case the exciton prefers not to hop from TET to PEN, if there are other TET neighbors. As mentioned above, the amount of increase of $\langle t_{\mathrm{ET}} \rangle$ due to this effect is difficult to determine analytically and would require a kinetic Monte Carlo simulation [105], which is beyond the scope of this work. Finally, even other effects than $t_{\mathrm{TP}} \neq t_{\mathrm{TT}}$, such as differing t_{TT} between different LECs (see Sec. 2.2.2) might contribute. Nevertheless, the considerations presented above indicate that the assignment of the observed exciton migration process from TET to PEN on the order of few picoseconds to diffusion-limited FRET is reasonable.

E. Sample lists

For each investigated system, tables with samples are given in the following, for which data is shown in figures of the main text. For all tables, the abbreviations used for reasons of space are as follows:

M – materials contained in the films
C – concentration of the first-named compound of blends
d – nominal film thickness in nm
R – total growth rate in Å/min
T – substrate temperature in °C

The columns right to T indicate the figures, in which data of the respective film are shown. An asterisk after a range of figures indicates that there are exceptions, which follow in the columns to the right. Rates or temperatures in parentheses indicate that the value is an average value from a larger range, e.g. if a rate calibration has been performed during growth.

Table E.1: Sample list for the investigations in Ch. 5. For the figures on TA spectroscopy the films are distinguished by *Vis-probe* and *IR-probe*, see Ch. 5.

M	C	d	R	T	5.2-5.4	5.5a	5.6	TA Figs.
PEN		80	3	40				*Vis-probe*
PEN		80	6	30			x	*IR-probe*
PEN		80	6	30	x	x		
2,3-F2PEN		80	(5)	30	x	x	x	*IR-probe*
2,3,9,10-F4PEN		90	(3)	30	x	x	x	*Vis-probe*
1,4,9,10-F4PEN		95	(4)	30	x	x	x	*Vis-probe*
1,4,8,11-F4PEN		80	6	30	x	x	x	*IR-probe*

Table E.2: Sample list for the investigations on TET:6PH blends in Ch. 6. The usages for Fig. 6.4e and Fig. 6.4f are the same as for Fig. 6.4a and Fig. 6.4c, respectively.

M	C	d	R	T	6.2	6.4a	6.4c	6.5	6.6	6.8	6.9a	6.9b
6PH		15	5	30	x		x					
6PH		80	(3)	35		x		x				
TET		20	(3)	-40	x		x					
TET		80	(6)	-30				x	x	x	x	x
TET		80	6	-30		x						
TET:6PH	25	40	10	30	x		x					
TET:6PH	40	40	(10)	30	x		x					
TET:6PH	50	40	10	30	x		x					
TET:6PH	2	80	6	30		x		x	x	x		x
TET:6PH	5	80	6	30					x			x
TET:6PH	10	80	6	30		x		x	x			x
TET:6PH	10	80	6	30						x		x
TET:6PH	17	80	6	30				x	x	x	x	x
TET:6PH	25	80	6	30		x		x	x	x		x
TET:6PH	33	80	6	30		x		x	x	x		x
TET:6PH	33	80	6	30								x
TET:6PH	40	80	6	30								x
TET:6PH	45	80	6	30				x	x	x	x	x
TET:6PH	50	80	6	30		x						x
TET:6PH	60	80	6	30		x						x

Table E.3: Sample list for the investigations on TET:PIC blends in Ch. 6. The usages for Fig. 6.4e and Fig. 6.4f are the same as for Fig. 6.4b and Fig. 6.4d, respectively.

M	C	d	R	T	6.2	6.4b	6.4d	6.5	6.6	6.8	6.9b
PIC		80	(3)	-30				x			
PIC		80	(4)	-20	x	x	x				
TET		20	(3)	-40	x		x				
TET		80	(6)	-30				x	x	x	x
TET		80	6	-30		x					
TET:PIC	9	80	6	30		x		x	x	x	x
TET:PIC	17	80	6	30		x		x	x	x	x
TET:PIC	17	80	6	30	x		x				
TET:PIC	33	80	5	30	x		x				
TET:PIC	50	80	6	30		x		x	x	x	x
TET:PIC	50	80	8	30	x		x				
TET:PIC	75	80	6	30		x		x	x		

Table E.4: Sample list for the investigations on ADT:6PH blends in Ch. 6.

M	C	d	R	T	6.14a	6.14b	6.15
6PH		80	(3)	35	x	x	
ADT		80	(5)	30	x		
ADT		80	6	30		x	x
ADT:6PH	5	80	6	30	x	x	x
ADT:6PH	25	80	6	30	x	x	x
ADT:6PH	33	80	(4)	30	x	x	x
ADT:6PH	50	80	6	30	x	x	x
ADT:6PH	75	80	6	30	x	x	x

Table E.5: Sample list for the investigations on PEN:TET blends in Ch. 7.

M	C	d	R	T	7.2	7.3	7.4-7.19*	7.8	7.9
PEN		20	6	30	x				
PEN		80	3	40		x	x		x
TET		20	(4)	-40	x				
TET		80	(5)	-25		x			
TET		80	6	-30			x		x
PEN:TET	25	20	6	30	x				
PEN:TET	50	20	6	30	x				
PEN:TET	75	20	6	30	x				
PEN:TET	5	80	6	30		x	x		x
PEN:TET	20	80	6	30		x			
PEN:TET	25	80	6	30			x		x
PEN:TET	25	80	6	30				x	
PEN:TET	25	80	6	30				x	x
PEN:TET	50	80	6	30		x	x		x
PEN:TET	75	80	6	30			x		
PEN:TET	80	80	6	30		x			
PEN:TET	95	80	6	30		x	x		

Table E.6: Sample list for the investigations on RUB:TET blends in Ch. 7.

M	C	d	R	T	7.21/7.23	7.22	7.24/7.25
RUB		20	6	30	x		x
TET		20	6	(0)	x	x	
TET		80	(4)	-15			x
RUB:TET	5	20	6	-20		x	
RUB:TET	5	20	6	-20	x		x
RUB:TET	10	20	6	-20		x	
RUB:TET	10	20	6	-20	x		x
RUB:TET	20	20	6	-20	x		x
RUB:TET	50	20	6	-20		x	
RUB:TET	50	20	6	-20	x		x
RUB:TET	80	20	6	-20		x	
RUB:TET	80	20	6	-20	x		x
RUB:TET	90	20	6	-20		x	
RUB:TET	90	20	6	-20	x		x

F. List of contributions

Contributions of others to the investigations of this thesis are listed below, sorted by project. For contributions of cooperation partners the name of the head of the lab is given in parentheses.

Fluorination (Ch. 5)

Compound synthesis	–	Dr. T. Geiger, L. Kalix (Prof. Dr. H. F. Bettinger)
Sample preparation	–	C.Z.
Structural characterization	–	C.Z.
Optical characterization	–	C.Z.
TA measurements	–	C.Z., Dr. L. Moretti (Prof. Dr. G. Cerullo)
TA analysis	–	C.Z.

Spacer blends (Ch. 6)

TET:6PH and TET:PIC

Sample preparation	–	C.Z.
Structural characterization	–	C.Z.
Optical characterization	–	C.Z.
TRPL measurements	–	Dr. C. Cruz (Prof. Dr. C. J. Bardeen)
TRPL analysis	–	C.Z.
Theor. calculations	–	Prof. Dr. D. R. Reichman, Prof. Dr. R. Tempelaar

ADT:6PH

Sample preparation	–	C.Z.
Structural characterization	–	C.Z.
Optical characterization	–	C.Z.
TCSPC measurements	–	C.Z., T. Rammler (Prof. Dr. A. Meixner)
TCSPC fits	–	T. Rammler (Prof. Dr. A. Meixner)

Heterofission (Ch. 7)

PEN:TET

Sample preparation	–	C.Z.
Structural characterization	–	C.Z.
Optical characterization	–	C.Z.
TA measurements	–	C.Z., Dr. L. Moretti (Prof. Dr. G. Cerullo)
TA analysis	–	C.Z.
FRET calculation	–	C.Z.

RUB:TET

Sample preparation	–	C.Z., F. Munko
Structural characterization	–	C.Z., F. Munko
Optical characterization	–	C.Z.
TCSPC measurements	–	C.Z., T. Rammler (Prof. Dr. A. Meixner)
TCSPC fits	–	T. Rammler (Prof. Dr. A. Meixner)

List of abbreviations

2DES	–	two-dimensional electronic spectroscopy
6PH	–	[6]-phenacene
ADT	–	anthradithiophene
BOA	–	Born-Oppenheimer approximation
BP	–	Bragg peak
CCD	–	charge-coupled device
CRY	–	chrysene
CT	–	charge-transfer
DS	–	Davydov splitting
EAS	–	evolution associated spectra
ESA	–	excited state absorption
FE	–	Frenkel exciton
FPEN	–	fluorinated pentacene
FRET	–	Förster resonance energy transfer
FTF	–	face-to-face
FWHM	–	full width at half maximum
GA	–	global analysis
GIWAXS	–	grazing-incidence wide-angle X-ray scattering
GSB	–	ground state bleach
HB	–	herringbone
HOMO	–	highest occupied molecular orbital
IC	–	internal conversion
ISC	–	intersystem crossing
IR	–	infrared
IRF	–	instrument response function
LCAO	–	linear combination of atomic orbitals
LEC	–	local environment configuration
LUMO	–	lowest unoccupied molecular orbital
MOI	–	molecule of interest
NIR	–	near infrared
OMBD	–	organic molecular beam deposition

OSC – organic semiconductor
OLED – organic light emitting diode
OPA – optical parametric amplifier
OPV – organic photovoltaic
PAH – polycyclic aromatic hydrocarbon
PEN – pentacene
PES – potential energy surface
PFP – perfluoro-pentacene
PIC – picene
PL – photoluminescence
QCM – quartz crystal microbalance
RUB – rubrene
SC – single crystal
SDD – sample-detector distance
SE – stimulated emission
SF – singlet fission
SSA – singlet-singlet annihilation
TA – transient absorption
TF – thin film
TCSPC – time-correlated single photon counting
TDM – transition dipole moment
TRPL – time-resolved photoluminescence
TET – tetracene
TT – triplet-pair
TTA – triplet-triplet annihilation
UHV – ultrahigh vacuum
UV – ultraviolet
Vis – visible
WLC – white light continuum
XRD – X-ray diffraction
XRR – X-ray reflectivity
YAG – yttrium aluminum garnet
ZINDO – Zerner's intermediate neglect of differential overlap

Bibliography

[1] A. Balasinski, Semiconductors: integrated circuit design for manufacturability, CRC Press, Boca Raton, doi:10.1201/b11189 (2012).

[2] S. Oktyabrsky and P. Ye, Fundamentals of III-V semiconductor MOSFETs, Springer, Boston, doi:10.1007/978-1-4419-1547-4 (2010).

[3] P. Dong, Y.-K. Chen, G.-H. Duan, and D. T. Neilson, Silicon photonic devices and integrated circuits, *Nanophotonics*, **3**, 215, doi:10.1515/nanoph-2013-0023 (2014).

[4] V. Petrova-Koch, R. Hezel, and A. Goetzberger, High-efficient low-cost photovoltaics, Springer, Berlin, Heidelberg, doi:10.1007/978-3-540-79359-5 (2009).

[5] A. Reinders, P. Verlinden, W. van Sark, and A. Freundlich, Photovoltaic solar energy: from fundamentals to applications, John Wiley & Sons, Chichester, doi:10.1002/9781118927496 (2016).

[6] J. T. Clemens, Silicon microelectronics technology, *Bell Labs Tech. J.*, **2**, 76, doi:10.1002/bltj.2084 (1997).

[7] S. E. Thompson and S. Parthasarathy, Moore's law: the future of Si microelectronics, *Mater. Today*, **9**, 20, doi:10.1016/S1369-7021(06)71539-5 (2006).

[8] M. Pope and C. E. Swenberg, Electronic processes in organic crystals and polymers, Oxford University Press, Oxford (1999).

[9] M. Schwoerer and H. C. Wolf, Organic molecular solids, Wiley-VCH, Weinheim, doi:10.1002/9783527618651 (2006).

[10] X. Gao and Z. Zhao, High mobility organic semiconductors for field-effect transistors, *Sci. China Chem.*, **58**, 947, doi:10.1007/s11426-015-5399-5 (2015).

[11] P. Friederich, V. Meded, A. Poschlad, T. Neumann, V. Rodin, V. Stehr, F. Symalla, D. Danilov, G. Lüdemann, R. F. Fink, I. Kondov, F. von Wrochem, and W. Wenzel, Molecular origin of the charge carrier mobility in small molecule organic semiconductors, *Adv. Funct. Mater.*, **26**, 5757, doi:10.1002/adfm.201601807 (2016).

[12] S. R. Forrest, Active optoelectronics using thin-film organic semiconductors, *IEEE J. Sel. Top. Quant.*, **6**, 1072, doi:10.1109/2944.902156 (2000).

[13] M. Graetzel, R. A. J. Janssen, D. B. Mitzi, and E. H. Sargent, Materials interface engineering for solution-processed photovoltaics, *Nature*, **488**, 304, doi:10.1038/nature11476 (2012).

[14] M. Riede, C. Uhrich, J. Widmer, R. Timmreck, D. Wynands, G. Schwartz, W.-M. Gnehr, D. Hildebrandt, A. Weiss, J. Hwang, S. Sundarraj, P. Erk, M. Pfeiffer, and K. Leo, Efficient organic tandem solar cells based on small molecules, *Adv. Funct. Mater.*, **21**, 3019, doi:10.1002/adfm.201002760 (2011).

[15] Y. Liu, P. Cheng, T. Li, R. Wang, Y. Li, S.-Y. Chang, Y. Zhu, H.-W. Cheng, K.-H. Wei, X. Zhan, B. Sun, and Y. Yang, Unraveling sunlight by transparent organic semiconductors toward photovoltaic and photosynthesis, *ACS Nano*, **13**, 1071, doi:10.1021/acsnano.8b08577 (2019).

[16] L. Meng, Y. Zhang, X. Wan, C. Li, X. Zhang, Y. Wang, X. Ke, Z. Xiao, L. Ding, R. Xia, H.-L. Yip, Y. Cao, and Y. Chen, Organic and solution-processed tandem solar cells with 17.3% efficiency, *Science*, **361**, 1094, doi:10.1126/science.aat2612 (2018).

[17] M. Pagliaro, R. Ciriminna, and G. Palmisano, Flexible solar cells, *ChemSusChem*, **1**, 880, doi:10.1002/cssc.200800127 (2008).

[18] S. E. Root, S. Savagatrup, A. D. Printz, D. Rodriquez, and D. J. Lipomi, Mechanical properties of organic semiconductors for stretchable, highly flexible, and mechanically robust electronics, *Chem. Rev.*, **117**, 6467, doi:10.1021/acs.chemrev.7b00003 (2017).

[19] B. Geffroy, P. le Roy, and C. Prat, Organic light-emitting diode (OLED) technology: materials, devices and display technologies, *Polym. Int.*, **55**, 572, doi:10.1002/pi.1974 (2006).

[20] T. Tsujimura, OLED display fundamentals and applications, John Wiley & Sons, Hoboken, doi:10.1002/9781119187493 (2017).

[21] L. Zuo, J. Yu, X. Shi, F. Lin, W. Tang, and A. K.-Y. Jen, High-efficiency nonfullerene organic solar cells with a parallel tandem configuration, *Adv. Mater.*, **29**, 1702547, doi:10.1002/adma.201702547 (2017).

[22] J. Yuan, Y. Zhang, L. Zhou, G. Zhang, H.-L. Yip, T.-K. Lau, X. Lu, C. Zhu, H. Peng, P. A. Johnson, M. Leclerc, Y. Cao, J. Ulanski, Y. Li, and Y. Zou, Single-junction organic solar cell with over 15% efficiency using fused-ring acceptor with electron-deficient core, *Joule*, **3**, 1140 , doi:10.1016/j.joule.2019.01.004 (2019).

[23] M. B. Smith and J. Michl, Singlet fission, *Chem. Rev.*, **110**, 6891, doi:10.1021/cr1002613 (2010).

[24] A. Rao and R. H. Friend, Harnessing singlet exciton fission to break the Shockley–Queisser limit, *Nat. Rev. Mater.*, **2**, 17063, doi:10.1038/natrevmats.2017.63 (2017).

[25] K. M. Felter and F. C. Grozema, Singlet fission in crystalline organic materials: recent insights and future directions, *J. Phys. Chem. Lett.*, **10**, 7208, doi:10.1021/acs.jpclett.9b00754 (2019).

[26] K. Miyata, F. S. Conrad-Burton, F. L. Geyer, and X.-Y. Zhu, Triplet pair states in singlet fission, *Chem. Rev.*, **119**, 4261, doi:10.1021/acs.chemrev.8b00572 (2019).

[27] R. E. Merrifield, P. Avakian, and R. P. Groff, Fission of singlet excitons into pairs of triplet excitons in tetracene crystals, *Chem. Phys. Lett.*, **3**, 386, doi:10.1016/0009-2614(69)80144-2 (1969).

[28] C. Jundt, G. Klein, B. Sipp, J. L. Moigne, M. Joucla, and A. A. Villaeys, Exciton dynamics in pentacene thin films studied by pump-probe spectroscopy, *Chem. Phys. Lett.*, **241**, 84, doi:10.1016/0009-2614(95)00603-2 (1995).

[29] I. Paci, J. C. Johnson, X. Chen, G. Rana, D. Popović, D. E. David, A. J. Nozik, M. A. Ratner, and J. Michl, Singlet fission for dye-sensitized solar cells: can a suitable sensitizer be found?, *J. Am. Chem. Soc.*, **128**, 16546, doi:10.1021/ja063980h (2006).

[30] M. J. Y. Tayebjee, S. N. Sanders, E. Kumarasamy, L. M. Campos, M. Y. Sfeir, and D. R. McCamey, Quintet multiexciton dynamics in singlet fission, *Nat. Phys.*, **13**, 182, doi:10.1038/nphys3909 (2017).

[31] K. Yunusova, S. Bayliss, T. Chanelière, V. Derkach, J. Anthony, A. Chepelianskii, and L. Weiss, Spin fine structure reveals biexciton geometry in an organic semiconductor, *Phys. Rev. Lett.*, **125**, 097402, doi:10.1103/physrevlett.125.097402 (2020).

[32] S. L. Bayliss, L. R. Weiss, F. Kraffert, D. B. Granger, J. E. Anthony, J. Behrends, and R. Bittl, Probing the wave function and dynamics of the quintet multiexciton state with coherent control in a singlet fission material, *Phys. Rev. X*, **10**, 021070, doi:10.1103/physrevx.10.021070 (2020).

[33] B. Ehrler, N. Yanai, and L. Nienhaus, Up- and down-conversion in molecules and materials, *J. Chem. Phys.*, **154**, 070401, doi:10.1063/5.0045323 (2021).

[34] M. A. Green, Third generation photovoltaics: ultra-high conversion efficiency at low cost, *Prog. Photovoltaics Res. Appl.*, **9**, 123, doi:10.1002/pip.360 (2001).

[35] W. Shockley and H. J. Queisser, Detailed balance limit of efficiency of *p*-*n* junction solar cells, *J. Appl. Phys.*, **32**, 510, doi:10.1063/1.1736034 (1961).

[36] M. C. Hanna and A. J. Nozik, Solar conversion efficiency of photovoltaic and photoelectrolysis cells with carrier multiplication absorbers, *J. Appl. Phys.*, **100**, 074510, doi:10.1063/1.2356795 (2006).

[37] P. J. Jadhav, P. R. Brown, N. Thompson, B. Wunsch, A. Mohanty, S. R. Yost, E. Hontz, T. Van Voorhis, M. G. Bawendi, V. Bulović, and M. A. Baldo, Triplet exciton dissociation in singlet exciton fission photovoltaics, *Adv. Mater.*, **24**, 6169, doi:10.1002/adma.201202397 (2012).

[38] M. Tabachnyk, B. Ehrler, S. Gélinas, M. L. Böhm, B. J. Walker, K. P. Musselman, N. C. Greenham, R. H. Friend, and A. Rao, Resonant energy transfer of triplet excitons from pentacene to PbSe nanocrystals, *Nat. Mater.*, **13**, 1033, doi:10.1038/nmat4093 (2014).

[39] D. N. Congreve, J. Lee, N. J. Thompson, E. Hontz, S. R. Yost, P. D. Reusswig, M. E. Bahlke, S. Reineke, T. Van Voorhis, and M. A. Baldo, External quantum efficiency above 100% in a singlet-exciton-fission–based organic photovoltaic cell, *Science*, **340**, 334, doi:10.1126/science.1232994 (2013).

[40] N. J. Thompson, D. N. Congreve, D. Goldberg, V. M. Menon, and M. A. Baldo, Slow light enhanced singlet exciton fission solar cells with a 126% yield of electrons per photon, *Appl. Phys. Lett.*, **103**, 263302, doi:10.1063/1.4858176 (2013).

[41] L. M. Pazos-Outón, J. M. Lee, M. H. Futscher, A. Kirch, M. Tabachnyk, R. H. Friend, and B. Ehrler, A silicon–singlet fission tandem solar cell exceeding 100% external quantum efficiency with high spectral stability, *ACS Energy Lett.*, **2**, 476, doi:10.1021/acsenergylett.6b00678 (2017).

[42] R. W. MacQueen, M. Liebhaber, J. Niederhausen, M. Mews, C. Gersmann, S. Jäckle, K. Jäger, M. J. Y. Tayebjee, T. W. Schmidt, B. Rech, and K. Lips, Crystalline silicon solar cells with tetracene interlayers: the path to silicon-singlet fission heterojunction devices, *Mater. Horiz.*, **5**, 1065, doi:10.1039/c8mh00853a (2018).

[43] M. Einzinger, T. Wu, J. F. Kompalla, H. L. Smith, C. F. Perkinson, L. Nienhaus, S. Wieghold, D. N. Congreve, A. Kahn, M. G. Bawendi, and M. A. Baldo, Sensitization of silicon by singlet exciton fission in tetracene, *Nature*, **571**, 90, doi:10.1038/s41586-019-1339-4 (2019).

[44] C. C. Gradinaru, J. T. M. Kennis, E. Papagiannakis, I. H. M. van Stokkum, R. J. Cogdell, G. R. Fleming, R. A. Niederman, and R. van Grondelle, An unusual pathway of excitation energy deactivation in carotenoids: singlet-to-triplet conversion on an ultrafast timescale in a photosynthetic antenna, *Proc. Natl. Acad. Sci. U.S.A.*, **98**, 2364, doi:10.1073/pnas.051501298 (2001).

[45] C. Wang, D. E. Schlamadinger, V. Desai, and M. J. Tauber, Triplet excitons of carotenoids formed by singlet fission in a membrane, *ChemPhysChem*, **12**, 2891, doi:10.1002/cphc.201100571 (2011).

[46] J. Yu, L.-M. Fu, L.-J. Yu, Y. Shi, P. Wang, Z.-Y. Wang-Otomo, and J.-P. Zhang, Carotenoid singlet fission reactions in bacterial light harvesting complexes as revealed by triplet excitation profiles, *J. Am. Chem. Soc.*, **139**, 15984, doi:10.1021/jacs.7b09809 (2017).

[47] K. J. Fallon, P. Budden, E. Salvadori, A. M. Ganose, C. N. Savory, L. Eyre, S. Dowland, Q. Ai, S. Goodlett, C. Risko, D. O. Scanlon, C. W. M. Kay, A. Rao, R. H. Friend, A. J. Musser, and H. Bronstein, Exploiting excited-state aromaticity to design highly stable singlet fission materials, *J. Am. Chem. Soc.*, **141**, 13867, doi:10.1021/jacs.9b06346 (2019).

[48] O. El Bakouri, J. R. Smith, and H. Ottosson, Strategies for design of potential singlet fission chromophores utilizing a combination of ground state and excited state aromaticity rules, *J. Am. Chem. Soc.*, **142**, 5602, doi:10.1021/jacs.9b12435 (2020).

[49] R. D. Pensack, A. J. Tilley, C. Grieco, G. E. Purdum, E. E. Ostroumov, D. B. Granger, D. G. Oblinsky, J. C. Dean, G. S. Doucette, J. B. Asbury, Y.-L. Loo, D. S. Seferos, J. E. Anthony, and G. D. Scholes, Striking the right balance of intermolecular coupling for high-efficiency singlet fission, *Chem. Sci.*, **9**, 6240,

doi:10.1039/c8sc00293b (2018).

[50] N. Monahan and X.-Y. Zhu, Charge transfer-mediated singlet fission, *Annu. Rev. Phys. Chem.*, **66**, 601, doi:10.1146/annurev-physchem-040214-121235 (2015).

[51] T. Zeng, R. Hoffmann, and N. Ananth, The low-lying electronic states of pentacene and their roles in singlet fission, *J. Am. Chem. Soc.*, **136**, 5755, doi:10.1021/ja500887a (2014).

[52] K. Broch, J. Dieterle, F. Branchi, N. J. Hestand, Y. Olivier, H. Tamura, C. Cruz, V. M. Nichols, A. Hinderhofer, D. Beljonne, F. C. Spano, G. Cerullo, C. J. Bardeen, and F. Schreiber, Robust singlet fission in pentacene thin films with tuned charge transfer interactions, *Nat. Commun.*, **9**, 954, doi:10.1038/s41467-018-03300-1 (2018).

[53] M. H. Farag and A. I. Krylov, Singlet fission in perylenediimide dimers, *J. Phys. Chem. C*, **122**, 25753, doi:10.1021/acs.jpcc.8b05309 (2018).

[54] A. K. Le, J. A. Bender, D. H. Arias, D. E. Cotton, J. C. Johnson, and S. T. Roberts, Singlet fission involves an interplay between energetic driving force and electronic coupling in perylenediimide films, *J. Am. Chem. Soc.*, **140**, 814, doi:10.1021/jacs.7b11888 (2018).

[55] S. J. Chung, C. J. McHugh, and J. Calvo-Castro, A 2-D π-π dimer model system to investigate structure-charge transfer relationships in rubrene, *J. Mater. Chem. C*, **7**, 2029, doi:10.1039/c8tc06412a (2019).

[56] W.-L. Chan, M. Ligges, and X.-Y. Zhu, The energy barrier in singlet fission can be overcome through coherent coupling and entropic gain, *Nat. Chem.*, **4**, 840, doi:10.1038/nchem.1436 (2012).

[57] S. R. Yost, J. Lee, M. W. B. Wilson, T. Wu, D. P. McMahon, R. R. Parkhurst, N. J. Thompson, D. N. Congreve, A. Rao, K. Johnson, M. Y. Sfeir, M. G. Bawendi, T. M. Swager, R. H. Friend, M. A. Baldo, and T. Van Voorhis, A transferable model for singlet-fission kinetics, *Nat. Chem.*, **6**, 492, doi:10.1038/nchem.1945 (2014).

[58] E. Busby, T. C. Berkelbach, B. Kumar, A. Chernikov, Y. Zhong, H. Hlaing, X.-Y. Zhu, T. F. Heinz, M. S. Hybertsen, M. Y. Sfeir, D. R. Reichman, C. Nuckolls, and O. Yaffe, Multiphonon relaxation slows singlet fission in crystalline hexacene, *J. Am. Chem. Soc.*, **136**, 10654, doi:10.1021/ja503980c (2014).

[59] A. B. Kolomeisky, X. Feng, and A. I. Krylov, A simple kinetic model for singlet fission: a role of electronic and entropic contributions to macroscopic rates, *J. Phys. Chem. C*, **118**, 5188, doi:10.1021/jp4128176 (2014).

[60] K. Miyata, Y. Kurashige, K. Watanabe, T. Sugimoto, S. Takahashi, S. Tanaka, J. Takeya, T. Yanai, and Y. Matsumoto, Coherent singlet fission activated by symmetry breaking, *Nat. Chem.*, **9**, 983, doi:10.1038/nchem.2784 (2017).

[61] N. R. Monahan, D. Sun, H. Tamura, K. W. Williams, B. Xu, Y. Zhong, B. Kumar, C. Nuckolls, A. R. Harutyunyan, G. Chen, H.-L. Dai, D. Beljonne, Y. Rao, and X.-Y. Zhu, Dynamics of the triplet-pair state reveals the likely coexistence of coherent and incoherent singlet fission in crystalline hexacene, *Nat. Chem.*, **9**, 341,

doi:10.1038/nchem.2665 (2017).

[62] A. M. Alvertis, S. Lukman, T. J. H. Hele, E. G. Fuemmeler, J. Feng, J. Wu, N. C. Greenham, A. W. Chin, and A. J. Musser, Switching between coherent and incoherent singlet fission via solvent-induced symmetry breaking, *J. Am. Chem. Soc.*, **141**, 17558, doi:10.1021/jacs.9b05561 (2019).

[63] X. Li, R. M. Parrish, and T. J. Martínez, An *ab initio* exciton model for singlet fission, *J. Chem. Phys.*, **153**, 184116, doi:10.1063/5.0028605 (2020).

[64] M. J. Y. Tayebjee, R. G. C. R. Clady, and T. W. Schmidt, The exciton dynamics in tetracene thin films, *Phys. Chem. Chem. Phys.*, **15**, 14797, doi:10.1039/c3cp52609g (2013).

[65] H. L. Stern, A. Cheminal, S. R. Yost, K. Broch, S. L. Bayliss, K. Chen, M. Tabachnyk, K. Thorley, N. Greenham, J. M. Hodgkiss, J. Anthony, M. Head-Gordon, A. J. Musser, A. Rao, and R. H. Friend, Vibronically coherent ultrafast triplet-pair formation and subsequent thermally activated dissociation control efficient endothermic singlet fission, *Nat. Chem.*, **9**, 1205, doi:10.1038/nchem.2856 (2017).

[66] D. G. Bossanyi, M. Matthiesen, S. Wang, J. A. Smith, R. C. Kilbride, J. D. Shipp, D. Chekulaev, E. Holland, J. E. Anthony, J. Zaumseil, A. J. Musser, and J. Clark, Emissive spin-0 triplet-pairs are a direct product of triplet-triplet annihilation in pentacene single crystals and anthradithiophene films, *Nat. Chem.*, **13**, 163, doi:10.1038/s41557-020-00593-y (2021).

[67] C. D. Cruz, E. L. Chronister, and C. J. Bardeen, Using temperature dependent fluorescence to evaluate singlet fission pathways in tetracene single crystals, *J. Chem. Phys.*, **153**, 234504, doi:10.1063/5.0031458 (2020).

[68] E. G. Fuemmeler, S. N. Sanders, A. B. Pun, E. Kumarasamy, T. Zeng, K. Miyata, M. L. Steigerwald, X.-Y. Zhu, M. Y. Sfeir, L. M. Campos, and N. Ananth, A direct mechanism of ultrafast intramolecular singlet fission in pentacene dimers, *ACS Cent. Sci.*, **2**, 316, doi:10.1021/acscentsci.6b00063 (2016).

[69] A. A. Bakulin, S. E. Morgan, T. B. Kehoe, M. W. B. Wilson, A. W. Chin, D. Zigmantas, D. Egorova, and A. Rao, Real-time observation of multiexcitonic states in ultrafast singlet fission using coherent 2D electronic spectroscopy, *Nat. Chem.*, **8**, 16, doi:10.1038/nchem.2371 (2016).

[70] A. F. Morrison and J. M. Herbert, Evidence for singlet fission driven by vibronic coherence in crystalline tetracene, *J. Phys. Chem. Lett.*, **8**, 1442, doi:10.1021/acs.jpclett.7b00230 (2017).

[71] R. Tempelaar and D. R. Reichman, Vibronic exciton theory of singlet fission. III. How vibronic coupling and thermodynamics promote rapid triplet generation in pentacene crystals, *J. Chem. Phys.*, **148**, 244701, doi:10.1063/1.5031778 (2018).

[72] C. Schnedermann, A. M. Alvertis, T. Wende, S. Lukman, J. Feng, F. A. Y. N. Schröder, D. H. P. Turban, J. Wu, N. D. M. Hine, N. C. Greenham, A. W. Chin, A. Rao, P. Kukura, and A. J. Musser, A molecular movie of ultrafast singlet fission,

Nat. Commun., **10**, 4207, doi:10.1038/s41467-019-12220-7 (2019).

[73] G.-H. Deng, Q. Wei, J. Han, Y. Qian, J. Luo, A. R. Harutyunyan, G. Chen, H. Bian, H. Chen, and Y. Rao, Vibronic fingerprint of singlet fission in hexacene, *J. Chem. Phys.*, **151**, 054703, doi:10.1063/1.5110263 (2019).

[74] W.-L. Chan, M. Ligges, A. Jailaubekov, L. Kaake, L. Miaja-Avila, and X.-Y. Zhu, Observing the multiexciton state in singlet fission and ensuing ultrafast multielectron transfer, *Science*, **334**, 1541, doi:10.1126/science.1213986 (2011).

[75] T. C. Berkelbach, M. S. Hybertsen, and D. R. Reichman, Microscopic theory of singlet exciton fission. I. General formulation, *J. Chem. Phys.*, **138**, 114102, doi:10.1063/1.4794425 (2013).

[76] S. Lukman, K. Chen, J. M. Hodgkiss, D. H. P. Turban, N. D. M. Hine, S. Dong, J. Wu, N. C. Greenham, and A. J. Musser, Tuning the role of charge-transfer states in intramolecular singlet exciton fission through side-group engineering, *Nat. Commun.*, **7**, 13622, doi:10.1038/ncomms13622 (2016).

[77] E. A. Margulies, C. E. Miller, Y. Wu, L. Ma, G. C. Schatz, R. M. Young, and M. R. Wasielewski, Enabling singlet fission by controlling intramolecular charge transfer in π-stacked covalent terrylenediimide dimers, *Nat. Chem.*, **8**, 1120, doi:10.1038/nchem.2589 (2016).

[78] V. O. Kim, K. Broch, V. Belova, Y. S. Chen, A. Gerlach, F. Schreiber, H. Tamura, R. G. D. Valle, G. D'Avino, I. Salzmann, D. Beljonne, A. Rao, and R. Friend, Singlet exciton fission via an intermolecular charge transfer state in coevaporated pentacene-perfluoropentacene thin films, *J. Chem. Phys.*, **151**, 164706, doi:10.1063/1.5130400 (2019).

[79] I. Papadopoulos, J. Zirzlmeier, C. Hetzer, Y. J. Bae, M. D. Krzyaniak, M. R. Wasielewski, T. Clark, R. R. Tykwinski, and D. M. Guldi, Varying the interpentacene electronic coupling to tune singlet fission, *J. Am. Chem. Soc.*, **141**, 6191, doi:10.1021/jacs.8b09510 (2019).

[80] A. J. Musser, M. Liebel, C. Schnedermann, T. Wende, T. B. Kehoe, A. Rao, and P. Kukura, Evidence for conical intersection dynamics mediating ultrafast singlet exciton fission, *Nat. Phys.*, **11**, 352, doi:10.1038/NPHYS3241 (2015).

[81] K. Bera, S. Y. Kwang, and R. R. Frontiera, Advances in singlet fission chromophore design enabled by vibrational spectroscopies, *J. Phys. Chem. C*, **124**, 25163, doi:10.1021/acs.jpcc.0c06725 (2020).

[82] J. J. Burdett, G. B. Piland, and C. J. Bardeen, Magnetic field effects and the role of spin states in singlet fission, *Chem. Phys. Lett.*, **585**, 1, doi:10.1016/j.cplett.2013.08.036 (2013).

[83] Z. Wang, C. Zhang, R. Wang, G. Wang, X. Wang, and M. Xiao, Weakly coupled triplet pair states probed by quantum beating in delayed fluorescence in tetracene crystals, *J. Chem. Phys.*, **151**, 134309, doi:10.1063/1.5110188 (2019).

[84] E. A. Buchanan, J. Kaleta, J. Wen, S. H. Lapidus, I. Císařová, Z. Havlas, J. C. Johnson, and J. Michl, Molecular packing and singlet fission: the parent and three fluorinated 1,3-diphenylisobenzofurans, *J. Phys. Chem. Lett.*, **10**, 1947, doi:10.1021/acs.jpclett.8b03875 (2019).

[85] N. Alagna, J. Han, N. Wollscheid, J. L. P. Lustres, J. Herz, S. Hahn, S. Koser, F. Paulus, U. H. F. Bunz, A. Dreuw, T. Buckup, and M. Motzkus, Tailoring ultrafast singlet fission by the chemical modification of phenazinothiadiazoles, *J. Am. Chem. Soc.*, **141**, 8834, doi:10.1021/jacs.9b01079 (2019).

[86] C. Hetzer, D. M. Guldi, and R. R. Tykwinski, Pentacene dimers as a critical tool for the investigation of intramolecular singlet fission, *Chem. Eur. J.*, **24**, 8245, doi:10.1002/chem.201705355 (2018).

[87] N. V. Korovina, N. F. Pompetti, and J. C. Johnson, Lessons from intramolecular singlet fission with covalently bound chromophores, *J. Chem. Phys.*, **152**, 040904, doi:10.1063/1.5135307 (2020).

[88] K. C. Krishnapriya, P. Roy, B. Puttaraju, U. Salzner, A. J. Musser, M. Jain, J. Dasgupta, and S. Patil, Spin density encodes intramolecular singlet exciton fission in pentacene dimers, *Nat. Commun.*, **10**, 33, doi:10.1038/s41467-018-07736-3 (2019).

[89] N. V. Korovina, C. H. Chang, and J. C. Johnson, Spatial separation of triplet excitons drives endothermic singlet fission, *Nat. Chem.*, **12**, 391, doi:10.1038/s41557-020-0422-7 (2020).

[90] A. B. Pun, A. Asadpoordarvish, E. Kumarasamy, M. J. Y. Tayebjee, D. Niesner, D. R. McCamey, S. N. Sanders, L. M. Campos, and M. Y. Sfeir, Ultra-fast intramolecular singlet fission to persistent multiexcitons by molecular design, *Nat. Chem.*, **11**, 821, doi:10.1038/s41557-019-0297-7 (2019).

[91] H. Liu, V. M. Nichols, L. Shen, S. Jahansouz, Y. Chen, K. M. Hanson, C. J. Bardeen, and X. Li, Synthesis and photophysical properties of a "face-to-face" stacked tetracene dimer, *Phys. Chem. Chem. Phys.*, **17**, 6523, doi:10.1039/c4cp05444j (2015).

[92] J. C. Dean, R. Zhang, R. K. Hallani, R. D. Pensack, S. N. Sanders, D. G. Oblinsky, S. R. Parkin, L. M. Campos, J. E. Anthony, and G. D. Scholes, Photophysical characterization and time-resolved spectroscopy of a anthradithiophene dimer: exploring the role of conformation in singlet fission, *Phys. Chem. Chem. Phys.*, **19**, 23162, doi:10.1039/c7cp03774k (2017).

[93] R. M. Young and M. R. Wasielewski, Mixed electronic states in molecular dimers: connecting singlet fission, excimer formation, and symmetry-breaking charge transfer, *Acc. Chem. Res.*, **53**, 1957, doi:10.1021/acs.accounts.0c00397 (2020).

[94] R. D. Pensack, A. J. Tilley, S. R. Parkin, T. S. Lee, M. M. Payne, D. Gao, A. A. Jahnke, D. G. Oblinsky, P.-F. Li, J. E. Anthony, D. S. Seferos, and G. D. Scholes, Exciton delocalization drives rapid singlet fission in nanoparticles of acene derivatives, *J. Am. Chem. Soc.*, **137**, 6790, doi:10.1021/ja512668r (2015).

[95] B. Alam, A. F. Morrison, and J. M. Herbert, Charge separation and charge transfer in the low-lying excited states of pentacene, *J. Phys. Chem. C*, **124**, 24653, doi:10.1021/acs.jpcc.0c07932 (2020).

[96] I. Breen, R. Tempelaar, L. A. Bizimana, B. Kloss, D. R. Reichman, and D. B. Turner, Triplet separation drives singlet fission after femtosecond correlated triplet pair production in rubrene, *J. Am. Chem. Soc.*, **139**, 11745, doi:10.1021/jacs.7b02621 (2017).

[97] M. W. B. Wilson, A. Rao, J. Clark, R. S. S. Kumar, D. Brida, G. Cerullo, and R. H. Friend, Ultrafast dynamics of exciton fission in polycrystalline pentacene, *J. Am. Chem. Soc.*, **133**, 11830, doi:10.1021/ja201688h (2011).

[98] M. W. B. Wilson, A. Rao, K. Johnson, S. Gélinas, R. di Pietro, J. Clark, and R. H. Friend, Temperature-independent singlet exciton fission in tetracene, *J. Am. Chem. Soc.*, **135**, 16680, doi:10.1021/ja408854u (2013).

[99] R. Katoh, M. Hashimoto, A. Takahashi, Y. Sonoda, T. Yago, and M. Wakasa, Singlet fission in fluorinated diphenylhexatrienes, *J. Phys. Chem. C*, **121**, 25666, doi:10.1021/acs.jpcc.7b06905 (2017).

[100] K. Ortstein, S. Hutsch, A. Hinderhofer, J. Vahland, M. Schwarze, S. Schellhammer, M. Hodas, T. Geiger, H. Kleemann, H. F. Bettinger, F. Schreiber, F. Ortmann, and K. Leo, Energy level engineering in organic thin films by tailored halogenation, *Adv. Funct. Mater.*, **30**, 2002987, doi:10.1002/adfm.202002987 (2020).

[101] A. K. Pandey, S. Dabos-Seignon, and J.-M. Nunzi, Pentacene: PTCDI-$C_{13}H_{27}$ molecular blends efficiently harvest light for solar cell applications, *Appl. Phys. Lett.*, **89**, 113506, doi:10.1063/1.2352800 (2006).

[102] A. Opitz, J. Wagner, W. Brütting, A. Hinderhofer, and F. Schreiber, Molecular semiconductor blends: microstructure, charge carrier transport, and application in photovoltaic cells, *Phys. Status Solidi A*, **206**, 2683, doi:10.1002/pssa.200925238 (2009).

[103] C. Wang, X. Liu, Y. Xiao, J. Bergqvist, X. Lu, F. Gao, and M. Fahlman, Diluted organic semiconductors in photovoltaics, *Sol. RRL*, **4**, 2000261, doi:10.1002/solr.202000261 (2020).

[104] K. Broch, A. Aufderheide, L. Raimondo, A. Sassella, A. Gerlach, and F. Schreiber, Optical properties of blends: influence of mixing-induced disorder in pentacene:diindenoperylene versus perfluoropentacene:diindenoperylene, *J. Phys. Chem. C*, **117**, 13952, doi:10.1021/jp4019487 (2013).

[105] S. Arnold, R. R. Alfano, M. Pope, W. Yu, P. Ho, R. Selsby, J. Tharrats, and C. E. Swenberg, Triplet exciton caging in two dimensions, *J. Chem. Phys.*, **64**, 5104, doi:10.1063/1.432184 (1976).

[106] N. E. Geacintov, J. Burgos, M. Pope, and C. Strom, Heterofission of pentacene excited singlets in pentacene-doped tetracene crystals, *Chem. Phys. Lett.*, **11**, 504, doi:10.1016/0009-2614(71)80395-0 (1971).

[107] J. Burgos, M. Pope, C. E. Swenberg, and R. R. Alfano, Heterofission in pentacene-doped tetracene single crystals, *Phys. Status Solidi B*, **83**, 249, doi:10.1002/pssb.2220830127 (1977).

[108] S. N. Sanders, E. Kumarasamy, A. B. Pun, M. L. Steigerwald, M. Y. Sfeir, and L. M. Campos, Intramolecular singlet fission in oligoacene heterodimers, *Angew. Chem. Int. Ed.*, **55**, 3373, doi:10.1002/anie.201510632 (2016).

[109] J. Clayden, N. Greeves, and S. G. Warren, Organic chemistry, Oxford University Press, Oxford (2012).

[110] A. Köhler and H. Bässler, Electronic processes in organic semiconductors: an introduction, Wiley-VCH, Weinheim, doi:10.1002/9783527685172 (2015).

[111] H. Bronstein, C. B. Nielsen, B. C. Schroeder, and I. McCulloch, The role of chemical design in the performance of organic semiconductors, *Nat. Rev. Chem.*, **4**, 66, doi:10.1038/s41570-019-0152-9 (2020).

[112] H. A. Becerril, M. E. Roberts, Z. Liu, J. Locklin, and Z. Bao, High-performance organic thin-film transistors through solution-sheared deposition of small-molecule organic semiconductors, *Adv. Mater.*, **20**, 2588, doi:10.1002/adma.200703120 (2008).

[113] R. Dabestani and I. N. Ivanov, A compilation of physical, spectroscopic and photophysical properties of polycyclic aromatic hydrocarbons, *Photochem. Photobiol.*, **70**, 10, doi:10.1111/j.1751-1097.1999.tb01945.x (1999).

[114] R. R. Burch, Y.-H. Dong, C. Fincher, M. Goldfinger, and P. E. Rouviere, Electrical properties of polyunsaturated natural products: field effect mobility of carotenoid polyenes, *Synth. Met.*, **146**, 43 , doi:10.1016/j.synthmet.2004.06.014 (2004).

[115] T. Zhuang, S. Sasaki, T. Ikeuchi, J. Kido, and X.-F. Wang, Natural-photosynthesis-inspired photovoltaic cells using carotenoid aggregates as electron donors and chlorophyll derivatives as electron acceptors, *RSC Adv.*, **5**, 45755, doi:10.1039/c5ra07099f (2015).

[116] J. Mei, Y. Diao, A. L. Appleton, L. Fang, and Z. Bao, Integrated materials design of organic semiconductors for field-effect transistors, *J. Am. Chem. Soc.*, **135**, 6724, doi:10.1021/ja400881n (2013).

[117] Y. Chen, L. Shen, and X. Li, Effects of heteroatoms of tetracene and pentacene derivatives on their stability and singlet fission, *J. Phys. Chem. A*, **118**, 5700, doi:10.1021/jp503114b (2014).

[118] Y.-D. Zhang, Y. Wu, Y. Xu, Q. Wang, K. Liu, J.-W. Chen, J.-J. Cao, C. Zhang, H. Fu, and H.-L. Zhang, Excessive exoergicity reduces singlet exciton fission efficiency of heteroacenes in solutions, *J. Am. Chem. Soc.*, **138**, 6739, doi:10.1021/jacs.6b03829 (2016).

[119] J. Herz, T. Buckup, F. Paulus, J. Engelhart, U. H. F. Bunz, and M. Motzkus, Acceleration of singlet fission in an aza-derivative of TIPS-pentacene, *J. Phys. Chem. Lett.*, **5**, 2425, doi:10.1021/jz501102r (2014).

[120] S. Ito and M. Nakano, Theoretical molecular design of heteroacenes for singlet fission: tuning the diradical character by modifying π-conjugation length and aromaticity, *J. Phys. Chem. C*, **119**, 148, doi:10.1021/jp5103737 (2014).

[121] B. Shen, T. Geiger, R. Einholz, F. Reicherter, S. Schundelmeier, C. Maichle-Mössmer, B. Speiser, and H. F. Bettinger, Bridging the gap between pentacene and perfluoropentacene: synthesis and characterization of 2,3,9,10-tetrafluoropentacene in the neutral, cationic, and dicationic states, *J. Org. Chem.*, **83**, 3149, doi:10.1021/acs.joc.7b03241 (2018).

[122] T. Geiger, S. Schundelmeier, T. Hummel, M. Ströbele, W. Leis, M. Seitz, C. Zeiser, L. Moretti, M. Maiuri, G. Cerullo, K. Broch, J. Vahland, K. Leo, C. Maichle-Mössmer, B. Speiser, and H. F. Bettinger, Modulating the electronic and solid-state structure of organic semiconductors by site-specific substitution: the case of tetrafluoropentacenes, *Chem. Eur. J.*, **26**, 3420, doi:10.1002/chem.201905843 (2020).

[123] T. Nagami, T. Tonami, K. Okada, W. Yoshida, H. Miyamoto, and M. Nakano, Vibronic coupling density analysis and quantum dynamics simulation for singlet fission in pentacene and its halogenated derivatives, *J. Chem. Phys.*, **153**, 134302, doi:10.1063/5.0024746 (2020).

[124] M. Schwarze, W. Tress, B. Beyer, F. Gao, R. Scholz, C. Poelking, K. Ortstein, A. A. Günther, D. Kasemann, D. Andrienko, and K. Leo, Band structure engineering in organic semiconductors, *Science*, **352**, 1446, doi:10.1126/science.aaf0590 (2016).

[125] E. Heilbronner and H. Bock, Das HMO-Modell und seine Anwendung: Grundlagen und Handhabung, Verlag Chemie, Weinheim (1968).

[126] T. Masubuchi, Y. Sugawara, and A. Nakajima, Adiabatic electron affinity of pentacene and perfluoropentacene molecules studied by anion photoelectron spectroscopy: molecular insights into electronic properties, *J. Chem. Phys.*, **145**, 244306, doi:10.1063/1.4973012 (2016).

[127] H. F. Bettinger, C. Tönshoff, M. Doerr, and E. Sanchez-Garcia, Electronically excited states of higher acenes up to nonacene: a density functional theory/multireference configuration interaction study, *J. Chem. Theory Comput.*, **12**, 305, doi:10.1021/acs.jctc.5b00671 (2016).

[128] N. C. Craig, P. Groner, and D. C. McKean, Equilibrium structures for butadiene and ethylene: compelling evidence for π-electron delocalization in butadiene, *J. Phys. Chem. A*, **110**, 7461, doi:10.1021/jp060695b (2006).

[129] N. C. Baird, On the driving force for the symmetric structure of benzene and the allyl radical: σ or π?, *J. Org. Chem.*, **51**, 3907, doi:10.1021/jo00370a034 (1986).

[130] E. Hückel, Quantentheoretische Beiträge zum Benzolproblem, *Z. Phys.*, **70**, 204, doi:10.1007/bf01339530 (1931).

[131] M. Randić, Aromaticity of polycyclic conjugated hydrocarbons, *Chem. Rev.*, **103**, 3449, doi:10.1021/cr9903656 (2003).

[132] A. D. Zdetsis, Classics illustrated: Clar's sextet and Hückel's (4n + 2) π-electron rules, *J. Phys. Chem. C*, **122**, 17526, doi:10.1021/acs.jpcc.8b05020 (2018).

[133] R. Gershoni-Poranne and A. Stanger, Magnetic criteria of aromaticity, *Chem. Soc. Rev.*, **44**, 6597, doi:10.1039/c5cs00114e (2015).

[134] F. Feixas, E. Matito, J. Poater, and M. Solà, Quantifying aromaticity with electron delocalisation measures, *Chem. Soc. Rev.*, **44**, 6434, doi:10.1039/c5cs00066a (2015).

[135] B. A. Lombos, P. Sauvageau, and C. Sandorfy, The electronic spectra of n-alkanes, *J. Mol. Spectrosc.*, **24**, 253, doi:10.1016/0022-2852(67)90089-6 (1967).

[136] P. Muller, Glossary of terms used in physical organic chemistry (IUPAC recommendations 1994), *Pure Appl. Chem.*, **66**, 1077, doi:10.1351/pac199466051077 (1994).

[137] F. London, The general theory of molecular forces, *Trans. Faraday Soc.*, **33**, 8b, doi:10.1039/tf937330008b (1937).

[138] J. Venables, Introduction to surface and thin film processes, Cambridge University Press, Cambridge, doi:10.1017/CBO9780511755651 (2000).

[139] A.-L. Barabási and H. E. Stanley, Fractal concepts in surface growth, Cambridge University Press, Cambridge (1995).

[140] S. Kowarik, A. Gerlach, and F. Schreiber, Organic molecular beam deposition: fundamentals, growth dynamics, and *in situ* studies, *J. Phys.: Condens. Matter*, **20**, 184005, doi:10.1088/0953-8984/20/18/184005 (2008).

[141] A. Aufderheide, K. Broch, J. Novák, A. Hinderhofer, R. Nervo, A. Gerlach, R. Banerjee, and F. Schreiber, Mixing-induced anisotropic correlations in molecular crystalline systems, *Phys. Rev. Lett.*, **109**, 156102, doi:10.1103/physrevlett.109.156102 (2012).

[142] H. Sirringhaus, P. J. Brown, R. H. Friend, M. M. Nielsen, K. Bechgaard, B. M. W. Langeveld-Voss, A. J. H. Spiering, R. A. J. Janssen, E. W. Meijer, P. Herwig, and D. M. de Leeuw, Two-dimensional charge transport in self-organized, high-mobility conjugated polymers, *Nature*, **401**, 685, doi:10.1038/44359 (1999).

[143] K. Kang, S. Watanabe, K. Broch, A. Sepe, A. Brown, I. Nasrallah, M. Nikolka, Z. Fei, M. Heeney, D. Matsumoto, K. Marumoto, H. Tanaka, S. Kuroda, and H. Sirringhaus, 2D coherent charge transport in highly ordered conducting polymers doped by solid state diffusion, *Nat. Mater.*, **15**, 896, doi:10.1038/nmat4634 (2016).

[144] Z.-F. Yao, J.-Y. Wang, and J. Pei, Control of π–π stacking via crystal engineering in organic conjugated small molecule crystals, *Cryst. Growth Des.*, **18**, 7, doi:10.1021/acs.cgd.7b01385 (2018).

[145] M. K. Corpinot and D.-K. Bučar, A practical guide to the design of molecular crystals, *Cryst. Growth Des.*, **19**, 1426, doi:10.1021/acs.cgd.8b00972 (2019).

[146] E. Koch, Summary of general formulae, International Union of Crystallography, Chester, doi:10.1107/97809553602060000103 (2006).

[147] C. Kittel, Einführung in die Festkörperphysik, Oldenbourg Wissenschaftsverlag, München (2013).

[148] A. M. Kosevich, The crystal lattice: phonons, solitons, dislocations, superlattices, Wiley-VCH, Weinheim, doi:10.1002/352760667x (1999).

[149] R. B. Campbell, J. M. Robertson, and J. Trotter, The crystal structure of hexacene, and a revision of the crystallographic data for tetracene, *Acta Crystallogr.*, **15**, 289, doi:10.1107/S0365110X62000699 (1962).

[150] I. Meyenburg, T. Breuer, A. Karthäuser, S. Chatterjee, G. Witte, and W. Heimbrodt, Temperature-resolved optical spectroscopy of pentacene polymorphs: variation of herringbone angles in single-crystals and interface-controlled thin films, *Phys. Chem. Chem. Phys.*, **18**, 3825, doi:10.1039/c5cp07836a (2016).

[151] S. C. B. Mannsfeld, A. Virkar, C. Reese, M. F. Toney, and Z. Bao, Precise structure of pentacene monolayers on amorphous silicon oxide and relation to charge transport, *Adv. Mater.*, **21**, 2294, doi:10.1002/adma.200803328 (2009).

[152] D. Holmes, S. Kumaraswamy, A. J. Matzger, and K. P. C. Vollhardt, On the nature of nonplanarity in the [N]phenylenes, *Chem. Eur. J.*, **5**, 3399, doi:10.1002/(SICI)1521-3765(19991105)5:11<3399::AID-CHEM3399>3.0.CO;2-V (1999).

[153] N. J. Hestand and F. C. Spano, Expanded theory of H-and J-molecular aggregates: the effects of vibronic coupling and intermolecular charge transfer, *Chem. Rev.*, **118**, 7069, doi:10.1021/acs.chemrev.7b00581 (2018).

[154] D.-M. Smilgies, Molecular axes and planes as an eigenvalue problem, *J. Appl. Crystallogr.*, **41**, 363, doi:10.1107/s0021889807067787 (2008).

[155] A. De, R. Ghosh, S. Roychowdhury, and P. Roychowdhury, Structural analysis of picene, $C_{22}H_{14}$, *Acta Crystallogr. C*, **41**, 907, doi:10.1107/S0108270185005959 (1985).

[156] D. M. Burns and J. Iball, Refinement of the structure of chrysene, *Proc. R. Soc. A*, **257**, 491, doi:10.1098/rspa.1960.0168 (1960).

[157] A. Hinderhofer and F. Schreiber, Organic–organic heterostructures: concepts and applications, *ChemPhysChem.*, **13**, 628, doi:10.1002/cphc.201100737 (2012).

[158] K. Broch, A. Gerlach, C. Lorch, J. Dieterle, J. Novák, A. Hinderhofer, and F. Schreiber, Structure formation in perfluoropentacene:diindenoperylene blends and its impact on transient effects in the optical properties studied in real-time during growth, *J. Chem. Phys.*, **139**, 174709, doi:10.1063/1.4827868 (2013).

[159] A. I. Kitaigorodsky, Mixed crystals, Springer, Berlin, Heidelberg, doi:10.1007/978-3-642-81672-7 (1984).

[160] M. Lusi, Engineering crystal properties through solid solutions, *Cryst. Growth Des.*, **18**, 3704, doi:10.1021/acs.cgd.7b01643 (2018).

[161] J. B. Birks, Photophysics of aromatic molecules, Wiley-Interscience, New York (1970).

[162] H. J. Kupka, Transitions in molecular systems, Wiley-VCH, Weinheim, doi:10.1002/9783527630219 (2010).

[163] A. Schild, On the probability density of the nuclei in a vibrationally excited molecule, *Front. Chem.*, **7**, 424, doi:10.3389/fchem.2019.00424 (2019).

[164] T. Carrington, Geometry of intersecting potential surfaces, *Acc. Chem. Res.*, **7**, 20, doi:10.1021/ar50073a004 (1974).

[165] M. Desouter-Lecomte, B. Leyh-Nihant, M. T. Praet, and J. C. Lorquet, Avoided crossings: a study of the nonadiabatic transition probabilities, *J. Chem. Phys.*, **86**, 7025, doi:10.1063/1.452351 (1987).

[166] R. Ramirez and M. C. Bohm, On the delocalization of the C nuclei in the C_{60} molecule; a Feynman path-integral Monte Carlo study, *J. Phys. Condens. Matter*, **7**, 4847, doi:10.1088/0953-8984/7/25/009 (1995).

[167] H. Reinhardt, Quantenmechanik 2: Pfadintegralformulierung und Operatorformalismus, Oldenbourg Wissenschaftsverlag, München, doi:10.1524/9783486855883 (2013).

[168] T. V. Voorhis, T. Kowalczyk, B. Kaduk, L.-P. Wang, C.-L. Cheng, and Q. Wu, The diabatic picture of electron transfer, reaction barriers, and molecular dynamics, *Annu. Rev. Phys. Chem.*, **61**, 149, doi:10.1146/annurev.physchem.012809.103324 (2010).

[169] J. R. Platt, Classification of spectra of cata-condensed hydrocarbons, *J. Chem. Phys.*, **17**, 484, doi:10.1063/1.1747293 (1949).

[170] N. S. Ham and K. Ruedenberg, Electronic interaction in the free-electron network model for conjugated systems. II. spectra of aromatic hydrocarbons, *J. Chem. Phys.*, **25**, 13, doi:10.1063/1.1742804 (1956).

[171] J. Michl and J. F. Muller, Nonalternant hydrocarbons: a classification of excited states in acenaphthylene and pleiadiene (cyclohepta[de]naphthalene) families, *J. Am. Chem. Soc.*, **98**, 4550, doi:10.1021/ja00431a036 (1976).

[172] I. V. Hertel and C.-P. Schulz, Atome, Moleküle und optische Physik 1, Springer, Berlin, Heidelberg, doi:10.1007/978-3-662-53104-4 (2017).

[173] J. B. Gallivan and J. S. Brinen, Polarization of electronic transitions of aromatic hydrocarbons, *J. Chem. Phys.*, **50**, 1590, doi:10.1063/1.1671245 (1969).

[174] H. B. Klevens and J. R. Platt, Spectral resemblances of cata-condensed hydrocarbons, *J. Chem. Phys.*, **17**, 470, doi:10.1063/1.1747291 (1949).

[175] J. B. Coon, R. E. DeWames, and C. M. Loyd, The Franck-Condon principle and the structures of excited electronic states of molecules, *J. Mol. Spectrosc.*, **8**, 285, doi:10.1016/0022-2852(62)90029-2 (1962).

[176] B. Valeur and M. N. Berberan-Santos, Molecular fluorescence: principles and applications, Wiley-VCH, Weinheim, doi:10.1002/9783527650002 (2012).

[177] N. Kanamaru, Radiationless transition between randomly fluctuating levels. S_1-T_2-T_1 intersystem crossing in condensed phase, *Bull. Chem. Soc. Jpn.*, **55**, 3093, doi:10.1246/bcsj.55.3093 (1982).

[178] W. R. Lambert and A. H. Zewail, Intersystem crossing rates of pentacene in naphthalene at 1.9 K following single-mode laser excitation, *Chem. Phys. Lett.*, **69**, 270, doi:10.1016/0009-2614(80)85061-5 (1980).

[179] M. Beer and H. C. Longuet-Higgins, Anomalous light emission of azulene, *J. Chem. Phys.*, **23**, 1390, doi:10.1063/1.1742314 (1955).

[180] D. Klemp and B. Nickel, Relative quantum yield of the $S_2 \rightarrow S_1$ fluorescence from azulene, *Chem. Phys. Lett.*, **130**, 493, doi:10.1016/0009-2614(86)80245-7 (1986).

[181] H. Fidder, M. Rini, and E. T. J. Nibbering, The role of large conformational changes in efficient ultrafast internal conversion: deviations from the energy gap law, *J. Am. Chem. Soc.*, **126**, 3789, doi:10.1021/ja038741y (2004).

[182] M. Kasha, Characterization of electronic transitions in complex molecules, *Discuss. Faraday Soc.*, **9**, 14, doi:10.1039/df9500900014 (1950).

[183] J. W. Arbogast, A. P. Darmanyan, C. S. Foote, F. N. Diederich, R. L. Whetten, Y. Rubin, M. M. Alvarez, and S. J. Anz, Photophysical properties of sixty atom carbon molecule (C60), *J. Phys. Chem.*, **95**, 11, doi:10.1021/j100154a006 (1991).

[184] M. Kasha, H. R. Rawls, and M. A. El-Bayoumi, The exciton model in molecular spectroscopy, *Pure Appl. Chem.*, **11**, 371, doi:10.1351/pac196511030371 (1965).

[185] J. B. Birks, Excimers, *Rep. Prog. Phys.*, **38**, 903, doi:10.1088/0034-4885/38/8/001 (1975).

[186] C. B. Dover, J. K. Gallaher, L. Frazer, P. C. Tapping, A. J. Petty, M. J. Crossley, J. E. Anthony, T. W. Kee, and T. W. Schmidt, Endothermic singlet fission is hindered by excimer formation, *Nat. Chem.*, **10**, 305, doi:10.1038/nchem.2926 (2018).

[187] R. R. Lunt, N. C. Giebink, A. A. Belak, J. B. Benziger, and S. R. Forrest, Exciton diffusion lengths of organic semiconductor thin films measured by spectrally resolved photoluminescence quenching, *J. Appl. Phys.*, **105**, 053711, doi:10.1063/1.3079797 (2009).

[188] J. Frenkel, On the transformation of light into heat in solids. II, *Phys. Rev.*, **37**, 1276, doi:10.1103/physrev.37.1276 (1931).

[189] F. C. Spano and H. Yamagata, Vibronic coupling in J-aggregates and beyond: a direct means of determining the exciton coherence length from the photoluminescence spectrum, *J. Phys. Chem. B*, **115**, 5133, doi:10.1021/jp104752k (2011).

[190] F. C. Spano, The spectral signatures of Frenkel polarons in H-and J-aggregates, *Acc. Chem. Res.*, **43**, 429, doi:10.1021/ar900233v (2010).

[191] E. E. Jelley, Spectral absorption and fluorescence of dyes in the molecular state, *Nature*, **138**, 1009, doi:10.1038/1381009a0 (1936).

[192] A. S. Davydov, The theory of molecular excitons, *Sov. Phys. Uspekhi*, **7**, 145, doi:10.1070/PU1964v007n02ABEH003659 (1964).

[193] J. D. Cook, T. J. Carey, and N. H. Damrauer, Solution-phase singlet fission in a structurally well-defined norbornyl-bridged tetracene dimer, *J. Phys. Chem. A*, **120**, 4473, doi:10.1021/acs.jpca.6b04367 (2016).

[194] B. S. Basel, C. Hetzer, J. Zirzlmeier, D. Thiel, R. Guldi, F. Hampel, A. Kahnt, T. Clark, D. M. Guldi, and R. R. Tykwinski, Davydov splitting and singlet fission in excitonically coupled pentacene dimers, *Chem. Sci.*, **10**, 3854, doi:10.1039/c9sc00384c (2019).

[195] H. Yamagata, J. Norton, E. Hontz, Y. Olivier, D. Beljonne, J. L. Brédas, R. J. Silbey, and F. C. Spano, The nature of singlet excitons in oligoacene molecular crystals, *J. Chem. Phys.*, **134**, 204703, doi:10.1063/1.3590871 (2011).

[196] D. Beljonne, H. Yamagata, J. L. Brédas, F. C. Spano, and Y. Olivier, Charge-transfer excitations steer the Davydov splitting and mediate singlet exciton fission in pentacene, *Phys. Rev. Lett.*, **110**, 226402, doi:10.1103/physrevlett.110.226402 (2013).

[197] S. Sharifzadeh, P. Darancet, L. Kronik, and J. B. Neaton, Low-energy charge-transfer excitons in organic solids from first-principles: the case of pentacene, *J. Phys. Chem. Lett.*, **4**, 2197, doi:10.1021/jz401069f (2013).

[198] M. Grover and R. Silbey, Exciton migration in molecular crystals, *J. Chem. Phys.*, **54**, 4843, doi:10.1063/1.1674761 (1971).

[199] R. Silbey, Electronic energy transfer in molecular crystals, *Annu. Rev. Phys. Chem.*, **27**, 203, doi:10.1146/annurev.pc.27.100176.001223 (1976).

[200] A. Köhler and H. Bässler, What controls triplet exciton transfer in organic semiconductors?, *J. Mater. Chem.*, **21**, 4003, doi:10.1039/c0jm02886j (2011).

[201] S. R. Yost, E. Hontz, S. Yeganeh, and T. Van Voorhis, Triplet vs singlet energy transfer in organic semiconductors: the tortoise and the hare, *J. Phys. Chem. C*, **116**, 17369, doi:10.1021/jp304433t (2012).

[202] T. Förster, Transfer mechanisms of electronic excitation energy, *Radiat. Res. Suppl.*, **2**, 326, doi:10.2307/3583604 (1960).

[203] S. Jang, M. D. Newton, and R. J. Silbey, Multichromophoric Förster resonance energy transfer, *Phys. Rev. Lett.*, **92**, 218301, doi:10.1103/physrevlett.92.218301 (2004).

[204] K. Feron, W. Belcher, C. Fell, and P. Dastoor, Organic solar cells: understanding the role of Förster resonance energy transfer, *Int. J. Mol. Sci.*, **13**, 17019, doi:10.3390/ijms131217019 (2012).

[205] J. E. Frost and G. A. Jones, A quantum dynamical comparison of the electronic couplings derived from quantum electrodynamics and Förster theory: application to 2D molecular aggregates, *New J. Phys.*, **16**, 113067, doi:10.1088/1367-2630/16/11/113067 (2014).

[206] J. J. Burdett, D. Gosztola, and C. J. Bardeen, The dependence of singlet exciton relaxation on excitation density and temperature in polycrystalline tetracene thin films: kinetic evidence for a dark intermediate state and implications for singlet fission, *J. Chem. Phys.*, **135**, 214508, doi:10.1063/1.3664630 (2011).

[207] T. S. Lee, Y. L. Lin, H. Kim, R. D. Pensack, B. P. Rand, and G. D. Scholes, Triplet energy transfer governs the dissociation of the correlated triplet pair in exothermic

singlet fission, *J. Phys. Chem. Lett.*, **9**, 4087, doi:10.1021/acs.jpclett.8b01834 (2018).

[208] L. R. Weiss, S. L. Bayliss, F. Kraffert, K. J. Thorley, J. E. Anthony, R. Bittl, R. H. Friend, A. Rao, N. C. Greenham, and J. Behrends, Strongly exchange-coupled triplet pairs in an organic semiconductor, *Nat. Phys.*, **13**, 176, doi:10.1038/nphys3908 (2017).

[209] T. Yago, Low magnetic field effects on triplet pair annihilations at canonical orientations, *J. Chem. Phys.*, **151**, 214501, doi:10.1063/1.5127904 (2019).

[210] D. Lubert-Perquel, E. Salvadori, M. Dyson, P. N. Stavrinou, R. Montis, H. Nagashima, Y. Kobori, S. Heutz, and C. W. M. Kay, Identifying triplet pathways in dilute pentacene films, *Nat. Commun.*, **9**, 4222, doi:10.1038/s41467-018-06330-x (2018).

[211] T. Minami, S. Ito, and M. Nakano, Theoretical study of singlet fission in oligorylenes, *J. Phys. Chem. Lett.*, **3**, 2719, doi:10.1021/jz3011749 (2012).

[212] G. B. Piland, J. J. Burdett, R. J. Dillon, and C. J. Bardeen, Singlet fission: from coherences to kinetics, *J. Phys. Chem. Lett.*, **5**, 2312, doi:10.1021/jz500676c (2014).

[213] R. G. Kepler, J. C. Caris, P. Avakian, and E. Abramson, Triplet excitons and delayed fluorescence in anthracene crystals, *Phys. Rev. Lett.*, **10**, 400, doi:10.1103/PhysRevLett.10.400 (1963).

[214] S. Singh, W. J. Jones, W. Siebrand, B. P. Stoicheff, and W. G. Schneider, Laser generation of excitons and fluorescence in anthracene crystals, *J. Chem. Phys.*, **42**, 330, doi:10.1063/1.1695695 (1965).

[215] C. E. Swenberg and W. T. Stacy, Bimolecular radiationless transitions in crystalline tetracene, *Chem. Phys. Lett.*, **2**, 327, doi:10.1016/0009-2614(68)80087-9 (1968).

[216] K. Von Burg and I. Zschokke-Gränacher, Singlet exciton fission in pure and doped anthracene, *J. Chem. Phys.*, **70**, 3807, doi:10.1063/1.437931 (1979).

[217] R. R. Alfano, S. L. Shapiro, and M. Pope, Fission rate of singlet excitons in a tetracene crystal measured with picosecond laser pulses, *Opt. Commun.*, **9**, 388, doi:10.1016/0030-4018(73)90278-2 (1973).

[218] M. Chabr, U. P. Wild, J. Fünfschilling, and I. Zschokke-Gränacher, Quantum beats of prompt fluorescence in tetracene crystals, *Chem. Phys.*, **57**, 425 , doi:10.1016/0301-0104(81)80221-2 (1981).

[219] P. W. Anderson, Antiferromagnetism. Theory of superexchange interaction, *Phys. Rev.*, **79**, 350, doi:10.1103/physrev.79.350 (1950).

[220] X. Feng, A. V. Luzanov, and A. I. Krylov, Fission of entangled spins: an electronic structure perspective, *J. Phys. Chem. Lett.*, **4**, 3845, doi:10.1021/jz402122m (2013).

[221] Y. Fujihashi, L. Chen, A. Ishizaki, J. Wang, and Y. Zhao, Effect of high-frequency modes on singlet fission dynamics, *J. Chem. Phys.*, **146**, 044101, doi:10.1063/1.4973981 (2017).

[222] H. Tamura, M. Huix-Rotllant, I. Burghardt, Y. Olivier, and D. Beljonne, First-principles quantum dynamics of singlet fission: coherent versus thermally acti-

vated mechanisms governed by molecular π stacking, *Phys. Rev. Lett.*, **115**, 107401, doi:10.1103/physrevlett.115.107401 (2015).

[223] X. Xie, A. Santana-Bonilla, W. Fang, C. Liu, A. Troisi, and H. Ma, Exciton–phonon interaction model for singlet fission in prototypical molecular crystals, *J. Chem. Theory Comput.*, **15**, 3721, doi:10.1021/acs.jctc.9b00122 (2019).

[224] D. Casanova, Theoretical modeling of singlet fission, *Chem. Rev.*, **118**, 7164, doi:10.1021/acs.chemrev.7b00601 (2018).

[225] N. V. Korovina, J. Joy, X. Feng, C. Feltenberger, A. I. Krylov, S. E. Bradforth, and M. E. Thompson, Linker-dependent singlet fission in tetracene dimers, *J. Am. Chem. Soc.*, **140**, 10179, doi:10.1021/jacs.8b04401 (2018).

[226] K. J. Laidler, A glossary of terms used in chemical kinetics, including reaction dynamics (IUPAC recommendations 1996), *Pure Appl. Chem.*, **68**, 149, doi:10.1351/pac199668010149 (1996).

[227] J. Cornil, J. P. Calbert, and J. L. Brédas, Electronic structure of the pentacene single crystal: relation to transport properties, *J. Am. Chem. Soc.*, **123**, 1250, doi:10.1021/ja005700i (2001).

[228] S. Varghese and S. Das, Role of molecular packing in determining solid-state optical properties of π-conjugated materials, *J. Phys. Chem. Lett.*, **2**, 863, doi:10.1021/jz200099p (2011).

[229] L. Wang, Y. Olivier, O. V. Prezhdo, and D. Beljonne, Maximizing singlet fission by intermolecular packing, *J. Phys. Chem. Lett.*, **5**, 3345, doi:10.1021/jz5015955 (2014).

[230] D. H. Arias, J. L. Ryerson, J. D. Cook, N. H. Damrauer, and J. C. Johnson, Polymorphism influences singlet fission rates in tetracene thin films, *Chem. Sci.*, **7**, 1185, doi:10.1039/c5sc03535j (2016).

[231] S. T. Roberts, R. E. McAnally, J. N. Mastron, D. H. Webber, M. T. Whited, R. L. Brutchey, M. E. Thompson, and S. E. Bradforth, Efficient singlet fission discovered in a disordered acene film, *J. Am. Chem. Soc.*, **134**, 6388, doi:10.1021/ja300504t (2012).

[232] J. Gierschner, J. Cornil, and H.-J. Egelhaaf, Optical bandgaps of π-conjugated organic materials at the polymer limit: experiment and theory, *Adv. Mater.*, **19**, 173, doi:10.1002/adma.200600277 (2007).

[233] P. Cudazzo, M. Gatti, and A. Rubio, Excitons in molecular crystals from first-principles many-body perturbation theory: picene versus pentacene, *Phys. Rev. B*, **86**, 195307, doi:10.1103/PhysRevB.86.195307 (2012).

[234] M. L. Tiago, J. E. Northrup, and S. G. Louie, *Ab initio* calculation of the electronic and optical properties of solid pentacene, *Phys. Rev. B*, **67**, 115212, doi:10.1103/physrevb.67.115212 (2003).

[235] S. Hirayama, R. A. Lampert, and D. Phillips, Photophysics of *meso*-substituted anthracenes. Part 1. Solutions and isolated vapours, *J. Chem. Soc., Faraday Trans. 2*, **81**, 371, doi:10.1039/f29858100371 (1985).

[236] P. Hervé and L. K. J. Vandamme, General relation between refractive index and energy gap in semiconductors, *Infared Phys. Technol.*, **35**, 609, doi:10.1016/1350-4495(94)90026-4 (1994).

[237] J. Ren, Q. Peng, X. Zhang, Y. Yi, and Z. Shuai, Role of the dark 2Ag state in donor–acceptor copolymers as a pathway for singlet fission: a DMRG study, *J. Phys. Chem. Lett.*, **8**, 2175, doi:10.1021/acs.jpclett.7b00656 (2017).

[238] M. Fumanal and C. Corminboeuf, Direct, mediated, and delayed intramolecular singlet fission mechanism in donor-acceptor copolymers, *J. Phys. Chem. Lett.*, **11**, 9788, doi:10.1021/acs.jpclett.0c03076 (2020).

[239] E. Busby, J. Xia, Q. Wu, J. Z. Low, R. Song, J. R. Miller, X.-Y. Zhu, L. M. Campos, and M. Y. Sfeir, A design strategy for intramolecular singlet fission mediated by charge-transfer states in donor–acceptor organic materials, *Nat. Mater.*, **14**, 426, doi:10.1038/nmat4175 (2015).

[240] X. Wang, X. Liu, R. Tom, C. Cook, B. Schatschneider, and N. Marom, Phenylated acene derivatives as candidates for intermolecular singlet fission, *J. Phys. Chem. C*, **123**, 5890, doi:10.1021/acs.jpcc.8b12549 (2019).

[241] C.-H. Chen, P.-H. Sher, C.-P. Chen, W.-K. Choi, C. J. Bardeen, T.-L. Chiu, J.-K. Wang, and J.-H. Lee, Thickness-dependent exciton dynamics in thermally evaporated rubrene thin films, *J. Phys. Chem. C*, **124**, 25729, doi:10.1021/acs.jpcc.0c07887 (2020).

[242] K. Kolata, T. Breuer, G. Witte, and S. Chatterjee, Molecular packing determines singlet exciton fission in organic semiconductors, *ACS Nano*, **8**, 7377, doi:10.1021/nn502544d (2014).

[243] G. Tao, Nonadiabatic simulation of singlet fission dynamics in tetracene clusters: the topology of quantum coherence in a global view, *J. Chem. Phys.*, **151**, 054308, doi:10.1063/1.5100196 (2019).

[244] P.-H. Sher, C.-H. Chen, T.-L. Chiu, C.-F. Lin, J.-K. Wang, and J.-H. Lee, Distinct routes of singlet fission and triplet fusion: a fluorescence kinetic study of rubrene, *J. Phys. Chem. C*, **123**, 3279, doi:10.1021/acs.jpcc.8b08677 (2019).

[245] F. Schreiber, Organic molecular beam deposition: growth studies beyond the first monolayer, *Phys. Status Solidi A*, **201**, 1037, doi:10.1002/pssa.200404334 (2004).

[246] G. Witte and C. Wöll, Growth of aromatic molecules on solid substrates for applications in organic electronics, *J. Mater. Res.*, **19**, 1889, doi:10.1557/jmr.2004.0251 (2004).

[247] R. Gutzler, W. M. Heckl, and M. Lackinger, Combination of a Knudsen effusion cell with a quartz crystal microbalance: *In situ* measurement of molecular evaporation rates with a fully functional deposition source, *Rev. Sci. Instrum.*, **81**, 015108, doi:10.1063/1.3292510 (2010).

[248] G. Witte and C. Wöll, Molecular beam deposition and characterization of thin organic films on metals for applications in organic electronics, *Phys. Status Solidi*

A, **205**, 497, doi:10.1002/pssa.200723433 (2008).

[249] N. W. Ashcroft and N. D. Mermin, Solid state physics, Saunders College Publishing, New York (1976).

[250] S. Kowarik, A. Gerlach, A. Hinderhofer, S. Milita, F. Borgatti, F. Zontone, T. Suzuki, F. Biscarini, and F. Schreiber, Structure, morphology, and growth dynamics of perfluoro-pentacene thin films, *Phys. Status Solidi Rapid Res. Lett.*, **2**, 120, doi:10.1002/pssr.200802052 (2008).

[251] M. Schmidbauer, P. Schäfer, S. Besedin, D. Grigoriev, R. Köhler, and M. Hanke, A novel multi-detection technique for three-dimensional reciprocal-space mapping in grazing-incidence X-ray diffraction, *J. Synchrotron Radiat.*, **15**, 549, doi:10.1107/s0909049508023856 (2008).

[252] H.-H. Perkampus, UV-VIS spectroscopy and its applications, Springer, Berlin, Heidelberg, doi:10.1007/978-3-642-77477-5 (1992).

[253] O. Stenzel, The physics of thin film optical spectra, Springer, Cham, doi:10.1007/978-3-319-21602-7 (2016).

[254] D. F. Swinehart, The Beer-Lambert law, *J. Chem. Educ.*, **39**, 333, doi:10.1021/ed039p333 (1962).

[255] C. K. Carniglia, Scalar scattering theory for multilayer optical coatings, *Opt. Eng.*, **18**, 182104, doi:10.1117/12.7972335 (1979).

[256] R. Berera, R. van Grondelle, and J. T. M. Kennis, Ultrafast transient absorption spectroscopy: principles and application to photosynthetic systems, *Photosynth. Res.*, **101**, 105, doi:10.1007/s11120-009-9454-y (2009).

[257] C. Ruckebusch, M. Sliwa, P. Pernot, A. de Juan, and R. Tauler, Comprehensive data analysis of femtosecond transient absorption spectra: a review, *J. Photochem. Photobiol., C*, **13**, 1, doi:10.1016/j.jphotochemrev.2011.10.002 (2012).

[258] I. H. M. van Stokkum, D. S. Larsen, and R. van Grondelle, Global and target analysis of time-resolved spectra, *BBA-Bioenergetics*, **1657**, 82, doi:10.1016/j.bbabio.2004.04.011 (2004).

[259] A. M. Kelley, Condensed-phase molecular spectroscopy and photophysics, John Wiley & Sons, Hoboken, doi:10.1002/9781118493052 (2012).

[260] A. Rao, M. W. B. Wilson, S. Albert-Seifried, R. Di Pietro, and R. H. Friend, Photophysics of pentacene thin films: the role of exciton fission and heating effects, *Phys. Rev. B*, **84**, 195411, doi:10.1103/PhysRevB.84.195411 (2011).

[261] S. Albert-Seifried and R. H. Friend, Measurement of thermal modulation of optical absorption in pump-probe spectroscopy of semiconducting polymers, *Appl. Phys. Lett.*, **98**, 223304, doi:10.1063/1.3595340 (2011).

[262] V. Klimov, S. Hunsche, and H. Kurz, Biexciton effects in femtosecond nonlinear transmission of semiconductor quantum dots, *Phys. Rev. B*, **50**, 8110, doi:10.1103/PhysRevB.50.8110 (1994).

[263] S. A. Kovalenko, A. L. Dobryakov, J. Ruthmann, and N. P. Ernsting, Femtosecond spectroscopy of condensed phases with chirped supercontinuum probing, *Phys. Rev. A*, **59**, 2369, doi:10.1103/physreva.59.2369 (1999).

[264] M. Liebel, C. Schnedermann, and P. Kukura, Vibrationally coherent crossing and coupling of electronic states during internal conversion in β-carotene, *Phys. Rev. Lett.*, **112**, 198302, doi:10.1103/PhysRevLett.112.198302 (2014).

[265] M. V. Lebedev, O. V. Misochko, T. Dekorsy, and N. Georgiev, On the nature of "coherent artifact", *J. Exp. Theor. Phys.*, **100**, 272, doi:10.1134/1.1884668 (2005).

[266] J. J. Snellenburg, S. Laptenok, R. Seger, K. M. Mullen, and I. H. M. Van Stokkum, Glotaran: A Java-based graphical user interface for the R package TIMP, *J. Stat. Softw.*, **49**, 3, doi:10.18637/jss.v049.i03 (2012).

[267] C. Manzoni and G. Cerullo, Design criteria for ultrafast optical parametric amplifiers, *J. Opt.*, **18**, 103501, doi:10.1088/2040-8978/18/10/103501 (2016).

[268] J. R. Lakowicz, Principles of fluorescence spectroscopy, Springer, Boston, doi:10.1007/978-0-387-46312-4 (2006).

[269] J. J. Burdett, A. M. Müller, D. Gosztola, and C. J. Bardeen, Excited state dynamics in solid and monomeric tetracene: the roles of superradiance and exciton fission, *J. Chem. Phys.*, **133**, 144506, doi:10.1063/1.3495764 (2010).

[270] A. M. Müller, Y. S. Avlasevich, W. W. Schoeller, K. Müllen, and C. J. Bardeen, Exciton fission and fusion in bis(tetracene) molecules with different covalent linker structures, *J. Am. Chem. Soc.*, **129**, 14240, doi:10.1021/ja073173y (2007).

[271] C. Zeiser, C. Cruz, D. R. Reichman, M. Seitz, J. Hagenlocher, E. L. Chronister, C. J. Bardeen, R. Tempelaar, and K. Broch, Vacancy control in acene blends links exothermic singlet fission to coherence, *Nat. Commun.*, **12**, 5149, doi:10.1038/s41467-021-25395-9 (2021).

[272] F. Cicoira, C. Santato, F. Dinelli, M. Murgia, M. A. Loi, F. Biscarini, R. Zamboni, P. Heremans, and M. Muccini, Morphology and field-effect-transistor mobility in tetracene thin films, *Adv. Funct. Mater.*, **15**, 375, doi:10.1002/adfm.200400278 (2005).

[273] H. Okamoto, R. Eguchi, S. Hamao, H. Goto, K. Gotoh, Y. Sakai, M. Izumi, Y. Takaguchi, S. Gohda, and Y. Kubozono, An extended phenacene-type molecule, [8]phenacene: synthesis and transistor application, *Sci. Rep.*, **4**, 5330, doi:10.1038/srep05330 (2014).

[274] N. Komura, H. Goto, X. He, H. Mitamura, R. Eguchi, Y. Kaji, H. Okamoto, Y. Sugawara, S. Gohda, K. Sato, and Y. Kubozono, Characteristics of [6]phenacene thin film field-effect transistor, *Appl. Phys. Lett.*, **101**, 083301, doi:10.1063/1.4747201 (2012).

[275] X. Tian, L. Zhou, X. Chen, Y. Meng, Z. Xiong, X. Zhou, and Y. Zhang, Nanoscale exponential distance dependence and electron-transfer model for intermolecular singlet exciton fission observed in rubrene-doped organic films, *Org. Electron.*, **50**, 429,

doi:10.1016/j.orgel.2017.08.009 (2017).

[276] D. Lubert-Perquel, D. K. Kim, P. Robaschik, C. W. M. Kay, and S. Heutz, Growth, morphology and structure of mixed pentacene films, *J. Mater. Chem. C*, **7**, 289, doi:10.1039/c8tc05525d (2019).

[277] S. Schiefer, M. Huth, A. Dobrinevski, and B. Nickel, Determination of the crystal structure of substrate-induced pentacene polymorphs in fiber structured thin films, *J. Am. Chem. Soc.*, **129**, 10316, doi:10.1021/ja0730516 (2007).

[278] M. Mamada, H. Katagiri, M. Mizukami, K. Honda, T. Minamiki, R. Teraoka, T. Uemura, and S. Tokito, *syn-/anti*-anthradithiophene derivative isomer effects on semiconducting properties, *ACS Appl. Mater. Interfaces*, **5**, 9670, doi:10.1021/am4027136 (2013).

[279] O. D. Jurchescu, A. Meetsma, and T. T. M. Palstra, Low-temperature structure of rubrene single crystals grown by vapor transport, *Acta Crystallogr. B*, **62**, 330, doi:10.1107/s0108768106003053 (2006).

[280] C. R. Groom, I. J. Bruno, M. P. Lightfoot, and S. C. Ward, The Cambridge Structural Database, *Acta Crystallogr. B*, **72**, 171, doi:10.1107/s2052520616003954 (2016).

[281] R. K. Nahm and J. R. Engstrom, Who's on first? Tracking in real time the growth of multiple crystalline phases of an organic semiconductor: tetracene on SiO_2, *J. Chem. Phys.*, **146**, 052815, doi:10.1063/1.4971288 (2017).

[282] C. C. Mattheus, A. B. Dros, J. Baas, A. Meetsma, J. L. De Boer, and T. T. M. Palstra, Polymorphism in pentacene, *Acta Crystallogr. C*, **57**, 939, doi:10.1107/S010827010100703X (2001).

[283] B. Gompf, D. Faltermeier, C. Redling, M. Dressel, and J. Pflaum, Tetracene film morphology: comparative atomic force microscopy, X-ray diffraction and ellipsometry investigations, *Eur. Phys. J. E*, **27**, 421, doi:10.1140/epje/i2008-10405-5 (2008).

[284] R. Mondal, C. Tönshoff, D. Khon, D. C. Neckers, and H. F. Bettinger, Synthesis, stability, and photochemistry of pentacene, hexacene, and heptacene: a matrix isolation study, *J. Am. Chem. Soc.*, **131**, 14281, doi:10.1021/ja901841c (2009).

[285] A. Bree and L. E. Lyons, The intensity of ultraviolet-light absorption by monocrystals. Part IV. Absorption by naphthacene of plane-polarized light, *J. Chem. Soc.*, 5206, doi:10.1039/jr9600005206 (1960).

[286] Y. Kawashima, T. Hashimoto, H. Nakano, and K. Hirao, Theoretical study of the valence $\pi \rightarrow \pi^\star$ excited states of polyacenes: anthracene and naphthacene, *Theor. Chem. Acc.*, **102**, 49, doi:10.1007/s002140050472 (1999).

[287] S. Tavazzi, L. Raimondo, L. Silvestri, P. Spearman, A. Camposeo, M. Polo, and D. Pisignano, Dielectric tensor of tetracene single crystals: the effect of anisotropy on polarized absorption and emission spectra, *J. Chem. Phys.*, **128**, 154709, doi:10.1063/1.2897436 (2008).

[288] C. Cocchi, T. Breuer, G. Witte, and C. Draxl, Polarized absorbance and Davydov splitting in bulk and thin-film pentacene polymorphs, *Phys. Chem. Chem. Phys.*, **20**, 29724, doi:10.1039/c8cp06384b (2018).

[289] K. Hummer, P. Puschnig, and C. Ambrosch-Draxl, Lowest optical excitations in molecular crystals: bound excitons versus free electron-hole pairs in anthracene, *Phys. Rev. Lett.*, **92**, 147402, doi:10.1103/PhysRevLett.92.147402 (2004).

[290] Y. Tomkiewicz, R. P. Groff, and P. Avakian, Spectroscopic approach to energetics of exciton fission and fusion in tetracene crystals, *J. Chem. Phys.*, **54**, 4504, doi:10.1063/1.1674702 (1971).

[291] H. Angliker, E. Rommel, and J. Wirz, Electronic spectra of hexacene in solution (ground state. triplet state. dication and dianion), *Chem. Phys. Lett.*, **87**, 208 , doi:10.1016/0009-2614(82)83589-6 (1982).

[292] H. Marciniak, M. Fiebig, M. Huth, S. Schiefer, B. Nickel, F. Selmaier, and S. Lochbrunner, Ultrafast exciton relaxation in microcrystalline pentacene films, *Phys. Rev. Lett.*, **99**, 176402, doi:10.1103/physrevlett.99.176402 (2007).

[293] W.-L. Chan, T. C. Berkelbach, M. R. Provorse, N. R. Monahan, J. R. Tritsch, M. S. Hybertsen, D. R. Reichman, J. Gao, and X.-Y. Zhu, The quantum coherent mechanism for singlet fission: experiment and theory, *Acc. Chem. Res.*, **46**, 1321, doi:10.1021/ar300286s (2013).

[294] P. M. Zimmerman, F. Bell, D. Casanova, and M. Head-Gordon, Mechanism for singlet fission in pentacene and tetracene: from single exciton to two triplets, *J. Am. Chem. Soc.*, **133**, 19944, doi:10.1021/ja208431r (2011).

[295] T. C. Berkelbach, M. S. Hybertsen, and D. R. Reichman, Microscopic theory of singlet exciton fission. III. Crystalline pentacene, *J. Chem. Phys.*, **141**, 074705, doi:10.1063/1.4892793 (2014).

[296] P. M. Zimmerman, C. B. Musgrave, and M. Head-Gordon, A correlated electron view of singlet fission, *Acc. Chem. Res.*, **46**, 1339, doi:10.1021/ar3001734 (2013).

[297] A. K. Pal, K. Bhattacharyya, and A. Datta, Remote functionalization through symmetric or asymmetric substitutions control the pathway of intermolecular singlet fission, *J. Chem. Theory Comput.*, **15**, 5014, doi:10.1021/acs.jctc.9b00419 (2019).

[298] Y. Sakamoto, T. Suzuki, M. Kobayashi, Y. Gao, Y. Fukai, Y. Inoue, F. Sato, and S. Tokito, Perfluoropentacene: high-performance p-n junctions and complementary circuits with pentacene, *J. Am. Chem. Soc.*, **126**, 8138, doi:10.1021/ja0476258 (2004).

[299] C. Zeiser, L. Moretti, T. Geiger, L. Kalix, A. M. Valencia, M. Maiuri, C. Cocchi, H. F. Bettinger, G. Cerullo, and K. Broch, Permanent dipole moments enhance electronic coupling and singlet fission in pentacene, *J. Phys. Chem. Lett.*, **12**, 7453, doi:10.1021/acs.jpclett.1c01805 (2021).

[300] I. J. Bruno, J. C. Cole, P. R. Edgington, M. Kessler, C. F. Macrae, P. McCabe, J. Pearson, and R. Taylor, New software for searching the Cambridge Struc-

tural Database and visualizing crystal structures, *Acta Crystallogr. B*, **58**, 389, doi:10.1107/s0108768102003324 (2002).

[301] K.-Y. Chen, H.-H. Hsieh, C.-C. Wu, J.-J. Hwang, and T. J. Chow, A new type of soluble pentacene precursor for organic thin-film transistors, *Chem. Commun.*, 1065–1067, doi:10.1039/b616511g (2007).

[302] M. Kytka, A. Gerlach, F. Schreiber, and J. Kováč, Real-time observation of oxidation and photo-oxidation of rubrene thin films by spectroscopic ellipsometry, *Appl. Phys. Lett.*, **90**, 131911, doi:10.1063/1.2717561 (2007).

[303] D. M. Finton, E. A. Wolf, V. S. Zoutenbier, K. A. Ward, and I. Biaggio, Routes to singlet exciton fission in rubrene crystals and amorphous films, *AIP Adv.*, **9**, 095027, doi:10.1063/1.5118942 (2019).

[304] J. E. Anthony, Functionalized acenes and heteroacenes for organic electronics, *Chem. Rev.*, **106**, 5028, doi:10.1021/cr050966z (2006).

[305] P. Irkhin, A. Ryasnyanskiy, M. Koehler, and I. Biaggio, Absorption and photoluminescence spectroscopy of rubrene single crystals, *Phys. Rev. B*, **86**, 085143, doi:10.1103/physrevb.86.085143 (2012).

[306] G. B. Piland, J. J. Burdett, D. Kurunthu, and C. J. Bardeen, Magnetic field effects on singlet fission and fluorescence decay dynamics in amorphous rubrene, *J. Phys. Chem. C*, **117**, 1224, doi:10.1021/jp309286v (2013).

[307] A. Ryasnyanskiy and I. Biaggio, Triplet exciton dynamics in rubrene single crystals, *Phys. Rev. B*, **84**, 193203, doi:10.1103/physrevb.84.193203 (2011).

[308] C. K. Yong, A. J. Musser, S. L. Bayliss, S. Lukman, H. Tamura, O. Bubnova, R. K. Hallani, A. Meneau, R. Resel, M. Maruyama, S. Hotta, L. M. Herz, D. Beljonne, J. E. Anthony, J. Clark, and H. Sirringhaus, The entangled triplet pair state in acene and heteroacene materials, *Nat. Commun.*, **8**, 15953, doi:10.1038/ncomms15953 (2017).

[309] E. A. Wolf, D. M. Finton, V. Zoutenbier, and I. Biaggio, Quantum beats of a multiexciton state in rubrene single crystals, *Appl. Phys. Lett.*, **112**, 083301, doi:10.1063/1.5020652 (2018).

[310] M. K. Gish, K. J. Thorley, S. R. Parkin, J. E. Anthony, and J. C. Johnson, Hydrogen bonding optimizes singlet fission in carboxylic acid functionalized anthradithiophene films, *ChemPhotoChem*, **5**, 68, doi:10.1002/cptc.202000168 (2020).

[311] A. D. Platt, J. Day, S. Subramanian, J. E. Anthony, and O. Ostroverkhova, Optical, fluorescent, and (photo)conductive properties of high-performance functionalized pentacene and anthradithiophene derivatives, *J. Phys. Chem. C*, **113**, 14006, doi:10.1021/jp904021p (2009).

[312] C. Y. Wong, B. D. Folie, B. L. Cotts, and N. S. Ginsberg, Discerning variable extents of interdomain orientational and structural heterogeneity in solution-cast polycrystalline organic semiconducting thin films, *J. Phys. Chem. Lett.*, **6**, 3155, doi:10.1021/acs.jpclett.5b01416 (2015).

[313] G. P. Moss, P. A. S. Smith, and D. Tavernier, Glossary of class names of organic compounds and reactivity intermediates based on structure (IUPAC recommendations 1995), *Pure Appl. Chem.*, **67**, 1307, doi:10.1351/pac199567081307 (1995).

[314] M. Zwadlo, J. Hagara, G. Duva, J. Hagenlocher, A. Gerlach, I. Zaluzhnyy, M. Hodas, A. Hinderhofer, P. Siffalovic, and F. Schreiber, Structure of thin films of [6] and [7]phenacene and impact of potassium deposition, *Adv. Opt. Mater.*, 2002193, doi:10.1002/adom.202002193 (2021).

[315] X. He, R. Eguchi, H. Goto, E. Uesugi, S. Hamao, Y. Takabayashi, and Y. Kubozono, Fabrication of single crystal field-effect transistors with phenacene-type molecules and their excellent transistor characteristics, *Org. Electron.*, **14**, 1673, doi:10.1016/j.orgel.2013.03.035 (2013).

[316] S. Fanetti, M. Citroni, R. Bini, L. Malavasi, G. A. Artioli, and P. Postorino, HOMO-LUMO transitions in solvated and crystalline picene, *J. Chem. Phys.*, **137**, 224506, doi:10.1063/1.4770265 (2012).

[317] M. Das, Computational investigation on tunable optical band gap in armchair polyacenes, *J. Chem. Phys.*, **143**, 064704, doi:10.1063/1.4928571 (2015).

[318] M. S. Gudipati, M. Maus, J. Daverkausen, and G. Hohlneicher, Higher excited states of aromatic hydrocarbons. III. Assigning the in-plane polarized transitions of low-symmetry molecules: chrysene and E-stilbene, *Chem. Phys.*, **192**, 37, doi:10.1016/0301-0104(94)00367-j (1995).

[319] B. D. Folie, J. B. Haber, S. Refaely-Abramson, J. B. Neaton, and N. S. Ginsberg, Long-lived correlated triplet pairs in a π-stacked crystalline pentacene derivative, *J. Am. Chem. Soc.*, **140**, 2326, doi:10.1021/jacs.7b12662 (2018).

[320] Z. Zhou, L. Ma, D. Guo, X. Zhao, C. Wang, D. Lin, F. Zhang, J. Zhang, and Z. Nie, Ultrafast dynamics of long-lived bound triplet pair generated by singlet fission in 6, 13-bis(triisopropylsilylethynyl) pentacene, *J. Phys. Chem. C*, **124**, 14503, doi:10.1021/acs.jpcc.0c03566 (2020).

[321] M. Wakasa, T. Yago, Y. Sonoda, and R. Katoh, Structure and dynamics of triplet-exciton pairs generated from singlet fission studied via magnetic field effects, *Commun. Chem.*, **1**, 9, doi:10.1038/s42004-018-0008-0 (2018).

[322] M. Klues and G. Witte, Crystalline packing in pentacene-like organic semiconductors, *CrystEngComm*, **20**, 63, doi:10.1039/c7ce01700f (2018).

[323] B. Milián-Medina, S. Varghese, R. Ragni, H. Boerner, E. Ortí, G. M. Farinola, and J. Gierschner, Excited-state switching by per-fluorination of para-oligophenylenes, *J. Chem. Phys.*, **135**, 124509, doi:10.1063/1.3643151 (2011).

[324] A. C. Mayer, A. Kazimirov, and G. G. Malliaras, Dynamics of bimodal growth in pentacene thin films, *Phys. Rev. Lett.*, **97**, 105503, doi:10.1103/physrevlett.97.105503 (2006).

[325] M. Mantina, A. C. Chamberlin, R. Valero, C. J. Cramer, and D. G. Truhlar, Consistent van der Waals radii for the whole main group, *J. Phys. Chem. A*, **113**, 5806,

doi:10.1021/jp8111556 (2009).

[326] S. Khan and S. Mazumdar, Theory of transient excited state absorptions in pentacene and derivatives: triplet–triplet biexciton versus free triplets, *J. Phys. Chem. Lett.*, **8**, 5943, doi:10.1021/acs.jpclett.7b02748 (2017).

[327] A. D. Poletayev, J. Clark, M. W. B. Wilson, A. Rao, Y. Makino, S. Hotta, and R. H. Friend, Triplet dynamics in pentacene crystals: applications to fission-sensitized photovoltaics, *Adv. Mater.*, **26**, 919, doi:10.1002/adma.201302427 (2013).

[328] J. Hoche, H.-C. Schmitt, A. Humeniuk, I. Fischer, R. Mitrić, and M. I. S. Röhr, The mechanism of excimer formation: an experimental and theoretical study on the pyrene dimer, *Phys. Chem. Chem. Phys.*, **19**, 25002, doi:10.1039/c7cp03990e (2017).

[329] R. D. Pensack, R. J. Ashmore, A. L. Paoletta, and G. D. Scholes, The nature of excimer formation in crystalline pyrene nanoparticles, *J. Phys. Chem. C*, **122**, 21004, doi:10.1021/acs.jpcc.8b03963 (2018).

[330] M. Son, K. H. Park, C. Shao, F. Würthner, and D. Kim, Spectroscopic demonstration of exciton dynamics and excimer formation in a sterically controlled perylene bisimide dimer aggregate, *J. Phys. Chem. Lett.*, **5**, 3601, doi:10.1021/jz501953a (2014).

[331] F. Mirjani, N. Renaud, N. Gorczak, and F. C. Grozema, Theoretical investigation of singlet fission in molecular dimers: the role of charge transfer states and quantum interference, *J. Phys. Chem. C*, **118**, 14192, doi:10.1021/jp503398a (2014).

[332] J.-O. Vogel, I. Salzmann, S. Duhm, M. Oehzelt, J. P. Rabe, and N. Koch, Phase-separation and mixing in thin films of co-deposited rod-like conjugated molecules, *J. Mater. Chem.*, **20**, 4055, doi:10.1039/b927594k (2010).

[333] J. Dieterle, K. Broch, H. Frank, G. Duva, T. Storzer, A. Hinderhofer, J. Novák, A. Gerlach, and F. Schreiber, Delayed phase separation in growth of organic semiconductor blends with limited intermixing, *Phys. Status Solidi RRL*, **11**, 1600428, doi:10.1002/pssr.201600428 (2017).

[334] C. Burgdorff, S. Ehrhardt, and H. G. Löhmannsröben, Photophysical properties of tetracene derivatives in solution. 2. Halogenated tetracene derivatives, *J. Phys. Chem.*, **95**, 4246, doi:10.1021/j100164a016 (1991).

[335] H. L. Stern, A. J. Musser, S. Gelinas, P. Parkinson, L. M. Herz, M. J. Bruzek, J. Anthony, R. H. Friend, and B. J. Walker, Identification of a triplet pair intermediate in singlet exciton fission in solution, *Proc. Natl. Acad. Sci. U.S.A.*, **112**, 7656, doi:10.1073/pnas.1503471112 (2015).

[336] G. Vaubel and H. Baessler, Diffusion of singlet excitons in tetracene crystals, *Mol. Cryst. Liq. Cryst.*, **12**, 47, doi:10.1080/15421407008082759 (1970).

[337] R. Tempelaar and D. R. Reichman, Vibronic exciton theory of singlet fission. I. Linear absorption and the anatomy of the correlated triplet pair state, *J. Chem. Phys.*, **146**, 174703, doi:10.1063/1.4982362 (2017).

[338] C. Zeiser, L. Moretti, D. Lepple, G. Cerullo, M. Maiuri, and K. Broch, Singlet heterofission in tetracene–pentacene thin-film blends, *Angew. Chem. Int. Ed.*, **59**, 19966, doi:10.1002/anie.202007412 (2020).

[339] S. N. Sanders, E. Kumarasamy, A. B. Pun, M. L. Steigerwald, M. Y. Sfeir, and L. M. Campos, Singlet fission in polypentacene, *Chem*, **1**, 505, doi:10.1016/j.chempr.2016.08.016 (2016).

[340] L. Vegard, Die Konstitution der Mischkristalle und die Raumfüllung der Atome, *Z. Phys.*, **5**, 17, doi:10.1007/bf01349680 (1921).

[341] T. Toccoli, P. Bettotti, A. Cassinese, S. Gottardi, Y. Kubozono, M. A. Loi, M. Manca, and R. Verucchi, Photophysics of pentacene-doped picene thin films, *J. Phys. Chem. C*, **122**, 16879, doi:10.1021/acs.jpcc.8b02978 (2018).

[342] Y. Han and L. H. Spangler, Use of isosbestic points for determination of quantum efficiency in transient absorption spectroscopy, *J. Phys. Chem. A*, **106**, 1701, doi:10.1021/jp013717x (2002).

[343] M. Orrit, J. Bernard, A. Zumbusch, and R. I. Personov, Stark effect on single molecules in a polymer matrix, *Chem. Phys. Lett.*, **196**, 595, doi:10.1016/0009-2614(92)86000-8 (1992).

[344] Y. Ishino, K. Miyata, T. Sugimoto, K. Watanabe, Y. Matsumoto, T. Uemura, and J. Takeya, Ultrafast exciton dynamics in dinaphtho[2, 3-b:2′3′-f]thieno[3, 2-b]-thiophene thin films, *Phys. Chem. Chem. Phys.*, **16**, 7501, doi:10.1039/c3cp54157f (2014).

[345] A. M. Berghuis, T. V. Raziman, A. Halpin, S. Wang, A. G. Curto, and J. G. Rivas, Effective negative diffusion of singlet excitons in organic semiconductors, *J. Phys. Chem. Lett.*, **12**, 1360, doi:10.1021/acs.jpclett.0c03171 (2021).

[346] M. Mitsui and Y. Kawano, Electronic energy transfer in tetracene-doped *p*-terphenyl nanoparticles: extraordinarily high fluorescence enhancement and quenching efficiency, *Chem. Phys.*, **419**, 30 , doi:10.1016/j.chemphys.2013.01.004 (2013).

[347] M. Dressel, B. Gompf, D. Faltermeier, A. K. Tripathi, J. Pflaum, and M. Schubert, Kramers-Kronig-consistent optical functions of anisotropic crystals: generalized spectroscopic ellipsometry on pentacene, *Opt. Express*, **16**, 19770, doi:10.1364/OE.16.019770 (2008).

[348] O. V. Mikhnenko, P. W. M. Blom, and T.-Q. Nguyen, Exciton diffusion in organic semiconductors, *Energy Environ. Sci.*, **8**, 1867, doi:10.1039/C5EE00925A (2015).

[349] L. Wang, Y. Li, F. Zou, H. Du, L. Sun, J. Zhang, X. Song, and G. Song, Insight into crystallization process of rubrene by binary solvent mixtures, *RSC Adv.*, **6**, 3532, doi:10.1039/C5RA21556K (2016).

[350] P. E. Hofmann, M. W. Tripp, D. Bischof, Y. Grell, A. L. C. Schiller, T. Breuer, S. I. Ivlev, G. Witte, and U. Koert, Unilaterally fluorinated acenes: synthesis and solid-state properties, *Angew. Chem. Int. Ed.*, **59**, 16501, doi:10.1002/anie.202006489 (2020).

[351] M. A. Castellanos and P. Huo, Enhancing singlet fission dynamics by suppressing destructive interference between charge-transfer pathways, *J. Phys. Chem. Lett.*, **8**, 2480, doi:10.1021/acs.jpclett.7b00972 (2017).

[352] R. Mason, The crystallography of anthracene at 95°K and 290°K, *Acta Crystallogr.*, **17**, 547, doi:10.1107/S0365110X64001281 (1964).

[353] T. Siegrist, C. Kloc, J. H. Schön, B. Batlogg, R. C. Haddon, S. Berg, and G. A. Thomas, Enhanced physical properties in a pentacene polymorph, *Angew. Chem. Int. Ed.*, **40**, 1732, doi:10.1002/1521-3773(20010504)40:9<1732::AID-ANIE17320>3.0.CO;2-7 (2001).

[354] M. Watanabe, Y. J. Chang, S.-W. Liu, T.-H. Chao, K. Goto, M. M. Islam, C.-H. Yuan, Y.-T. Tao, T. Shinmyozu, and T. J. Chow, The synthesis, crystal structure and charge-transport properties of hexacene, *Nat. Chem.*, **4**, 574, doi:10.1038/NCHEM.1381 (2012).

[355] G. M. Akselrod, P. B. Deotare, N. J. Thompson, J. Lee, W. A. Tisdale, M. A. Baldo, V. M. Menon, and V. Bulović, Visualization of exciton transport in ordered and disordered molecular solids, *Nat. Commun.*, **5**, 3646, doi:10.1038/ncomms4646 (2014).

Publikationen

ORCID: https://orcid.org/0000-0003-3613-2243

1. C. Zeiser, L. Moretti, D. Lepple, G. Cerullo, M. Maiuri and K. Broch, Singlet Heterofission in Tetracene–Pentacene Thin-Film Blends, *Angew. Chem. Int. Ed.* **59**, 19966-19973 (2020), doi:10.1002/anie.202007412

2. C. Zeiser, L. Moretti, F. Reicherter, H. Bettinger, M. Maiuri, G. Cerullo and K. Broch, Singlet fission in dideuterated tetracene and pentacene, *ChemPhotoChem* **5**, 758 (2021), doi:10.1002/cptc.202000284

3. C. Zeiser, L. Moretti, T. Geiger, L. Kalix, M. Maiuri, H. F. Bettinger, G. Cerullo and K. Broch, Singlet Fission in Partially Fluorinated Pentacenes, *J. Phys. Chem. Lett.* **12**, 7453 (2021), doi:10.1021/acs.jpclett.1c01805

4. C. Zeiser, C. Cruz, D. R. Reichman, M. Seitz, J. Hagenlocher, E. L. Chronister, C. J. Bardeen, R. Tempelaar and K. Broch, Vacancy control in acene blends links exothermic singlet fission to coherence, *Nat. Commun.* **12**, 5149 (2021), doi:10.1038/s41467-021-25395-9

5. B. Reisz, S. Weimer, R. Banerjee, C. Zeiser, C. Lorch, G. Duva, J. Dieterle, K. Yonezawa, J.-P. Yang, N. Ueno, S. Kera, A. Hinderhofer, A. Gerlach and F. Schreiber, Structural, optical, and electronic characterization of perfluorinated sexithiophene films and mixed films with sexithiophene, *J. Mater. Res.* **32**, 1908-1920 (2017), doi:10.1557/jmr.2017.99

6. T. Storzer, A. Hinderhofer, C. Zeiser, J. Novák, Z. Fišer, V. Belova, B. Reisz, S. Maiti, G. Duva, R. K. Hallani, A. Gerlach, J. E. Anthony and F. Schreiber, Growth, Structure, and Anisotropic Optical Properties of Difluoro-anthradithiophene Thin Films, *J. Phys. Chem. C* **121**, 21011-21017 (2017), doi:10.1021/acs.jpcc.7b06558

7. G. Duva, L. Pithan, C. Zeiser, B. Reisz, J. Dieterle, B. Hofferberth, P. Beyer, L. Bogula, A. Opitz, S. Kowarik, A. Hinderhofer, A. Gerlach and F. Schreiber, Thin-Film Texture and Optical Properties of Donor/Acceptor Complexes. Diindenoperylene/F6TCNNQ vs Alpha-Sexithiophene/F6TCNNQ, *J. Phys. Chem. C* **122**, 18705-18714 (2018), doi:10.1021/acs.jpcc.8b03744

8. V. Belova, B. Wagner, B. Reisz, C. Zeiser, G. Duva, J. Rozbořil, J. Novák, A. Gerlach, A. Hinderhofer and F. Schreiber, Real-Time Structural and Optical Study of Growth and Packing Behavior of Perylene Diimide Derivative Thin Films: Influence of Side-Chain Modification, *J. Phys. Chem. C* **122**, 8589-8601 (2018), doi:10.1021/acs.jpcc.8b00787

9. T. Geiger, S. Schundelmeier, T. Hummel, M. Ströbele, W. Leis, M. Seitz, C. Zeiser, L. Moretti, M. Maiuri, G. Cerullo, K. Broch, J. Vahland, K. Leo, C. Maichle-Mössmer, B. Speiser and H. F. Bettinger, Modulating the Electronic and Solid-State Structure of Organic Semiconductors by Site-Specific Substitution: The Case of Tetrafluoropentacenes, *Chem. Eur. J.* **26**, 3420-3434 (2020), doi:10.1002/chem.201905843

10. V. Belova, A. Hinderhofer, C. Zeiser, T. Storzer, J. Rozbořil, J. Hagenlocher, J. Novák, A. Gerlach, R. Scholz and F. Schreiber, Structure-Dependent Charge Transfer in Molecular Perylene-Based Donor/Acceptor Systems and Role of Side Chains, *J. Phys. Chem. C* **124**, 11639-11651 (2020), doi:10.1021/acs.jpcc.0c00230

11. S. Hammer, C. Zeiser, M. Deutsch, B. Engels, K. Broch and J. Pflaum, Spatial Anisotropy of Charge Transfer at Perfluoropentacene-Pentacene (001) Single-Crystal Interfaces and its Relevance for Thin Film Devices, *ACS Appl. Mater. Interfaces* **12**, 53547-53556 (2020), doi:10.1021/acsami.0c17152

12. B. Reisz, V. Belova, G. Duva, C. Zeiser, M. Hodas, J. Hagara, P. Šiffalovič, L. Pithan, T. Hosokai, A. Hinderhofer, A. Gerlach and F. Schreiber, Polymorphism and structure formation in copper phthalocyanine thin films, *J. Appl. Cryst.* **54**, 203-210 (2021), doi:10.1107/s1600576720015472

13. C. P. Theurer, A. M. Valencia, J. Hausch, C. Zeiser, V. Sivanesan, C. Cocchi, P. Tegeder and K. Broch, Photophysics of Charge Transfer Complexes Formed by Tetracene and Strong Acceptors, *J. Phys. Chem. C* **125**, 6313–6323 (2021), doi:10.1021/acs.jpcc.0c10815

14. B. Reisz, E. Empting, M. Zwadlo, M. Hodas, G. Duva, V. Belova, C. Zeiser, J. Hagenlocher, S. Maiti, A. Hinderhofer, A. Gerlach, M. Oettel and F. Schreiber, Thin film growth of phase-separating phthalocyanine-fullerene blends: A combined experimental and computational study, *Phys. Rev. Materials* **5**, 045601 (2021), doi:10.1103/PhysRevMaterials.5.045601

Danksagung

An dieser Stelle möchte ich mich für die Unterstützung bedanken, die ich beim Erstellen dieser Arbeit erhalten habe.

An erster Stelle danke ich JProf. Dr. Katharina Broch für die Möglichkeit, diese Doktorarbeit in ihrer Arbeitsgruppe zu verfassen, sowie ihre hervorragende Betreuung in jeglicher Hinsicht. Prof. Dr. Frank Schreiber danke ich für die Zweitbetreuung und den regen wissenschaftlichen Austausch. Beiden Betreuern danke ich außerdem für die zur Verfügung gestellten Labore und Instrumente zur Herstellung und Charakterisierung der Filme. Prof. Dr. Monika Fleischer danke ich für das Erstellen eines zweiten Gutachtens dieser Arbeit.

Für die Synthese untersuchter Materialien danke ich Prof. Dr. Holger F. Bettinger sowie seinen Mitarbeitern Dr. Thomas Geiger und Lukas Kalix. Prof. Dr. Alfred J. Meixner danke ich für die Ermöglichung der TCSPC Messungen, sowie seinem Mitarbeiter Tim Rammler für deren Durchführung. Ich danke Prof. Dr. Christopher J. Bardeen und seinem Mitarbeiter Dr. Chad Cruz für die zeitaufgelösten Photolumineszenz-Messungen, sowie Prof. Dr. R. Tempelaar für die theoretischen Rechnungen und Beiträge beim Publizieren.

Ich möchte mich bei Prof. Dr. Giulio Cerullo bedanken, dass er mir im Rahmen der Kooperation der beiden Arbeitsgruppen bei mehreren Besuchen in Mailand die Möglichkeit gab, persönlich zu zeitaufgelösten Messungen beitragen zu können. Des weiteren danke ich ihm, seiner Mitarbeiterin Dr. Margherita Maiuri sowie seinem Mitarbeiter Dr. Luca Moretti für die investierte Zeit in die Messungen und ihre Beiträge beim Publizieren. Außerdem möchte ich mich bei der gesamten Arbeitsgruppe in Mailand für die außergewöhnliche Gastfreundschaft während meiner drei Besuche bedanken. Es war mir insbesondere eine große Freude mit Dr. Luca Moretti arbeiten zu dürfen, der einen großen Beitrag an der interessanten, erfolgreichen und schönen Zeit hatte.

Ich danke allen Studenten der Arbeitsgruppe von JProf. Dr. Katharina Broch, die nicht nur die Grundsteine für diese Arbeit gelegt haben, sondern auch großen Anteil daran hatten, dass die Laborarbeit stets von munterer Atmosphäre begleitet wurde. Ein großes Dankeschön insbesondere an Lisa Egenberger, Daniel Lepple, Katja Schick und Frederik Munko. Für das Korrekturlesen dieser Arbeit danke ich Madeleine Fries, Julian Hausch, Berthold Reisz, Christoph Theurer und Frederik Unger.

Ein besonderer Dank gilt Jan Hagenlocher und Madeleine Fries, mit denen ich auch abseits der Arbeit während meiner gesamten Zeit in der Promotion eine großartige Zeit und viele schöne Momente erleben durfte. Auch meinen Arbeits- und Bürokollegen Julian Hausch, Christoph Theurer und Frederik Unger bin ich sehr dankbar für die enge, unkomplizierte Zusammenarbeit, viele wissenschaftliche Diskussionen und eine stets angenehme und heitere Arbeitsumgebung. Darüber hinaus danke ich auch den gesamten Arbeitsgruppen von JProf. Dr. Katharina Broch und Prof. Dr. Frank Schreiber für eine sehr angenehme Zeit, insbesondere auch abseits des Alltags bei gemeinsamen Freizeit-Aktivitäten, Konferenzen und Klausurtagungen.

Zu guter Letzt gilt ein riesiger Dank meinen Eltern, meiner Schwester, sowie meiner Partnerin Yvonne für die Geduld und die ausnahmslos großartige Unterstützung während dieser Zeit.